Solid Supported Model Membranes Containing Plant Glycolipids: A Tool to Study Interactions between Diatom Biomolecules and the Silicalemma *in vitro*

Dissertation
for the award of the degree

Doctor rerum naturalium

of the Georg-August University of Göttingen

within the doctoral program of the
Georg-August University School of Science (GAUSS)

submitted by

Oliver Gräb
from Kassel

Göttingen, 2017

MEMBERS OF THE THESIS COMMITTEE:

Prof. Dr. Claudia Steinem,
Institute of Organic and Biomolecular Chemistry,
Georg-August University of Göttingen

Prof. Dr. Daniel J. Jackson,
Geoscience Centre,
Georg-August University of Göttingen

MEMBERS OF THE EXAMINATION BOARD:

Prof. Dr. Burkhard Geil,
Institute of Physical Chemistry,
Georg-August University of Göttingen

Prof. Dr. Bert de Groot,
Max Planck Institute for Biophysical Chemistry, Göttingen

Dr. Jochen Hub,
Department of Molecular Structural Biology,
Georg-August University of Göttingen

Dr. Sebastian Kruss,
Institute of Physical Chemistry,
Georg-August University of Göttingen

DATE OF ORAL EXAMINATION:

June 13th, 2017

DECLARATION

I, Oliver Gräb, hereby certify that my doctoral thesis entitled “Solid Supported Model Membranes Containing Plant Glycolipids: A Tool to Study Interactions between Diatom Biomolecules and the Silicalemma *in vitro*” has been written independently and with no other sources and aids than quoted.

Göttingen, 2017

Oliver Gräb

Meiner Familie

ABSTRACT Silica biomineralization in diatoms is presumably controlled by a self-assembly of biomolecules inside membrane-enclosed silica deposition vesicles. The fine-patterned structure of the diatom's cell wall is thereby determined by the morphology of the templating organic matrix. Several studies addressed self- or co-aggregation of silica-associated biomolecules in solution but no research focusing on the influence of the organelle surrounding lipid bilayer was published so far.

This study aimed on the investigation of interactions between exemplary diatom biomolecules and lipid membranes *in vitro*.

As a basis for all experiments, protocols for the preparation of solid supported model membranes, mimicking the overall lipid composition of diatoms and containing the three glycolipids monogalactosyldiacylglycerol, digalactosyldiacylglycerol and sulfoquinovosyl-diacylglycerol were established. Artificial model membranes were successfully prepared and characterized on hydrophobically functionalized gold and glass supports as well as on hydrophilic silicon dioxide and mica surfaces.

These model systems were first applied to study the interactions of two exemplary recombinant cingulins with lipid membranes. Cingulins show structural similarities to silaffins and were recently identified as part of the organic matrix inside the diatom biosilica. Adsorption measurements revealed no significant interactions between these proteins and lipid membranes.

In addition, long-chain polyamines (LCPA) marked a second class of biomolecules localized in the diatom biosilica and were used in this study as well. LCPA are known to aggregate in solution and catalyze silica precipitation. Herein, for the first time, synthetic LCPA with molecular masses matching the range of LCPA isolated from diatoms were investigated with regard to their interaction with lipid membranes. Upon adsorption of LCPA the formation of membrane stacks was observed and characterized. These stacks were formed from vesicles in solution and were proven to be connected to the underlying membrane. While stack formation was found to be independent of the membrane composition, a clear dependency on polyamine chain-length was observed since only LCPA with more than five amine groups mediated stack formation.

ZUSAMMENFASSUNG Die Silika-Biomineralisation in Kieselalgen wird vermutlich durch aggregierte Biomoleküle innerhalb der Silika-Ablagerungsvesikel kontrolliert. Die Struktur der gebildeten Zellwand wird dabei durch die Morphologie der organischen Vorlage definiert. Mehrere Studien haben sich bereits mit der Selbst- und Co-Aggregation verschiedener Biomoleküle in Lösung beschäftigt, aber es wurden bisher noch keine Forschungen zum Einfluss der Organell-umschließenden Lipiddoppelschicht durchgeführt.

Diese Studie zielte auf die Untersuchung von Wechselwirkungen zwischen beispielhaften Kieselalgenbiomolekülen und Lipidmembranen *in vitro* ab.

Als Grundlage für alle Experimente wurden Protokolle für die Präparation festkörperunterstützter Modellmembranen entwickelt, die die Gesamtlipidzusammensetzung von Kieselalgen widerspiegeln und die drei Glycolipide, Monogalactosyldiacylglycerol, Digalactosyldiacylglycerol und Sulfoquinovosyldiacylglycerol, enthalten. Künstliche Modellmembranen konnten sowohl auf hydrophob funktionalisiertem Gold und Glas als auch auf hydrophilen Siliziumdioxid- und Glimmeroberflächen erzeugt und charakterisiert werden.

Diese Modellsysteme wurden zuerst für die Untersuchung der Wechselwirkung zweier exemplarischer, rekombinanter Cinguline mit Lipidmembranen angewandt. Cinguline zeigen strukturelle Ähnlichkeiten zu Silaffinen und wurden kürzlich als Teil der organischen Matrix innerhalb des Kieselalgenbiosilikas identifiziert. Adsorptionsmessungen zeigten keine signifikanten Wechselwirkungen dieser Proteine mit Lipidmembranen.

Zusätzlich wurde mit langkettigen Polyaminen (englisch *long-chain polyamines*, LCPA) eine zweite Klasse von Biomolekülen untersucht, die ebenfalls im Kieselalgenbiosilika lokalisiert wurden. Es ist bekannt, dass LCPA in Lösung aggregieren und die Silikafällung katalysieren. In dieser Arbeit wurden zum ersten Mal LCPA, deren molekulare Massen denen aus Kieselalgen isolierten Molekülen entsprachen, im Hinblick auf ihre Wechselwirkung mit Lipidmembranen untersucht. Nach Adsorption der LCPA wurde die Bildung von Membranmultischichten beobachtet und charakterisiert. Diese Multischichten wurden aus Vesikeln aus der Lösung gebildet und es konnte eine Verbindung zur unterliegenden Membran nachgewiesen werden. Während die Multischichtbildung von der Membran-zusammensetzung unabhängig war, zeigte sich eine klare Abhängigkeit von der Kettenlänge der LCPA. Mehr als fünf Aminogruppen waren für die Multischichtbildung nötig.

CONTENTS

1 INTRODUCTION 1

1.1 Biomineralization 1

1.2 Diatoms 1

1.2.1 Cell Wall Biogenesis 2

1.2.2 Biomolecules Involved in Silica Formation 3

1.2.3 Shaping the Silica Cell Wall 7

1.2.4 Lipid Composition of Diatoms 8

1.3 Artificial Model Membranes 10

2 SCOPE OF THESIS 13

3 MATERIALS AND METHODS 15

3.1 Used Materials 15

3.1.1 Lipids 15

3.1.2 Polyamines 18

3.1.3 Silicic Acid 21

3.2 Proteinbiochemical Methods 22

3.2.1 Recombinant Cingulin W2 22

3.2.2 Recombinant Cingulin Y3 29

3.3 Lipidchemical Methods 30

3.3.1 Overview on Preparation Conditions 30

3.3.2 Vesicle Preparation 31

3.3.3 Solid Supported Lipid Monolayers 32

3.3.4 Solid Supported Lipid Bilayers 34

3.4 Biophysical Methods 35

3.4.1 Lipid Characterization by Nuclear Magnetic Resonance Spectroscopy and Surface Pressure-Area Isotherms 35

3.4.2 Surface Plasmon Resonance Techniques 41

3.4.3 Reflectometric Interference Spectroscopy 45

3.4.4 Electrochemical Impedance Spectrometry 47

3.4.5 Fluorescence Microscopy 49

3.4.6 Atomic Force Microscopy 55

3.4.7 Contact Angle Measurements 58

4 MODEL MEMBRANES 61

4.1 Surface Areas of Plant Lipids 62

4.2 Solid Supported Lipid Monolayers 66

4.2.1 Thiol-Functionalized Gold Surfaces 66

4.2.2 Silanized Glass Surfaces 70

4.3 Solid Supported Lipid Bilayers 73

4.3.1 Hydrophilized Silicon Dioxide 74

4.3.2 Mica Surfaces 76

4.4 Discussion 79

4.4.1 Surface Pressure Area Isotherms 79

4.4.2 Solid Supported Model Membranes 81

5 CINGULINS 87

5.1 Cingulin W2 88

5.1.1 Protein Isolation 88

5.1.2 Protein Solubility 91

5.1.3 Protein-Membrane Interactions 93

5.2 Cingulin Y3 94

5.2.1 Protein-Membrane Interactions 95

5.3 Discussion 96

5.3.1 Protein Isolation and Solubility 97

5.3.2 Protein-Membrane Interactions 100

6 LONG-CHAIN POLYAMINES 103

6.1 Adsorption on Membrane-Covered Surfaces 104

6.2 Fluorescence Imaging 106

6.3 Characterization of LCPA-Induced Structures 107

6.3.1 Localization of Polyamines 108

6.3.2 Quantification of Fluorescence Intensities 109

6.3.3 Topography of LCPA-Induced Domains 110

6.3.4 Fluorescence Recovery after Photobleaching 112

6.3.5 Experiments on Lipid Monolayers 114

6.4 Requirements for Membrane Stacking 115

6.4.1 Origin of Lipid Material 116

6.4.2 Influence of Lipid Composition 121

6.4.3 Influence of Polyamine Chain Length ... 125
6.5 Silica Precipitation on Membrane Surfaces ... 126
6.6 Discussion ... 128
6.6.1 LCPA Adsorption and Fluorescence Imaging ... 129
6.6.2 Characterization of Membrane Stacks ... 131
6.6.3 Requirements for LCPA-Induced Membrane Stacking ... 138
6.6.4 Silica Precipitation on Membrane Surfaces ... 148
6.6.5 LCPA-Membrane Interactions in the SDV ... 149
7 CONCLUSION ... 151
APPENDIX ... VII
Amino Acid Sequences of Cingulins ... vii
Self-Written Scripts for Data Analysis ... ix
List of Symbols and Abbreviations ... xi
List of Chemicals and Consumables ... xiii
List of Devices and Software ... xvi
List of Figures ... xvii
List of Tables ... xxii
BIBLIOGRAPHY ... XXIII

1 INTRODUCTION

1.1 Biomineralization

The connection between biological processes and inorganic mineralization started already 3.5 billion years ago – approximately 1 billion years after the formation of earth – with the generation of stromatolites.[1] Since these early days of life on earth, organisms perfected the deposition of inorganic material, so called biominerals, formed in the process of biomineralization.[2] Impressive examples can be found in the invertebrate shells and vertebrate skeletons, both made out of calcium carbonates or calcium phosphates.[3,4] Ever since, those biominerals have been a great inspiration for scientists, looking for new materials.[5] Nature has not only developed strategies to precisely control the structure of biominerals but also to carry out their deposition under ambient conditions. One other prominent example is the formation of silica by diatoms. Industrial synthesis of silica requires extreme conditions regarding temperature, pH and pressure.[6] In contrast, biomineralization in diatoms is carried out under physiological conditions with impressive control over the structure of the formed material.

1.2 Diatoms

Nearly all marine environments are inhabited by diatoms, small unicellular algae that appeared first about 185 million years ago.[7] Since diatoms are capable of photosynthesis, they contribute to about a fifth of global CO_2 fixation.[7] Up to today over 10 thousand different species are known[8] but the total number is estimated to be at least 200 thousand.[9] Each of these species is protected by a cell wall made of amorphous silica and with a species-specific shape (see **Figure 1.1 A**).[10] The silica cell wall does not only provide mechanical stability and protection against predators[11] but also might act as pH buffer[12] or photolytic crystal.[13] The schematic structure of a diatom cell wall is illustrated in **Figure 1.1 B**.

The diatom enclosing silica cell wall can be compared to a petri dish containing two overlapping parts: a larger one, called epitheca, and a smaller one, called hypotheca.[14] Each of these two parts consists of a valve part at the top or bottom and several girdle bands that expand the halves and overlap in the middle. In general diatoms can be divided into three subgroups in regard to the symmetry of their cell wall: radial centrics, polar centrics and pennates. For all of them both the valve and the girdle band parts exhibit a fine patterned, hierarchical pore structure.[15–17]

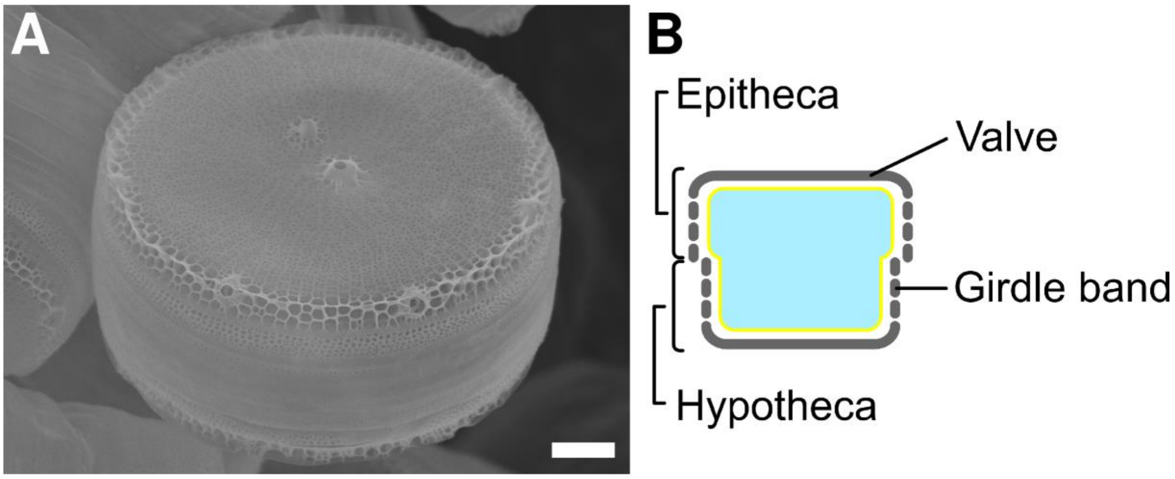

Figure 1.1. Electron micrograph of the diatom species *Thalassiosira oceanica* (A, scale bar: 1 µm). The image was provided by courtesy of DAMIAN PAWOLSKI from the group of PROF. DR. NILS KRÖGER (B CUBE, Technical University of Dresden). A cross-section showing both parts of the diatom cell wall is illustrated in B.[14]

1.2.1 Cell Wall Biogenesis

Electron micrographs revealed the formation of fragments of the diatom’s cell wall in membrane-enclosed compartments, the so called silica deposition vesicles (SDVs).[18–20] The lipid bilayer enclosing the organelle is called silicalemma. Similar strategies to localize biomineralization processes in highly specified, vesicular compartments were also observed in several other silica-forming organisms, for example sponges, radiolarians, synurophytes and choanoflagellates.[21] Such organelles enable local fine tuning of reaction conditions as for example the pH, which in case of diatom SDVs was found to be acidic.[22] Silicic acid, the monomeric precursor for the formation of silica, is enriched in the SDVs by specific silica transporter proteins[23–27] and silica transportation vesicles.[28] The local silicon concentration can thereby be increased from the micromolar level in the surrounding aqueous environment up to several hundred millimolar in the SDV.[29,30] Since monomeric silicic acid is only stable up to a concentration of about 1 µM,[31] polymerization has to be prohibited by a molecular machinery as well, before directed biomineralization is facilitated. Cell wall formation is mainly carried out during and short after cell division. **Figure 1.2** illustrates the different steps involved in this process.[14]

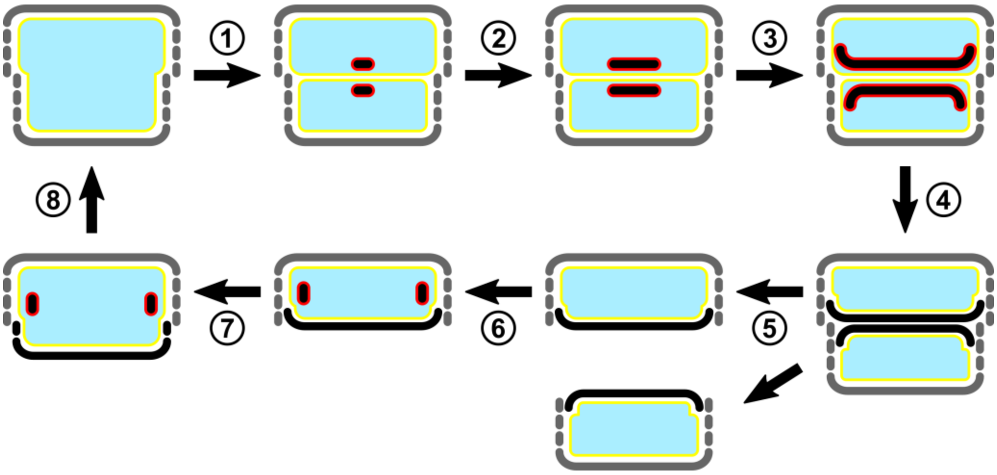

Figure 1.2. Schematic illustration of the diatom cell cycle. After division of the protoplast (1) new valves are formed inside SDVs at the interface between both new cells (2,3). The cell wall fragments are afterwards released by exocytosis (4) and the cells separate (5). During growth the cell wall is expanded by stepwise elongation of the girdle band region (6–8).[14]

Division of the protoplast takes place inside the cell wall encapsulated compartment. One of the newly formed cells is localized in the epitheca, the other one in the hypotheca. At the interface between both cells new valves are formed inside expanding SDVs. Once completed, the valve is released by exocytosis and both cells disengage. During further growth of the new diatom cells, the cell wall is expanded by elongation of the girdle band region. As a consequence of sequential cell division, diatom cells shrink in size after every division. To overcome this problem, diatoms are also able to replicate via sexual reproduction.[14]

1.2.2 Biomolecules Involved in Silica Formation

As mentioned before, the structure and patterning of the diatom cell wall is species-specific.[10] Hence, structural information has to be encoded within the diatom's genome and translated by a sophisticated biomolecular machinery into precisely shaped silica particles.[32] Deciphering of the involved machinery would not only provide new insight into processes *in vivo* but might also enable new *in vitro* strategies to synthesize nanometer-sized particles with well-defined structure and possible applications for example in drug delivery.[33]

As many other biominerals, the silica cell wall of diatoms is a composite material composed of inorganic silica and organic components.[34] As these components end up inside the biosilica, they might be directly involved in controlling silica biomineralization. A common way to identify the organic material is by dissolution of silica with HF or NH_4F yielding a soluble, biomolecule-containing fraction as well as insoluble organic microrings and microplates.[35,36] The composition of those fractions can then be further analyzed for example by means of mass spectrometry. Within the past years several classes of biosilica-associated biomolecules have been identified, including long-chain polyamines (LCPA)[37], silaffins[38], silacidins[39], cingulins[35] and pleuralins[40] as well as a chitin network.[41] Detailed overviews on those biomolecules, their discovery and function are given for example in the review articles by Kröger and Poulsen[14] or Lechner and Becker.[42] Herein only three exemplary biomolecule classes, most relevant for this study, will be presented in detail.

Long-Chain Polyamines

LCPA were first isolated by Kröger *et al.* in 2000.[37] After dissolution of biosilica in liquid HF, these biomolecules were found in the soluble fraction. Structural analysis was carried out using mass spectrometry. An overview on the structure of LCPA is given in **Figure 1.3**.

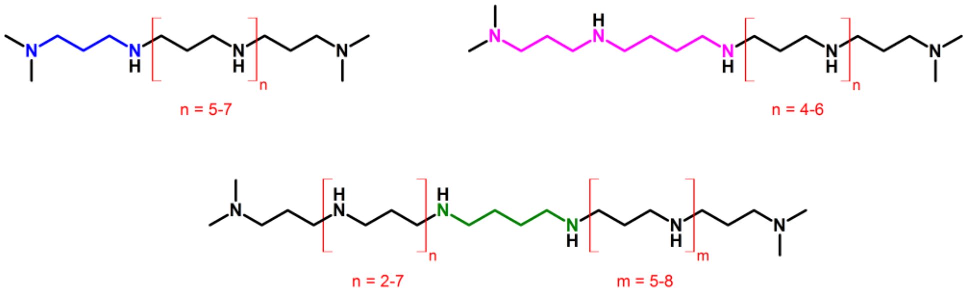

Figure 1.3. Chemical structures of LCPA from diatoms. The precursor molecules propyldiamine (blue), putrescine (pink) and spermidine (green) are emphasized.[14]

In general LCPA consist of a propyldiamine, putrescine or spermidine moiety, elongated with linear oligo-propyleneimine chains. Additionally, amine groups can be methylated. For their study Kröger *et al.* isolated LCPA from six different diatom species.[37] Masses of the isolated LCPA were typically in the range of 600–1500 $g\cdot mol^{-1}$ but significant differences in mass distribution between different species were observed. Hence, a direct influence of the LCPA structure on the patterning of the formed diatom cell wall was postulated. Also in this very first study the influence of LCPA on silicic acid polycondensation was investigated.

An accelerating effect of LCPA was observed leading to the deposition of spherical silica particles. The study on LCPA-induced silica precipitation was later intensified by, among others, BERNECKER *et al.* who observed an aggregation of LCPA in presence of phosphate anions into droplets which later become encapsulated with a shell of silica.[43] Regarding the underlying mechanism, an acid-base catalysis for the condensation reaction by the amine groups inside the molecules was discussed (see **Figure 1.4**).[44]

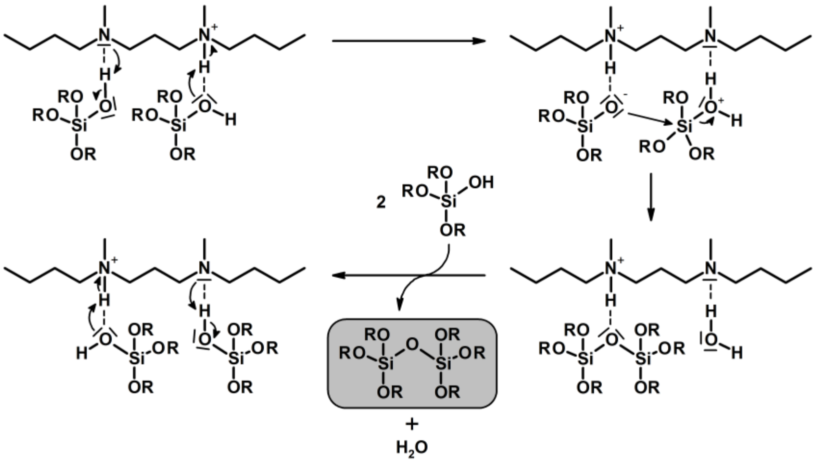

Figure 1.4. Postulated mechanism for acid-base catalysis of silicic acid polycondensation by polyamines. A proton transfer is carried out via the amine groups of the LCPA.[44]

A general problem regarding early studies on LCPA and their influence on silica precipitation was the poor availability of native LCPA or synthetic polyamines with similar molecular mass. Thus, model components like polyethyleneimine[45–48] were used as substitutes. Total synthesis of polyamines with physiological relevant chain lengths was first established in the group of PROF. DR. ARMIN GEYER (see **Chapter 3.1.2** for details) and published by BERNECKER *et al.* in 2010.[43]

Silaffins

Besides LCPA the soluble fraction after dissolution of diatom biosilica with HF also contained proteins. One class of these proteins with high silica affinity was isolated from *Cylindrotheca fusiformis* (*C. fusiformis*), identified by KRÖGER *et al.* and respectively called silaffins.[38,49] Their amino acid composition turned out to be very restricted containing high contents of serine (36%), lysine (20%) and glycine (15%). Lysine moieties are mainly localized in KXXK sequences with two other amino acids in between. Replacement of HF by NH_4F for silica dissolution enabled the isolation of native silaffins and revealed numerous

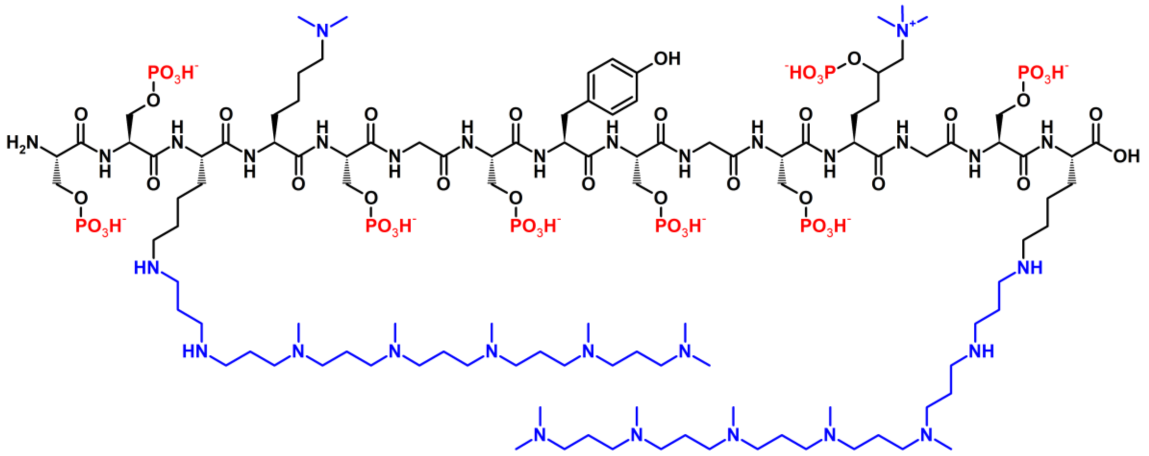

Figure 1.5. Structure of native Silaffin-1A$_1$ from *C. fusiformis*.[50] Aliphatic hydroxyl groups are phosphorylated (red) and lysine residues are either methylated or extended with polyamine chains (blue).

posttranslational modifications.[50,51] These modifications include phosphorylation of hydroxyl groups as well as methylation of lysine residues and extension by polyamine chains (see **Figure 1.5**).

Silaffin proteins were also isolated from other diatom species.[52–55] Interestingly those proteins do not only vary in primary structure and posttranslational modifications, they also exhibit drastically different influences on silica precipitation (see **Table 1.1**). While some showed an accelerating effect, others did not increase silica precipitation from solution. A good overview on the properties of different silaffins is given for example in a review paper by Lechner and Becker.[42]

Table 1.1. Overview on posttranslational modifications in silaffins of different diatom species as well as their influence on silica precipitation. Data was compiled by Lechner and Becker.[42]

Diatom species	Silaffin	Posttranslational modifications		Silica precipitation activity
		at lysine	at hydroxyl amino acids	
Cylindrotheca fusiformis	silaffin-1A silaffin-1B	methylations and polyamine modification at ε-amino group; hydroxylation and phosphorylation at δ-position	phosphorylation	yes
	silaffin-2		sulfation, glycosylation and phosphorylation	no
Thalassiosira pseudonana	tpSil1p tpSil2p tpSil3p tpSil4p	methylations and polyamine modification at ε-amino group; hydroxylation and phosphorylation at δ-position	sulfation, glycosylation and phosphorylation	no
Eucampia zodiacus		methylations and polyamine modification at ε-amino group	*not analyzed*	*not analyzed*
Chaetoceros gracilis		*not analyzed*	*not analyzed*	yes

Cingulins

In 2004 the genome of *Thalassiosira pseudonana* (*T. pseudonana*) was analyzed and published by ARMBRUST *et al*.[56] This landmark study opened new ways in diatom research. In 2011 SCHEFFEL *et al.* used the data to search for silaffin-like proteins in *T. pseudonana*.[35] Those proteins should contain domains (≥ 100 amino acids) with high contents of serine (≥ 18%) and lysine (≥ 10%) as well as an *N*-terminal endoplasmic reticulum signal peptide. In the end, six proteins with yet unknown function were revealed: three tyrosine-rich cingulins (CinY1–3) and three tryptophan-rich cingulins (CinW1–3, see **Figure 1.6**)

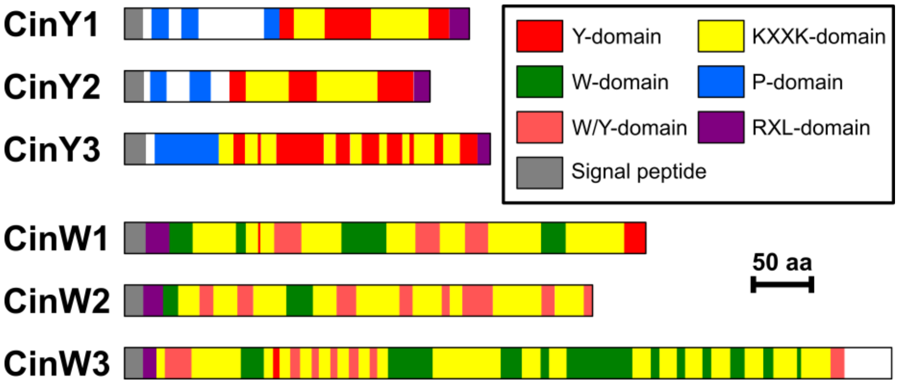

Figure 1.6. Schematic illustration of cingulin primary structures. The different domains inside the proteins are emphasized. In general cingulins can be divided into tyrosine-rich (Y-cingulins) and tryptophan-rich proteins (W-cingulins).[35]

SCHEFFEL *et al.* were also able to localize green fluorescent protein-fusion proteins in the girdle band region of diatoms.[35] Since those proteins became entrapped inside the biosilica, a direct participation in control of silica biomineralization was postulated. KOTZSCH *et al.* were later able to identify cingulins in the organic microrings remaining after dissolution of biosilica and discovered a seventh member of the cingulin family in *T. pseudonana* (CinY4).[36] Furthermore they revealed a silica forming activity of recombinant cingulins, strengthening their postulated role in cell wall genesis.

1.2.3 Shaping the Silica Cell Wall

Since several biomolecules have been identified in the biosilica and were predicted to play a crucial role in silica biomineralization, the most important question is still unanswered: How do these biomolecules direct silicic acid polymerization and thus shape the diatom's cell wall? Within the past years several models have been developed that include processes inside and outside the SDV.[14] While growth and aggregation of silica particles in general could be limited by diffusion inside the SDV,[57] biomolecules inside the organelle could also influence aggregation of silica particles[58] or directly regulate their formation.[48,59] *In vitro* studies demonstrated an aggregation of LCPA in presence of phosphate ions in solution.[43,46] The structure of LCPA does not only affect the size of these aggregates but also of the silica particles precipitated from solution. *In vivo* silica precipitation could be regulated for example by co-aggregation of LCPA and silaffins, thereby shaping the cell wall fragments (see **Figure 1.7**).[14]

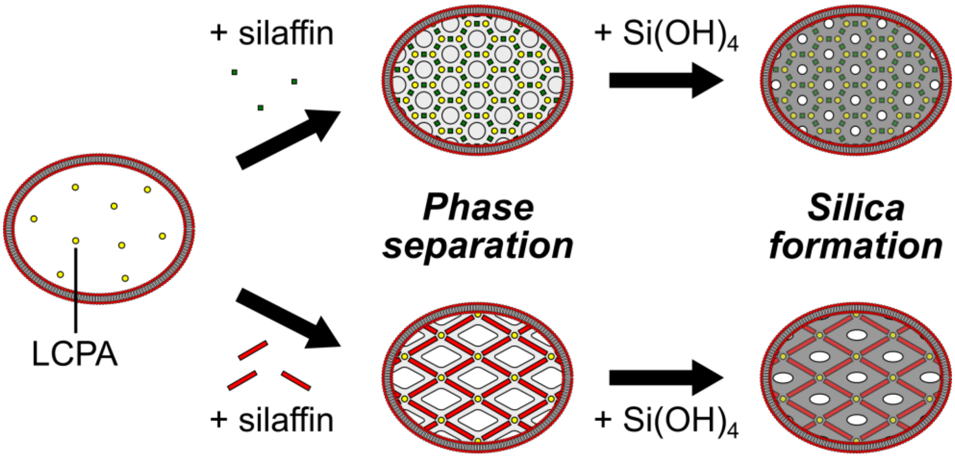

Figure 1.7. Phase separation model for the control of silica morphogenesis by aggregates of biomolecules (*e.g.* LCPA and silaffins) inside the SDV. Depending on the structure of the individual biomolecules, the template's shape is altered. Silica deposition is catalyzed by the biomolecules as well.[14]

In addition to soluble components, dissolution of biosilica revealed insoluble microrings and microplates containing cingulins and other so called silica matrix proteins.[35,36] These organic structures show many similarities to the silicified diatom cell wall and might most likely act as a matrix for cell wall formation after interaction with soluble biomolecules.

Besides internal aggregation of biomolecules inside the SDV, external factors, like interactions with the cytoskeleton, might also influence molecular organization within the organelle.[60,61] Still unaddressed is the question if and how the SDV enclosing silicalemma influences template formation inside the organelle.

1.2.4 Lipid Composition of Diatoms

Up to this day the SDV has not been isolated, thus no data on the exact lipid composition of the silicalemma exists. However, the overall lipid composition of diatoms was investigated for example by KATES and VOLCANI.[62] As with many other algae, the predominant lipid classes in diatoms are the three glycolipids monogalactosyldiacylglycerol (MGDG), digalactosyldiacylglycerol (DGDG) and sulfoquinovosyldiacylglycerol (SQDG).[63–65] A more detailed study on the overall lipid composition of the diatom species *Cyclotella meneghiniana* (*C. meneghiniana*) was published in 2007 by Vieler *et al*.[66] An overview on their data gathered by a combination of thin-layer chromatography and mass spectrometry is given in **Table 1.2**.

Table 1.2. Overall lipid composition of the diatom *C. meneghiniana* reported by Vieler *et al*.[66] R^1 and R^2 represent alkyl chains of the fatty acids which vary in length and degree of saturation. Lipid ratios are given as molar ratios.

Lipid	MGDG	DGDG	SQDG	PG	PC
General lipid structure	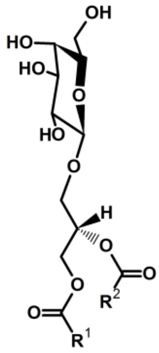	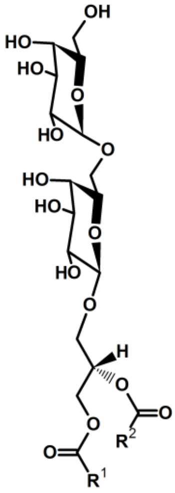	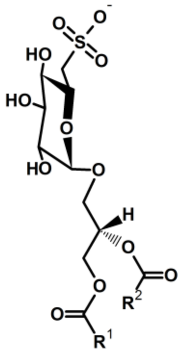	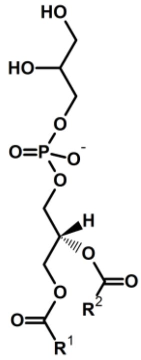	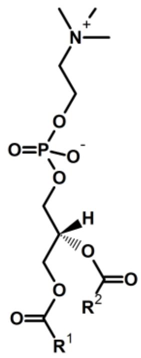
Lipid ratio in *C. meneghiniana*	33.7%	17.5%	24.7%	15.4%	8.7%

The three glycolipids, MGDG, DGDG and SQDG, are among the most occurring lipids on earth as they are the main lipids in thylakoids of photosynthetic organisms.[67–71] Mainly caused by their sugar containing headgroups, some quite unique properties of these lipids have been observed.

Interestingly the most abundant polar lipid in nature, unsaturated MGDG, is in general a non-bilayer forming lipid.[71] Instead, MGDG aggregates in aqueous solution into inverted tube-like structures (H_{II}).[72] MGDG can still be incorporated into lamellar structures alongside at least 50% of bilayer-forming lipids[73,74] and aggregation behavior is also altered by an increase in saturation.[75] In contrast to MGDG, DGDG forms lamellar structures in the L_α phase independent of the degree of saturation.[74] While both of these lipids are neutral, SQDG carries a sulfonic acid moiety in its sugar headgroup which results in a negative net charge in a wide pH region.[76]

Despite MGDG, DGDG and SQDG being ubiquitous in nature, only a few studies included all of them into artificial model membranes (see **Chapter 1.3**) to study their properties *in vitro*. Most of the work published so far focused on the preparation and investigation of lipid vesicles [77–82] and black lipid membranes.[83] On the other hand some studies employed lipid monolayers at the air-water interface or transferred onto solid supports by LANGMUIR-BLODGETT technique which incorporated these glycolipids.[67,84,85] Still no data on the preparation of protein-free solid supported lipid mono- and bilayers by vesicle spreading, reflecting the overall lipid composition of diatoms[66], has been reported.

1.3 Artificial Model Membranes

Native cell membranes are complex assemblies that do not only consist of a lipid bilayer but also harbor a variety of different membrane proteins. To be able to study processes involving biomembranes under well-defined conditions, model systems have been established. These models do not only enable the study of protein-membrane interactions *in vitro*, but also allow the investigation of the influence of certain membrane components (*e.g.* specific receptor lipids) on the interactions. An overview on different artificial model membranes, each with individual advantages and disadvantages regarding stability and addressability, is given in **Figure 1.8**.[86–89]

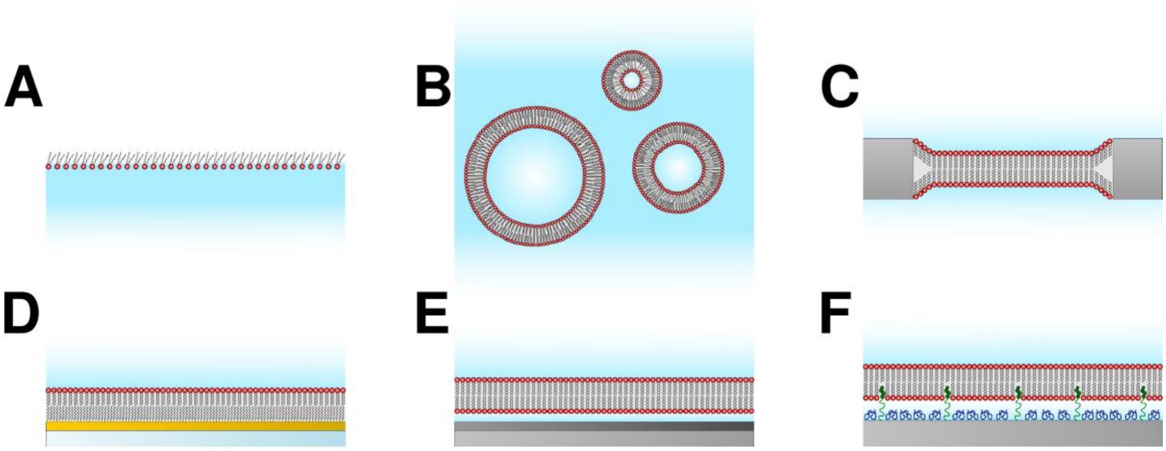

Figure 1.8. Six exemplary artificial model membrane systems: lipid monolayers at air-water interfaces (A), vesicles (B), black lipid membranes (C), solid supported lipid monolayers (D), solid supported lipid bilayers (E) and tethered membranes (F).[86]

Lipid monolayers can be prepared at the interface between a hydrophilic (*e.g.* water) and a hydrophobic medium (*e.g.* air, see **Figure 1.8 A**). Due to their amphiphilic nature, lipids self-assemble at the interface. Besides investigation of physical properties of the lipid layers, these model membranes provide a membrane surface that allows interactions with biomolecules from within the hydrophilic medium.[90] Lipid vesicles on the other hand are spherical lipid bilayers formed in aqueous solution (see **Figure 1.8 B**). Diameters of vesicles can reach from tens of nanometers (small vesicles) up to the size of cells with several micrometers (giant vesicles).[89] Since vesicles circumvent an aqueous compartment, they are widely used to study transport processes through lipid bilayers.[91] Two aqueous compartments can also be separated by black lipid membranes (see **Figure 1.8 C**). Lipids in organic solvent are applied to a small hole for example inside a Teflon foil. Depletion of the solvent leads to formation of a lipid bilayer spanning the hole. This model system is often used for electrochemical characterization of membranes and transport processes as both aqueous media are easily addressable.[92] An increase in long-term membrane stability can be provided by deposition of lipid membranes on solid supports.[86,87] This technique also enables the use of surface sensing techniques to probe for example membrane properties and biomolecule-membrane interactions. Solid supported membranes can be further divided by the nature of the support.[88] Lipid monolayers are deposited on hydrophobic surfaces (see **Figure 1.8 D**) while lipid bilayers can be prepared on hydrophilic surfaces (see **Figure 1.8 E**).[93] The space between the lipid membrane and the support can be increased for example by preparing tethered membranes (see **Figure 1.8 F**). Linkage is provided by molecules bound on one end to the surface and intercalate with the other end (*e.g.* via phospholipid or sterol groups) into a lipid bilayer. Tethered membranes are widely used to incorporate transmembrane proteins into solid supported model membranes.[94,95]

2 SCOPE OF THESIS

Formation of fine-patterned silica cell wall fragments in diatoms takes place in silica deposition vesicles, organelles enclosed by a lipid bilayer, the silicalemma. Within the past years several biomolecules including long-chain polyamines (LCPA), silaffins, silacidins, cingulins and pleuralins were identified that become incorporated into newly formed biosilica during cell wall biogenesis. Hence these molecules might be directly involved in catalyzing silicic acid polycondensation as well as shaping of the cell wall. Several studies revealed aggregation of these biomolecules in solution and proved their silica precipitating activity, leading to the proposal of a phase-separation model for templated silica formation. Yet unaddressed is the influence of the silicalemma enclosing the organelle. Biomolecule-membrane interactions can influence molecule aggregation and thereby shape the organic template for cell wall formation.

In this study, for the first time, interactions between two different classes of diatom biomolecules, synthetic LCPA and cingulins, and artificial model membranes, mimicking the silicalemma, were investigated *in vitro*.

Lipid membranes in diatoms are mainly composed of the three glycolipids monogalactosyldiacylglycerol, digalactosyldiacylglycerol and sulfoquinovosyldiacylglycerol. Even since these lipids are the most occurring lipids on earth, they have rarely been incorporated into artificial model membranes. Up to this point no studies reported the formation of protein-free solid supported lipid membranes by vesicle spreading that contain all of the three glycolipids. Thus protocols for the preparation of solid supported lipid mono- and bilayers on various supports were developed. Lipid mixtures should reflect the overall lipid composition of diatoms as close as possible and the model membranes should allow further investigations of biomolecule-membrane interactions by various surface-sensing techniques.

The first class of diatom biomolecules investigated in this study was the cingulins. Two exemplary cingulins, tyrosine-rich rCinY3 and tryptophan-rich rCinW2, were expressed as recombinant proteins in *Escherichia coli*, extracted and purified. The adsorption of cingulins on solid supported lipid membranes was studied as well as the stability of cingulins in solution.

In addition to cingulins, LCPA and their interactions with lipid membranes were investigated. For the first time synthetic polyamines with molecular masses in the range of LCPA isolated from diatoms were studied in regard to their interaction with lipid membranes. Beside quantification of LCPA adsorption, influences of LCPA on the membrane structure were analyzed by several techniques. Additionally the effect of LCPA adsorbed on membrane surfaces on silicic acid polycondensation was investigated.

Overall this study should shed light on the role and the involvement of the silicalemma into diatom cell wall formation in the silica deposition vesicle. Besides expanding the current knowledge about biomineralization in diatoms and other silica forming organisms, the understanding of diatom biomolecule-membrane interactions could open new ways in fabrication of new materials with fine-patterned structure in the nanometer range and possible applications in medicine and material science.

3 MATERIALS AND METHODS

3.1 Used Materials

3.1.1 Lipids

In order to mimic the lipid composition of diatoms[66], mixtures of the five major lipid components were used. All lipids were commercially available and were either isolated from plants or synthesized. To study membrane properties by means of fluorescence microscopy synthetic fluorescent labeled lipids were deployed.

Monogalactosyldiacylglycerol

The neutral galactolipid monogalactosyldiacylglycerol (MGDG) contains a polar 1-*β*-galactose linked to the *sn*-3 position of a central glycerol. Both *sn*-1 and *sn*-2 hydroxyl groups are esterified to two long-chain acyl groups forming the hydrophobic part of the molecule. MGDG used in this study was either obtained from Avanti Polar Lipids (Alabaster, US) or Larodan (Solna, SE) and has been isolated from plant leafs. The predominant species in the isolated mixture is MGDG 16:3/18:3 containing a hexadecatrienoic acid and a linolenic acid (see **Figure 3.1**).

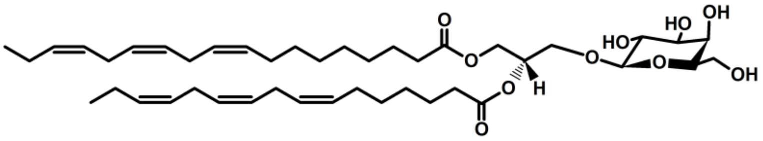

Figure 3.1. Structure of the predominant component of isolated monogalactosyl-diacylglycerol (MGDG 16:3/18:3). Average molar mass M = 752 g·mol^{-1}.

Digalactosyldiacylglycerol

In contrast to MGDG, the digalactosyldiacylglycerol (DGDG) headgroup contains *α*-galactose-(1,6)-*β*-galactose attached via a *β*-glycosidic linkage to the *sn*-3 hydroxyl group of a central glycerol. Isolated DGDG purchased from Avanti Polar Lipids (Alabaster, US) or Larodan (Solna, SE) predominantly contained two linolenic acids (DGDG 18:3/18:3, see **Figure 3.2**).

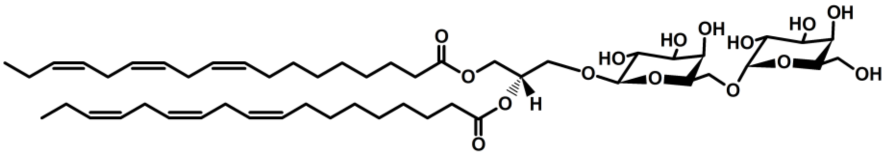

Figure 3.2. Structure of the predominant component of isolated digalactosyldiacylglycerol (DGDG 18:3/18:3). Average molar mass *M* = 927 g·mol^{-1}.

Sulfoquinovosyldiacylglycerol

The anionic glycolipid sulfoquinovosyldiacylglycerol (SQDG) carries a *β*-glycosidic linked 6-deoxyglucose headgroup which contains a sulfonic acid group at C-6 position. The predominant component of isolated SQDG (from Larodan, Solna, SE) contained a saturated palmitic acid at *sn*-2 and a polyunsaturated linolenic acid at *sn*-1 (SQDG 16:0/18:3, see **Figure 3.3**).

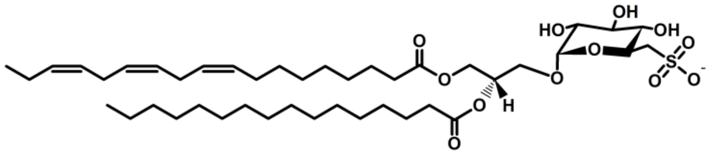

Figure 3.3. Structure of the predominant component of isolated sulfoquinovosyldiacylglycerol (SQDG 16:0/18:3). Average molar mass *M* = 834 g·mol^{-1}.

1-Palmitoyl-2-oleoyl-*sn*-glycero-3-phosphoglycerol

The polar headgroup of the phospholipid 1-palmitoyl-2-oleoyl-*sn*-glycero-3-phosphoglycerol (POPG) is formed by a glycerol moiety esterified to a phosphate group which is linked to the glycerol backbone of the lipid at *sn*-3 position. The synthetic lipid contains a defined fatty acid composition with a palmitic acid (16:0) at *sn*-1 and an oleic acid (18:1) at *sn*-2 position (see **Figure 3.4**). Its main phase transition temperature is –2 °C.[96] Deprotonation of the phosphate group even under mild acidic conditions results in an overall negative charge of the lipid.

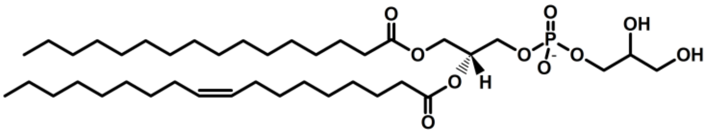

Figure 3.4. Structure of 1-palmitoyl-2-oleoyl-*sn*-glycero-3-phospho-(1'-*rac*-glycerol) (POPG). Molar mass *M* = 748 g·mol^{-1}.

1,2-Dioleoyl-*sn*-glycero-3-phosphocholine

1,2-Dioleoyl-*sn*-glycero-3-phosphocholine (DOPC) is a phospholipid with a choline moiety esterified to a phosphate group at the *sn*-3 position of the glycerol backbone. The deprotonated, negatively charged phosphate group and the permanently positively charged quaternary ammonium group cause an overall neutral, zwitterionic structure. The hydrophobic part of the lipid is formed by two oleic acids (18:1) at *sn*-1 and *sn*-2 position (see **Figure 3.5**) and its main phase transition temperature is –17 °C.[96]

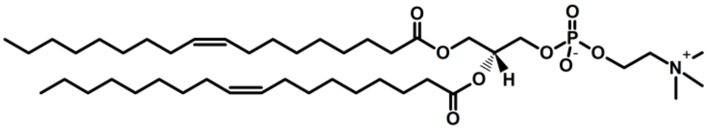

Figure 3.5. Structure of 1,2-dioleoyl-*sn*-glycero-3-phosphocholine (DOPC). Molar mass *M* = 786 g·mol^{-1}.

Lipid-Bound Dyes

Because all lipids lack intrinsic fluorescence in the visible region, fluorescent markers were added to allow visualization of lipid membranes by means of fluorescence microscopy. Hence modified lipids were added which carried fluorescent moieties and were incorporated into lamellar lipid aggregates. Both headgroup-labeled and fatty acid-labeled dyes were used in this study. TexasRed-DHPE and Atto488-DHPE consist of either TexasRed ($\lambda_{ex/em}$ = 595/615 nm, see **Figure 3.6**) or Atto488 dyes ($\lambda_{ex/em}$ = 500/520 nm, see **Figure 3.7**) linked to the primary amine of 1,2-dihexadecanoyl-*sn*-glycero-3-phosphoethanolamine. Bodipy-C_{12}HPC is a fatty acid labeled dye. A phosphatidylcholine with a palmitic acid at *sn*-1 also contains a modified fatty acid at *sn*-2 position: A Bodipy dye ($\lambda_{ex/em}$ = 500/510 nm) attached at the end of a lauric acid (see **Figure 3.8**).

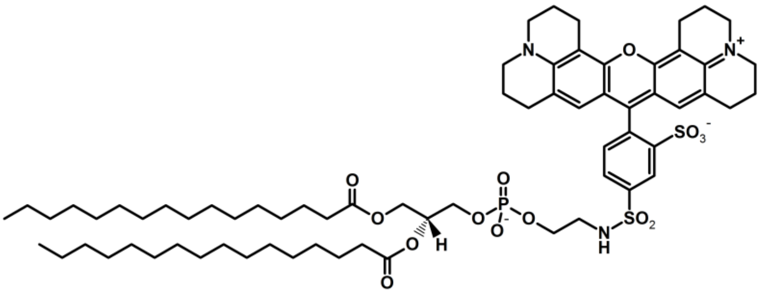

Figure 3.6. Structure of the headgroup-labeled lipid dye TexasRed 1,2-dihexadecanoyl-*sn*-glycero-3-phosphoethanolamine (TexasRed-DHPE). Excitation and emission maxima $\lambda_{ex/em}$ = 595/615 nm, molar mass *M* = 1382 g·mol^{-1}.

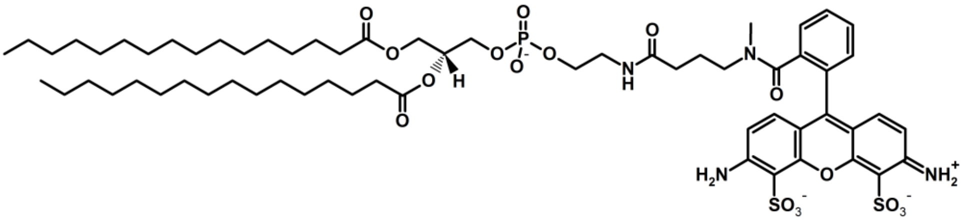

Figure 3.7. Structure of the headgroup-labeled lipid dye Atto 488 1,2-dihexadecanoyl-*sn*-glycero-3-phosphoethanolamine (Atto488-DHPE). Excitation and emission maxima $\lambda_{ex/em}$ = 500/520 nm molar mass *M* = 1264 g·mol^{-1}.

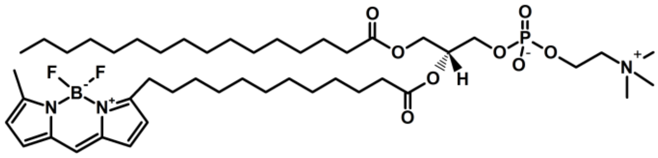

Figure 3.8. Structure of the fatty acid-labeled lipid dye (2-(4,4-difluoro-5-methyl-4-bora-3a,4a-diaza-*s*-indacene-3-dodecanoyl)-1-hexadecanoyl-*sn*-glycero-3-phosphocholine) (Bodipy-C$_{12}$HPC). Excitation and emission maxima $\lambda_{ex/em}$ = 500/510 nm, molar mass *M* = 882 g·mol^{-1}.

3.1.2 Polyamines

Long-chain polyamines (LCPA) identified in diatoms have typical molecular masses between 600 and 1500 g·mol^{-1}.[37,97] Normally only shorter polyamines with up to six amine functions (*e.g.* pentaethylenehexamine, *M* = 232 g·mol^{-1}) or very long polyethylenimines (*M* > 1500 g·mol^{-1}) are commercially available. On the other hand isolation of LCPA from diatoms is only possible in very limited amounts and would yield a hardly separable mixture of polyamines.

The polyamines used in this study were synthesized by the group of PROF. DR. ARMIN GEYER (Faculty of Chemistry, Philipps-University Marburg). These polyamines exhibited a distinct chemical structure and were respectively named C*X*N*Y*. *X* describes the length of the alkyl spacers between nitrogen atoms and denotes the number of carbon atoms within one spacer. *Y* represents the overall length of the linear polyamines as it denotes the total number of amine groups within the molecules. All stated polyamine concentrations c_N were related to this number of amine groups Y instead of the number of polyamine molecules.

The vast majority of experiments was performed using the polyamine C3N13 (see **Figure 3.9**). Its molecular mass of $M = 702\ g\cdot mol^{-1}$ is in the physiological relevant range, making it a suitable model component for diatom LCPA.[37,97]

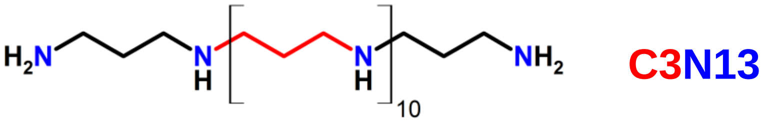

Figure 3.9. Molecular structure of the long-chain polyamine C3N13 ($C_{36}H_{87}N_{13}$, $M = 702\ g\cdot mol^{-1}$) which was mostly used in this study. The name C*X*N*Y* denotes the length of the alkyl spacers by the number *X* of carbon atoms between two nitrogen atoms (*red*). The total number of amine groups is expressed by *Y* (*blue*).

Synthesis of C3N13 was performed by the group of PROF. DR. ARMIN GEYER using solid phase peptide synthesis techniques (see **Figure 3.10**).[98] A norspermidine precursor was attached to a resin via its internal secondary amine. Subsequently, both side chains were extended by sequential coupling of β-alanine. In the final steps the carboxyl groups were reduced and the LCPA was cleaved from the resin.

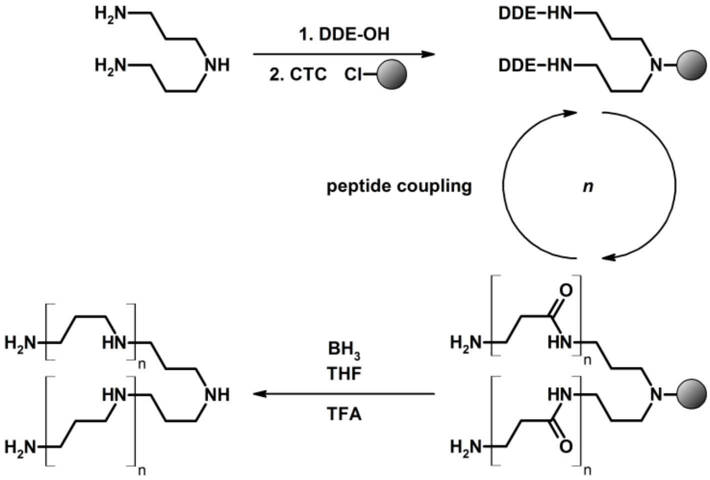

Figure 3.10. Synthesis of LCPA with odd numbers of amine functions (*e.g.* C3N13, *n* = 5) performed by the group of PROF. DR. ARMIN GEYER. A CTC resin (chloro-(2'-chlorotrityl) polystyrene resin) was loaded with terminal DDE-protected norspermidine. After deprotection both side chains were subsequently elongated by binding Fmoc-protected β-alanine to the primary amine groups and deprotection. Reduction of all carboxyl groups was accomplished in a combined step using BH_3 in tetrahydrofuran (THF). LCPA were cleaved from the resin by trifluoroacetic acid (TFA).[98]

Besides unlabeled C3N13 a fluorescently labeled derivative FITC-C3N13 (see **Figure 3.11**) was provided by the group of Prof. Dr. Armin Geyer, too. The addition of a terminal fluorescein moiety ($\lambda_{\text{ex/em}}$ = 490/525 nm) enabled the use of fluorescence microscopy to locate LCPA. Labeling was achieved by binding fluorescein isothiocyanate to a primary amine group of C3N13.[99]

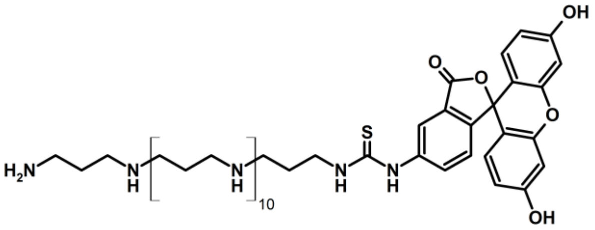

Figure 3.11. Structure of the fluorescent LCPA FITC-C3N13 carrying a terminal fluorescein moiety. Excitation and emission maxima $\lambda_{\text{ex/em}}$ = 490/525 nm, molar mass M = 1092 g·mol^{-1}.

In addition to C3N13 four other polyamines with different chain lengths had been synthesized by the group of Prof. Dr. Armin Geyer (see **Table 3.2**).

Table 3.1. Overview on synthetic polyamines with different chain lengths.

Compound name	Molecular structure	Empirical formula	Molar mass / g·mol^{-1}
C3N4	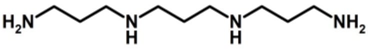	$C_9H_{24}N_4$	188
C3N5	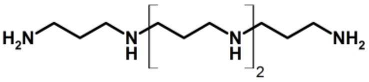	$C_{12}H_{31}N_5$	245
C3N7	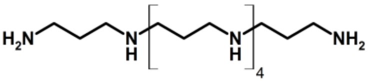	$C_{18}H_{45}N_7$	360
C3N18	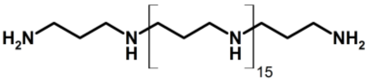	$C_{51}H_{122}N_{18}$	988

The synthesis of C3N4, C3N5, C3N7 and C3N18 was achieved using an alternative approach (see **Figure 3.12**).[43] In contrast to the synthesis of C3N13 (see **Figure 3.10**) a diamine was attached to a resin and the polyamine chain was subsequently elongated at only one side. While this strategy involved more steps, it enabled the synthesis of polyamines with either even or odd numbers of amine groups as well as a larger variety of possible derivatives (*e.g.* isotope labeling or spacer variation).

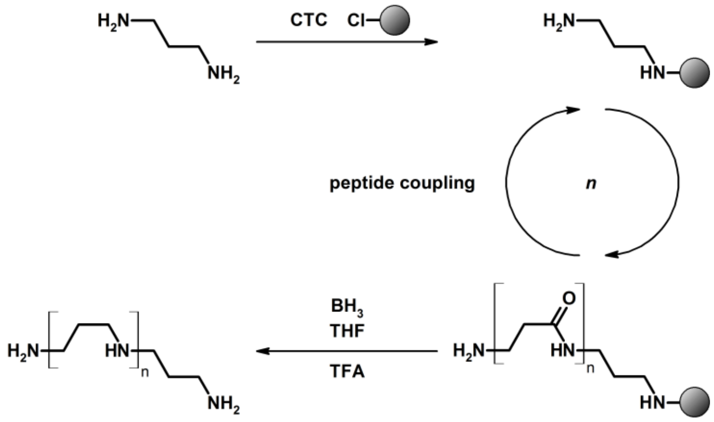

Figure 3.12. Synthesis of LCPA with even or odd numbers of amine groups (*e.g.* C3N7, *n* = 5) performed by the group of Prof. Dr. Armin Geyer. 1,3-Diaminopropane was attached to a CTC resin and subsequently elongated using *β*-alanine. Reduction was achieved by BH_3·THF and the polyamine was cleaved from the resin using TFA.[43]

In comparison to LCPA two short polyamines were purchased from Sigma-Aldrich (St. Louis, US, see **Table 3.2**): spermidine containing three and spermine containing four amine groups.

Table 3.2. Overview on two commercially available short polyamines used in this study.

Compound name	Molecular structure	Empirical formula	Molar mass / g·mol^{-1}
Spermidine	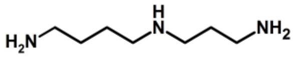	$C_7H_{19}N_3$	145
Spermine	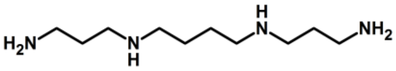	$C_{10}H_{26}N_4$	202

3.1.3 Silicic Acid

Since aqueous solutions of monomeric silicic acid are only stable up to a concentration of about 1 mM $Si(OH)_4$,[31] silicic acid was freshly prepared for each experiment via acidic hydrolysis of tetramethoxysilane (TMOS, see **Figure 3.13**).

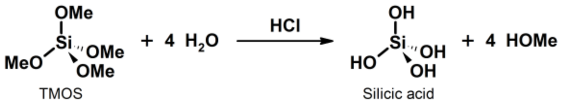

Figure 3.13. Reaction scheme of the acidic hydrolysis of tetramethoxysilane (TMOS) yielding silicic acid.

A 1 M stock solution of $Si(OH)_4$ was prepared by mixing TMOS with 1 mM HCl (3:17 (*v*/*v*)), brief stirring and incubation for precisely 20 min at room temperature.[100] The solution was used immediately afterwards.

3.2 Proteinbiochemical Methods

To study the interactions of cingulins with lipid bilayers two exemplary cingulins from the diatom species *Thalassiosira pseudonana* (*T. pseudonana*) were chosen: a tryptophan-rich cingulin, cingulin W2, and a tyrosine-rich one, cingulin Y3. These two proteins represent the two major classes of cingulins distinguished by their most occurring aromatic amino acids.[35] To easily provide sufficient amounts of these proteins, recombinant expression systems in *Escherichia coli* (*E. coli*) were deployed.[101] The two recombinant cingulins were therefore called rCinW2 and rCinY3.

Expression systems for both cingulins in *E. coli* were introduced by the group of Prof. Dr. Nils Kröger (B CUBE, Technical University of Dresden).[36] A protocol for the transformation and expression of rCinW2 in *E. coli* was provided by his group while strategies for protein isolation and purification were developed in this study. Samples containing purified rCinY3 were directly provided by the group of Prof. Dr. Nils Kröger.

3.2.1 Recombinant Cingulin W2

The plasmid encoding rCinW2 was synthesized by the group of Prof. Dr. Nils Kröger.[35] Protein expression was carried out using the *E. coli* strain DH5α. Incorporation of a *C*-terminal His$_6$-tag enabled protein isolation and purification by immobilized metal ion affinity chromatography (IMAC, see **Figure 3.14**).

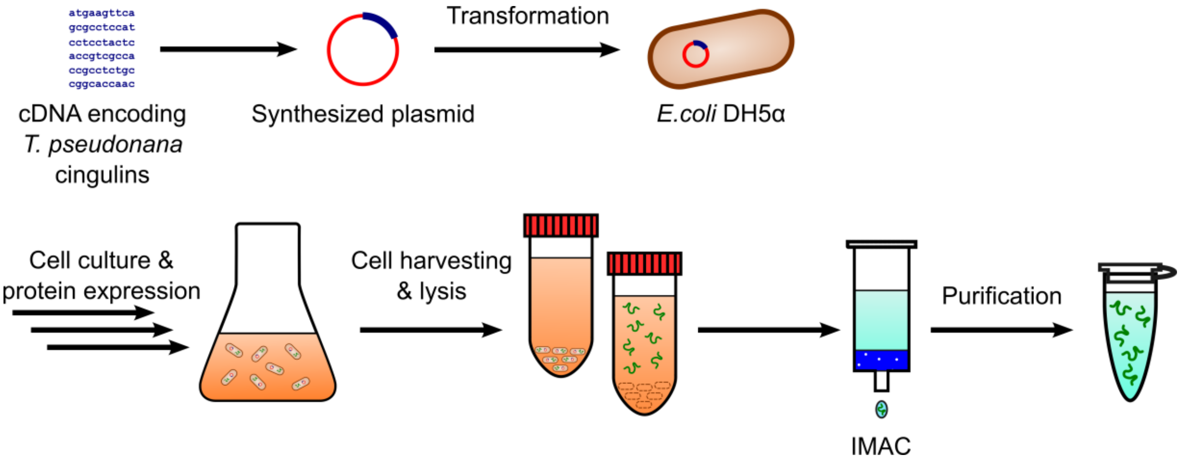
atgaagttca
gcgcctccat
cctcctactc
accgtcgcca
ccgcctctgc
cggcaccaac
cDNA encoding *T. pseudonana* cingulins
Synthesized plasmid
Transformation
E.coli DH5α
Cell culture & protein expression
Cell harvesting & lysis
IMAC
Purification

Figure 3.14. Schematic illustration of the isolation of rCinW2 using *E. coli* DH5α as host system. A plasmid containing the cDNA of cingulin W2 was transferred into *E. coli* cells. After cultivation and protein expression cells were harvested and lysed. Purification of the target protein was achieved by immobilized metal ion affinity chromatography (IMAC) exploiting a *C*-terminal His$_6$-tag on rCinW2.

3.2.1.1 Transformation

Plasmids (pJ404 vector including ampicillin resistance and *lac* operon) containing the cDNA for cingulin W2 from *T. pseudonana* were transferred into calcium-competent *E. coli* DH5α cells. Calcium-competent cells were generated by MICHAELA LUDOLPHS.[102] In short *E. coli* DH5α cells (ThermoFischer Scientific) were incubated twice for 30 min on ice in $CaCl_2$ solution (100 mM). Cell suspensions were afterwards mixed with 80% glycerol solution (cell suspension/glycerol 1:5 (*v*/*v*)) and stored at –80 °C until further use.

Competent cells (600 µL) were stored on ice and plasmids (2 µL, 420 $ng{\cdot}\mu L^{-1}$) were added. After incubation for 30 min on ice, cells were heated for 30 s to 42 °C. SOC medium (250 µL, see **Table 3.3**) was added and the suspension was incubated for 1 h at 37 °C (225 rpm). Afterwards cell suspensions (40 µL or 100 µL) were streaked on ampicillin-containing LB agar plates (100 $\mu g{\cdot}mL^{-1}$ ampicillin, 20 $g{\cdot}L^{-1}$ agar in LB medium, see **Table 3.3**) and incubated overnight at 37 °C.

Table 3.3. Composition of media used for cell transformation. All media were autoclaved.

Media	**Composition**
SOC medium	20 $g{\cdot}L^{-1}$ tryptone, 5 $g{\cdot}L^{-1}$ yeast extract, 10 mM NaCl, 10 mM $MgSO_4$, 20 mM glucose, pH 7.0
LB medium	10 $g{\cdot}L^{-1}$ tryptone, 5 $g{\cdot}L^{-1}$ yeast extract, 5 $g{\cdot}L^{-1}$ NaCl, pH 7.0

3.2.1.2 Protein Expression

Overnight cultures were prepared by inoculating LB medium (50 mL) containing ampicillin (100 $\mu g{\cdot}mL^{-1}$) with either a single colony from agar plates after cell transformation or glycerol stock solution from previous protein expressions (see below). The media were incubated overnight at 37 °C. After cell growth samples of the overnight culture (700 µL) were mixed with glycerol (80%, 1 mL) and frozen at –80 °C. These glycerol stocks could be used to inoculate future cell cultures.

The overnight cultures (10 mL each) were transferred into ampicillin-containing LB medium (100 $\mu g{\cdot}mL^{-1}$ ampicillin, 250 mL each, see **Table 3.3**) and grown until an optical density at the wavelength λ = 600 nm of $OD_{600} = 0.6$ was reached.

Protein expression was induced by addition of isopropyl *β*-D-1-thiogalactopyranoside (IPTG, 1 mM). Cell incubation was continued for 3 h and stopped by cooling of the suspensions to 0 °C.

Cells were harvested by centrifugation (3900 ×g, 20 min, 4 °C). The supernatants were discarded and the pellets were resuspended on ice in 1% NaCl solution. Cell suspensions were centrifuged again (3220 ×g, 15 min, 4 °C) and the pellets were stored at –80 °C before cell lysis.

3.2.1.3 Protein Isolation and Purification

Cell pellets were resuspended in lysis buffer (at least 15 mL per pellet, see **Table 3.4**). DNase I in DNase buffer (5 $\text{mg}\cdot\text{mL}^{-1}$ stock solution diluted 1:1000, see **Table 3.4**) and an applicator tip of lysozyme were added. The cell suspensions were stirred at 4 °C until homogeneity was observed. Afterwards cells were lysed by sonification on ice with ultrasound (10× 30 s with 2 min breaks, 60% power, Bandelin Sonoplus UW 2070). Insoluble cell components were separated by centrifugation (12000 ×g, 30 min, 4 °C) and the target protein was purified from supernatants by IMAC.

Table 3.4. Composition of buffers used during protein isolation and purification. Phenylmethylsulfonyl fluoride (PMSF) and protease inhibitor tablets (Roche complete EDTA-free) were added immediately before use.

Solution	Composition
Lysis buffer	50 mM TRIS, 1 M NaCl, 10 mM imidazole, 4 M urea, 0.1 mM PMSF, 1 tablet of protease inhibitor per 100 mL, pH 8.0
Washing buffer	50 mM TRIS, 1 M NaCl, 25 mM imidazole, 4 M urea, 0.1 mM PMSF, 1 tablet of protease inhibitor per 100 mL, pH 8.0
Elution buffer	50 mM TRIS, 1 M NaCl, 250 mM imidazole, 4 M urea, 0.1 mM PMSF, 1 tablet of protease inhibitor per 100 mL, pH 8.0
Rinsing buffer	50 mM TRIS, 1 M NaCl, 1000 mM imidazole, 4 M urea, 0.1 mM PMSF, 1 tablet of protease inhibitor per 100 mL, pH 8.0
DNase buffer	50% Glycerol, 20 mM TRIS, 1 mM $MgCl_2$, pH 7.5

The target protein, rCinW2, was expressed with a *C*-terminal His_6-tag. Its high binding affinity to transition metal ions (*e.g.* nickel(II) or cobalt(II)) allows easy purification by IMAC.[103–105] Proteins from the applied supernatant can bind to metal ions immobilized on a solid matrix. While unspecific bound proteins are eluted by low concentrations of imidazole, competing for binding to the metal ions, higher imidazole concentrations are needed to replace proteins bound via poly histidine sequences. With an average content of about 2% of all amino acids in globular proteins, histidine is a relative rare one.[106] Since only half of them are accessible at the outside of the proteins, IMAC offers an easy way to separate recombinant His_6-tagged proteins from cell extracts.[107]

Nickel nitrilotriacetic acid (Ni-NTA) agarose beads (2.5 mL, Qiagen Ni-NTA Agarose) were washed with ultrapure water (12.5 mL) and lysis buffer (12.5 mL). The beads were combined with the supernatant after cell lysis and incubated overnight at 4 °C. The suspension was transferred into a column with frit. The flow-through was collected and the column was washed with washing buffer (4× 10 mL, see **Table 3.4**). The target protein was eluted with elution buffer (3× 10 mL, see **Table 3.4**) and the column was rinsed afterwards with rinsing buffer (3× 10 mL, see **Table 3.4**).

3.2.1.4 Gel Electrophoresis and Western Blotting

Identification of the isolated protein was performed by gel electrophoresis and Western blotting.

Gel electrophoresis is a technique to separate a mixture of proteins by mass-to-charge ratio. In this study a discontinuous SDS polyacrylamide gel electrophoresis (SDS-PAGE) was employed, first introduced by LAEMMLI.[108] Before separation proteins were denatured. Under reducing conditions proteins lose their distinct secondary or higher ordered structure. Intrinsic protein charge is masked by binding of negatively charged sodium dodecyl sulfate (SDS) to hydrophobic protein parts (0.7–1.4 g SDS per g protein) resulting in an even mass-to-charge ratio for all protein-SDS aggregates.[109] After application to a polyacrylamide gel protein-SDS aggregates are moved by an electric field. Propagation through the gel is influenced by the mesh size of the gel and the size or respectively the mass of the denaturized proteins. Discontinuous SDS-PAGE increases the resolution of the gel by addition of a stacking gel which narrows protein bands before separation. The lower pH in this gel leads to the formation of an electrical potential between leading chloride ions and following partially protonated glycine (or tricine) molecules. Proteins are concentrated in between until the following ions become deprotonated in the separation gel and pass the protein band allowing for undisturbed separation of the protein mixture. In the end protein bands can be visualized by staining for example with Coomassie Brilliant Blue.[110] Besides SDS-PAGE by LAEMMLI, a variation of the protocol introduced by SCHÄGGER and JAGOW was used which offered better separation of low-weight proteins.[111]

The Western blot is used to selectively detect proteins by immunologic binding of antibodies to a target protein or specific peptide sequences. After transfer of proteins for example from a SDS-PAGE gel onto a nitrocellulose membrane by electroblotting, antibodies are applied. These antibodies bind to their specific antigens and can later be localized for example by a second antibody carrying a group catalyzing a luminescent reaction (see **Figure 3.15**).[112,113]

In this study a Western blot analysis against penta histidine sequences in peptides or proteins was performed to probe the target protein's *C*-terminal His$_6$-tag.

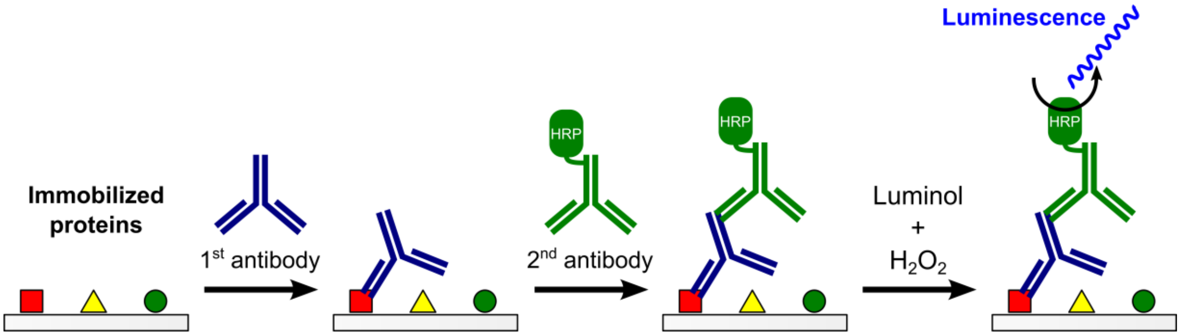

Figure 3.15. Schematic illustration of a Western blot. Proteins were immobilized on a nitrocellulose membrane. A first antibody binds specifically to its antigen (red). Antigen localization is visualized by binding of a second antibody, carrying a horseradish peroxidase (HRP), to the first antibody. HRP catalyzes the oxidation of luminol resulting in detectable chemiluminescence.

SDS Polyacrylamide Gel Electrophoresis

LAEMMLI polyacrylamide gels (thickness 0.8 mm) were prepared by first pouring the 12.5% separation gel from separation gel stock solution (4 mL, see **Table 3.5**) under addition of tetramethylethylenediamine (TEMED, 2 µL) and ammonium persulfate solution (APS, 40 µL 10% (*w*/*v*) stock solution). The gel was allowed to polymerize for at least 45 min covered with isopropyl alcohol before pouring the 5% stacking gel (2 mL stacking gel stock solution (see **Table 3.5**), 20 µL APS, 2 µL TEMED). Polymerization was allowed for at least 45 min, too.

Polyacrylamide gels according to SCHÄGGER and JAGOW consisted of a 10% separation gel and a 4% stacking gel on top. The separation gel was poured from freshly mixed ultrapure water (0.57 mL), 50% glycerol (1.06 mL), gel buffer (1.68 mL, see **Table 3.5**) and acrylamide/bis-acrylamide solution (30%, 37.5:1, 1.66 mL) as well as TEMED (3 µL) and APS (25 µL 10% (*w*/*v*) stock solution). The stacking gel contained ultrapure water (1.23 mL), gel buffer (0.50 mL, see **Table 3.5**), acrylamide/bis-acrylamide solution (30%, 37.5:1, 267 µL), TEMED (2.65 µL) and APS (13.4 µL 10% (*w*/*v*) stock solution) and was freshly prepared before use, too. Polymerization times were as mentioned before.

Protein samples were equally mixed with 2× SDS-sample buffer (see **Table 3.5**) and heated for 5 min to 95 °C (300 rpm).

After polymerization the gel holder was filled with running buffer in case of LAEMMLI gels (see **Table 3.5**) or cathode and anode buffers for SCHÄGGER and JAGOW gels (see **Table 3.5**). Sample pockets were filled with the denatured protein samples (1–20 µL each) as well as a mass standard (5 µL GE LMW-SDS Marker Kit or 2 µL Thermo Fisher Scientific PageRuler Plus). Electrophoresis was performed at a constant voltage of 160 V.

Staining of protein bands was done by rinsing the gel twice with almost boiling ultrapure water for 1 min each, followed by shaking in almost boiling staining solution (see **Table 3.5**) for 5 min. The gel was afterwards washed multiple times with ultrapure water at room temperature. Additional contrast enhancement could be achieved by shaking the gel in destaining solution (see **Table 3.5**) overnight at room temperature.

Table 3.5. Buffer solutions used for SDS polyacrylamide gel electrophoresis.

Solution	**Composition**
LAEMMLI gels:	
Stacking gel stock solution (5%)	125 mM TRIS, 16% (*v*/*v*) acrylamide/bis-acrylamide solution (30%, 37.5:1), 0.1% (*w*/*v*) SDS, pH 6.8 (HCl)
Separation gel stock solution (12.5%)	390 mM TRIS, 42% (*v*/*v*) acrylamide/bis-acrylamide solution (30%, 37.5:1), 0.1% (*w*/*v*) SDS, pH 8.8 (HCl)
Running buffer	25 mM TRIS, 192 mM glycine, 0.1% (*w*/*v*) SDS
SCHÄGGER and JAGOW gels:	
Gel buffer	3 M TRIS, 0.3% SDS, pH 8.45
Cathode buffer	0.1 M TRIS, 0.1 M tricine, 0.1% SDS, pH 8.25
Anode buffer	0.2 M TRIS, 0.3% SDS, pH 8.45
Both:	
2× SDS-sample buffer	125 mM TRIS, 100 mM DTT, 20% (*v*/*v*) glycerol, 2% (*w*/*v*) SDS, 0.02% (*w*/*v*) bromphenol blue, pH 6.8
Staining solution	80 $\text{mg}\cdot\text{L}^{-1}$ Coomassie G-250, 35 mM HCl
Destaining solution	5% (*v*/*v*) Ethanol, 7.5% (*v*/*v*) acetic acid

Western Blotting

Protein bands were transferred from a SDS-PAGE gel before staining. Therefore two cellulose filter papers (Whatman filter paper), a nitrocellulose membrane (Bio-Rad Trans-Plot, 0.2 µm) and the SDS-PAGE gel were preincubated in blotting buffer (see **Table 3.6**) for 30 min at room temperature. The SDS-PAGE gel (cathode side) and the nitrocellulose membrane (anode side) were placed in between both filter papers inside the transfer cell and the blot was performed at a constant current of 180 mA for 45 min. After blotting the SDS-PAGE gel could additionally be stained as mentioned above.

The nitrocellulose membrane was stained with 0.2% PonceauS solution and washed with ultrapure water twice. To avoid unspecific antibody binding the membrane was passivated with 5% powdered milk containing TBT buffer (see **Table 3.6**) overnight at 4 °C. The first antibody (antigen: penta histidine sequences, host: mouse, Qiagen Penta His Antibody, BSA-free) was added in 5% powdered milk containing TBT buffer in a ratio of 1:1000 (*v*/*v*) for 1 h at room temperature. After rinsing with TBT buffer (3× 40 mL, 10 min) the second antibody (antigen: mouse antibodies, host: goat, additional functions: horseradish peroxidase (HRP), Santa Cruz Biotechnology) was added in a ratio of 1:2000 (*v*/*v*) in 5% powdered milk containing TBT buffer for 1 h at 4 °C. After rinsing with TBT buffer (3× 40 mL, 20 min) and ultrapure water (2× 40 mL) HRP-containing antibodies could be localized by a chemiluminescent reaction.

Both ELC 1 and ELC 2 solutions (1 mL each, see **Table 3.6**) were mixed before use and applied to the nitrocellulose membrane for 2 min. The membrane was afterwards placed in dark on a photographic film (Biomax XAR Film, Carestream) for 1 min. The film was developed directly afterwards (GBX, Carestream, 1 min), washed in water and fixed (GBX, Carestream, 1 min).

Table 3.6. Buffer solutions used for Western blot analysis.

Solution	Composition
Blotting buffer	20 mM TRIS, 150 mM glycine, 0.05% (*w*/*v*) SDS, 20% (*v*/*v*) methanol
TBT buffer	10 mM TRIS, 150 mM NaCl, 0.2% (*v*/*v*) Tween 20, pH 7.4 (HCl)
ELC 1 solution	100 mM TRIS, 2.5 mM luminol, 0.4 mM *p*-coumaric acid, pH 8.5
ELC 2 solution	100 mM TRIS, 0.02% (*v*/*v*) H_2O_2, pH 8.5

3.2.1.5 Buffer exchange

After IMAC the target protein was stored in buffer containing high amounts of urea (4 M). To avoid interference of urea with lipid membranes in further experiments, the content of urea had to be reduced by buffer exchange.[114–116] Therefore two different methods were used. On the one hand exchange of buffer components by diffusion through a tubular cellulose dialysis membrane and on the other hand buffer exchange using centrifugal concentrators. Both methods trap the target protein within a defined compartment while small buffer components can traverse a membrane. New conditions are either stated by an equilibrium between inner and outer buffers (tubular cellulose dialysis membrane) or by constant addition of target buffer to the protein-containing compartment (centrifugal concentrators).

Dialysis through Cellulose Membranes

Protein solutions were filled into tubular cellulose dialysis membranes (molecular weight cut-off: 14 kDa, Carl Roth Visking) and placed in target buffer with 125 times the sample's volume. The buffer was replaced twice and stirred for at least 6 h each at 4 °C.

Buffer Exchange via Centrifugal Concentrators

Centrifugal concentrators (molecular weight cut-off: 5 kDa, Sigma Aldrich Vivaspin 500) were rinsed with target buffer (15000 ×g, 20 min, 4 °C). The protein sample was added, eventually diluted with target buffer and centrifuged (15000 ×g, 20 min, 4 °C). The flow-through was discarded and the protein containing residual buffer was refilled with target buffer. Centrifugation and refilling was repeated at least three times.

Protein Concentration Measurement

Protein concentrations of the purified samples could be determined by UV/VIS absorption spectroscopy. The wavelength λ dependent absorption $A(\lambda)$ of the sample also depends on the sample concentration c, the optical path length d and the extinction coefficient of the sample $\varepsilon(\lambda)$ as described by the LAMBERT-BEER law:

$$A(\lambda) = \varepsilon(\lambda) \cdot c \cdot d\,. \qquad \textbf{3-1}$$

The extinction coefficient $\varepsilon(\lambda)$ at the wavelength λ = 280 nm of proteins with known primary structure (see **Appendix**) can be calculated from the amount of aromatic amino acids and disulfide bonds using the online tool ProtParam.[117] The following extinction coefficients $\varepsilon(\lambda$ = 280 nm) were calculated for rCinW2 and rCinY3 (see **Table 3.7**):

Table 3.7. Extinction coefficients $\varepsilon(\lambda)$ of rCinW2 and rCinY3 at the wavelength λ = 280 nm calculated from the primary amino acid sequence (see Appendix) using ProtParam.[117]

Protein	Extinction coefficient $\varepsilon(\lambda$ = 280 nm)
rCinW2	123870 $\mathrm{M^{-1}{\cdot}cm^{-1}}$
rCinY3	34270 $\mathrm{M^{-1}{\cdot}cm^{-1}}$

3.2.2 Recombinant Cingulin Y3

Recombinant cingulin Y3 (rCinY3) was isolated and provided by the group of PROF. DR. NILS KRÖGER. Protein expression was identical to the protocol for expression of rCinW2 (see **Chapter 3.2.1**) using pJ404 vectors and the *E. coli* strain DH5α, too. In contrast buffers for cell lysis and IMAC did not contain any urea during the isolation of rCinY3. To receive the protein in sufficient purity an additional ion exchange chromatography (IEC) was performed using a NaCl gradient (0–1 M) to elute the target protein. The protein was provided in buffer solution (50 mM TRIS, ca. 300 mM NaCl, 0.1 mM PMSF, protease inhibitor, pH 8.0).

3.3 Lipidchemical Methods

Preparation of solid supported model membranes was performed by spreading of small unilamellar vesicles (SUVs) on various supports. Starting with the rehydration of dry lipid films, SUVs were prepared from multilamellar vesicles using ultrasound sonification. Depending on the hydrophobicity of the substrate either lipid bilayers or monolayers were deposited.[93] Lipid monolayers were prepared on hydrophobically functionalized gold or glass surfaces. In contrast lipid bilayers were formed on hydrophilized silicon/silicon dioxide wafers or mica surfaces. The major benefit of solid supported lipid membranes is their accessibility to various surface sensitive techniques (see **Chapter 3.4**) for the study of both properties of the membrane itself and interaction of biomolecules with membranes *in vitro*.[86,87,118–120]

3.3.1 Overview on Preparation Conditions

For all following types of solid supported model membranes some common preparation conditions were chosen that worked for all systems and ensured comparability.

The lipid mixture used in this study was deviated from the overall lipid composition of the diatom *Cyclotella meneghiniana* published by VIELER *et al.* (see **Table 3.8**).[66] The native lipid mixture contains in total over 40% of negatively charged lipids (SQDG and phosphatidylglycerol (PG)). This ratio has been reduced by increasing the amount of neutral lipids (MGDG, DGDG and phosphatidylcholine (PC)) in order to lower repulsive electrostatic interactions between lipids and the negatively charged surfaces of silicon/silicon dioxide wafers[121] or mica.[122,123] At the same time the amount of non-bilayer forming lipids, in this case MGDG, had to be kept below a certain threshold. In aqueous solution pure MGDG forms inverted tube-like hexagonal H_{II} structures instead of lamellar aggregates. Nevertheless MGDG can be integrated into lamellar lipid structures by adding more than 50% of bilayer-forming lipids.[67,73,74] Since MGDG, DGDG and SQDG are commercially only available as plant extracts, these samples contain mixtures of the lipids with different fatty acid chains and degrees of saturation. On the other hand POPG and DOPC were used as exemplary lipids of the PG and PC class. Main phase transition temperatures of these two lipids are below 0 °C.[96] Thus phase separation due to different packing of the fatty acid chains at room temperature was not expected.[124] The lipid mixture employed for most of the experiments is stated in **Table 3.8**. If deviating lipid mixtures were used for experiments it is explicitly denoted.

Table 3.8. Comparison of the overall lipid composition of *Cyclotella meneghiniana* published by VIELER *et al.*[66] and the lipid composition used in this study for the formation of model membranes. POPG and DOPC were used as lipids of the PG and PC class. Compositions were denoted as molar lipid ratios.

	MGDG	DGDG	SQDG	PG	PC
Cyclotella meneghiniana, by VIELER *et al.*[66]	33.7%	17.5%	24.7%	15.4%	8.7%
Model systems introduced in this study	35%	20%	15%	5%	25%

Regarding buffer conditions, previous *in vivo* studies on diatoms revealed the SDV to be an organelle with an acidic interior.[22] Hence all experiments were carried out in mild acidic buffers at pH 5.5 to reflect physiological conditions (see **Table 3.9**). When different buffer compositions were used, these deviations are clearly denoted.

Spreading of vesicles with lipid mixtures containing high amounts of negatively charged lipids on negatively charged silicon/silicon dioxide surfaces was successful by partial protonation of the surface under acidic buffer conditions hence lowering the surface charge.[125] The spreading buffer from the protocol by BRAUNGER *et al.* was adapted for this study (see **Table 3.9**).

Table 3.9. Composition of sample and spreading buffers[125] mainly used in this study.

Buffer	Composition
Sample buffer	50 mM KCl, 40 mM NaOAc, pH 5.5 (HOAc)
Spreading buffer[125]	50 mM KCl, 20 mM Na-citrate, 0.1 mM EDTA, 0.1 mM NaN_3, pH 4.8 (HCl)

3.3.2 Vesicle Preparation

Lipid stock solutions (1–10 mg·mL^{-1}) were prepared in chloroform or chloroform/methanol (4:1 (*v*/*v*)) and mixed in glass test tubes according to the desired lipid ratios for each experiment. Organic solvent was evaporated at 30 °C under a mild nitrogen stream. Afterwards remaining solvent within the deposited lipid films was removed under vacuum for at least 3.5 h at 30 °C. Lipid films were stored at 4 °C until further use.

Vesicle suspensions were freshly prepared before each experiment by rehydration of a lipid film with spreading buffer (see **Table 3.9**) for 30 min at room temperature followed by vortexing (3× 30 s with 5 min breaks). Sonification of the suspension (30 min, 60% power, Bandelin Sonoplus HD2070) led to the formation of SUVs.

3.3.3 Solid Supported Lipid Monolayers

3.3.3.1 Thiol-functionalized Gold Surfaces

Gold surfaces can easily be modified by thiol-gold chemistry.[126] Organic molecules containing thiol groups covalently bind to the surface forming a self-assembled monolayer on top of it. This layer alters and determines the surface properties of the support.[127] The use of octanethiol renders the surface hydrophobic allowing the additional deposition of lipid monolayers for example by vesicle spreading (see **Figure 3.16**).[128] Despite gold surfaces interfere with the use of fluorescence microscopy due to quenching of visible fluorescence,[129] the application of surface plasmon resonance (SPR) techniques allow the study of biomolecule binding to the functionalized surface (see **Chapter 3.4.2**).

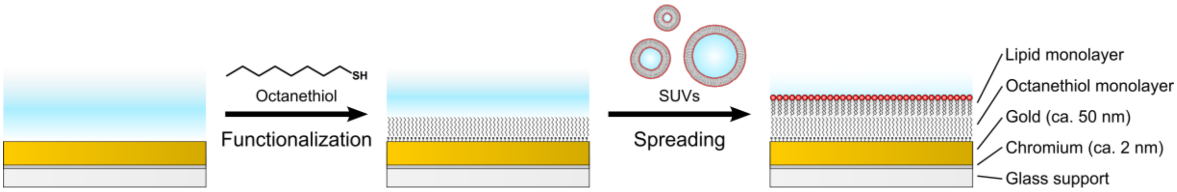

Figure 3.16. Schematic illustration of the formation of a lipid monolayer on a gold surface. Octanethiol covalently binds to gold evaporated on a glass support. A self-assembled monolayer is formed with the alkyl chains of the thiol facing away from the gold and drastically increasing the hydrophobicity of the surface. Upon addition of small unilamellar vesicles (SUVs) a lipid monolayer is deposited on the surface.

Surface Functionalization

Glass slides (LaSFN9 (Hellma Optick) for SPR or cover slides (Thermo Fischer) for impedance measurements) were first evaporated (MED020, Bal-Tec) with chromium (ca. 2 nm) and then with gold (ca. 60 nm). Before functionalization the surfaces were cleaned by argon plasma (30 s, Diener electronics Zepto) and afterwards directly incubated in a solution of octanethiol in ethanol (16 mM) overnight. After rinsing with ethanol and drying under nitrogen stream, the samples were ready for membrane preparation.

Membrane preparation

SUV suspensions in spreading buffer (see **Table 3.9**) were added to the functionalized gold surfaces either in a flow cell during SPR measurements (0.2 mg·mL^{-1}, for details see **Chapter 3.4.2**) until a constant response was measured or alternatively in static by direct addition in a measuring chamber for electrochemical impedance spectroscopy (0.5 mg·mL^{-1}, 30 min, for details see **Chapter 3.4.4**). After rinsing with spreading or sample buffer (see **Table 3.9**) membranes were ready for further characterization and application.

3.3.3.2 Silanized Glass Surfaces

To overcome the drawbacks of gold-thiol-substrates (see **Chapter 3.3.3.1**) in regard to fluorescence quenching modified glass surfaces were introduced as an alternative hydrophobic solid support. A protocol for substrate functionalization and vesicle spreading was adapted from SABINE BOSK.[130] Covalent binding of a trimethylated silane to free hydroxyl groups on the glass surface exposes a hydrophobic layer on the surface which can be employed to deposit lipid monolayers (see **Figure 3.17**).[47]

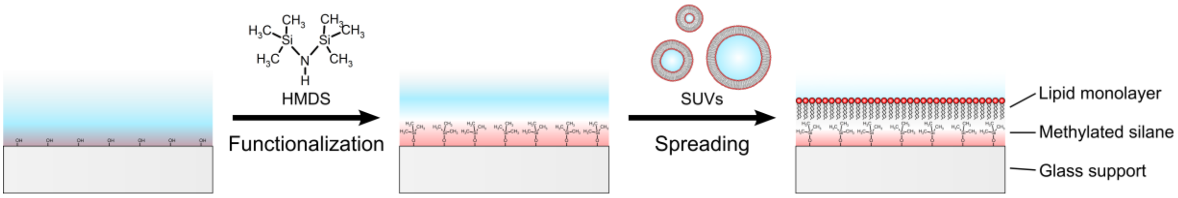

Figure 3.17. Schematic illustration of the formation of a lipid monolayer on a hydrophobically functionalized glass substrate. Upon the addition of hexamethyldisilazane (HMDS) free hydroxyl groups of the glass surface bind trimethylated silane moieties. Exposure of the methyl groups renders the surface hydrophobic. A lipid monolayer is deposited after addition of small unilamellar vesicles (SUVs).

Surface Functionalization

Glass cover slides (D263M Schott glass) were cut into quadratic pieces (ca. 6× 6 mm^2) and glued with UV curing glue (Norland optical adhesive) onto glass slides. The surfaces were rinsed with detergent solution (1× 15 min, Hellmanex) and ultrapure water (2× 15 min) and dried afterwards at 90 °C under vacuum for 2 h. After cooling to room temperature hexamethyldisilazane (HMDS, 20 µL) was added to the cover slides. The liquid was allowed to evaporate over night at room temperature. If measurements were performed in solution, an area including the cover slide of about 15×15 mm^2 was confined by adhesive Teflon foil (thickness 0.5 mm). Measurements were performed in a droplet (ca. 500 µL) on the surface.

Membrane preparation

SUV suspension (0.5 mg·mL^{-1} in spreading buffer (see **Table 3.9**), 500 µL) were added to the hydrophobically functionalized cover slides and incubated for 1 h at room temperature. Afterwards the surfaces were rinsed with sample buffer (5× 500 µL, see **Table 3.9**).

3.3.4 Solid Supported Lipid Bilayers

3.3.4.1 Hydrophilized Silicon Dioxide

Silicon wafers with an additional layer of silicon dioxide (~100 nm) on the surface are used as a support for lipid bilayers for a huge variety of different analytical techniques including fluorescence and atomic force microscopy.[131] Besides these applications silicon wafers with a few micrometers thick oxide layers can also be used in reflectometric interference spectroscopy (RIfS, see **Chapter 3.4.3**) to monitor kinetics of vesicle spreading[125] as well as binding of biomolecules to solid supported lipid bilayers.[132] To increase the hydrophilicity of the silicon dioxide surface and facilitate vesicle spreading further treatment of the surface is needed.

Surface Functionalization

In a first step silicon wafers with a 5 µm silicon dioxide layer on the top (<100>, *p*-type, Active Business Company WSI04-1011004) were hydrophilized in an aqueous solution of ammonium hydroxide and hydrogen peroxide (H_2O/NH_4OH (25%)/H_2O_2 (30%) 5:1:1 (*v*/*v*)) at 70 °C for 20 min. In a second step wafers were treated with O_2 plasma for 30 s (Diener Zepto). After functionalization wafers could be stored under ultrapure water for up to four days.

Membrane preparation

During RIfS experiments spreading of SUVs (0.1 mg·mL^{-1} in spreading buffer (see **Table 3.9**)) was performed by rinsing the silicon dioxide surface with vesicle suspension in a flow cell until a constant optical thickness was detected, followed by rinsing with sample buffer (see **Table 3.9**; for details see **Chapter 3.4.3**). Alternatively, for example for measurements by fluorescence microscopy, SUVs (0.5 mg·mL^{-1} in spreading buffer) were added statically to a silicon/silicon dioxide wafer. After incubation for at least 30 min at room temperature, the surface was rinsed with sample buffer.

3.3.4.2 Mica Surfaces

Common mica, also called muscovite, is a sheet silicate with the empirical formula $KAl_2(Si_3Al)O_{10}(OH)_2$.[133,134] The sheets are formed by two tetrahedral Si/Al sheets connected by an Al dioctahedral layer. In a ratio of Al/Si = 1:3, silicon(IV) ions in the Si/Al sheets are replaced by aluminum(III), resulting in an overall negative charge of the sheets. The charge is neutralized and the sheets are linked by potassium(I) ions.[122,123] These sheets can easily be cleaved and contain an atomically flat surface with high hydrophilicity.[135] Due to the hydrophilicity mica is a commonly used solid substrate for the deposition of lipid bilayers.[136]

Sample Preparation

Mica sheets (Plano Glimmer "V5") were cut into quadratic pieces (ca. 6×6 mm^2) and fixed onto glass slides with UV curing glue (Norland optical adhesive). An area including the mica of about 15×15 mm^2 was confined by adhesive Teflon foil (thickness 0.5 mm). Immediately before vesicle spreading, the uppermost layers of the mica were removed by adhesive film until a plain surface was attained. This preparation allowed measurements from above the sample, for example by an upright fluorescence microscope. If measurements were performed using an inverse optical microscope the removal of mica sheets was repeated until a clear transparent surface was formed. Vesicle suspensions (0.1–0.5 mg·mL^{-1} in spreading buffer (see **Table 3.9**), 500 µL) were given directly onto the mica and vesicles were incubated for at least 30 min at room temperature before rinsing with sample buffer (5–10×, see **Table 3.9**).

3.4 Biophysical Methods

3.4.1 Lipid Characterization by Nuclear Magnetic Resonance Spectroscopy and Surface Pressure-Area Isotherms

In this study complex lipid mixtures with up to six different components were prepared from numerous lipid stock solutions. To ensure reproducibility of mixture preparations, a reliable method for determination of lipid concentrations had to be established. Two widely used methods are on the one hand the wet chemical and spectroscopic detection of inorganic phosphate in lipid cinder[137] and on the other hand the measurement of surface pressure-area-isotherms (Π/A-isotherms) of lipid monolayers at the air-water interface using a LANGMUIR-BLODGETT trough.[138] Quantification of inorganic phosphate is of course limited to lipids containing phosphorous and thus not applicable to the three glycolipids MGDG, DGDG and SQDG. To be able to determine the concentration of the spread lipid solutions from Π/A-isotherms the molecular area consumption A of a lipid at a certain surface pressure Π has to be known. In order to determine this area consumption A a third method for concentration measurement was employed – quantitative ^{1}H nuclear magnetic resonance (qHNMR) spectroscopy.[139,140] Π/A-Isotherms of stock solutions characterized by this technique were used afterwards to calculate surface areas A of individual lipids which enable the routine use of a LANGMUIR-BLODGETT trough for future experiments.

3.4.1.1 Nuclear Magnetic Resonance Spectroscopy

Nuclear magnetic resonance (NMR) spectroscopy probes the interaction of electromagnetic radiation with nuclei inside a magnetic field. In addition to the extraction of structural data, quantitative NMR spectroscopy (*e.g.* quantitative ^{1}H-NMR, qHNMR) enables the determination of sample concentrations.[139,140]

For NMR nuclei need a nuclei spin $\vec{P}$ unequal zero, calculated from the nuclei spin quantum number $J = \frac{1}{2}, 1, \frac{3}{2}, \ldots$ and the reduced PLANCK constant $\hbar = \frac{h}{2\pi}$ by:

$$\left|\vec{P}\right| = \hbar \cdot \sqrt{J(J+1)}\,. \qquad \textbf{3-2}$$

This results in a permanent magnetic dipole moment $\vec{\mu}_{\mathrm{N}}$:

$$\vec{\mu}_{\mathrm{N}} = \gamma_{\mathrm{N}} \cdot \vec{P}\,. \qquad \textbf{3-3}$$

The relation between both physical quantities is given by the nuclei-specific gyromagnetic ratio γ_{N}. In field-free space, magnetic dipoles are randomly orientated and energy levels are degenerated. Addition of an external magnetic field (B-field) leads to splitting of nuclei magnetic energy levels (see **Figure 3.18**).

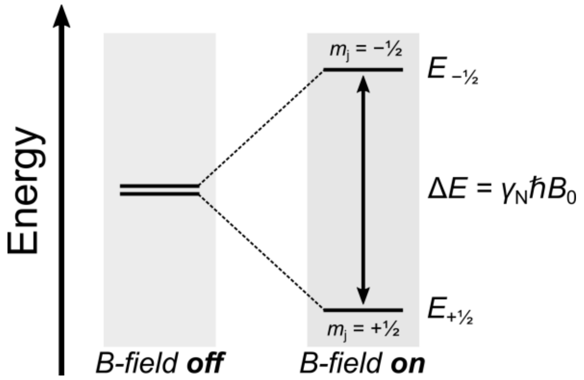

Figure 3.18. Schematic energy diagram of splitting energy levels of a spin J = ½ nucleus (*e.g.* ^{1}H) in an external magnetic field (B-field). The energy difference ΔE between the two states $E_{+½}$ and $E_{-½}$ can be calculated from the gyromagnetic ratio γ_{N}, the reduced PLANCK constant $\hbar = \frac{h}{2\pi}$ and the strength of the magnetic field B_0.[141,142]

The number of possible orientations of the dipole moments is defined by the nuclei spin quantum number J and characterized by the magnetic quantum number $m_j = J, J-1, J-2, \dots, -J$ with a total number of $2J+1$ possible orientations. The potential energy E_{m_j} of these states depends on the strength of the external B-field B_0:

$$E_{m_j} = -\gamma_N \hbar m_j B_0 \,. \qquad \textbf{3-4}$$

For the nucleus ^1H ($J = ½$, $m_j = \pm½$) the energy difference ΔE between the two possible states is calculated by:

$$\Delta E = \gamma_N \hbar B_0 \,. \qquad \textbf{3-5}$$

The gyromagnetic ratio of ^1H is $\gamma_{^1H} = 2.675 \cdot 10^8\ T^{-1} \cdot s^{-1}$.[141] In an external B-field with $B_0 = 14$ T the resonance frequency ν_0 for energy state transition is in the ultra high frequency (UHF) radio frequency region at 600 MHz. Influenced by the chemical environment, resonance frequencies ν_0 enable the determination of molecular structures.

Important for this study was the quantitative analysis of NMR data by the intensity I of a specific resonance signal. The signal intensity I is proportional to the number N of resonating, chemically equivalent nuclei in a molecule as well as the molecules concentration c:

$$I = N \cdot c \cdot k \,. \qquad \textbf{3-6}$$

k is a machine specific proportionalality constant. Since this constant is hard to address, concentration measurements are normally carried out using either an internal or an external standard. Sample concentrations c_A can be related to the reference's concentration c_B by comparison of both signal intensities $I_{A/B}$ and the number of resonating nuclei $N_{A/B}$:

$$\frac{c_A}{c_B} = \frac{I_A}{I_B} \cdot \frac{N_B}{N_A} \,. \qquad \textbf{3-7}$$

3.4.1.2 LANGMUIR-BLODGETT Trough

The physical properties of lipid monolayers at air-water interfaces can be characterized by a LANGMUIR-BLODGETT trough. During isothermal compression the surface pressure Π can be monitored to study the phase behavior of lipid monolayers. If the amount of lipids in the monolayer is known, the molecular surface area A, a lipid-specific structural parameter, can be obtained.[138]

A LANGMUIR-BLODGETT trough is made of a Teflon trough filled with a liquid subphase (*e.g.* ultrapure water or buffer). A WILHELMY plate functions as a probe for surface pressure Π, the difference between surface tension σ with or without a surfactant. The force applied

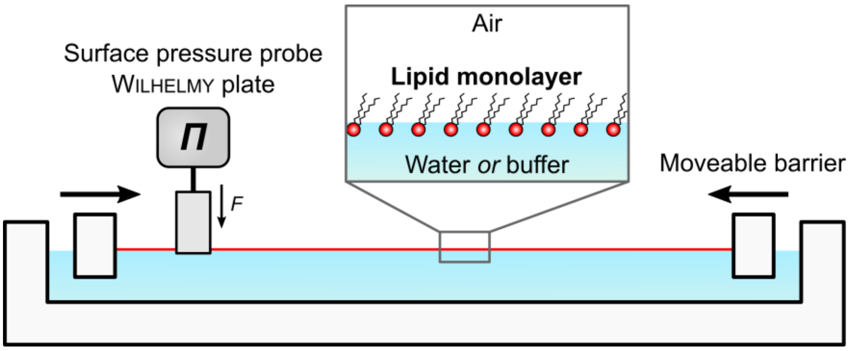

Figure 3.19. Schematic illustration of a LANGMUIR-BLODGETT trough. A Teflon trough is filled with a water or buffer subphase on which a lipid monolayer is spread. Two moveable Teflon barriers allow the reduction of the surface area. During monolayer compression the surface pressure *Π* is monitored by a WILHELMY plate.

to the plate due to wetting depends on the surface tension which can therefore be measured. Two movable Teflon barriers allow variation of the trough surface area (see **Figure 3.19**).

To generate a lipid monolayer at the air-water interface, lipids dissolved in a volatile solvent (*e.g.* chloroform) are applied on top of the surface. During equilibration, the solvent evaporates and the lipids form a unimolecular layer at the interface with the hydrophilic headgroups in the polar subphase and the hydrophobic fatty acids facing towards the air.

At a large surface area A, lipid-lipid interactions are negligible and fatty acid chains lie flat and unordered on the surface. This phase is denoted gaseous (g, see **Figure 3.20**). During compression, interactions between lipids begin to increase. This leads to a raising of the fatty acid chains and an increase in surface pressure Π. In general this phase is called liquid (l) but can, depending on the lipid's structure, be subdivided into a liquid expanded phase (l_e) at lower surface pressures Π and a liquid condensed phase (l_c) at higher surface pressure with more erected and stretched alkyl chains tilted towards the surface. Highest compression of the monolayer is reached in the solid phase (s) where lipid headgroups become dehydrated and fatty acid chains point orthogonally away from the surface. Further compression results in collapsing of the monolayer and formation of three-dimensional aggregates.[143]

A typical benchmark for the area consumption of a lipid is the area per molecule A_{20} at a surface tension of $\Pi = 20\ \mathrm{mN \cdot m^{-1}}$ (*e.g.* A_{20}(DPPC) = 46 Å^2 [144]). This area can be used to calculate the amount of lipids applied to the surface from the through area A_0 at this specific surface pressure.

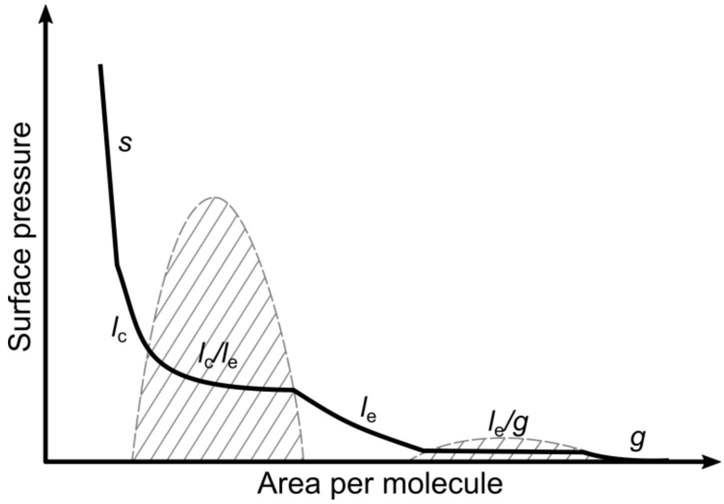

Figure 3.20. Exemplary illustration of a *Π*/*A*-isotherm of a lipid monolayer. The different phases of the monolayer are denoted: gaseous (g), liquid expanded (*l*$_e$), liquid condensed (*l*$_c$) and solid (*s*). For this example coexistence regimes of *l*$_e$ and *g* as well as *l*$_c$ and *l*$_e$ phases are visible and emphasized by grey areas.[143]

3.4.1.3 Experimental Procedure

Lipid stock solutions were prepared and their concentrations were determined by qHNMR spectroscopy. Afterwards these solutions were applied to a LANGMUIR-BLODGETT trough to measure *Π*/*A*-isotherms.

Quantitative ^{1}H NMR Spectroscopy

Lipid stock solutions of MGDG, DGDG, SQDG, POPG and 1,2-dipalmitoyl-*sn*-glycero-3-phosphocholine (DPPC) were transferred into glass vials (approximated lipid mass: 1 mg) and the organic solvent was removed under a gentle nitrogen stream. A mixture of fully deuterated d_1-chloroform and d_4-methanol (4:1 (*v*/*v*)) was prepared and used to solubilize all of the lipid films (150 µL each). Exactly the same solvent mixture was used for all samples within one preparation series.

^{1}H-NMR measurements were performed on a 600 MHz NMR spectrometer (Varian Inova 600).

Surface Pressure-Area Isotherms

Isotherms were taken at 20 °C. The LANGMUIR-BLODGETT trough and the barriers were rinsed with detergent solution (1×, Mucasol universal detergent solution) and ultrapure water (3×/10×). The trough was filled with the corresponding subphase (120 mL, see **Table 3.10**) and the barriers were integrated. After calibration of the WILHELMY plate, a defined volume of lipid solution (5–10 µL) was spread onto the surface. After equilibration for 5 min the barriers were contracted (7 $\mathrm{cm^2 \cdot min^{-1}}$) and the surface pressure Π as well as the trough area A_0 were recorded. Lipid monolayers were compressed until a surface pressure of at least $\Pi = 20\ \mathrm{mN \cdot m^{-1}}$ was reached. Within one preparation series the experiment was repeated at least three times for each lipid.

Table 3.10. Liquid subphases used for Π/A-isotherm measurements. POPG measurements were performed on buffer solution containing calcium ions to stabilize the monolayer.

Lipid	Liquid subphase
MGDG	Ultrapure water
DGDG	Ultrapure water
SQDG	Ultrapure water
POPG	150 mM NaCl, 5 mM TRIS, 0.5 mM $CaCl_2$, pH 7.0 (HCl) [145]
DPPC	Ultrapure water

Data Analysis

The general procedure for data analysis is shown in **Figure 3.21**. DPPC was used as an external standard for qHNMR. The concentration of the DPPC sample was determined by Π/A-isotherm measurements.

The surface area A_0 of a unimolecular lipid monolayer at an air-water interface can be derived from the area per lipid molecule A and the number of molecules on the surface N:

$$A_0 = N \cdot A\,. \qquad \textbf{3-8}$$

The number of molecules N depends on the volume V and the concentration c of the lipid stock solution spread onto the surface:

$$N = c \cdot V\,. \qquad \textbf{3-9}$$

Thus the molar concentration c and mass concentration ρ can be expressed by:

$$c = \frac{A_0}{A \cdot V} \qquad \textbf{3-10}$$

and

$$\rho = \frac{A_0}{A \cdot V} \cdot \frac{M}{N_\mathrm{A}}\,. \qquad \textbf{3-11}$$

M is the molar mass of the lipid and N_A the AVOGADRO constant. With A being known (*e.g.* at a specific surface pressure of $\Pi = 20\ \mathrm{mN \cdot m^{-1}}$; A_{20}(DPPC) = 46 $\mathrm{Å^2}$ [144]) the concentration of the lipid stock solution can be calculated.

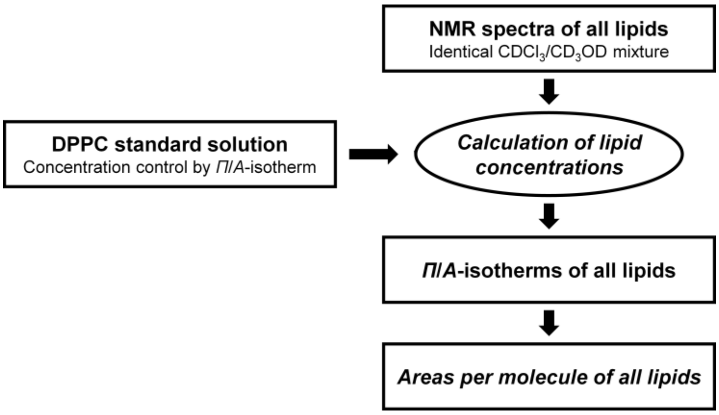
NMR spectra of all lipids
Identical CDCl3/CD3OD mixture
DPPC standard solution
Concentration control by Π/A-isotherm
Calculation of lipid concentrations
Π/A-isotherms of all lipids
Areas per molecule of all lipids

Figure 3.21. Illustrated procedure to calculate areas per molecules A_{20} by a combination of qHNMR and Π/A-isotherm measurements.

With all NMR measurements being made in exactly the same solvent mixture as the reference, signal intensities can be related to a signal from the solvent and compared within one preparation series. For this purpose the singlet of traces of $CHCl_3$ at a chemical shift of $\delta = 7.3$ ppm was chosen.[146] From the lipid spectra, integrals of the triplet signals of terminal methyl groups of the fatty acids at $\delta = 0.9–0.8$ ppm were compared (number of protons $N = 6$). Lipid concentrations could be calculated according to **Equation 3-7** by comparison to the DPPC reference.

Π/A-isotherms of the lipid solutions previously characterized by qHNMR were afterwards recorded and the areas per molecule A_{20} at a surface pressure of $\Pi = 20$ mN·m^{-1} were calculated according to **Equation 3-10**.

3.4.2 Surface Plasmon Resonance Techniques

Surface plasmon resonance (SPR) based sensors enable real-time investigation of the properties of thin films and processes at the interface between a metal surface and a medium with lower refractive index (*e.g.* aqueous solutions). Excited surface plasmons propagate along the interface, interact with the surrounding media and are sensitive to changes in refractive indices. Hence, in contrast to for example fluorescence-based techniques, SPR sensors do not require any labeling of the samples, making them very useful as a method to study processes at interfaces without manipulation of the samples themselves.[147–153]

In the field of biochemistry and biophysics, SPR based sensors are employed to study for example the selective binding of biomolecules from solution to antibodies immobilized on a metal surface or vice versa.[154,155] Furthermore, functionalization of the metal surface allows for coating with a lipid monolayer (see **Chapter 3.3.3.1**) enabling kinetic studies on the binding of biomolecules onto membrane surfaces as well.[128,156,157]

Physical background

Surface plasmons are charge-density oscillations at the interface between a metal and another medium.[158] The momentum of the plasmons k_{SP} is expressed by[147,148,152]:

$$k_{\mathrm{SP}} = \frac{\omega}{c}\sqrt{\frac{\varepsilon_{\mathrm{M}}\varepsilon_{\mathrm{D}}}{\varepsilon_{\mathrm{M}}+\varepsilon_{\mathrm{D}}}} = k\sqrt{\frac{\varepsilon_{\mathrm{M}}\varepsilon_{\mathrm{D}}}{\varepsilon_{\mathrm{M}}+\varepsilon_{\mathrm{D}}}}\,. \qquad \textbf{3-12}$$

$k = \frac{\omega}{c}$ is the free-space wavenumber calculated from the angular frequency ω and the speed of light c. The influence of the interface's properties is included in the relative permittivities of the metal ε_{M} (*e.g.* gold, 60 nm) and of the contiguous dielectric medium ε_{D} (*e.g.* buffer solution). These permittivities $\varepsilon = \varepsilon' + i\,\varepsilon''$ are complex quantities describable with a real ε' and an imaginary part ε''. To be able to excite surface plasmons the momentum of the incident photons k_{Photon} must equal the momentum of the plasmons k_{SP}. Considering the dispersion relation, the momentum of photons coming from vacuum (or air) is altered by the permittivity of the metal ε_{M} according to:

$$k_{\mathrm{Photon}} = \frac{\omega}{c}\sqrt{\varepsilon_{\mathrm{M}}}\,. \qquad \textbf{3-13}$$

Hence the momentum of these photons k_{Photon} is always smaller than the momentum of the surface plasmons k_{SP}. Excitation can nevertheless be realized for example by coupling of *p*-polarized light through a prism with the relative permittivity $\varepsilon_{\mathrm{Prism}}$ to the surface and the resulting evanescent field penetrating the metal. In this case the momentum is calculated by:

$$k_{\mathrm{Prism}} = \frac{\omega}{c}\sqrt{\varepsilon_{\mathrm{Prism}}}\sin\Phi\,. \qquad \textbf{3-14}$$

k_{Prism} also depends on the angle of incident Φ. Resonance is maximal if both momentums are equal:

$$k_{\mathrm{Prism}} = \frac{\omega}{c}\sqrt{\varepsilon_{\mathrm{Prism}}}\sin\Phi = k_{\mathrm{SP}}\,. \qquad \textbf{3-15}$$

The dispersion relation is visualized in **Figure 3.22 A**. The prism-coupled excitation of surface plasmons is realized for example in the KRETSCHMANN configuration shown in **Figure 3.22 B**. A thin metal layer is in this case positioned directly on top of the prism. The sensor surface, facing towards buffer solution, is revealed on the other side.

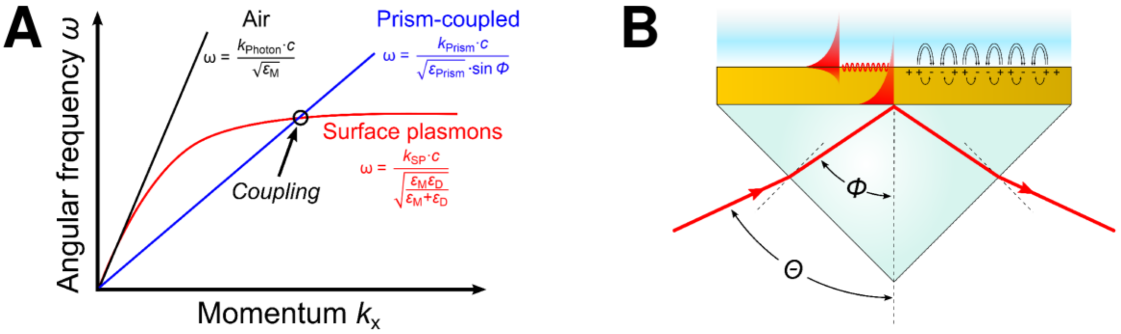
A
Angular frequency ω
Air
ω = $\frac{k_{Photon} \cdot c}{\sqrt{\varepsilon_M}}$
Prism-coupled
ω = $\frac{k_{Prism} \cdot c}{\sqrt{\varepsilon_{Prism}} \cdot \sin \Phi}$
Surface plasmons
ω = $\frac{k_{SP} \cdot c}{\sqrt{\frac{\varepsilon_M \varepsilon_D}{\varepsilon_M + \varepsilon_D}}}$
Coupling
Momentum k_x
B
Φ
Θ

Figure 3.22. Schematic plot of dispersion relation of free (black) and prism-coupled (blue) photons as well as surface plasmons (red, A).[152,158] Non-linearity is mainly caused by the frequency dependency of the permittivity of the metal ε_M. Excitation of surface plasmons after coupling of p-polarized light through a prism is realized for example in the KRETSCHMANN configuration (B).

During propagation the electromagnetic field of the surfaces plasmons penetrates both media at the interface and interacts with them (a few tens of nanometers for gold and a few hundreds of nanometers for water).[147] According to **Equation 3-15** coupling efficiency depends on the angle of incident *Φ*. By scanning the angle *Θ*-dependent intensity of the totally reflected light, physical properties (layer thicknesses, refractive indices) of both media can be extracted. Since changes in refractive index at the interface alter the angle of maximal coupling efficiency, intensity measurement at a specific angle also allows real-time observation of processes at the interface (*e.g.* substrate binding, see **Figure 3.23**).

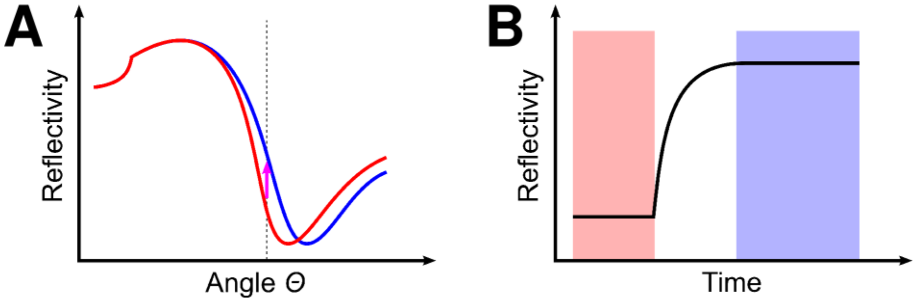

Figure 3.23. Schematic angle-reflectivity spectra before (red) and after (blue) binding of an organic substrate to the metal surface (B). Time-resolved recording of reflectivity at a specific angle provides kinetic data on substrate adsorption (C).

Experimental Procedure and Data Analysis

Hydrophobically functionalized gold surfaces evaporated on glass slides (see **Chapter 3.3.3.1**) were placed on a glass prism (LaSFN9 glass, $n = 1.84$; triangular, prism angle: 90°). Contact between the prism and the glass slide was mediated by refractive index matching oil (Series B 1.7000, Cargille Labs). The flow cell was placed on the gold surface closing the sample compartment and connecting it to a tube system and a peristaltic pump (flow rate 0.2 mL·min^{-1}).

All SPR measurements were performed on a Res-Tec RT2005 spectrometer. A HeNe laser was used as a light source (λ = 632.8 nm). Light intensity and polarization could be adjusted by two linear polarization filters. The flow cell with the attached prism was placed on a goniometric stage, allowing for both the variation of the angle of incident and the position of a photomultiplier to record reflected light intensity. Kinetic measurements were performed at a fixed angle.

The flow cell was rinsed with ethanol and spreading buffer (see **Table 3.9**). To characterize the functionalized surface an angle-reflectivity spectrum was recorded (Θ = 45–67°). Vesicle spreading (0.2–0.5 mg·mL^{-1} in spreading buffer) was afterwards performed in a closed circuit and monitored at a fixed angle at the lower end of the nearly linear part between the reflectivity maximum and minimum of the previously recorded spectrum. After a constant reflectivity was observed the surface was rinsed with spreading buffer and again an angle-reflectivity spectrum was recorded. Additional spectra were measured after every change of buffer or addition of samples followed by rinsing. After preparation of a lipid monolayer the buffer was changed to sample buffer (see **Table 3.9**) and biomolecule samples were added subsequently in the same buffer. During these steps kinetic data was recorded at a fixed angle.

Analysis of angle-reflectivity spectra was done using the software WinSpall (version 3.02, Res-Tec). A simulated spectrum including all layers of the sample (see **Table 3.11**) was fitted to the data to estimate physical thicknesses of the layers. For the addition and adsorption of sample molecules an additional layer was added to the fitting. Only parameters of this new layer were refined to determine the layer's thickness.

Table 3.11. Refractive indices of all layers used as starting points for spectra fitting by the software WinSpall. Data was compiled for λ = 633 nm using the refractive index database.[159] The organic material's layer was added after vesicle spreading.

Layer	Estimated thickness / nm	Refractive indices	
		ε'	ε''
Prism (LaSFN9)[160]		3.404	$1.526\cdot10^{-7}$
Chromium[161]	~2	−7.163	28.474
Gold[161]	~60	−10.577	1.275
Octanethiol	~1.8	~2.1	~0
Organic material		~2.1	~0
Buffer		~1.8	~0

3.4.3 Reflectometric Interference Spectroscopy

Alongside refractometric biosensors (*e.g.* SPR, see **Chapter 3.4.2**) reflectometric techniques can be employed to study optical and physical properties of thin films as well as the kinetics of processes at interfaces without the need for additional labels. Reflectometric interference spectroscopy (RIfS) monitors the interference of visible light at thin films which is influenced by the film's thickness and refractive index.[153,162–167]

In the last years RIfS was established as a tool to study among others the interactions of soluble biomolecules with supported model membranes on solid surfaces.[131,132,168,169]

Physical Background

At an interface between two media with different refractive indices n_1 and n_2 light can be reflected (I_1, see **Figure 3.24 A**) or refracted. Refraction is described by SNELL's law:

$$\frac{\sin \Theta_1}{\sin \Theta_2} = \frac{n_2}{n_1}. \qquad \textbf{3-16}$$

Θ_1 and Θ_2 are the angles of incident and refraction. In case of RIfS biosensors, after passing a thin film, the light is nearly completely reflected at the interface to a third layer n_3. The light traverses back through the film and is again refracted at the interface between the layers n_1 and n_2. Both emerging rays, I_1 and I_2, overlay afterwards. Due to a difference in path length s for I_1 and I_2 constructive or destructive interference occurs. The additional path length s of I_2 depends on the physical thickness d of the thin film, the angle of refraction Θ_2 as well as the refractive index of the film n_2:

$$s = \frac{2 \cdot n_2 d}{\cos \Theta_2}. \qquad \textbf{3-17}$$

If the angle of incident is perpendicular to the surface ($\Theta_1 = \Theta_2 = 0°$) **Equation 3-17** is reduced to:

$$s = 2 \cdot n_2 d = 2 \cdot OT\,. \qquad \textbf{3-18}$$

The product of the refractive index n_2 of the film and its physical thickness d is referred as optical thickness $OT = n_2 \cdot d$. Destructive interference is observed when a phase shift of $\Delta\phi = \frac{\lambda}{2}$ between both rays I_1 and I_2 exists. For constructive interference the phase shift $\Delta\phi$ has to be a multiple of the light's wavelength λ. By partially passing a thin film a phase shift $\Delta\phi$ is induced depending on the optical thickness OT of the film, which can by described under perpendicular illumination by:

$$\Delta\phi = \frac{2\pi}{\lambda} \cdot OT\,. \qquad \textbf{3-19}$$

The intensity R of the reflected light of I_1 and I_2 depends on the phase shift $\Delta\phi$ and the FRESNEL coefficients $r_{\mathrm{ij}} = \frac{n_{\mathrm{i}}-n_{\mathrm{j}}}{n_{\mathrm{i}}+n_{\mathrm{j}}}$ influenced by the media's refractive indices $n_{\mathrm{i/j}}$[170]:

$$R(\lambda, \Delta\phi) = \frac{r_{12}^2 + r_{23}^2 + 2r_{12}r_{23}\cos(2\cdot\Delta\phi)}{1 + r_{12}^2 r_{23}^2 + r_{12}r_{23}\cos(2\cdot\Delta\phi)} \qquad \textbf{3-20}$$

or with the expression for the phase shift $\Delta\phi$ (see **Equation 3-19**):

$$R(\lambda, OT) = \frac{r_{12}^2 + r_{23}^2 + 2r_{12}r_{23}\cos\left(\frac{4\pi}{\lambda}\cdot OT\right)}{1 + r_{12}^2 r_{23}^2 + r_{12}r_{23}\cos\left(\frac{4\pi}{\lambda}\cdot OT\right)}. \qquad \textbf{3-21}$$

Hence the optical thickness OT can be calculated from a reflectivity spectrum $R(\lambda)$ (see **Figure 3.24 B**) if the refractive indices n and therefore the FRESNEL coefficients r_{ij} of all involved media are known.

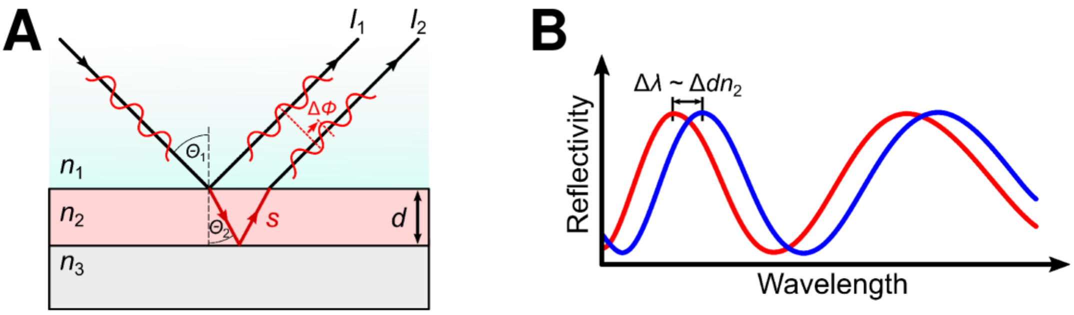

Figure 3.24. Schematic illustration of interference at a thin film (A). An incoming light ray is partially reflected (I_1) or refracted at the interface between two media n_1 and n_2. The refracted ray is again reflected after passing the film at the interface between the media n_2 and n_3. After reentering the medium n_1, I_2 overlaps with I_1 causing constructive or destructive interference depending on the phase difference $\Delta\phi$ between both rays. An exemplary reflectivity spectrum (B) shows alternating high and low intensities of the reflected white light due to wavelength-dependent interference. Changes in optical thickness $OT = d\cdot n_2$ of the interference layer n_2 cause a shift of the pattern of the reflectivity spectrum.[153]

Experimental Procedure and Data Analysis

All kinetic studies were performed in a custom-made flow-through cell (flow rate: 0.4 mL·min^{-1}) housing a hydrophilized silicon/silicon dioxide wafer (see **Chapter 3.3.4.1**).[168,169] For reflectivity measurements a tungsten halogen lamp was used as a light source (Nanocalc-2000 or HL-2000-FHSA, Ocean Optics). Spectral analysis was performed on a UV/VIS-spectrometer (Nanocalc-2000 or SD-2000, Ocean Optics) and data was recorded every 2 s by the software Spectra Suite (Ocean Optics). As a reference for full reflection of the illuminating light, a polished aluminum plate was used.

Data analysis and calculation of the optical thickness OT was performed on the fly via a Matlab-based script developed by MILENA STEPHAN[168] and revised by DR. INGO MEY. In short the reflectivity $R(\lambda,OT)$ between 500 and 700 nm was extracted and the optical thickness OT was determined by fitting **Equation 3-21** to the data.

At the beginning of each experiment the flow-through cell was rinsed with spreading buffer (see **Table 3.9**). Vesicles (0.2 mg·mL^{-1} in spreading buffer) were added in a closed loop to the surface until a constant optical thickness OT was observed, indicating full coverage of the surface. Vesicle addition was followed by rinsing with sample buffer (see **Table 3.9**). Eventually further steps of biomolecule binding were appended. Therefore solutions were added within a closed loop followed by open rinsing with sample buffer after a constant optical thickness was observed.

3.4.4 Electrochemical Impedance Spectrometry

The electrochemical properties of supported lipid membranes can be characterized by electrochemical impedance spectroscopy (EIS).[171,172] It is based on the frequency-dependent conductivity of a sample in an alternating electrical potential.[173,174] The comparison with theoretical models allows to determine for example membrane capacitance or resistance. These parameters can give insight into the successful preparation of lipid membranes on a surface.[175]

Physical Background

Impedance $Z(\nu)$ is the resistance within an alternating electrical potential at the frequency ν. In comparison to OHM's law it is defined by the time t-dependent ratio of the applied voltage U and resulting current I:

$$Z(\nu) = \frac{U(\nu,t)}{I(\nu,t)} = \frac{U_0 \cdot e^{i\cdot 2\pi\cdot\nu\cdot t}}{I_0 \cdot e^{i\cdot 2\pi\cdot\nu\cdot t - \Theta(\nu)}} = |Z|(\nu)\cdot e^{-i\cdot\Theta(\nu)}\,. \qquad \textbf{3-22}$$

The phase angle Θ denotes the frequency-dependent lag between applied voltages and induced currents. $|Z|$ is the absolute value of the impedance. The impedance itself is a complex parameter characterized by a real Z' and an imaginary component Z'':

$$Z(\nu) = Z'(\nu) + iZ''(\nu)\,. \qquad \textbf{3-23}$$

With these two components Z' and Z'' the absolute value of the impedance $|Z|$ and the phase angle Θ can be expressed as:

$$|Z| = \sqrt{(Z')^2 + (Z'')^2} \qquad \textbf{3-24}$$

and

$$\Theta = \tan^{-1}\left(\frac{Z''}{Z'}\right). \qquad \textbf{3-25}$$

To access physical properties of a sample, impedance spectra have to be compared to theoretical models describing its electronical properties. A solid supported lipid bilayer can be regarded as a parallel circuit of a membrane capacitance C_m and a membrane resistance R_m. The membrane resistance R_m is characterized by the permeability for charged particles. The membrane capacitance C_m is determined by the dielectric properties of the membrane and can be described itself as a series of headgroup and hydrophobic core capacitances. Because the dielectric constant of the headgroup region is very high ($\varepsilon_\mathrm{r} = 20$ [176]) the membrane capacitance is mainly defined by the dielectric constant of the hydrophobic core region ($\varepsilon_\mathrm{r} = 2.1$ [177]).[178] The measuring cell for EIS also contains buffer solution with its resistance R_b and the electrodes with additional capacitances C_el. Both are connected in series to the membrane (see **Figure 3.25 A**).

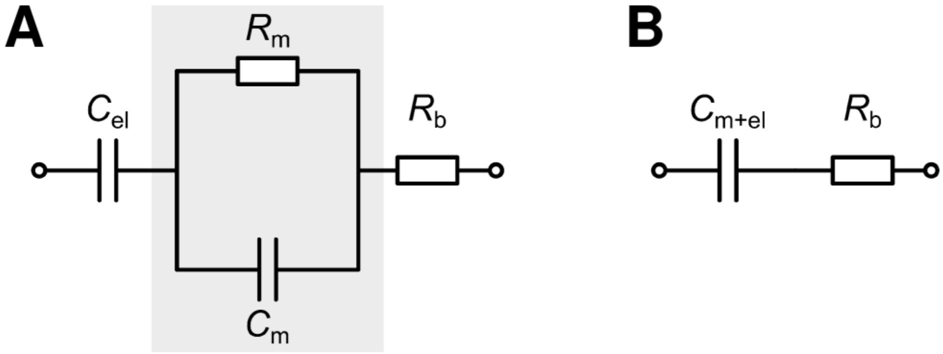

Figure 3.25. Equivalent circuit for a solid supported membrane (grey) with a membrane capacitance C_m and resistance R_m embedded in a measuring cell with a buffer resistance R_b and electrode capacitance C_el (A). Under the assumption of very high membrane resistance the equivalent circuit can be simplified to a serial circuit of the buffer resistance R_b and an undistinguishable combined capacitance of the membrane and the electrodes $C_\mathrm{m+el}$ (B).

Under the assumption of very high membrane resistance R_m[176] the resistance parallel to the membrane capacitance C_m can be neglected. Additionally, it is not possible to distinguish by means of EIS between two capacitances connected in series without for example parallel resistances, thus the capacitances of the membrane C_m and the electrodes C_el were combined to $C_\mathrm{m+el}$ (see **Figure 3.25 B**). The absolute value of the impedance $|Z|$ of the equivalent circuit can be calculated by:

$$|Z|(\nu) = \sqrt{R_\mathrm{b}^2 + \left(\frac{1}{2\pi \cdot \nu \cdot C_\mathrm{m+el}}\right)^2} \qquad \textbf{3-26}$$

and the phase angle Θ by:

$$\Theta(\nu) = \tan^{-1}\left(-\frac{1}{2\pi \cdot \nu \cdot C_\mathrm{m+el} \cdot R_\mathrm{b}}\right). \qquad \textbf{3-27}$$

Experimental Procedure and Data Analysis

Measurements were performed on a frequency analyzer (Impedance Gain Phase Analyzer and Dielectric Interface SI 1260, Solartron Instruments) in a frequency range of $\nu = 10^{-1}$–10^{6} Hz at an alternating voltage of U_{pp} = 30 mV without any direct current bias.

Solid supported membranes on functionalized gold surfaces (see **Chapter 3.3.3.1**) were analyzed by directly contacting the gold surface. A counter electrode (platinated platinum wire) and an Ag/AgCl reference electrode were placed in the buffer solution.

Data analysis was performed by the software ZPlot and ZView (Solartron Instruments). Fitting of the measured data according to the simplified equivalent circuit (see **Figure 3.25**, **Equation 3-26** and **Equation 3-27**) yielded absolute values of the capacitance $C_{\mathrm{m+el}}$ and the resistance R_{b}.

3.4.5 Fluorescence Microscopy

Visualization of solid supported lipid membranes was mainly achieved by fluorescence microscopy. This imaging technique uses autofluorescence or fluorescence of dye molecules attached to specific specimen to localize them with low invasiveness, high sensitivity and low background intensities. In this study two different setups of fluorescence microscopes were deployed: An epifluorescence microscope, which was combined with an atomic force microscope (AFM, see **Chapter 3.4.6**) and allowed direct correlation between fluorescence and topological data, and a confocal laser scanning microscope (CLSM), which was used for imaging and also allowed the study of membrane dynamics by fluorescence recovery after photobleaching (FRAP) experiments.

3.4.5.1 Physical Background

Fluorescence microscopy images the fluorescence of a sample.[179] By excitation with light of the wavelength λ_{ex} an excited electronic state S_1 of the absorbing molecule can be reached (see **Figure 3.26**). Electronic excitation is accompanied by an increase in vibrational state. By radiation-free relaxation the vibrational ground state of the electronic state S_1 is reached before transition back into the electronic ground state S_0. This relaxation process includes the emission of light of the wavelength λ_{em}. Since a fraction of the absorbed energy was released by radiation-free vibronic relaxation, the wavelength of the emitted light λ_{em} is red-shifted compared to the excitation wavelength λ_{ex} (STOKES shift). Light emitted from the sample can therefore easily be separated from scattered excitation light to effectively reduce background signals and enhance the contrast. The use of multiple dye molecules with spectrally separated excitation and emission wavelengths also allows simultaneous observation of different specimen.

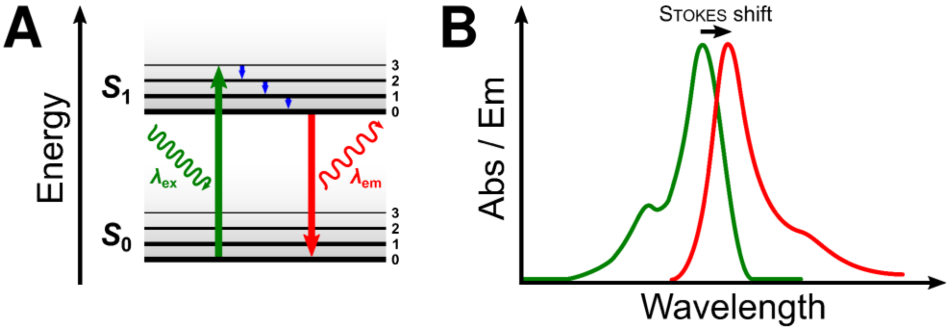

Figure 3.26. Schematic energy diagram with two electronic states S_0 and S_1 as well as four of their vibrational states (A). Absorption of light λ_{ex} excites the molecule to an exited vibrational state of the excited electronical state S_1. A part of the absorbed energy is emitted by radiation-free relaxation into the vibrational ground state of S_1. By transition back into S_0 radiation with $\lambda_{em} > \lambda_{ex}$ is emitted. The change in wavelength between excitation and emission is illustrated as a red-shift in an exemplary absorbance (green) and emission (red) spectrum (B).

Epifluorescence Microscopy

The basic setup of an epifluorescence microscope is illustrated in **Figure 3.27**. A mercury-vapor lamp is used as a light source. An optical bandpass filter extracts the excitation wavelength λ_{ex}. Afterwards the beam is directed by a dichroic mirror through the objective to the sample. Light emitted from the sample is collected by the objective as well and redirected to the dichroic mirror. The properties of this mirror are mainly defined by its cutoff wavelength. Light with shorter wavelength (*e.g.* excitation light λ_{ex}) is reflected while light with a longer wavelength (*e.g.* light emitted by fluorescence of the sample λ_{em}) can pass the mirror. The dichroic mirror therefore pre-separates the fluorescent light from scattered emission light. An additional selection of the fluorescent light is done via a second optical filter, transmitting only the light to be detected subsequently by a CCD camera.[179]

During imaging, the whole visualized area of the sample is illuminated and simultaneously recorded by the CCD camera. The resolution of an epifluorescence microscope is limited by ABBE's law giving the smallest possible distance d_{FWHM} between two distinguishable points:

$$d_{\mathrm{FWHM}} = \frac{0.51 \cdot \lambda_{\mathrm{em}}}{n \cdot \sin\alpha} = \frac{0.51 \cdot \lambda_{\mathrm{em}}}{NA}. \qquad \textbf{3-28}$$

n is the refractive index of the sample medium and α the opening angle of the objective. Both parameters are commonly combined into the numerical aperture $NA = n \cdot \sin\alpha$.[180]

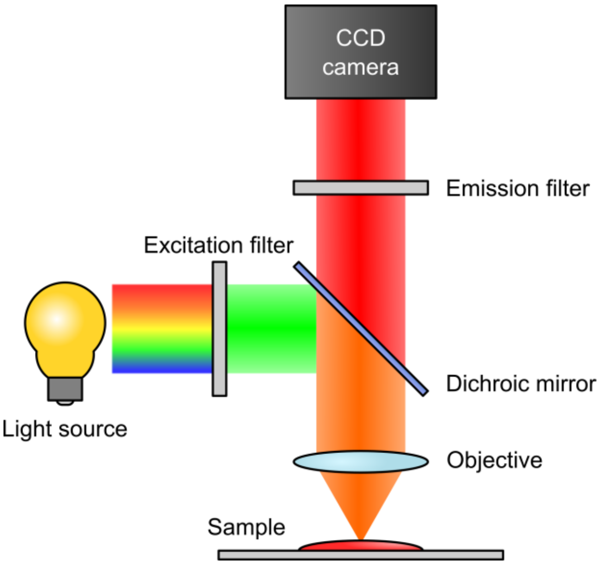

Figure 3.27. Schematic illustration of the optical path of an epifluorescence microscope. The excitation wavelength λ_{ex} is selected from the emission spectrum of mercury-vapor lamp by an optical excitation filter. The beam is guided via a dichroic mirror and through the objective to the sample. Emitted light from the sample is collected by the objective and partially transverses the dichroic mirror. Through an emission filter only light of the wavelength λ_{em} is able to pass and is afterwards recorded by a CCD camera.

Confocal Laser Scanning Microscopy

The confocal laser scanning microscope (CLSM, see **Figure 3.28**) is an improvement of the fluorescence microscope first introduced in 1969 by DAVIDOVITS and EGGER.[181,182] In contrast to an epifluorescence microscope, a laser is used as light source. During a measurement the surface is scanned in *x*- and *y*-direction with a small illumination spot rather than full illumination of the sample. Overall this reduces light exposure of the sample and lowers bleaching of fluorescent dyes but increases recording time.[183] Another major difference to a conventional fluorescence microscope is the adjustable pinhole in the optical path after emitted light passed the dichroic mirror. It is positioned at the focus point of the emitted light hence it can be used to increase resolution in *z*-direction. Light emitted outside the focus plane within the sample is not focused inside the pinhole and therefore mainly blocked. Since the CLSM works in a scanning mode a more sensitive single detector (*e.g.* photomultiplier tube) can be employed to quantify light intensities after passing an emission filter.[180,184,185]

The lateral resolution limit of the CLSM depends on the opening of the pinhole and is influenced by the excitation wavelength λ_{ex}. For wide pinholes the smallest possible distance d_{FWHM} between two distinguishable points is given by:

$$d_{FWHM} = \frac{0.51 \cdot \lambda_{ex}}{NA}. \qquad \textbf{3-29}$$

NA is the numerical aperture $NA = n \cdot \sin\alpha$ of the objective.[180,185,186] For small pinholes with an opening diameter below the AIRY pattern of the light the lateral resolution can be improved up to:

$$d_{\mathrm{FWHM}} = \frac{0.37 \cdot \bar{\lambda}}{NA}, \tag{3-30}$$

where $\bar{\lambda}$ is the mean wavelength of both excitation and emitted light ($\bar{\lambda} = \sqrt{\lambda_{\mathrm{ex}} + \lambda_{\mathrm{em}}}$).[180] The CLSM can be used to detect multiple spectrally separated dyes at the same time, too. Therefore more than one laser can be deployed for sample illumination. Spectral separation of the emitted light can be realized for example by splitting the beam by a series of dichroic mirrors with different cutoff wavelengths. Before detection with separate detectors further wavelength selection can be achieved by additional emission filters.

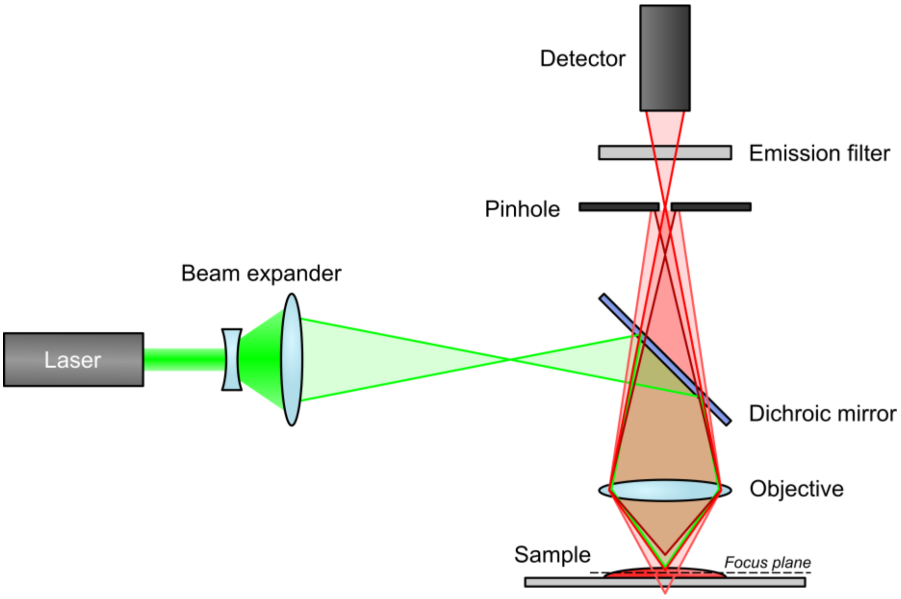

Figure 3.28. Schematic illustration of the optical path of a confocal laser scanning microscope (CLSM). An expanded laser beam is used to illuminate the sample. Emitted light is collected and focused through an objective. After passing a dichroic mirror the light reaches an adjustable pinhole. Only light emitted within the focus plane is focused in the pinhole and passes it unblocked. Final selection of the observed wavelength is done by an optical emission filter before the light is detected for example by a photo multiplier tube.

Fluorescence Recovery after Photobleaching

Lipid diffusion within a lipid bilayer can be studied by fluorescence recovery after photobleaching (FRAP).[187] Lipid-bound dye molecules embedded in the lipid bilayer are bleached by a strong laser pulse. After bleaching mobile lipids can diffuse within the membrane leading to a mixing of both bleached and unbleached dye molecules. Thus fluorescence intensity in the bleached area recovers over time. Immobile fractions would limit fluorescence recovery.

Since recovery of fluorescence after bleaching already indicates lateral mobility of lipids within the lipid membrane, additional quantitative analysis of lipid diffusion can be carried out for example according to ALEXROD.[188,189] Thereby bleaching is interpreted as an irreversible first-order reaction. The GAUSSIAN bleaching profile with the radial r-symmetric intensity profile $C(r,t = 0)$ generated by the laser pulse can be described as:

$$C(r,t=0) = C_0 \exp\left(-\alpha T \frac{2P_0}{\pi\omega^2} \exp\left(-\frac{2r^2}{\omega^2}\right)\right). \tag{3-31}$$

C_0 is the fluorescence intensity before bleaching. The profile is mainly influenced by the rate constant for bleaching α and the laser, specified by its intensity P_0, its half width ω and the bleaching time T. Diffusion of lipids can be described according to FICK's law by the diffusion coefficient D.[190] Time-dependent recovery of the bleached profile can thus be expressed as:

$$C(r,t) = C_0 - \frac{A}{4\pi D(t)} \exp\left(-\frac{r^2}{4D(t)}\right). \tag{3-32}$$

A is the total area of the GAUSSIAN function. Integration of the centrosymmetric bleaching profile $C(r,t)$ to the radius of the bleachspot r_B yield the following expression for the fluorescence intensity I within this area:

$$I(t) = A - \exp\left(-\frac{r_B^2}{4D(t)}\right). \tag{3-33}$$

Experimental intensity data $I(t)$ (see **Figure 3.29**) can be fitted according to this model by the exponential decay function:

$$I(t) = I_{\max} - I_{\text{bleach}} \exp\left(-\frac{t}{T_1}\right). \tag{3-34}$$

$I_{\max} = I(t = \infty)$ is the maximal fluorescence intensity after (partial) recovery and $I_{\text{bleach}} = I(t = \infty) - I(t = 0)$ the decrease of fluorescence intensity during bleaching. T_1 is introduced as a recovery constant. An estimate for the diffusion coefficient can be calculated from the half-time value $\tau_{1/2} = \ln(0.5)\cdot(-T_1)$ of the recovery by:

$$D = \frac{r_B^2}{4\tau_{1/2}}. \tag{3-35}$$

In the past years new methods for procession of FRAP data have been developed. One example is the technique by JÖNSSON *et al.* who use HANKEL transformations to calculate diffusion coefficients more precisely.[191]

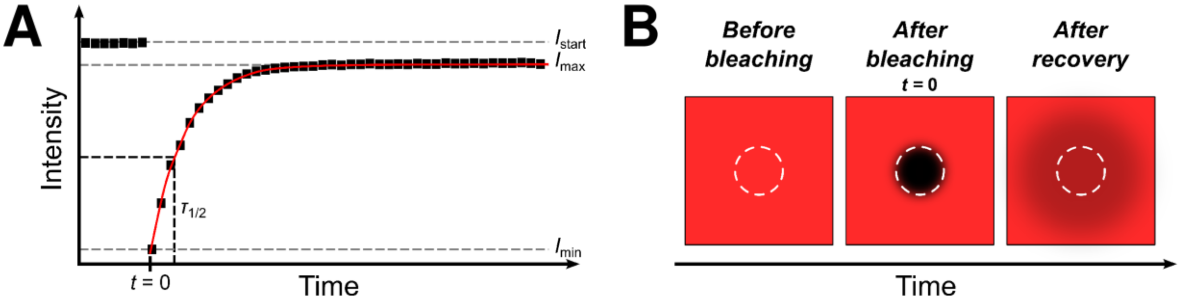

Figure 3.29. Exemplary intensity data from a FRAP experiment (A) as well as corresponding schematic fluorescent micrographs (B). Before bleaching a homogeneous fluorescence with the intensity I_{start} is observed. After bleaching (t = 0) the intensity within the bleached area (white circle) is decreased to I_{min}. Fluorescence recovery up to I_{max} is observed afterwards.

3.4.5.2 Experimental Procedures and Data Analysis

Instrumentation

Epifluorescence measurements were performed parallel to atomic force microscopy (see **Chapter 3.4.6**) on an inverse microscope (Olympus IX51). A 60× air objective (*NA* = 0.7, Olympus LUCPLFLN 60X) was used to image the sample through a glass slide and the thin plate of mica glued onto it (see **Chapter 3.3.4.2**). To monitor TexasRed fluorescence a U-FYW filter cube (Olympus, λ_{ex} = 540–585 nm, λ_{em} = 600 nm, λ_{Dichro} = 595 nm) was installed. Fluorescent micrographs were recorded by a CCD camera (Lumenera Infinity 2).

CLSM and FRAP were carried out on an upright laser scanning microscope (Olympus FV1200). Either a 20× (Olympus UMPLFLN 20XW, *NA* = 0.5) or a 60× water immersion objective (Olympus LUMPLFLN 60XW, *NA* = 1) was used. Selected laser and emission filters are summarized in **Table 3.12**. Signal detection was either done by standard photomultipliers or more sensitive GaAsP detector units.

In general, data visualization and analysis was performed with the software ImageJ.[192] For all images printed in this work brightness and contrast were enhanced in a last step to improve picture quality in the printed version.

Table 3.12. Lasers and filters used for confocal laser scanning microscopy.

Dyes	Lasers (λ_{ex})	Emission filters (λ_{em})
TexasRed-DHPE	561 nm	570–670 nm
TexasRed-DHPE	561 nm	575–675 nm
FITC-C3N13	488 nm	505–540 nm
TexasRed-DHPE	561 nm	608–690 nm
Bodipy-C_{12}HPC	488 nm	500–550 nm
TexasRed-DHPE	561 nm	608–690 nm
Atto488-DHPE	488 nm	500–550 nm

Experimental Procedures

Imaging of Solid Supported Membranes and Fluorescence Recovery after Photobleaching Experiments

Solid supported membranes on hydrophobically functionalized glass, silicon/silicon dioxide wafers or mica were prepared as described previously in **Chapter 3.3.3** and **Chapter 3.3.4**. Lipid mixtures contained 0.5–1.0 mol% of lipid-bound dyes (*e.g.* TexasRed-DHPE). After rinsing with sample buffer (see **Table 3.9**) the surface was imaged.

FRAP experiments were performed by selecting an area to be bleached. For lipid membranes in absence of polyamines the radius was about ω = 5–10 µm. Before bleaching a time series of about ten frames was recorded to determine the initial membrane fluorescence. TexasRed dye molecules in the selected area were bleached with at laser intensity of 20 mW and a GAUSSIAN intensity profile for 3 s. Recovery was monitored afterwards at low laser intensity for at least 2 min.

From the FRAP data diffusion coefficients D could be calculated according to **Equation 3-34** and **3-35** or by using the Matlab-based software FRAP analysis 2.5 by JÖNSSON that performs HANKEL transformations.[191]

Addition of Polyamines

Polyamine stock solutions were either added directly to the buffer covering the membrane or alongside SUV suspension (final SUV concentration in the sample: 4 µg·mL^{-1}). In both cases the final polyamine concentration, standardized to the number of nitrogen atoms, was c_N = 30 µM. If the effect of polyamines was not observed in real-time by time laps fluorescence microscopy during polyamine addition, the sample was incubated for at least 2 h at room temperature before imaging.

FRAP experiments after polyamine addition were carried out as described previously for the investigation of lipid membranes but the radius of the bleach spot ω was adjusted to cover a complete structure to be bleached.

3.4.6 Atomic Force Microscopy

The atomic force microscope (AFM) is a scanning probe microscope that uses a sharp tip to scan a surface and determine topological and other physical properties. Within its broad field of applications AFM has intensively been used to study lipid membranes.[193–197] The field of research includes the visualization of height differences between membrane domains,[198,199] mechanical studies on lipid vesicles[200] or free-standing lipid bilayers[127,201] as well as analysis of protein accumulation on or within lipid membranes.[131,202] In this study AFM was used to characterize solid supported lipid bilayers and visualize changes in topography after addition of long-chain polyamines.

Physical Background

AFM probes the properties of a sample by scanning its surface with a sharp tip. Tip diameters are typically less than 100 Å wide, enabling down to atomic resolution of the AFM.[203] Interactions between the tip and the sample can be approximately described by a Lennard-Jones potential V(r) (see **Figure 3.30**):

$$V(r) = 4\varepsilon\left[\left(\frac{r_0}{r}\right)^{12} - \left(\frac{r_0}{r}\right)^{6}\right]. \tag{3-36}$$

r is the distance between the tip and the sample. The parameter ε defines the maximal attractive potential and r_0 is the distance where the potential $V(r_0) = 0$. On long distances between the tip and the sample attractive Van-der-Waals interactions dominate while on shorter distances repulsive interactions prevail.

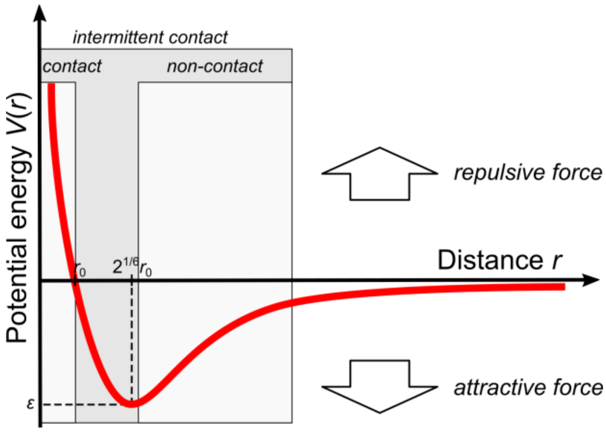

Figure 3.30. Illustration of a Lennard-Jones potential denoting the potential energy *V*(*r*) between two bodies in the distance *r*. Additionally the working regions of contact, non-contact and intermittent contact AFM modes are emphasized.[142,203]

Interactions between the surface and the tip are typically in the range of piconewtons[204] thus a sophisticated setup for force measurement is required. A schematic of an AFM is illustrated in **Figure 3.31**. The AFM tip is fabricated on a cantilever with a spring constant k, commonly made of silicon or silicon nitride (Si_3N_4). If force F is applied to the tip, the cantilever is deflected which can be described by Hooke's law:

$$F = -k \cdot z\,. \tag{3-37}$$

The deflection of the cantilever z can be detected by a laser beam pointed onto the reflective backside of the cantilever. The reflected light traverses to the middle of an array of a four quadrant photodiode. If the cantilever is deflected the reflection angle of the laser beam changes and a displacement of the light spot on the photodiode can be detected. This signal is compared to a setpoint and used to readjust the cantilever-surface-distance via a piezo in *z*-direction. Additionally the height of the sample can be determined. To measure a full topographical map of the surface, the sample is moved via two piezos in *x*- and *y*-direction and scanned by the cantilever tip.

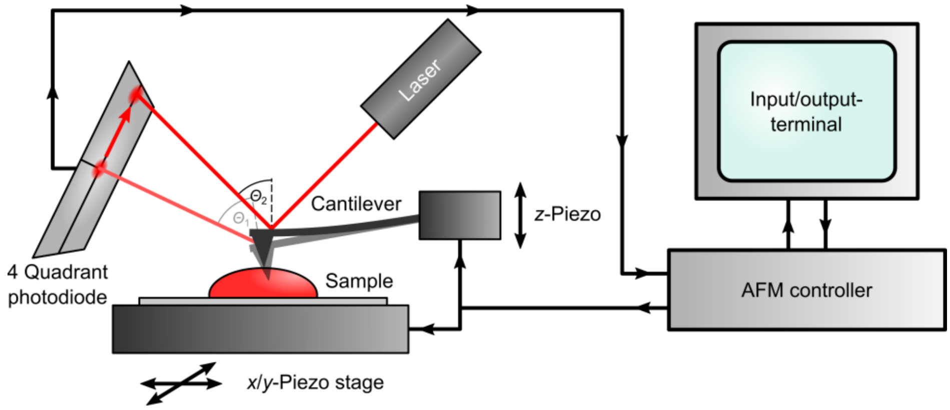

Figure 3.31. Schematic illustration of an AFM. If the tip at the cantilever gets in repulsive contact with the sample, it is deflected. As a result, the reflection angle Θ of a laser pointed on the backside of the cantilever is changed and reflected to a different position on a segmented photodiode. This signal is detected and processed by an AFM controller constantly readjusting the cantilever height and transferring information to an input/output-terminal. Scanning is performed by movement of a *x*/*y*-piezo stage.

The AFM offers a variety of different imaging modes, which can be divided into static and dynamic modes. An example for a static mode is the so called contact mode. Herein the tip is in constant contact with the surface while scanning the sample. On the other hand dynamic modes like the intermittent contact mode drive the cantilever in oscillation near its resonance frequency ν_0. Contact to the surface is only punctiformly induced which lowers frictional forces.[204]

Besides imaging modes the AFM provided the feature to perform force spectroscopy. While approaching the surface with the cantilever the force applied to the surface, causing a deflection of the cantilever, is recorded. In general this technique is used to study mechanical properties of samples. In regard to the investigation of lipid bilayers it is possible to apply that much force to the membrane that the tip of the cantilever breaks through the bilayer.[194,196,197] From the recorded force-distance-curves (FDC) the bilayer thickness can be extracted as illustrated in **Figure 3.32**.

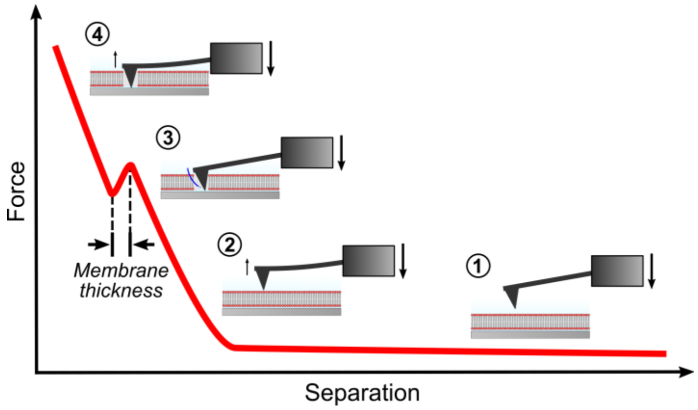

Figure 3.32. Schematic illustration of a force distance curve on a solid supported lipid bilayer. Application of force on the membrane during the approach can lead to a breakthrough event through the lipid bilayer. The membrane thickness can be calculated from the depth of the breakthrough.

Experimental Procedure

All experiments were performed in intermittent contact mode on a MFP-3D AFM (Asylum Research). For measurements in air Olympus OMCL-AC160TS-R3 cantilevers ($\nu_{0,\mathrm{air}}$ = 280–340 kHz, k = 31.7–36.9 N·m^{-1}) were employed while Bruker MSNL-10 ($\nu_{0,\mathrm{air}}$ = 90–160 kHz, k = 0.3–1.4 N·m^{-1}) or Bruker MLCT cantilevers ($\nu_{0,\mathrm{air}}$ = 90–160 kHz, k = 0.3–1.2 N·m^{-1}) were used in solution. Images were recorded with a line rate of 1 Hz.

An additional inverse epifluorescence microscope (Olympus IX51, see **Chapter 3.4.5.2**) enabled correlative atomic force and fluorescence microscopy. Fluorescence micrographs were taken on transparent substrates (glass or mica) immediately before and after imaging by AFM.

In order to perform force spectroscopy and measure FDC the spring constant of the cantilever was determined by the thermal noise method[205] incorporated into the AFM control software. Measurements were performed up to a maximal repulsive force of 4 nN at an approach and retrace velocity of 2 µm·s^{-1} and a sampling rate of 12.5 kHz.

Data processing was done by the software Gwyddion (version 2.45)[206] or Igor Pro (version 6.37, WaveMetrics, Inc.). It mainly consisted of polynomial flattening of the sample.

3.4.7 Contact Angle Measurements

A common way to probe surface hydrophilicity or hydrophobicity is the measurement of contact angles at phase interfaces (air/liquid/support). After addition of a droplet to a surface the wetting of the support, and therefore the contact angle, depends on the interaction of both phases.[207–209]

Physical Background

The surface tension σ_{ij} at the interface between the two phases i and j consist of a nonpolar part $\sigma_{\mathrm{ij}}^{\mathrm{d}}$ (dispersive interactions between molecules) and a polar part $\sigma_{\mathrm{ij}}^{\mathrm{p}}$ ((induced) dipole-dipole interactions and hydrogen bonds):

$$\sigma_{\mathrm{ij}} = \sigma_{\mathrm{ij}}^{\mathrm{p}} + \sigma_{\mathrm{ij}}^{\mathrm{d}}\,. \qquad \textbf{3-38}$$

Per definition the work of adhesion W_{ad} describes the reversible work necessary to create an 1 cm^2 interface between a solid s and a liquid l phase. It depends on the surface tensions between the different phases (gaseous phase: g):

$$W_{\mathrm{ad}} = 4\left(\frac{\sigma_{\mathrm{gl}}^{\mathrm{d}}\sigma_{\mathrm{gs}}^{\mathrm{d}}}{\sigma_{\mathrm{gl}}^{\mathrm{d}} + \sigma_{\mathrm{gs}}^{\mathrm{d}}} + \frac{\sigma_{\mathrm{gl}}^{\mathrm{p}}\sigma_{\mathrm{gs}}^{\mathrm{p}}}{\sigma_{\mathrm{gl}}^{\mathrm{p}} + \sigma_{\mathrm{gs}}^{\mathrm{p}}}\right) = (1 + \cos\theta)\sigma_{\mathrm{gl}}\,. \qquad \textbf{3-39}$$

Θ is the contact angle (see **Figure 3.33**) and is used as a measure for liquid-solid interactions.[210] By application of a polar liquid (*e.g.* water) the contact angle Θ decreases the more hydrophilic the surface is.

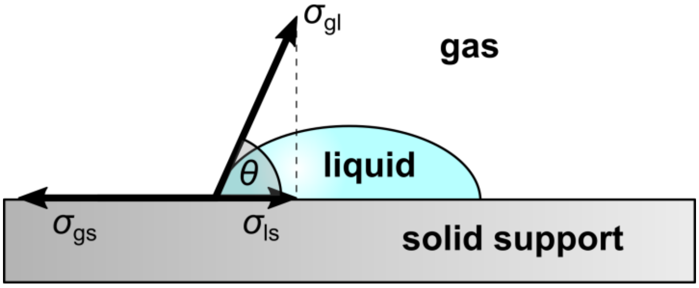

Figure 3.33. Schematic illustration of a droplet of liquid on a solid support. The contact angle *Θ* depends on the surface tensions σ_{ij} between all phases (g: gaseous, l: liquid, s: solid).[210]

Experimental Procedures

A droplet of ultrapure water (2 µL) was placed on the surface and a photograph was taken from the plane of the surface. Extraction of the contact angle Θ was done by the ImageJ[192] plug-in Drop Shape Analysis.[211,212]

4 MODEL MEMBRANES

This study deals with an *in vitro* approach to investigate interactions of diatom biomolecules with lipid membranes. All of the examined biomolecules were found in the biosilica and are therefore presumably involved in silica biogenesis within the silica deposition vesicle (SDV). Artificial membranes should represent the SDV membrane, called silicalemma, and shed light on a possible influence of the silicalemma on self-assembly processes within the SDV.[14,59] While aggregation of various diatom biomolecules, including long-chain polyamines (LCPA)[8,43], silaffins[50] and cingulins[36], has already been studied in solution only a few studies on model peptides address the influence of a lipid membrane.[213]

As a first step, an *in vitro* model system had to be established which enables the use of a variety of different biophysical techniques to probe interactions of biomolecules and lipid membranes. Within the past decades, solid supported lipid membranes were commonly used to mimic biomembranes and proved to be a valuable system addressable for both kinetic and imaging studies.[86,88,120,171]

Up to this point it was not possible to isolate SDVs from diatoms and study their exact chemical composition. Thus also the exact lipid composition of the silicalemma remains unknown. Although the organelle's lipid composition is unknown, some studies analyzed the overall lipid composition of algae and diatoms in particular.[62–64] For this study the work of VIELER *et al.* is interesting as it revealed the overall lipid compositions of the two diatom species *Chlamydomonas reinhardtii* and *Cyclotella meneghiniana* (*C. meneghiniana*).[66] The lipid composition of *C. meneghiniana* has been chosen as a starting point to find a suitable lipid composition for the formation of solid supported artificial model membranes in this study. The main components of the diatom's membranes are the three glycolipids monogalactosyldiacylglycerol (MGDG, 33.7%), digalactosyldiacylglycerol (DGDG, 17.5%) and sulfoquinovosyldiacylglycerol (SQDG, 24.7%) alongside smaller fractions of phosphatidylglycerol (PG, 15.4%) and phosphatidylcholine (PC, 8.7%). Similar lipid compositions had yet only been employed in a few *in vitro* studies using either vesicles[77–82], black lipid membranes[83] or lipid monolayers at air-water interfaces or transferred by LANGMUIR-BLODGETT techniques onto solid supports.[67,84,85,214] Here, for the first time, solid supported lipid bilayers and solid supported lipid monolayers formed by vesicle spreading are introduced.

Since lipid compositions used in this study are rather complex, consisting of five or more components (mostly 35% MGDG, 20% DGDG, 15% SQDG, 5% POPG and 25% DOPC), at first a protocol for stock solution preparation and reproducible lipid mixture compilation had to be established (see **Chapter 4.1**). Afterwards solid supported lipid monolayers (see **Chapter 4.2**) and bilayers (see **Chapter 4.3**), reflecting the native lipid composition of *C. meneghiniana* as close as possible, were prepared and characterized by a variety of different biophysical techniques. Both protocols for kinetic studies and imaging of the surface were established for later studies on interactions between lipid membranes and different biomolecules.

Results shown in this sections have partially been published in the peer-reviewed article "3D-Membrane stacks on supported membranes composed of diatom lipids induced by long-chain polyamines" (*Langmuir* **2016**, *32*, 10144–10152, co-authors: MARYNA ABACILAR, FABIAN DAUS, PROF. DR. ARMIN GEYER and PROF. DR. CLAUDIA STEINEM; [99]).

4.1 Surface Areas of Plant Lipids

To use surface pressure-area isotherms (*Π*-*A*-isotherms), recorded on a LANGMUIR-BLODGETT trough, as a routine for lipid concentration determination, the molecular surface area A_{20} of a lipid monolayer at a certain surface pressure $\Pi = 20\ \mathrm{mN \cdot m^{-1}}$ has to be known. For DOPC (A_{20}(DOPC) = 70 Å^2 [215]) this method is well established but for MGDG, DGDG, SQDG and POPG, despite several published studies on lipid monolayers,[216–220] suitable reference values also representing the proper fatty acid composition were not available. Therefore a combination of quantitative ^{1}H-nuclear magnetic resonance (qHNMR) spectroscopy and monolayer investigation on a LANGMUIR-BLODGETT trough were employed to determine the molecular surface areas A_{20} of these lipids. qHNMR provided lipid stock solutions with known concentration, which could be used to calculate the molecular surface areas A_{20} from the *Π*-*A*-isotherms.

Surface Pressure-Area Isotherm of DPPC

1,2-Dipalmitoyl-*sn*-glycero-3-phosphocholine (DPPC) was used as an external standard for concentration measurements by qHNMR. Since its molecular surface area is known (A_{20}(DPPC) = 46 Å^2 [144]), the concentration of a DPPC solution can be determined from a Π-A-isotherm of a DPPC monolayer at an air-water-interface. An exemplary Π-A_0-isotherm is shown in **Figure 4.1**. For each sample isotherms were measured at least three times.

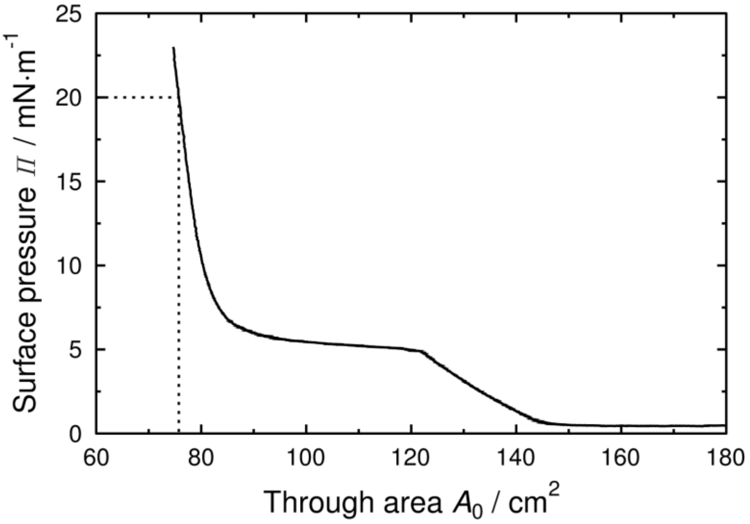

Figure 4.1. Exemplary Π-A_0-isotherm of DPPC on ultrapure water at 20 °C.

The mass concentration ρ of the lipid stock solution could be calculated from the trough area A_0 at a surface pressure of $\Pi = 20$ mN·m^{-1} and the volume V of spread lipid solution by **Equation 3-11**. From the exemplary preparations (including **Figure 4.1**, $A_0(\Pi = 20$ mN·m$^{-1}) = (75\pm1)$ cm^2) a stock solution concentration of $\rho = (8.0\pm0.1)$ mg·mL^{-1} ($c = (10.9\pm0.1)$ mM) was calculated.

It is important to mention that the DPPC stock solution was prepared in exactly the same mixture of d$_1$-chloroform and d$_4$-methanol (4:1 (*v*/*v*)) as all other lipid samples within one preparation. In total, three independent preparations were performed.

Quantitative ^{1}H-Nuclear Magnetic Resonance Spectroscopy

^{1}H-NMR spectra of all five lipids – MGDG, DGDG, SQDG, POPG and DPPC – were recorded. An exemplary ^{1}H-NMR spectrum of POPG is shown in **Figure 4.2**.

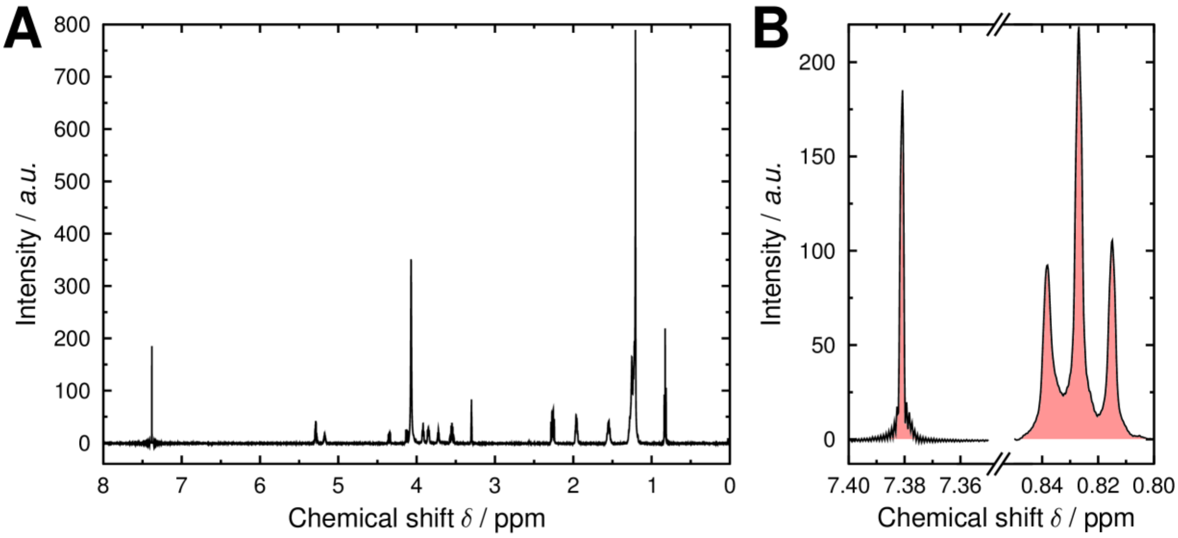

Figure 4.2. **Exemplary ^{1}H-NMR spectrum of POPG in CDCl$_3$/CD$_3$OD (4:1 (*v*/*v*)) (A) and emphasized signals of CHCl$_3$ traces (δ = 7.38 ppm) and terminal methyl groups of the fatty acids (δ = 0.83 ppm) (B). Integrals (red) of both signals were used for comparison of signal intensities and calculation of lipid concentrations.**

As mentioned before, the DPPC solution was used as an external standard for quantitative measurements. As an inter-sample reference, the singulett of CHCl$_3$-traces (δ = 7.3 ppm [146]) was used. Since exactly the same solvent mixture was used for all samples within one preparation, an identical concentration of CHCl$_3$ can be assumed. Internal comparison between the solvent signal and the lipid signal was achieved via the isolated triplett signals of the fatty acids' terminal methyl groups (δ = 0.8–0.9 ppm). An exemplary dataset of lipid concentrations of one preparation calculated according to **Equation 3-7** is shown in **Table 4.1**.

Table 4.1. **Exemplary concentration dataset from one preparation. As a reference the previously characterized DPPC solution was used. *I* is the relative signal intensity of the solvent or the terminal methyl groups. N_{Lipid} denotes the number of protons contributing to the methyl group's signals and $\rho = c \cdot M$ is the mass concentration of the lipid solution.**

Lipid	$I_{\text{C}\underline{\text{H}}\text{Cl3}}$	$I_{\text{C}\underline{\text{H}}3}$	N_{Lipid}	c_{Lipid} / mM	ρ_{Lipid} / mg·mL^{-1}
MGDG	1.00	1.37	6	7.39±0.09	5.56±0.07
DGDG	1.00	2.28	6	1.81±0.02	1.68±0.02
SQDG	1.00	2.56	6	4.58±0.06	3.77±0.05
POPG	1.00	5.26	6	6.82±0.09	5.26±0.07

Additional Surface Pressure-Area Isotherms

Π-*A*-Isotherm of all lipid solutions were measured at least three times. Characteristic isotherms of all four lipids are shown in **Figure 4.3**. Since the concentration of the spread lipid solutions had been determined, molecular surface areas *A* could be calculated according to **Equation 3-11**.

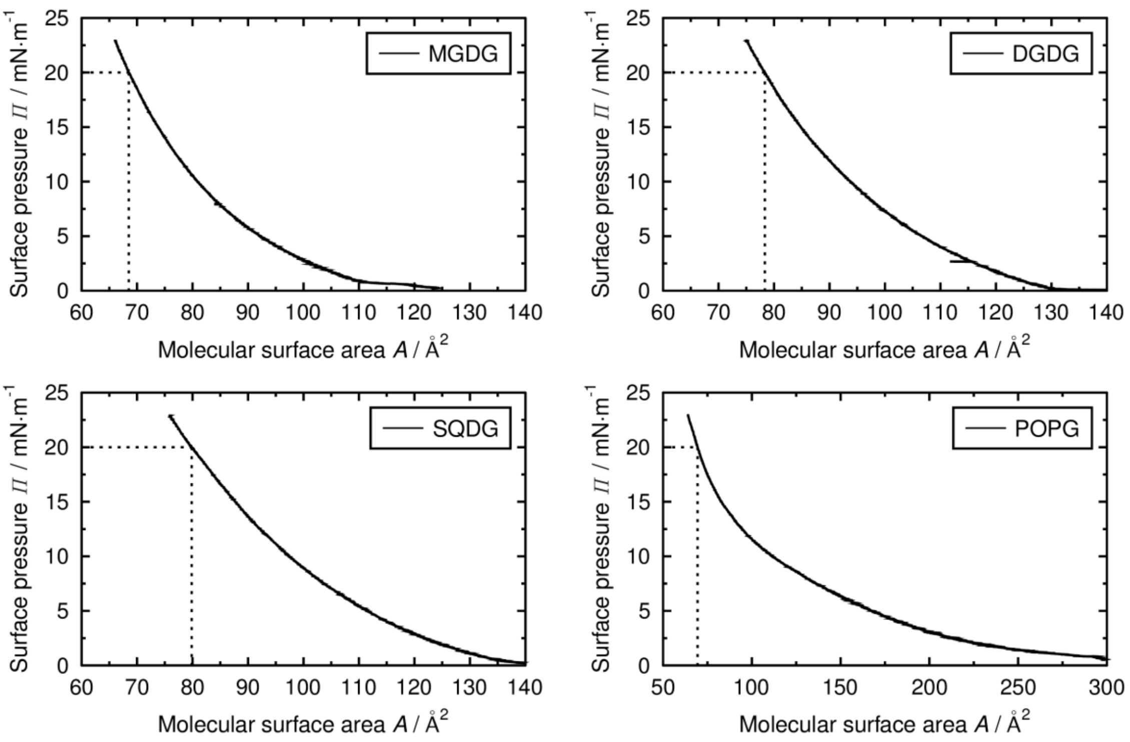

Figure 4.3. Exemplary Π-A-isotherms of MGDG, DGDG, SQDG and POPG at 20 °C. MGDG, DGDG and SQDG were measured on ultrapure water while the POPG monolayer was spread on buffer solution (150 mM NaCl, 5 mM TRIS, 0.5 mM $CaCl_2$, pH 7.0 (HCl) [145]).

Repeated compression-expansion cycles of POPG monolayers on ultrapure water revealed a shift of the compression isotherms to much lower surface areas after being compressed once. This observation indicated a loss of lipid material from the air-water-interface into the subphase. Thus, the subphase was changed to a buffer containing calcium ions (see **Table 3.10**) in order to stabilize the monolayer.[145]

Resulting Molecular Surface Areas

In total, three independent preparations with one qHNMR measurement and at least three Π-A-isotherms per lipid were performed. The resulting molecular surface areas A_{20} at a surface pressure of $\Pi = 20$ mN·m^{-1} are summarized in **Table 4.2**.

Table 4.2. Molecular surface areas A_{20} at a surface pressure of $\Pi = 20$ mN·m^{-1} and the temperature $T = 20$ °C for the five major lipids used in this study as well as the reference DPPC.

Lipid	DPPC	MGDG	DGDG	SQDG	POPG	DOPC
A_{20} / Å^2	46 [144]	76±13	82±11	79±6	67±4	70 [215]

4.2 Solid Supported Lipid Monolayers

The main difference between different types of solid supported lipid membranes is the anchoring of a continuous lamellar lipid aggregate onto a solid support and thereby the structure of the lipid aggregate itself.[88] Although even more sophisticated techniques for membrane preparations exist (*e.g.* tethered membranes), in general two different types can be distinguished: Solid supported lipid bilayers deposited on hydrophilic supports and solid supported lipid monolayers on hydrophobic surfaces.[93] While bilayers tend to represent a more physiological system with generally higher lateral mobility of the lipids,[221–223] the main advantage of lipid monolayers lies in their very high stability due to strong hydrophobic interactions.[88]

In this study, two different kinds of hydrophobic solid supports were used. On the one hand gold surfaces functionalized by thiol-gold chemistry and on the other hand silanized glass surfaces. Gold substrates are suitable for surface plasmon resonance (SPR) techniques whereas glass surfaces can be used for visualization by means of fluorescence microscopy.

Unique to this work is the incorporation of high amounts of plant glycolipids into a lipid mixture mimicking the overall lipid composition of diatoms.[66] Solid supported lipid monolayers were prepared by spreading of small unilamellar vesicles (SUVs) and characterized by various techniques.

4.2.1 Thiol-Functionalized Gold Surfaces

Substrate Functionalization

Hydrophobic functionalization of gold surfaces by thiol-gold chemistry and the binding of octanethiol (OT) is well established and reported in several publications.[128,224–229] A self-assembly process leads to the formation of a monomolecular layer of octanethiol on the surface with the hydrophobic alkyl chains facing away from the surface and rendering it hydrophobic. The success of the formation of an OT layer can be verified by electrochemical impedance spectroscopy (EIS). The OT layer acts as a dielectric layer between the gold electrode and the buffer.[230] Improper layer formation would result in a increased specific capacitance and decreased resistance. An exemplary impedance spectrum of a hydrophobically functionalized surface is shown in **Figure 4.4**.

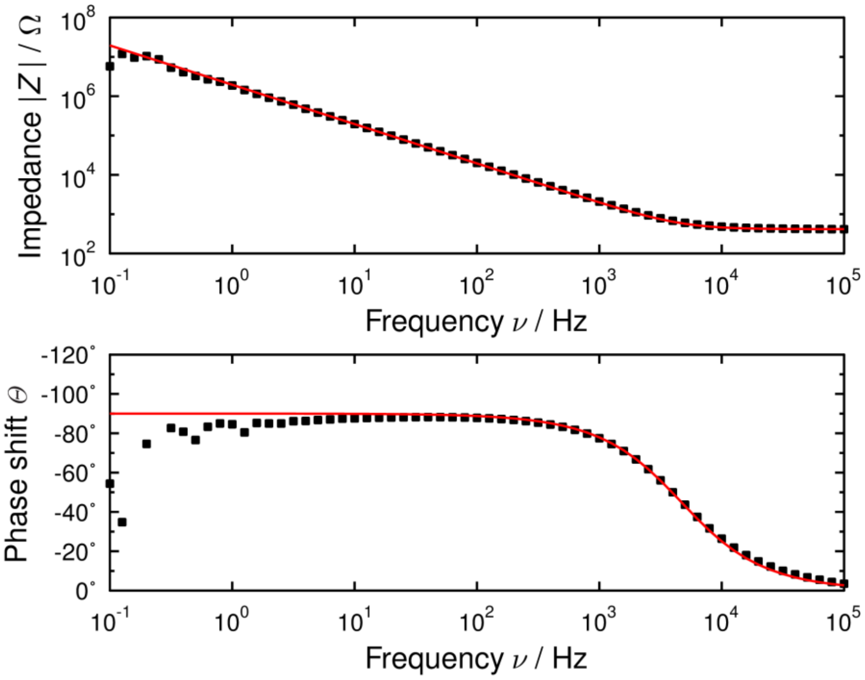

Figure 4.4. Typical impedance spectrum of an OT layer on gold, visualized as BODE plot (black). The measurement was carried out in spreading buffer (see Table 3.9). A fit to the data using a sequential resistance and capacitance is drawn in red (see Figure 3.25 B, $C_{\mathrm{m+el,spec}}$ = 1.80 µF·cm^{-2}, R_{b} = 417 Ω).

The electrical properties of the sample can be described by the equivalent circuit shown in **Figure 3.25** consisting of a capacitance $C_{\mathrm{m+el}}$ and resistance R_{b} in series. Fitting **Equation 3-26** and **3-27** to the data yielded a specific capacitance of the monolayer of $C_{\mathrm{m+el,spec}}$ = (1.84±0.05) µF·cm^{-2} (n = 2; gold electrode surface area: A = 0.0452 cm^2) as well as an OHMic resistance of R_{b} = (393±35) Ω.

Membrane Preparation

Surface Plasmon Resonance Technique

The deposition of a lipid monolayer on top of the hydrophobic substrate was achieved by spreading of SUVs (MGDG/DGDG/SQDG/POPG/DOPC, 35:20:15:5:25). The process of vesicle spreading was monitored and evaluated by SPR technique. The angle Θ-dependent reflectivity $R(\Theta)$ was measured in spreading buffer (see **Table 3.9**) before and after vesicle addition (**Figure 4.5 A**). During spreading, reflectivity changes $R(t)$ were monitored at a fixed angle Θ (**Figure 4.5 B**).

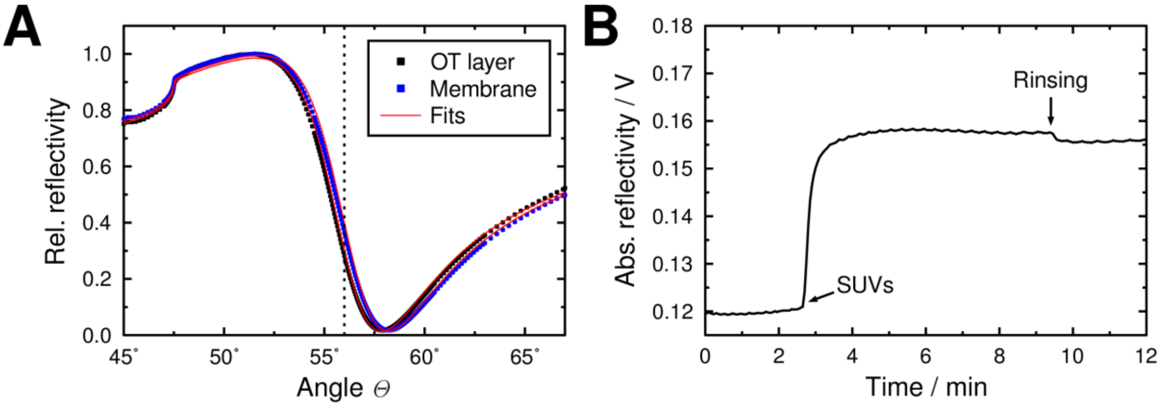

Figure 4.5. SPR data for the preparation of a lipid monolayer (MGDG/DGDG/SQDG/POPG/DOPC, 35:20:15:5:25) on OT-functionalized gold. Angle *Θ*-dependent reflectivities showed a shift of the minimum after monolayer formation towards larger angles (A). Physical properties (*e.g.* physical thicknesses) could be determined by fitting of the data (Fits). During vesicle spreading (0.5 mg·mL^{-1} in spreading buffer (see Table 3.9)) an increase of the reflectivity at *Θ* = 56.0° was detected (B). The absolute reflectivity is denoted as a spectrometer-specific photosensor voltage.

During spreading, a shift of the minimum in the angle *Θ*-dependent reflectance towards larger reflection angles was observed. This shift results in an approximately linear increase of the reflectivity in between the reflectivity maximum and minimum, too. Hence lipid monolayer deposition was observable in real-time during the kinetic study at a fixed angle. Vesicle spreading was terminated after about three minutes as no further increase in reflectivity was observed. During rinsing with spreading buffer (see **Table 3.9**) only a minor decrease in reflectivity was observed. Further insight on the lipid monolayer properties was gathered by fitting of the angle *Θ*-dependent reflectivity *R*(*Θ*) before and after spreading of vesicles. Physical thicknesses of all layers of the exemplary sample are summarized in **Table 4.3**.

Table 4.3. Parameters chosen for the fitting of the previously shown exemplary angle *Θ*-dependent SPR data (see Figure 4.5). Changes during vesicle spreading were only fitted by the addition of the lipid monolayer.

Layer	Physical thickness / nm	Refractive indices	
		ε'	*ε*''
Prism (LaSFN9)		3.404	0
Chromium	2.6	–1.019	20.96
Gold	38.3	–12.685	1.61
Octanethiol	1.9	2.114	0
Lipid monolayer	2.1	2.202	0
Spreading buffer		1.783	0

Fitting of the spectrum before vesicle addition included a variety of different parameters for each layer. Absolute values of these parameters should therefore be treated with caution. To evaluate the changes during vesicle spreading and to characterize the lipid monolayer, the only change between both steps of fitting was the addition and refinement of an additional lipid layer on top of the substrate. Physical thicknesses determined for this layer were typically about 2 nm (2.1 nm ($n = 1$) for MGDG/DGDG/SQDG/POPG/DOPC (35:20:15:5:25); (1.9±0.2) nm ($n = 4$) for MGDG/DGDG/SQDG/POPG/DOPC (35:15:25:15:10)).

Electrochemical Impedance Spectroscopy

As for the characterization of the OT layer, EIS has been employed to study the hybrid membrane's properties as well. Changes in resistance and especially the specific capacitance can indicate a successful spreading of a lipid monolayer. The monolayer deposition would result in an increase of the physical thickness of the dielectric and therefore a decrease in capacitance.[231] An exemplary impedance spectrum after vesicle spreading (MGDG/DGDG/SQDG/POPG/DOPC, 35:20:15:5:25) is shown in **Figure 4.6**.

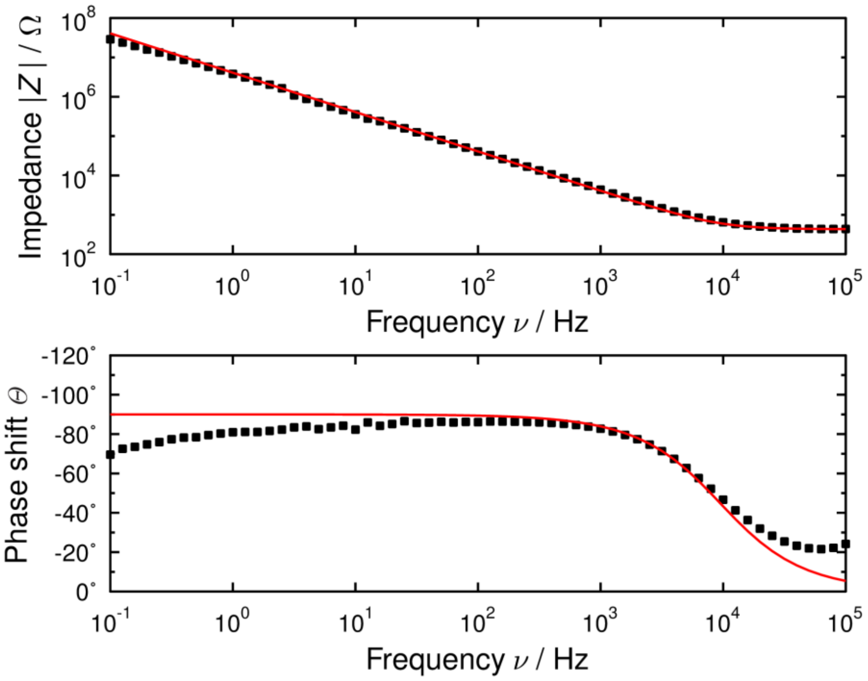

Figure 4.6. Exemplary impedance spectrum of a hybrid membrane (MGDG/DGDG/SQDG/POPG/DOPC, 35:20:15:5:25) on OT-functionalized gold visualized as BODE plot (black). The measurement was carried out in sample buffer (see Table 3.9). A fit to the data using a sequential resistance and capacitance is drawn in red (see Figure 3.25 B, $C_{\mathrm{m+el,spec}}$ = 0.86 µF·cm^{-2}, R_{b} = 433 Ω).

The system can be described as a series of a capacitance $C_{\mathrm{m+el}}$ and resistance R_{b} (see **Figure 3.25 B**). For the impedance spectrum, a specific capacitance $C_{\mathrm{m+el,spec}}$ = (0.84±0.03) µF·cm^{-2} ($n = 2$) and OHMic resistance R_{b} = (411±31) Ω were calculated by fitting **Equation 3-26** and **3-27** to the data. The specific capacitance of the lipid monolayer $C_{\mathrm{mono,spec}}$ can be calculated from the measured total capacitance $C_{\mathrm{total,spec}}$ and the capacitance of the OT monolayer $C_{\mathrm{OT,spec}}$ by

$$C_{\mathrm{total,spec}}^{-1} = C_{\mathrm{mono,spec}}^{-1} + C_{\mathrm{OT,spec}}^{-1}, \qquad \textbf{4-1}$$

since both capacitances are connected in series. A specific monolayer capacitance of $C_{\mathrm{mono,spec}} = (1.5\pm0.1)\ \mu\mathrm{F\cdot cm^{-2}}$ was determined.

4.2.2 Silanized Glass Surfaces

Substrate Functionalization

Silanization is a widespread technique for glass surface functionalization.[232] In this study hexamethyldisilazane (HMDS) was used to render a glass surface hydrophobic. Binding of pure HMDS was performed from its liquid state under ambient conditions.[130]

Contact Angle Measurements

Changes in surface hydrophilicity were determined by contact angle measurements. A droplet of water (2 µL) was placed on a glass cover slide before and after silanization. Photographs of the droplets are shown in **Figure 4.7**.

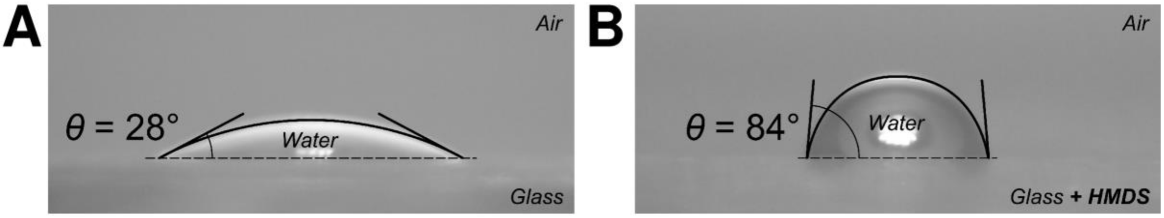

Figure 4.7. Water droplets on glass cover slides before (A) and after (B) treatment with hexamethyldisilazane (HMDS). Water-air-contact angles *Θ* change from 28° to 84°, proving an increase in hydrophobicity of the surface.

On unfunctionalized glass cover slides a contact angle of about $\Theta = 28°$ was measured. The angle increased after treatment with HMDS to about $\Theta = 84°$. Thus a significant increase in surface hydrophobicity was observed.[233]

Atomic Force Microscopy

Since functionalization of the surface was carried out by reaction with liquid HMDS, changes in surface topography should be investigated as well. For this purpose intermitted contact mode atomic force microscopy (AFM) in air was used on both glass substrates before (see **Figure 4.8 A**) and after functionalization (see **Figure 4.8 B**).

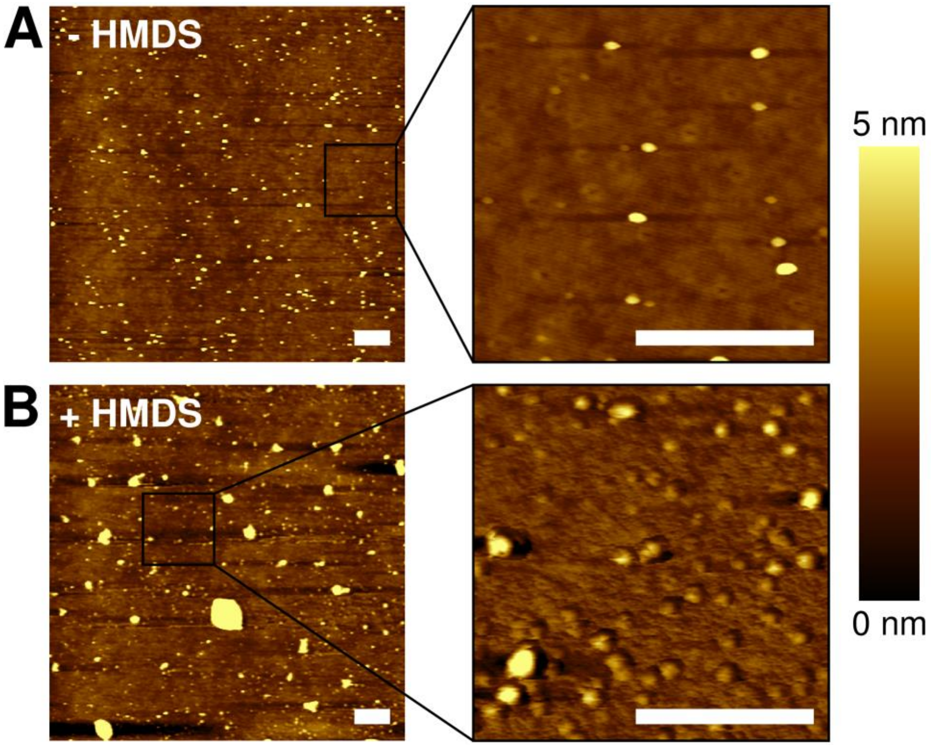

Figure 4.8. Topography of a glass cover slide before (A) and after (B) functionalization with hexamethyldisilazane (HMDS). In both cases the average surface roughness is below 1 nm with larger particles with a height of mainly about 10 nm on top of it. Images were taken in intermitted contact mode in air. Scale bars: 500 nm.

The blank glass surface before functionalization has an average roughness below 1 nm. A few particles with an average height of 10 nm are evenly distributed over the surface but make no less than 3% of the surface. After treatment with HMDS, the roughness is mainly unchanged and still below 1 nm. On the other hand the particles on the surface seem to have grown in size with their height being now predominantly about 10 nm and at maximum 40 nm. But overall they still cover less than 3% of the surface.

Membrane Preparation

Lipid monolayers on the hydrophobically functionalized glass surfaces were prepared by spreading of SUVs (MGDG/DGDG/SQDG/POPG/DOPC/TexasRed-DHPE, 34:20:15:5:25:1). The addition of a lipid-bound fluorescent dye enabled the use of fluorescence microscopy to image lipid deposits on the surface. To evaluate if the surface was not only homogenously covered with lipid material but also if a continuous lipid monolayer was formed, fluorescence recovery after photobleaching (FRAP) experiments were performed. This technique provides information on the fluidity of the monolayer and allows estimation of diffusion coefficients of the lipids.

Fluorescence Imaging

A representative fluorescence micrograph of a lipid monolayer doped with TexasRed-DHPE and prepared on a silanized glass surface is shown in **Figure 4.9**.

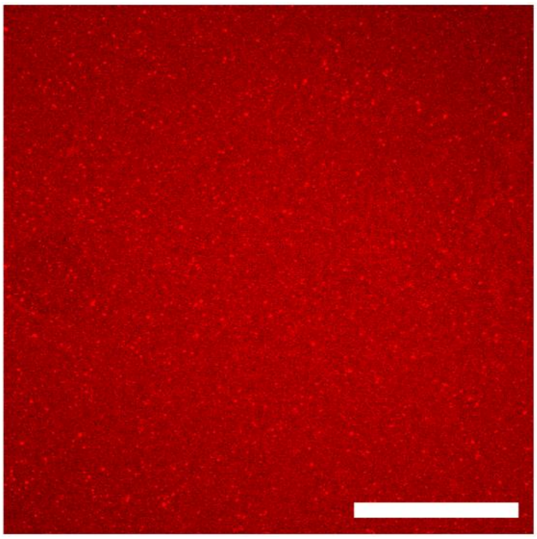

Figure 4.9. Fluorescence micrograph of a lipid monolayer (MGDG/DGDG/SQDG/POPG/DOPC/TexasRed-DHPE, 34:20:15:5:25:1) in sample buffer (see Table 3.9) on hydrophobically functionalized glass. A homogeneous bright fluorescence was observed with evenly distributed brighter protrusions all over the substrate. Scale bar: 50 µm.

Full coverage of the substrate with lipid material was observed by red TexasRed-DHPE fluorescence. A homogeneous fluorescence was observed with brighter spots evenly distributed all over the substrate. These brighter structures could not be removed by intense rinsing of the surface with buffer and had therefore to be tightly connected to the formed lipid monolayer.

Fluorescence Recovery after Photobleaching Experiments

A predefined part of the lipid monolayer's fluorescence was bleached by a strong laser pulse. Before and after bleaching, membrane fluorescence was monitored by time lapse fluorescence microscopy. An exemplary time-series of fluorescence micrographs during a FRAP experiment is shown in **Figure 4.10 A**. The white circle marks the bleached area as well as the region of interest from which the fluorescence intensity F was read out, normalized to the fluorescence intensity at start F_0, and plotted in **Figure 4.10 B**.

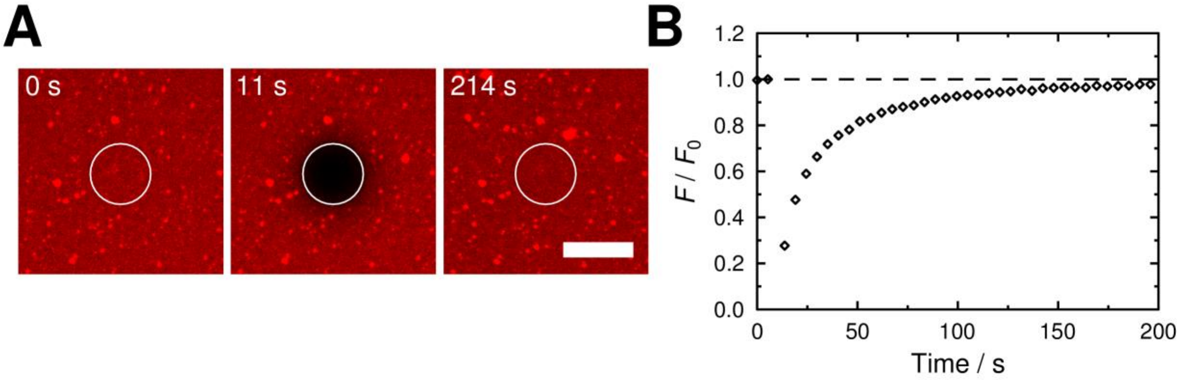

Figure 4.10. FRAP experiment on a lipid monolayer (MGDG/DGDG/SQDG/POPG/DOPC/TexasRed-DHPE, 34:20:15:5:25:1) on hydrophobically functionalized glass shown as a time-series of fluorescence micrographs (A). Fluorescence intensities F within the region of interest (white circle) normalized to the initial fluorescence intensity F_0 are plotted against time (B). Full fluorescence recovery was observed within two to three minutes.

Within two to three minutes after bleaching, fluorescence recovery in the bleached area was observed. This observation proved the formation of a continuous, fluid lipid monolayer on the surface. FRAP experiments wherein also the brighter spots on the surface became bleached, showed also recovery of their fluorescence. This indicates a connection between the bright structures and the surrounding lipid monolayer, enabling an exchange of lipid material. Hence these structures were identified as membrane protrusions.

Quantitative analysis of multiple FRAP experiments enabled the calculation of the diffusion coefficient D of the lipids in the plane of the lipid monolayer. Time series were processed by the method of JÖNSSON *et al.* using the Matlab-based script FRAP analysis 2.5 to perform HANKEL transformations.[191] By this technique a diffusion coefficient of $D = (0.3 \pm 0.1)\ \mu m^2 \cdot s^{-1}$ ($n = 11$) was determined.

4.3 Solid Supported Lipid Bilayers

As a second type of solid supported membranes lipid bilayers were generated on hydrophilic supports. Planar bilayers can be formed by the spreading of SUVs on the surface. Spreading efficiency is thereby mainly influenced by the hydrophilicity of the support.[86,120] Compared to lipid monolayers, lipid bilayers mark the more physiological of the two model systems as they include two continuous lipid monolayers. Lipid mobility is usually higher than in case of solid supported lipid monolayers.[222,223] In regard to interactions with various biomolecules, the bilayer structure is of particular interest if insertion of biomolecules into a membrane is discussed.

For this study, two different solid supports were chosen: silicon/silicon dioxide wafers, whose hydrophilicities were additionally increased, and freshly cleaved mica sheets. While both systems are addressable by fluorescence microscopy, silicon/silicon dioxide wafers offer an additional and easy way to study processes at the interface in a time-resolved manner by reflectometric interference spectroscopy (RIfS).

Although solid supported lipid bilayers are of great interest for many researchers, the incorporation of the three glycolipids, MGDG, DGDG and SQDG, into a planar, solvent-free and solid-supported membrane has not yet been reported.

4.3.1 Hydrophilized Silicon Dioxide

Reflectometric Interference Spectroscopy

The kinetics of adsorption of SUVs (0.2 mg·mL^{-1} in spreading buffer (see **Table 3.9**), MGDG/DGDG/SQDG/POPG/DOPC, 35:20:15:5:25) on a silicon dioxide surface were monitored by RIfS. Deposition of organic material can be observed as a change in optical thickness *OT*. **Figure 4.11** shows an exemplary kinetic study on the addition of SUVs to a hydrophilized silicon dioxide surface.

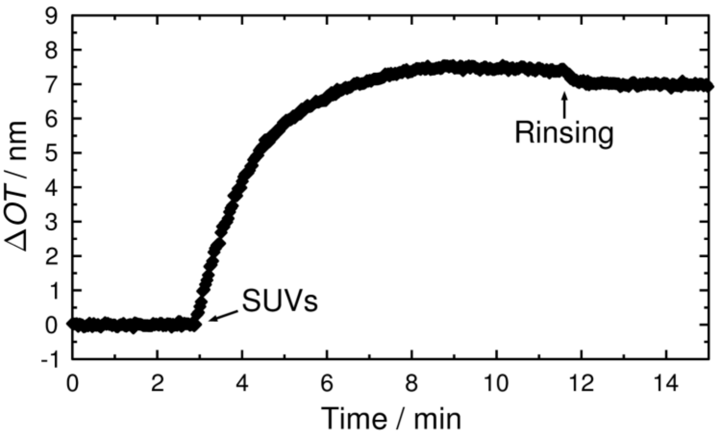

Figure 4.11. Kinetics of the adsorption of SUVs (0.2 mg·mL^{-1} in spreading buffer (see Table 3.9), MGDG/DGDG/SQDG/POPG/DOPC, 35:20:15:5:25) on hydrophilized silicon/ silicon dioxide wafers. Rinsing was performed with sample buffer (see Table 3.9). An increase in optical thickness Δ*OT* proves the deposition of lipid material on the surface.

Within 5–20 min saturation was observed, resulting in a relative increase in optical thickness of $\Delta OT = (7.4\pm0.8)$ nm ($n = 32$). Under the assumption of a refractive index of $n_2 = 1.50$ [234] for the deposited organic material, a physical thickness of $d = (4.9\pm0.5)$ nm could be calculated from the optical thickness $OT = n_2 \cdot d$.

Fluorescence Imaging

After addition of TexasRed-DHPE-doped vesicles (0.5 mg·mL^{-1} in spreading buffer (see **Table 3.9**), MGDG/DGDG/SQDG/POPG/DOPC/TexasRed-DHPE, 34.5:20:15:5:25:0.5) to a silicon/ silicon dioxide wafer, the TexasRed fluorescence was imaged by fluorescence microscopy to localize and characterize the deposited structures. An exemplary fluorescence micrograph is shown in **Figure 4.12**.

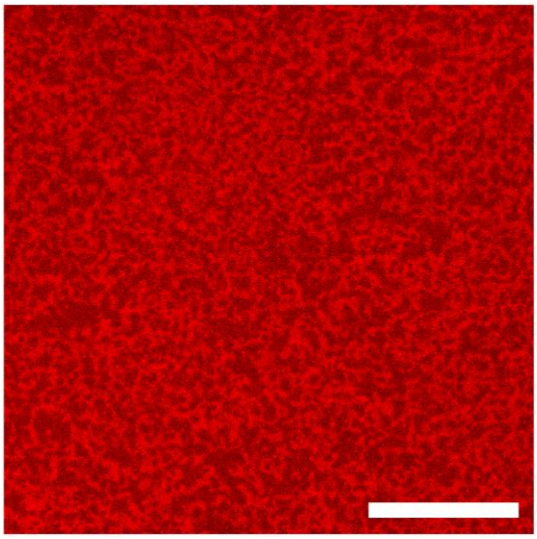

Figure 4.12. Fluorescence micrograph of a silicon dioxide surface after addition of TexasRed-DHPE-doped SUVs (0.5 mg·mL^{-1} in spreading buffer (see Table 3.9), MGDG/DGDG/ SQDG/POPG/DOPC, 34.5:20:15:5:25:0.5). A fine patterning of the TexasRed fluorescence was observed. Scale bar: 20 µm.

Red TexasRed fluorescence was observed all over the substrate but in contrast to previous data on solid supported lipid monolayers, a clear patterning of the deposit was observed. While coverage of the surface with lipid material was detected, probing the formation of a continuous lipid bilayer had to be performed by fluorescence recovery after photobleaching (FRAP).

Fluorescence Recovery after Photobleaching

Bleaching experiments were carried out after addition of SUVs to the silicon dioxide surface. An exemplary time-series of a FRAP experiment is shown in **Figure 4.13 A**. TexasRed-DHPE fluorescence was bleached in the region of interest from which the fluorescence intensity F was read out, normalized to the initial fluorescence intensity F_0 and plotted in **Figure 4.13 B** against time.

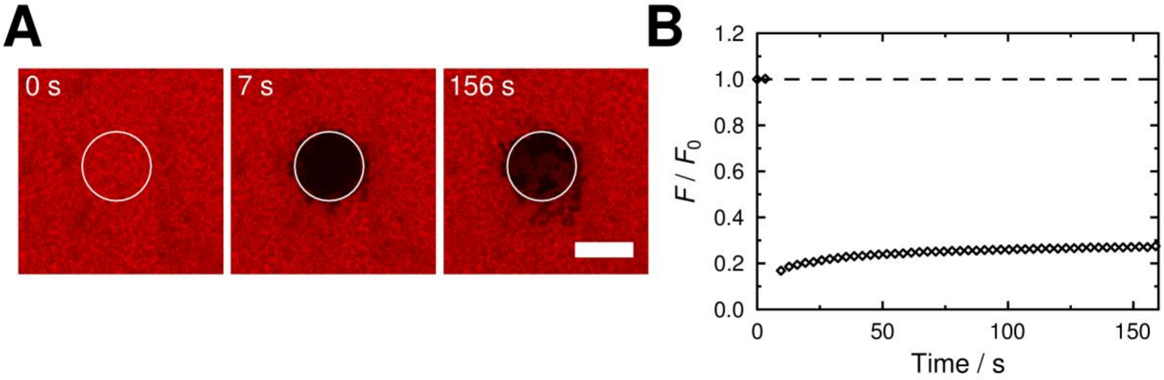

Figure 4.13. FRAP experiment on a silicon/silicon dioxide wafer after SUV addition (MGDG/DGDG/SQDG/POPG/DOPC/TexasRed-DHPE, 34.5:20:15:5:25:0.5). A time-series of fluorescence micrographs shows no recovery or only partial recovery in restricted areas (A). Fluorescence intensities *F* within the bleached area (white circle) were read out, normalized to the initial fluorescence intensity F_0 and plotted against time, showing only recovery of a fraction of the initial fluorescence intensity (B). Scale bar: 10 µm.

A patterning of the TexasRed fluorescence intensity on the surface was observed before bleaching. After bleaching an inhomogeneous and only partial fluorescence recovery was detected. Within certain areas no fluorescence recovery was measured. Hence lipid-bound dye molecules were unable to cross longer distances of several micrometers. This huge immobile fraction indicated the coverage of the surface with adhered and unspread vesicles. On the other (partial) recovery was observed in defined areas. Lipids were in these restricted areas incorporated into continuous, fluid membrane patches. No full fluorescence recovery was observed since the amount of mobile dye molecules was limited.

4.3.2 Mica Surfaces

Fluorescence Imaging

Mica sheets were freshly cleaved immediately before addition of SUVs (0.5 mg·mL^{-1} in spreading buffer (see **Table 3.9**), MGDG/DGDG/SQDG/POPG/DOPC/TexasRed-DHPE, 34.5:20:15:5:25: 0.5). After incubation and rinsing with sample buffer (see **Table 3.9**), TexasRed-DHPE fluorescence on the surface was imaged by means of fluorescence microscopy. A representative fluorescence micrograph is shown in **Figure 4.14**.

A homogeneous red fluorescence was observed all over the substrate showing nearly defect-free coverage of the mica surface with lipid material. Additionally, all over the substrate brighter spots with increased TexasRed-DHPE fluorescence were visible. Even intense rinsing of the surface with sample buffer (see **Table 3.9**) did not remove these structures.

The same results were obtained with other dyes. As an additional headgroup-labeled, lipid-bound dye Atto488-DHPE (MGDG/DGDG/SQDG/POPG/DOPC/Atto488-DHPE, 34.5:20: 15:5:25:0.5) was used as well as the fatty acid-labeled Bodipy-C_{12}HPC (MGDG/DGDG/ SQDG/POPG/DOPC/Bodipy-C_{12}HPC, 34.5:20:15:5:25:0.5).

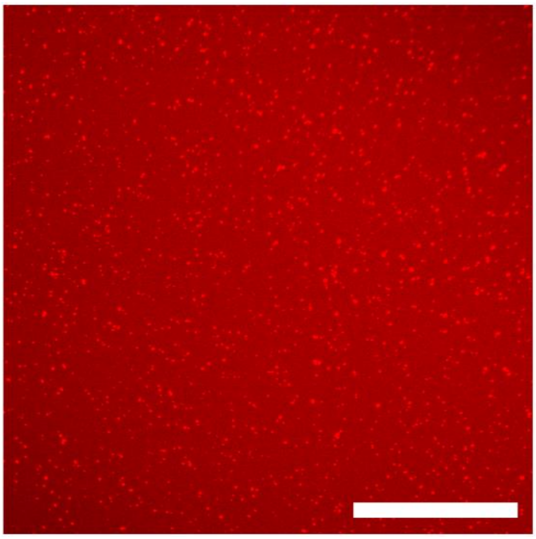

Figure 4.14. Fluorescence micrograph of an exemplary lipid bilayer on mica (MGDG/DGDG/SQDG/POPG/DOPC/TexasRed-DHPE, 34.5:20:15:5:25:0.5) showing a homogeneous TexasRed fluorescence without any visible defects but bright protrusions evenly distributed all over the substrate. Scale bar: 50 µm.

Fluorescence Recovery after Photobleaching

Whether spreading of SUVs led to the formation of a continuous lipid bilayer on the mica surface was investigated by FRAP experiments. Additionally, lipid diffusion was analyzed quantitatively to estimate diffusion coefficients. An exemplary series of fluorescence micrographs taken during the course of a bleaching experiment is shown in **Figure 4.15 A**. The bleached region is emphasized by a white circle. Fluorescence intensities F in this region of interest were read out from each image, normalized to the initial fluorescence intensity before bleaching F_0 and are plotted in **Figure 4.15 B**.

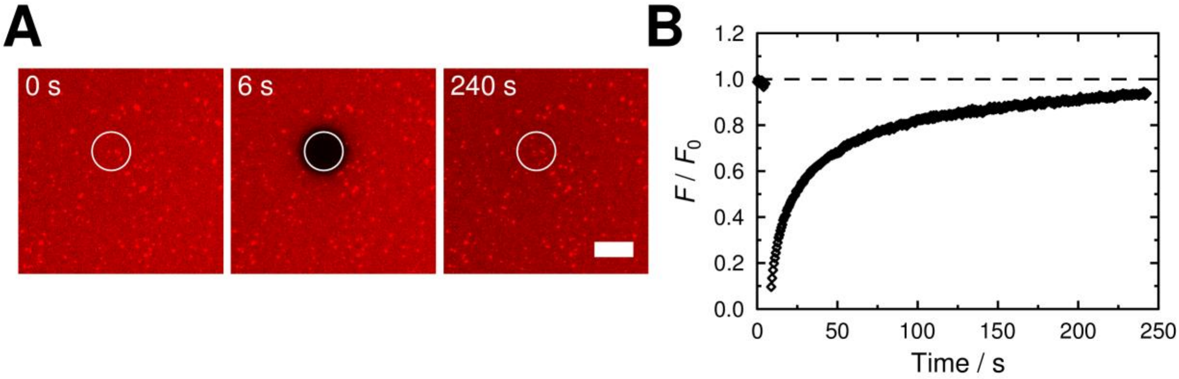

Figure 4.15. Exemplary FRAP experiment on mica after spreading of SUVs (0.5 mg·mL^{-1} in spreading buffer (see Table 3.9), MGDG/DGDG/SQDG/POPG/DOPC/TexasRed-DHPE, 34.5:20:15:5:25:0.5) visualized as a series of fluorescence micrographs (A). Dye molecules in the emphasized area (white circle) were bleached and fluorescence intensities F in this area were read out from all fluorescence micrographs. Intensities normalized to the initial fluorescence intensity F_0 are plotted against time (B). Scale bar: 10 µm.

FRAP experiments showed full recovery of the initial fluorescence intensities within about three to four minutes. This observation proved the formation of a continuous, fluid lipid bilayer. Besides recovery of the homogeneous parts of the solid supported membrane after bleaching, recovery of the brighter, evenly distributed spots was observed as well and on the same timescale. Hence a tight connection between these structures and the surrounding membrane is assumed as lipid material diffuses into the parts. Therefore it was concluded that these structures are protrusions of the lipid bilayer. Adhered vesicles would not be connected to the underlying lipid bilayer and thus would not show fluorescence recovery.

The regeneration of fluorescence intensity was analyzed quantitatively. Diffusion coefficients D were calculated using the Matlab-based script FRAP analysis 2.5 by JÖNSSON *et al.*[191] By performing HANKEL transformations, a diffusion coefficient of $D = (0.3 \pm 0.1)\ \mu\text{m}^2 \cdot \text{s}^{-1}$ ($n = 9$) was determined.

Atomic Force Microscopy

The topography of the solid supported membrane on mica was studied by AFM. In general, lipid bilayers showed a nearly defect-free, plane surface. No fine-patterning of the bilayer (*e.g.* by phase separation) was observed. Protrusions observed by fluorescence microscopy could not be imaged by intermittent contact mode AFM.

To determine the physical thickness of the lipid bilayer, a defect within the membrane had to be imaged. For this reason, the spreading conditions were adjusted to decrease the amount of lipid material adhered to the surface. On the one hand the vesicle concentration was reduced to 15 $\mu\text{g} \cdot \text{mL}^{-1}$ (in contrast to 0.5 $\text{mg} \cdot \text{mL}^{-1}$) and on the other hand spreading was performed at an increased temperature of 40 °C (instead of room temperature) before cooling the sample down to room temperature. A topography map of a defect-containing lipid bilayer prepared by this protocol is shown in **Figure 4.16 A**. The height profile along the white line is plotted in **Figure 4.16 B**.

As mentioned before, the solid supported lipid bilayer showed a homogeneous, plane surface. The height difference between the support and the membrane surface was determined to be about 4 nm.

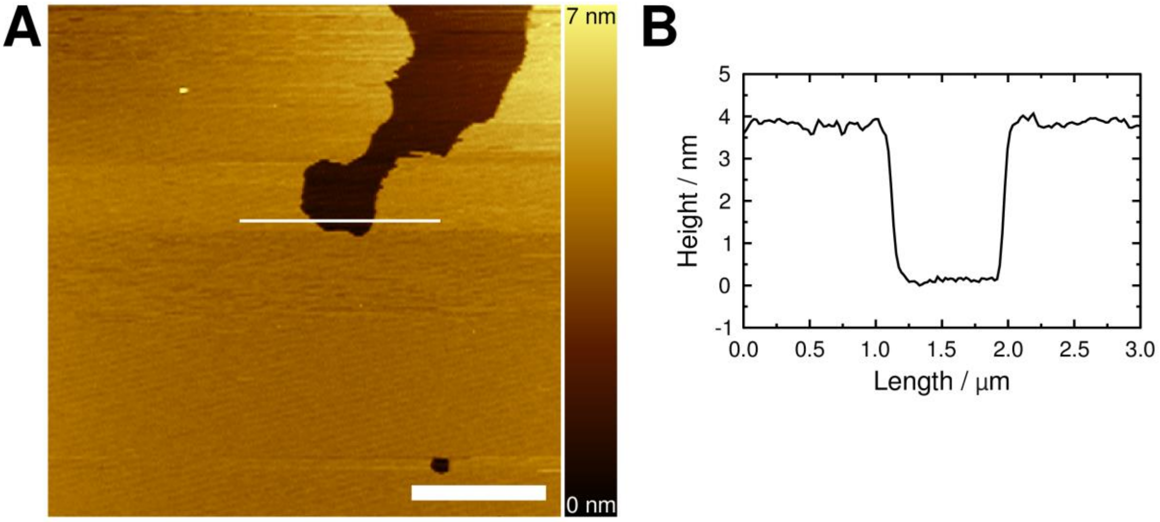

Figure 4.16. Topographical map of a solid supported lipid bilayer (MGDG/DGDG/SQDG/POPG/DOPC/TexasRed-DHPE, 34.5:20:15:5:25:0.5) on mica with defects (A). The membrane showed a homogeneous, plane surface. Along the white line a height profile was extracted and is plotted in B. A height difference of about 4 nm between the top of the lipid bilayer and the underlying substrate was detected. Scale bar: 2 µm.

4.4 Discussion

This subproject aimed for the introduction of solid supported lipid membranes as model systems to study the interaction of biomolecules, identified in the diatom biosilica, with lipid membranes representing the silicalemma *in vitro*. The main focus was placed on the remodeling of the lipid composition of the native membrane. Up to this point, the SDV has not been isolated and hence the exact lipid composition of the silicalemma remains unknown. Nevertheless overall lipid compositions of some diatom species have been identified.[62,66] For this work the overall lipid composition of *C. meneghiniana* was used as a starting point.[66] This mixture contains high amounts of the three glycolipids MGDG, DGDG and SQDG. These three lipids have already been successfully incorporated into artificial model membranes[67,77–85,214] but none of these studies introduced solvent-free, planar and solid-supported membranes containing all of the three relevant glycolipids to mimic the diatom lipid composition.

4.4.1 Surface Pressure Area Isotherms

To guarantee reproducible preparation of lipid mixtures, MGDG, DGDG, SQDG and POPG were first characterized by surface pressure-area-isotherms (Π-A-isotherms). Once determined, molecular surface areas A_{20} of all lipids could be used for routine concentration measurements of all lipid stock solutions by LANGMUIR-BLODGETT trough measurements.

The results of these experiments are summarized in **Table 4.2**. Most of similar studies reported in literature provide Π-A-isotherms of the investigated lipids on different liquid subphases or with alternative fatty acid compositions. Both parameters influence the molecular surface areas of the lipids and thus these data show only limited comparability.[219,235]

BOTTIER *et al.* measured Π-A-isotherms of MGDG and DGDG on 0.1 M NaCl at 19 °C.[216] Molecular surface areas A_{20} at a surface pressure of $\Pi = 20\ \text{mN}\cdot\text{m}^{-1}$ of about $A_{20,\text{Lit}}$(MGDG) = 104 Å^2 and $A_{20,\text{Lit}}$(DGDG) = 84 Å^2 respectively were reported. Both lipids used in their study were isolated from wheat with MGDG 18:2/18:2 (75%) and DGDG 18:2/18:2 (65%) being their major components. Isolated MGDG and DGDG used in this study had a lower degree of saturation with MGDG 16:3/18:3 (70%) and DGDG 18:3/18:3 (45%) as the two major lipids. Nevertheless, for DGDG both data are in good agreement with a determined surface area of A_{20}(DGDG) = (82±11) Å^2. On the other hand, data for MGDG shows significant deviations from the determined surface area of A_{20}(MGDG) = (76±13) Å^2. As the headgroup of MGDG is smaller than that of DGDG, changes in fatty acid structure have a much larger influence on the overall area consumption of MGDG molecules at the air-water-interface.[220] Π-A-isotherms on fully saturated SQDG 18:0/18:0 have been published by MATSUMOTO *et al.*[217] Their measurements were performed on phosphate-buffered saline (137 mM NaCl, 2.7 mM KCl, 10 mM Na_2HPO_4, 1.8 mM KH_2PO_4, pH 7.4 (HCl)) at 24 °C and a molecular surface area of about $A_{20,\text{Lit}}$(SQDG) = 57 Å^2 was reported. Not only does the different subphase composition (containing ions shielding electrostatic repulsion[236]) and temperature explain differences to the experimental molecular surface area of A_{20}(SQDG) = (79±6) Å^2, especially the favored packing of fully saturated fatty acids reduces the surface area of SQDG significantly.[237,238]

In contrast to the previous results on glycolipids, experimental conditions for POPG Π-A-isotherms were adapted from the work of BACKOW *et al.*[145] In their study the molecular surface area A_{20} of POPG at a surface pressure of $\Pi = 20\ \text{mN}\cdot\text{m}^{-1}$ was determined to be about $A_{20,\text{Lit}}$(POPG) = 79 Å^2 at 25 °C. Again, the increased temperature could explain the larger area compared to A_{20}(POPG) = (67±4) Å^2 observed in this study.[239]

Overall, the characterization of all lipids used in this study and the determination of their molecular surface areas A_{20} enables the use of Π-A-isotherms, measured on a LANGMUIR-BLODGETT trough, to identify lipid concentrations as long as identical conditions were used. This method is very suitable as a routine technique to ensure high reproducibility of the compilation of lipid mixtures. In contrast, the use of qHNMR requires high amounts of deuterated solvents for all stock solutions and would only be of limited practicability as a routine technique.

4.4.2 Solid Supported Model Membranes

Four different solid supported model membrane systems were introduced in this study: Solid supported lipid monolayers on hydrophobically functionalized gold and glass as well as lipid bilayers on hydrophilic silicon dioxide surfaces and mica. All systems were already well established in studies using lipid mixtures lacking the three glycolipids MGDG, DGDG and SQDG.[88] Since incorporation of these lipids might alter the lipid mixture's properties considerably, characterization of the introduced model membranes was essential to validate the success of preparation and the adaptability for further experiments. The lipid mixture employed for all experiments was inspired by the overall lipid composition of *C. meneghiniana* identified by VIELER *et al.*[66] and included 35 mol% MGDG, 20 mol% DGDG, 15 mol% SQDG, 5 mol% POPG and 25 mol% DOPC.

Solid Supported Lipid Monolayers

The properties of lipid monolayers on hydrophobically functionalized gold were investigated by means of EIS and SPR technique. SPR enabled the real time observation of SUVs spreading on the surface. Membrane formation was completed within about three minutes. This observation was in good agreement with the time scale of spreading of EggPC vesicles on such surfaces, observed by quartz crystal microbalance studies reported by KELLER and KASEMO.[93] The thickness of the lipid monolayer could be estimated by fitting of the angle-dependent reflectivity $R(\Theta)$. A physical thickness of typically 2 nm was in good agreement with defect-free monolayer thicknesses reported in literature[240] and indicated the successful preparation on the substrate. The high stability of the layer would enable further kinetic studies on biomolecule adsorption by SPR. The success of monolayer deposition was also verified by EIS measurements. After functionalization with OT, a specific capacitance of $C_{\text{m+el,spec}} = (1.84\pm0.05)\ \mu\text{F}\cdot\text{cm}^{-2}$ at the interface was measured. Depending on buffer conditions and preparation protocols, specific capacitances of OT-monolayers on gold are about 1.7–2.3 $\mu\text{F}\cdot\text{cm}^{-2}$.[229,231] This data is in good agreement with the experimentally determined values and proves the formation of a rather defect-free OT-layer, on which vesicles could spread into a lipid monolayer. After SUV addition, a specific monolayer capacitance of $C_{\text{mono,spec}} = (1.5\pm0.1)\ \mu\text{F}\cdot\text{cm}^{-2}$ was measured. In comparison, specific capacitances of 1-palmitoyl-2-oleoyl-*sn*-glycero-3-phosphocholine (POPC) monolayers are typically about 1.4–1.9 $\mu F \cdot cm^{-2}$ [231] but are influenced by the lipid composition and sample preparation.[172] In conclusion, the formation of lipid monolayers on hydrophobically functionalized gold was successful and provided the first adaptable system for further studies.

While sharing the high stability of lipid monolayers but circumventing the drawback of fluorescence quenching on gold, the preparation of lipid monolayers on hydrophobically functionalized glass was marked as an alternative approach. The surface was functionalized by silanization with HMDS. An increase in hydrophobicity was observed by an increase of the air-water contact angle from about 28° to 84°. In literature, contact angles of $\Theta = 90°$–$100°$ for glass substrates hydrophobically functionalized with HMDS are reported.[241,242] Experimental values came close to this data but also a strong influence of pretreatment of the substrate, reaction conditions and surface roughness is reported in literature.[241,242] In this study only minor changes in surface topography were observed. Surface roughnesses below 1 nm were measured by AFM which were in good agreement with literature reporting roughnesses below 1 nm as well.[242] The roughness of the HMDS-treated substrates is mainly influenced by the roughness of the glass surface to begin with. After spreading of fluorescently labeled SUVs the formed membrane was visualized by fluorescence microscopy. A homogeneous lipid-covered surface was observed with several bright protrusions evenly distributed. FRAP experiments proved the fluidity and continuity of the lipid monolayer with a lipid diffusion coefficient of about $D = (0.3\pm0.1)\ \mu m^2 \cdot s^{-1}$ similar to diffusion coefficients reported for other solid supported lipid monolayers prepared by vesicle spreading.[222,223] Hence the preparation of lipid monolayers on hydrophobically functionalized glass with a lipid composition similar to the native mixture in diatoms[66] was possible and additionally enabled the use of fluorescence microscopy. Besides kinetic measurements on lipid monolayers by SPR and functionalized gold surfaces, an imaging technique was introduced employing those lipid monolayers on glass.

Solid Supported Lipid Bilayers

The formation of lipid bilayers was first tested on hydrophilized silicon dioxide surfaces. Kinetics of SUV adsorption on the surface were measured by RIfS. Saturation was observed within 5 min to 20 min and resulted in the deposition of organic material and an increase in physical thickness of $d = (4.9\pm0.5)$ nm. In general, this thickness is larger than the physical thicknesses of lipid bilayers, typically in the range of 4 nm.[240] Compared to other RIfS-based experiments to study negatively charged lipid bilayers, the determined thickness is also slightly increased.[131,132] The physical thickness determined herein might not only be influenced by the structure of the fatty acids but also significantly by the glycolipid headgroups and their hydration shell. Visualization of the lipid deposits was achieved by fluorescence microscopy. Fluorescence micrographs already indicated a distinct patterned structure on the surface, but especially FRAP experiments proved an insufficient spreading of the SUVs, resulting in only restricted patches with internal lateral lipid mobility. Since spreading of vesicles on solid surfaces is mainly influenced by the adhesion energy and hydrophilicity of the surface, hydrophilization of the silicon dioxide surface turned out not to be sufficient for spreading of SUVs containing high contents of glycolipids.[243] Even if the formation of a completely substrate covering continuous lipid bilayer was not successful, full coverage of the surface with lipid material was observed. Silicon dioxide surfaces were therefore used as substrates for RIfS to probe interactions of biomolecules with lipid membrane surfaces but quantitative predictions of surface coverage might be limited.

On mica surfaces the formation of a continuous lipid bilayer with homogeneous fluorescence and evenly distributed protrusions was observed. The continuity of the bilayer was proven by FRAP experiments which also provided a lateral lipid diffusion coefficient of $D = (0.3\pm0.1)\ \mu\text{m}^2\cdot\text{s}^{-1}$. This diffusion coefficient is smaller than coefficients reported in literature for phosphatidylcholine bilayers of about $D = 0.5\text{–}5\ \mu\text{m}^2\cdot\text{s}^{-1}$ [223,244,245] and more similar to diffusion coefficients previously measured for lipid monolayers on hydrophobically functionalized glass. This observation hints to a decreased mobility of the bilayer leaflet in direct contact with the mica support. A decrease of lipid mobility on mica and in the lower leaflet was already stated in literature.[246] Mica provides an atomically flat surface which reduces the thickness of the water layer between the support and the membrane compared to rougher surfaces as for example glass.[247] Strong interactions between the membrane and the support decrease lipid diffusion.[248] Interactions between the lipid headgroups and the support could also be significantly increased by the sugar headgroups of MGDG, DGDG and SQDG, which represent the majority of the incorporated lipids. Multiple hydroxyl groups might enable stronger hydrogen bonding and interactions compared to other lipids.[249] Deceleration of lipid diffusion was also reported for lipid bilayers interacting with sugar molecules in solution.[247,250,251] Additionally to fluorescence micrographs, the topography of the lipid bilayer was investigated by means of AFM. While in general a plane and homogenous membrane surface without any fine-structure was observed, the imaging of a defect in the bilayer revealed a bilayer thickness of about 4 nm which is in good agreement with bilayer thicknesses reported in literature.[240] Compared to physical thicknesses determined by RIfS on silicon dioxide, this data should represent the bilayer thickness more accurately as insufficient spreading was observed on silicon dioxide in contrast to mica surfaces and might cause elevated heights respectively. Due to the more physiological nature of lipid bilayers, reliable membrane preparation and especially easy substrate handling, mica was used as solid support for lipid bilayers in the vast majority of experiments in this study.

Solid Supported Lipid Membranes as Model Systems for the Silicalemma

Including all previously mentioned model systems, in total four different types of solid supported membranes were introduced in this study. An overview on the different model membranes introduced in this study is given in **Figure 4.17**.

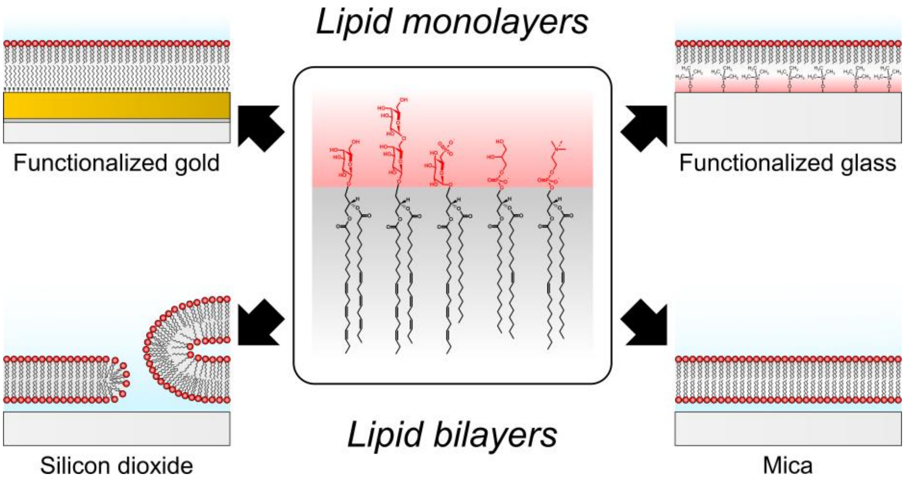

Figure 4.17. Overview on the different model membrane systems introduced in this study. All model membranes employed a lipid mixture (MGDG/DGDG/SQDG/POPG/DOPC, 35:20:15:5:25) close to the overall lipid composition of diatoms.[66] Lipid monolayers were formed on hydrophobically functionalized gold and glass surfaces. On silicon dioxide lipid bilayers were deposited. While the whole surface was covered with lipid material, only about half of it fused into continuous lipid bilayers. On the other hand substrate spanning, continuous lipid bilayers were formed on mica after addition of SUVs.

As already mentioned, the inspiration for the lipid composition used in this study was the overall lipid composition in *C. meneghiniana*.[66] Since the SDV remains unisolated up to this date no information on the actual lipid composition of the silicalemma exists. Besides the SDV membrane, all other organelle’s membranes and the plasma membrane contribute to the overall lipid composition. By far the largest contribution to the overall lipid pool comes from the chloroplasts and their stacked thylakoid membranes. Thylakoid membranes have been under intense investigation as they house the photosystem and play a key role in photosynthesis. The main lipid components in this organelle are the glycolipids MGDG, DGDG and SQDG.[67–70] While this fact also makes the herein presented model systems of particular interest for research, for example on thylakoid proteins, the content of glycolipids in the silicalemma might be overestimated. On the other hand the plasma membrane of algae – the membrane the silicalemma presumably fuses with to release cell wall fragments by exocytosis[14] – mainly consists of phospholipids.[252,253] Since the used lipid composition reflects nearly the highest possible content of glycolipids (especially of MGDG[67,73,74]) eventual changes lowering the glycolipid content should be easy to realize. Currently the isolation of SDVs is still a goal for many researchers. New advances in proteomic approaches on the biomolecular machinery used for silica biomineralization in diatoms revealed the first putative transmembrane protein, silicanin-1, of the SDV.[254] Targeting this protein could allow selective isolation of SDVs and enable lipidomic studies on the silicalemma. Once new insight on the lipid composition is gathered, the herein presented model systems could easily by adjusted.

5 CINGULINS

A central question of this study was the influence of lipid membranes on biomolecules presumably involved in silica biogenesis in diatoms. The biomineralization process itself takes place in membrane enclosed silica deposition vesicles (SDVs) and is most likely directed by an assembly of soluble and insoluble biomolecules within the organelle. During silicic acid polymerization those biomolecules can become trapped inside the newly formed biosilica and hence be detected inside the diatom cell wall.[14] One class of biomolecules investigated in this study were the cingulins. They were first identified in 2011 by SCHEFFEL *et al.* screening the genome of the diatom *Thalassiosira pseudonana* (*T. pseudonana*) for proteins with structural similarity to silaffins, a class of small proteins previously isolated from diatom cell walls, and became also localized inside the biosilica.[35] In 2016 KOTZSCH *et al.* were able to identify cingulins as part of the insoluble organic matrix remaining after dissolution of diatom cell walls with NH_4F.[36] In general cingulins can be divided into two classes according to their predominant aromatic amino acids: tryptophan-rich W-cingulins and tyrosine-rich Y-cingulins. Herein two exemplary cingulins, cingulin W2 and cingulin Y3, representing both classes were investigated in respect to their interactions with solid supported lipid membranes reflecting the overall lipid composition of diatoms (see **Chapter 4**).

Instead of native cingulins, recombinant proteins expressed in *Escherichia coli* (*E. coli*) were used. While recombinant cingulin Y3 (rCinY3) was provided by the group of PROF. DR. NILS KRÖGER (B CUBE, Technical University of Dresden), recombinant cingulin W2 (rCinW2) was isolated on-site. A protocol for expression of rCinW2 in *E. coli*, based on the experience with rCinY3, was provided by the group of PROF. DR. NILS KRÖGER[36] but steps involving protein isolation and purification had to be revised for rCinW2. Besides protein isolation, solubility of rCinW2 was investigated.

Interactions of both recombinant cingulins with artificial lipid membranes mimicking the SDV membrane were mainly studied by reflectometric interference spectroscopy (RIfS) and characterized by the amount of protein adhering to the membrane surface.

5.1 Cingulin W2

5.1.1 Protein Isolation

Recombinant cingulin W2 was expressed in the *E. coli* strain DH5α transformed with a pJ404 plasmid also containing the genetic information encoding the target protein as well as an ampicillin resistance and *lac* operon. At its *C*-terminal end a His$_6$-tag was fused to rCinW2. This tag enabled the use of immobilized metal ion affinity chromatography (IMAC) for target protein purification. Cells were grown in LB medium and protein expression was induced by the addition of isopropyl *β*-D-1-thiogalactopyranoside (IPTG). Cell growth could be monitored as change in the optical density OD_{600} at a wavelength of λ = 600 nm (see **Figure 5.1 A**).

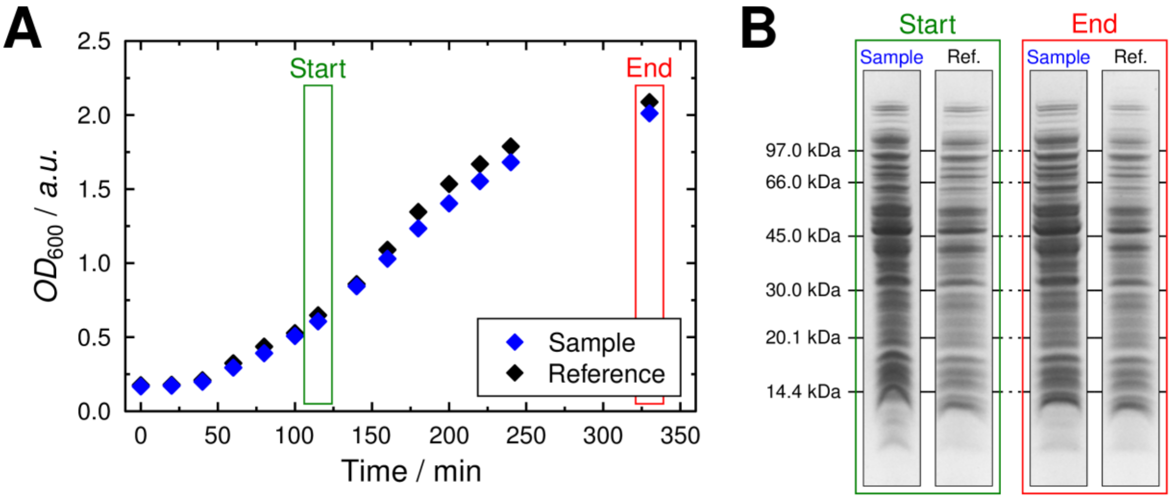

Figure 5.1. Growth of *E. coli* cells before and during expression of rCinW2. The increase in optical density OD_{600} for sample cells induced with IPTG and uninduced reference cells are plotted against time (A). At the point of IPTG addition to the sample cells (Start) and at the end of protein expression (End) samples were drawn and analyzed by SCHÄGGER and JAGOW SDS-PAGE (B). No significant overexpression of rCinW2 was observed in the sample's gel at the end (M_{th}(rCinW2) = 37 kDa) and cell growth of the sample cells did not decrease significantly after IPTG addition.

Induction of protein expression by IPTG addition was triggered at an optical density of about OD_{600} = 0.6. Compared to uninduced cell cultures no significant decrease of cell growth after IPTG addition was observed. Analysis of whole cell lysates by SDS-PAGE at the point with an optical density of $OD_{600} = 0.6$ and at the end of cell growth showed no emerging overexpression of the target protein (see **Figure 5.1 B**).

All further steps of cell lysis and protein purification were monitored by SDS-PAGE as well (see **Figure 5.2**). Lysis of *E. coli* cells and release of the target protein was mainly carried out by addition of lysozyme and sonification with ultrasound. Solubilized rCinW2 could be separated from insoluble cell components by centrifugation. Protein purification was performed by IMAC using Ni-NTA containing agarose beads. rCinW2 strongly coordinates nickel(II) via its *C*-terminal His_6-tag and could be separated from weakly bound cell components by elution with buffers containing an increasing amount of imidazole.

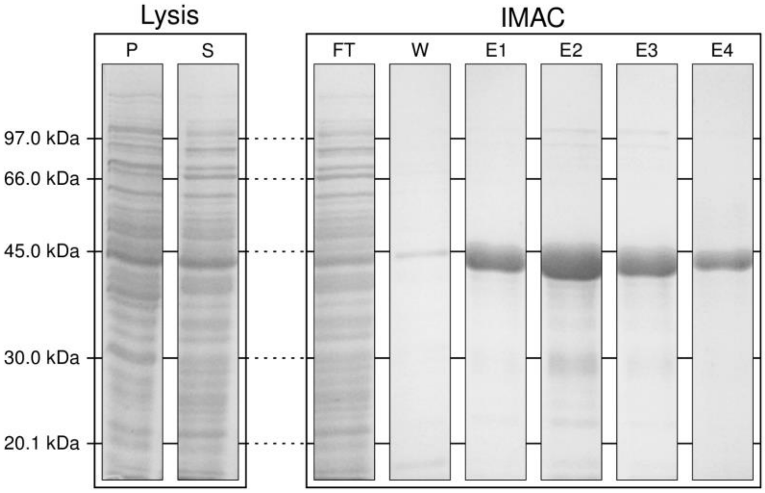

Figure 5.2. LAEMMLI SDS-PAGE gels from cell lysis (P: pellet, S: supernatant) and immobilized metal ion affinity chromatography (FT: flow-through (10 mM imidazole), W: washing (25 mM imidazole), E1–4: elution (250 mM imidazole)). During elution only one protein with a molecular mass of 40–45 kDa (M_{th}(rCinW2) = 37 kDa) was eluted. Impurities in this fractions are negligible compared to the amount of target protein.

After application of the supernatant after cell lysis to the Ni-NTA beads nearly all components of the cell lysate were contained in the flow-through of the IMAC. During the first washing step nearly no proteins were eluted. Thus very little unspecific binding of the cell extract to the column material was observed. Elution of the target protein occurred at an imidazole concentration of 250 mM. A single protein band at about 40–45 kDa was identified in the SDS-PAGE gel. This mass was slightly above the theoretical mass of rCinW2 of about M_{th}(rCinW2) = 37 kDa. Deviations can be related to the structure of the protein.[109] rCinW2 (pI 6.25) contained a negative charge of –5.6 at pH 8.0 which might affect the binding of SDS and therefore the propagation behavior of the protein in the gel. Also fusion with a His_6-tag is known to affect and slow down mobility of protein samples in the gel.[255]

In contrast to the herein performed protocol, the initial protocol developed by the group of PROF. DR. NILS KRÖGER for the isolation of recombinant cingulin Y3 used urea-free buffers for IMAC and an additional step of ion exchange chromatography (IEC). Adaption of this protocol to rCinW2 yielded the target protein but on the other hand SDS-PAGE revealed several impurities that could not be removed by nickel(II)- or cobalt(II)-IMAC as well as by an additional step of IEC (see **Figure 5.3 A**).

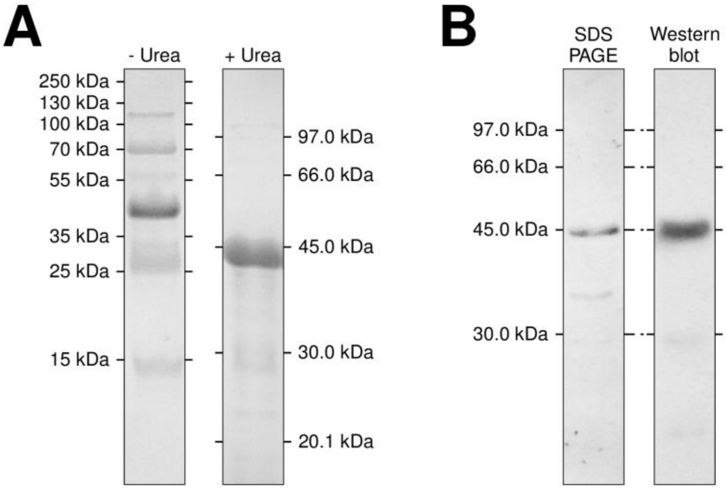

Figure 5.3. Comparison of SDS-PAGE gels after protein isolation and purification with or without 4 M urea in all deployed buffers (- Urea: SCHÄGGER and JAGOW-type, + Urea: LAEMMLI-type; A). The gel of the sample in absence of urea was run after IMAC and IEC while the one in presence of urea was purified by just one IMAC. The amount of impurities was decreased significantly by the addition of urea. The isolated protein was identified as the target protein, rCinW2, by Western blotting and the use of antibodies against the additional *C*-terminal His_6-tag (initial SDS-PAGE: LAEMMLI-type; B).

Presumably those impurities were associated to the target protein during all steps of purification and only became dissociated after denaturation of protein samples for SDS-PAGE analysis. The association of impurities to the target protein was avoided by the addition of 4 M urea to all buffers used for cell lysis and protein purification (see **Figure 5.3 A**). Addition of chaotropic urea supports the stability of monomeric proteins in solution amongst others by decreasing the hydrophobic effect.[256–258]

The identity of the isolated protein was tested by Western blotting. A specific antibody was used to probe the *C*-terminal His_6-tag fused to rCinW2. The antibody was afterwards located by a second HRP-containing antibody and the detection of catalyzed chemiluminescence after addition of luminol and H_2O_2 (see **Figure 5.3 B**). The Western blot showed only one clearly visible band at about 45 kDa previously also identified as the only prominent band in the SDS-PAGE gel. Thus in conclusion, isolation of rCinW2 from *E. coli* was successful providing the target protein in high purity. The amount of isolated protein could be estimated as about 6 mg per liter main culture by later performed concentration measurements.

5.1.2 Protein Solubility

After purification rCinW2 was stored in the elution buffer containing 4 M urea. Since high concentrations of urea are known to alter the properties of lipid membranes,[114–116] urea had to be removed before addition of rCinW2 to lipid membranes. Additionally the buffer's pH should be reduced to about 5.5 as the interior of the SDV, the native environment of the protein, is acidic as well.[22]

Buffer exchange was carried out by either dialysis or centrifugal concentration. Direct transfer of rCinW2 into acidic low salt-buffer (50 mM KCl, 40 mM NaOAc, 0.1 mM EDTA, 0.1 mM NaN_3, pH 5.5 (HOAc)) caused protein precipitation. During buffer exchange, besides removal of urea, the salt concentration was decreased significantly from 1 M NaCl in elution buffer to 50 mM KCl in sample buffer (see **Table 3.9**). Lowering the salt concentration weakens the shielding effect of ions on (attractive) electrostatic interactions between protein molecules[236] and might therefore allow aggregation. On the other hand lowering the pH from 8.0 in elution buffer to 5.5 in sample buffer involves a passing of the isoelectric point of rCinW2 at pI 6.27. At its neutral state, electrostatic repulsion is minimized allowing easier protein aggregation for example due to hydrophobic effects. To investigate influences of the different steps involved in buffer exchange and to get an insight on the aggregation behavior of rCinW2 in general a systematic approach has been taken as visualized in **Figure 5.4**.

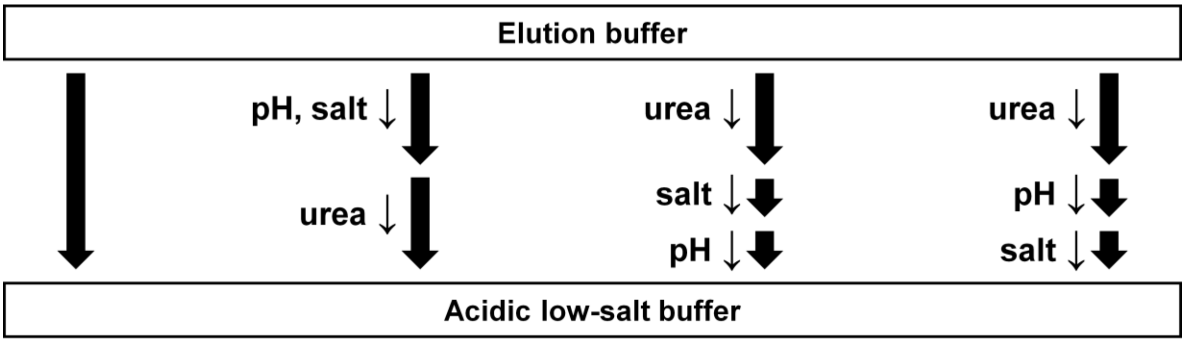

Figure 5.4. Schematic illustration of the steps involved in buffer exchange. Goal was the removal of urea and the transition into an acidic buffer (*e.g.* pH 5.5) with low salt concentration (*e.g.* 50–250 mM KCl).

Formation of protein aggregates was not investigated quantitatively (*e.g.* by dynamic light scattering for size measurements). Protein stability was only evaluated by the formation of protein precipitates. Those precipitates were either clearly visible with the naked eye as a cloudiness of the solution or detected by UV absorption spectroscopy as the precipitates cause scattering of light especially in the UV region ($\lambda < 400$ nm). On the other hand UV absorption spectroscopy ($\lambda = 280$ nm) could reveal significant losses in protein concentration due to partial precipitation of rCinW2 from solution. A detailed overview on all steps of buffer exchange is given in **Figure 5.5**. EDTA and NaN_3 were added in some of the buffers to capture divalent ions that might interfere with studies on lipid membranes or to increase long-term stability of the buffer, respectively. Since both components did not show an influence on protein precipitation they were omitted from some of the later buffers. All experiments were carried out at initial protein concentrations of 0.17 $mg\cdot mL^{-1}$ but might temporarily be increased up to 0.67 $mg\cdot mL^{-1}$ due to the use of centrifugal concentrators.

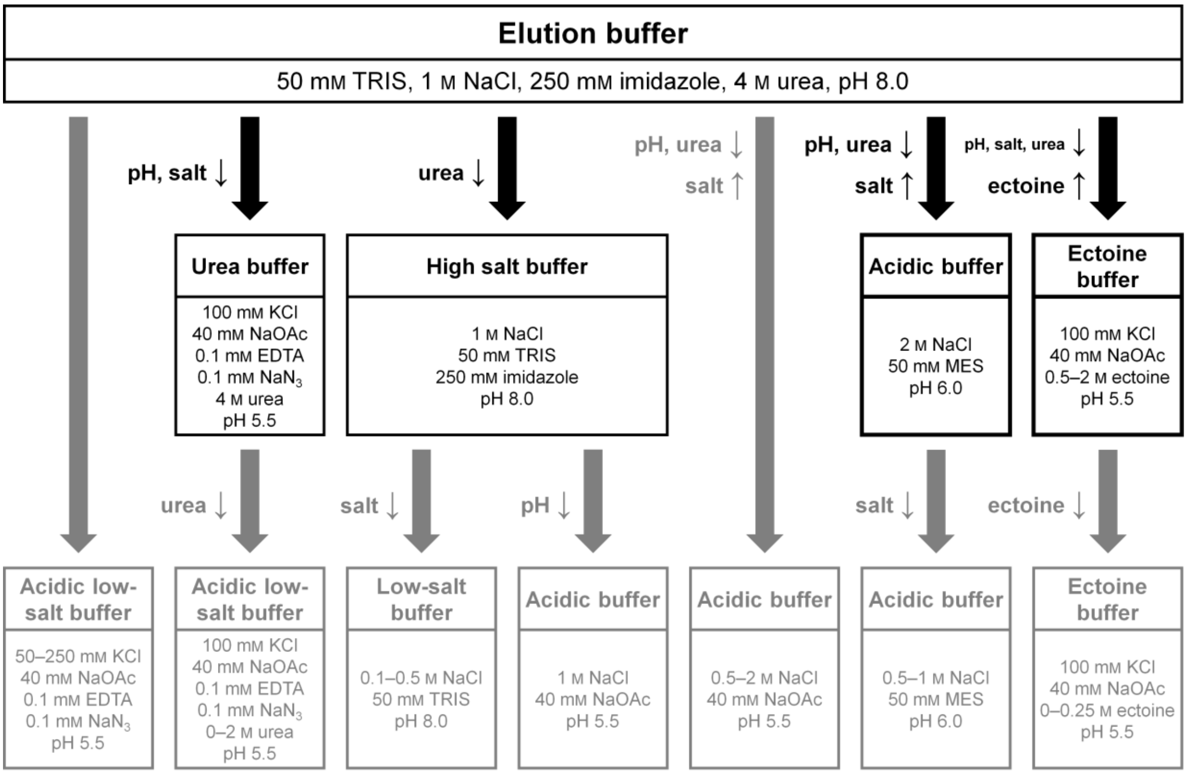
Elution buffer
50 mM TRIS, 1 M NaCl, 250 mM imidazole, 4 M urea, pH 8.0
pH, salt ↓
urea ↓
pH, urea ↓
salt ↑
pH, urea ↓
salt ↑
pH, salt, urea ↓
ectoine ↑
Urea buffer
100 mM KCl
40 mM NaOAc
0.1 mM EDTA
0.1 mM NaN3
4 M urea
pH 5.5
High salt buffer
1 M NaCl
50 mM TRIS
250 mM imidazole
pH 8.0
Acidic buffer
2 M NaCl
50 mM MES
pH 6.0
Ectoine buffer
100 mM KCl
40 mM NaOAc
0.5–2 M ectoine
pH 5.5
urea ↓
salt ↓
pH ↓
salt ↓
ectoine ↓
Acidic low-salt buffer
50–250 mM KCl
40 mM NaOAc
0.1 mM EDTA
0.1 mM NaN3
pH 5.5
Acidic low-salt buffer
100 mM KCl
40 mM NaOAc
0.1 mM EDTA
0.1 mM NaN3
0–2 M urea
pH 5.5
Low-salt buffer
0.1–0.5 M NaCl
50 mM TRIS
pH 8.0
Acidic buffer
1 M NaCl
40 mM NaOAc
pH 5.5
Acidic buffer
0.5–2 M NaCl
40 mM NaOAc
pH 5.5
Acidic buffer
0.5–1 M NaCl
50 mM MES
pH 6.0
Ectoine buffer
100 mM KCl
40 mM NaOAc
0–0.25 M ectoine
pH 5.5

Figure 5.5. Summary of different approaches to exchange the buffer containing rCinW2 to an acidic buffer (*e.g.* pH 5.5) with low salt concentration (*e.g.* 50–250 mM KCl) lacking urea. Conditions under which rCinW2 precipitated from solution are colored in gray. Since even stepwise buffer exchange was not successful, additional buffers containing either higher amounts of salt or ectoine were deployed.

As mentioned before direct dialysis of rCinW2 into an acidic low-salt buffer (50–250 mM KCl, 40 mM NaOAc, 0.1 mM EDTA, 0.1 mM NaN_3, pH 5.5 (HOAc)) was not successful. In presence of urea lowering the pH to 5.5 and a decrease of salt concentration (100 mM KCl, 40 mM NaOAc, 0.1 mM EDTA, 0.1 mM NaN_3, 4 M urea, pH 5.5 (HOAc)) did not cause protein precipitation. Removal of urea afterwards lowered the solubility of rCinW2 and caused precipitation. On the other hand the exclusive depletion of urea (1 M NaCl, 50 mM TRIS, 250 mM imidazole, 0.1 mM NaN_3, pH 8.0) in presence of high amounts of salt and weak basic pH did not lead to protein precipitation. Only if either the pH or the salt concentration was lowered, rCinW2 became instable in solution and precipitates. Since rCinW2 could not be transferred by stepwise buffer exchange into the desired buffer with low pH and salt concentration, the stability of the protein under these conditions in general was considered insufficient. In order to still enable studies on interactions with lipid membranes, the addition of stabilizing agents or weakening of the constraints causing precipitation were tested.

Since salt concentration turned out to influence protein stability, increased NaCl concentrations were applied. Higher salt concentrations shield (attractive) electrostatic interactions more efficiently by shortening the DEBYE length.[236] This could influence protein-protein interactions but also impact the interaction of charged proteins with charged lipid membranes. At pH 5.5 in presence of 1–2 M NaCl (and additionally 40 mM NaOAc) a decrease of protein precipitation was observed as smaller decreases in protein concentration during buffer exchange were measured. Reduction of acidity of the buffer to pH 6.0 yielded a stable protein solution in presence of 2 M NaCl (and additionally 50 mM MES). Further decrease of salt concentration resulted in reduced protein stability. Even as pure electrostatic interactions between proteins and lipid membranes can be considered rather unspecific a second buffer with low salt concentration was employed to validate the specificity of interactions.

An alternative approach to keep rCinW2 soluble under acidic conditions and in absence of urea was the addition of mild stabilizing agents. OBERDÖRFER *et al.* reported the supporting effect of ectoine on fibronectin[259] and ROYCHOUDHURY *et al.* made similar observations on the stability of bacteriorhodopsin.[260] Application of 0.5–2 M ectoine was sufficient to replace urea and stabilize rCinW2 at pH 5.5, too (100 mM KCl, 40 mM NaOAc, 0.5–2 M ectoine, pH 5.5 (HOAc)). Lower ectoine concentrations were not addressable in this buffer system.

5.1.3 Protein-Membrane Interactions

After transfer of rCinW2 in either 2 M NaCl-containing (2 M NaCl, 50 mM MES, pH 6.0) or 1 M ectoine-containing buffer (100 mM KCl, 40 mM NaOAc, 1 M ectoine, pH 5.5 (HOAc)) interactions of the protein with lipid bilayers (MGDG/DGDG/SQDG/POPG/DOPC, 35:20:

15:5:25, see **Chapter 4.3.1**) were investigated by RIfS. After addition of small unilamellar vesicles (SUVs) and detection of a constant optical thickness *OT* protein solutions were added in a closed loop. In several steps the protein concentration was increased. Two exemplary kinetic studies by RIfS are shown in **Figure 5.6**. Alongside rCinW2 ectoine was added to the membrane-covered surface. HARISHCHANDRA *et al.* reported on an increased hydration of the lipid headgroups and fluidity of the membrane after addition of ectoine to lipid bilayers,[261] but no data on the effect on lipid membranes on silicon dioxide monitored by RIfS was available. Blind measurements showed a reversible increase of optical thickness after addition of the ectoine containing buffer to the membrane-covered surface of about $\Delta OT = 1$ nm. During rinsing with ectoine containing buffer over a cause of about 30 min no change in optical thickness *OT*, indicating for example a degradation of the deposited lipid membrane, was observed.

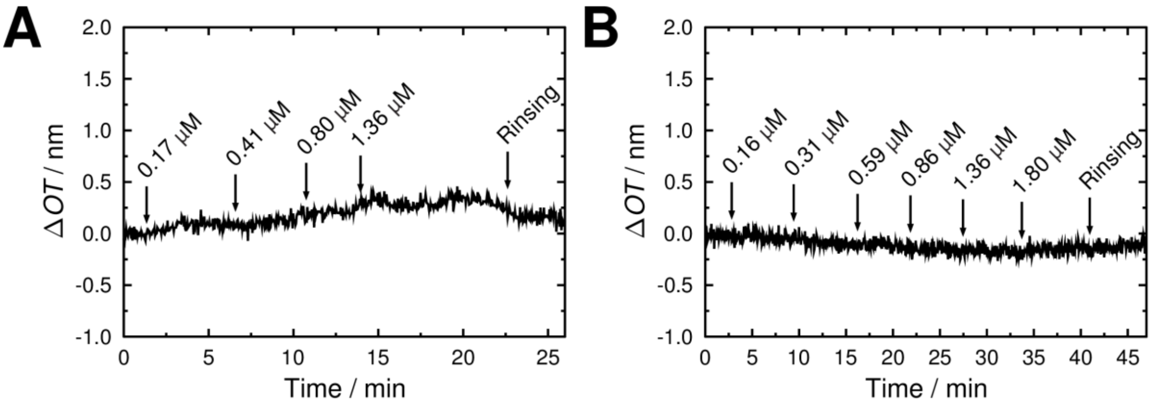

Figure 5.6. Two exemplary kinetic studies by RIfS on the adsorption of rCinW2 on membrane-covered surfaces (MGDG/DGDG/SQDG/POPG/DOPC, 35:20:15:5:25). Measurements were performed in ectoine-containing buffer (100 mM KCl, 40 mM NaOAc, 1 M ectoine, pH 5.5 (HOAc), A) or buffer with elevated salt concentration (2 M NaCl, 50 mM MES, pH 6.0, B). Under both conditions no significant increase in optical thickness Δ*OT*, indicating a binding of the protein to the surface, was observed.

After addition of rCinW2 with increasing concentration no significant increase in optical thickness *OT* was observed under both chosen buffer conditions. An increase in optical thickness would indicate the deposition of organic material from solution onto the membrane surface. Thus no binding of rCinW2 was identified.

5.2 Cingulin Y3

Purified rCinY3 expressed in *E. coli* was provided by the group of PROF. DR. NILS KRÖGER. It was stored in urea-free buffer (50 mM TRIS, ca. 300 mM NaCl, 0.1 mM PMSF, protease inhibitor, pH 8.0) and, in contrast to rCinW2, did not precipitate after transfer in acidic buffer (250 mM KCl, 40 mM NaOAc, 0.1 mM EDTA, 0.1 mM NaN_3, pH 5.5 (HOAc)).

5.2.1 Protein-Membrane Interactions

Reflectometric Interference Spectroscopy

Interactions of rCinY3 and lipid membranes (MGDG/DGDG/SQDG/POPG/DOPC, 35:20:15:5:25) were mainly investigated by RIfS. rCinY3 was added to a membrane-covered surface in various concentrations (1–8 µM) under acidic conditions (pH 5.5, 40 mM NaOAc/HOAc) in buffers with low to medium salt concentrations (50–250 mM KCl). The highest protein concentration employed for these studies was 8 µM (in 250 mM KCl, 40 mM NaOAc, 0.1 mM EDTA, 0.1 mM NaN_3, pH 5.5 (HOAc)). Exemplary data using up to this maximal protein concentration is shown in **Figure 5.7**.

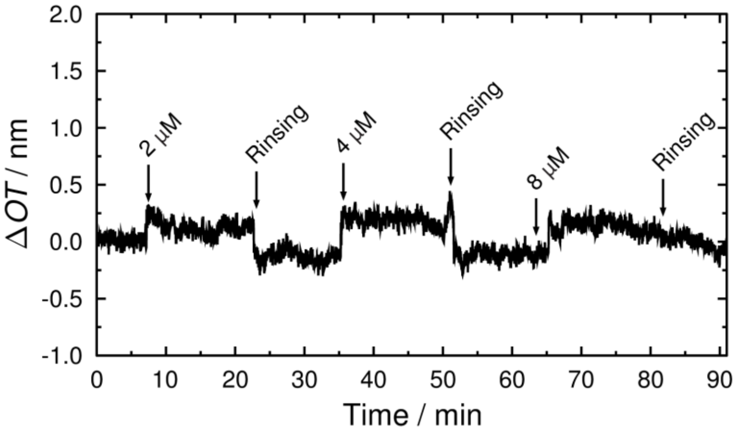

Figure 5.7. Exemplary kinetic data on the binding of rCinY3 to a membrane-covered surface (MGDG/DGDG/SQDG/POPG/DOPC, 35:20:15:5:25) under acidic conditions (250 mM KCl, 40 mM NaOAc, 0.1 mM EDTA, 0.1 mM NaN_3, pH 5.5 (HOAc)). Reversible increases in optical thickness of less than ΔOT = 0.5 nm were observed.

Only weak and fully reversible interactions were observed as an increase in optical thickness of less than $\Delta OT = 0.5$ nm after protein application. This change in optical thickness $OT = n_2 \cdot d$ corresponded to the deposition of a protein layer ($n_2 = 1.46$ [262]) with an average physical thickness of less than $d = 0.3$ nm. Similar observations were made in all experiments but no statistical analysis was performed because specific protein-membrane interactions were expected to result in higher surface coverage and therefore changes in optical thickness.

Surface Plasmon Resonance Techniques

To validate observations made by RIfS, protein adsorption was also studied by surface plasmon resonance (SPR) on lipid monolayers (MGDG/DGDG/SQDG/POPG/DOPC, 35:20:15:5:25, see **Chapter 4.2.1**). Time-resolved SPR data for the addition of 1 µM rCinY3 (in 250 mM KCl, 40 mM NaOAc, 0.1 mM EDTA, 0.1 mM NaN_3, pH 5.5 (HOAc)) is shown in **Figure 5.8**.

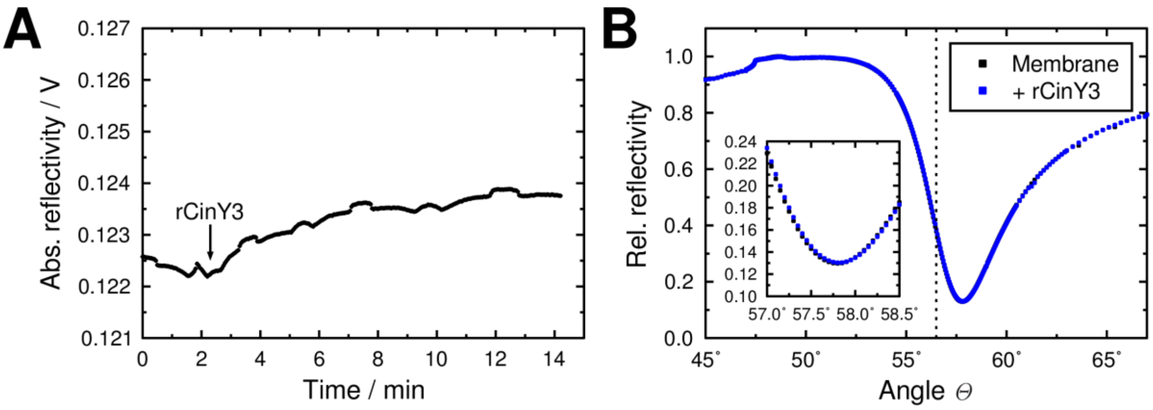

Figure 5.8. Exemplary SPR data for the addition of rCinY3 (1 µM) to a lipid monolayer (MGDG/DGDG/SQDG/POPG/DOPC, 35:20:15:5:25; 250 mM KCl, 40 mM NaOAc, 0.1 mM EDTA, 0.1 mM NaN_3, pH 5.5 (HOAc)). Kinetic data shows the deposition of organic material on the surface as an increase in reflectivity at *Θ* = 56.5° (A). Angle-dependent reflectivity before and after addition of rCinY3 reveals nearly no changes and allowed no further processing (B). The most sensitive part of the spectrum including the minimum position is magnified.

Time-resolved monitoring of the reflectivity at a fixed angle during rCinY3 addition showed a weak increase which indicated the deposition of organic material from solution onto the membrane surface. Differences in angle-dependent reflectivity before and after protein addition were diminishing and not quantifiable by fitting of the data. The physical thickness of the deposited protein layer was therefore expected to be in the range around 0.1 nm. SPR supported the observations made by RIfS which indicated only very weak or no interactions between rCinY3 and membrane surfaces.

5.3 Discussion

The first class of biomolecules presumably involved in silica biomineralization inside the SDV and investigated in this study were the cingulins. Two recombinant cingulins expressed in *E. coli* and representing the two main classes of cingulins were used.[35] rCinY3, a tyrosine-rich cingulin provided by the group of PROF. DR. NILS KRÖGER, and rCinW2, a tryptophan-rich cingulin isolated on-site according to a modified protocol originating from the group of PROF. DR. NILS KRÖGER as well. Both proteins were investigated in regard to their interaction with lipid membranes using model systems for the silicalemma introduced in **Chapter 4**.

5.3.1 Protein Isolation and Solubility

Expression of rCinW2 in *E. coli* DH5α was performed according to a protocol from the group of PROF. DR. NILS KRÖGER derived from the protocol for the isolation of rCinY3. Using this *E.coli* strain no overexpression of rCinW2 was detected by SDS-PAGE and cell growth did not decrease significantly after induction of protein expression by IPTG (see **Figure 5.1**). In the end protein yield was about 6 mg per liter main culture thus being relatively low. The *E. coli* strain DH5α was initially selected and developed for routine cloning and is therefore not optimized for high protein expression,[263] explaining these results. Regarding future isolations protein yield could most likely be improved by the use of a bacterial strain specifically designed for protein expression (*e.g. E. coli* BL21(DE3)).[263] The protocol for rCinW2 was revised regarding protein isolation and purification. Using the same buffer solutions as for rCinY3, protein impurities remained bound to the target protein during all steps (see **Figure 5.3**). The addition of 4 M urea to buffers used during cell lysis and IMAC (see **Table 3.4**) allowed very good purification of rCinW2 within one step of nickel(II)-IMAC. Urea is a chaotropic additive commonly used during protein isolation and purification, especially of proteins that tend to aggregate into inclusion bodies.[101,264] It reduces the hydrophobic effect and stabilizes proteins in solution.[256–258] The primary structure of rCinW2 consists of 12% hydrophobic amino acids (A, V, I, L, M, F, Y, W; especially tyrosine (4%) and tryptophan (5%), see **Table App.1**) favoring aggregation or folding to shield hydrophobic regions. On the other hand, with a total of 27%, rCinW2 contains a significant amount of charged amino acids (R, H, K, D, E). About half of them are positively charged and mainly located in the silaffin-like KXXK motives while the other half represents the acidic domains of the protein (see **Figure App.1**).[35] Thus site-specific electrostatic interactions could allow binding of smaller proteins or peptides, too.

After purification rCinW2 had to be transferred into a suitable buffer for studies on interactions with lipid membranes. On the one hand the content of urea had to be reduced as it interacts with both the core and the headgroup region of lipid membranes[114–116] and on the other hand the salt concentration should be lowered to weaken the shielding of electrostatic interactions.[236] Additionally acidic conditions were favored (*e.g.* pH 5.5) as the SDV interior – the native environment of the protein – is acidic as well.[22] Direct transfer of rCinW2 into a buffer fulfilling this conditions (50–250 mM KCl, 40 mM NaOAc, 0.1 mM EDTA, 0.1 mM NaN_3, pH 5.5 (HOAc)) resulted in precipitation of the protein from solution. Hence protein solubility and aggregation was studied but no quantification (*e.g.* by dynamic light scattering) has been performed. In summary it was not possible to transfer rCinW2 even by stepwise dialysis into the desired target buffer. The protein had to be stabilized in solution under acidic conditions either by increasing the salt concentration and elevating the pH value (2 M NaCl, 50 mM MES, pH 6.0) or by addition of ectoine (100 mM KCl, 40 mM NaOAc, 0.5–2 M ectoine, pH 5.5 (HOAc)). The nature of protein-protein interactions are expected to be as described previously for the binding of smaller impurities to the target protein and might involve both electrostatic (shielded by higher salt concentrations) and hydrophobic interactions (suppressed by urea or ectoine). Especially the division into positively and negatively charged domains has been hypothesized to induce the formation of supramolecular assemblies of cingulins by ionic interactions.[36] The stabilizing effect of ectoine has previously been reported by OBERDÖRFER *et al.*[259] and ROYCHOUDHURY *et al.*[260] and could fulfill the role of urea. On the other hand ectoine also interacts with lipid membrane as it decreases headgroup hydration and increases membrane fluidity.[261] RIfS experiments performed in this study demonstrated an influence of ectoine on the detected optical thickness of a membrane-covered surface but this observation could not only relate to structural changes of the lipid membranes but also to changes in refractive index of the buffer solution due to significantly increased particle concentration (see **Equation 3-21**).

In contrast rCinY3 was also transferred into acidic low-salt buffer (250 mM KCl, 40 mM NaOAc, 0.1 mM EDTA, 0.1 mM NaN_3, pH 5.5 (HOAc)) but no precipitation of the protein from solution was observed. rCinY3 was significantly smaller than rCinW2 (M(rCinY3) = 28.7 kDa, M(rCinW2) = 37.4 kDa) but while the content of charged amino acids (26% for rCinY3) was nearly identical to rCinW2, the content of hydrophobic amino acids was even significantly increased with 21% in rCinY3 compared to 12% in rCinW2 (see **Table App.3**).

A quantitative study on the aggregation of rCinW2 and another recombinant, tyrosine-rich cingulin, rCinY2, was published in 2016 by KOTZSCH *et al.*[36] They used dynamic light scattering to determine changes in size of protein aggregates in solution while lowering the pH from 7.7 down to 5.5. Measurements were performed in presence of 150 mM or 1 M NaCl (10 mM MOPS buffered solutions; pH adjustment with acetic acid). Already at pH 7.7 and at lower salt concentrations particle radii of about 4 nm were detected. These radii were roughly twice the size expected for monomeric proteins but the increase in size could also be contributed to the intrinsically disordered structure of the proteins. For rCinW2 at pH 5.5 significantly grown aggregates with radii about 170 nm were detected whereas no changes for rCinY2 were observed. At high salt concentrations opposing results were obtained: At pH 5.5 aggregates of rCinY2 with radii of about 360 nm were detected while on the other hand no changes regarding rCinW2 were observed. In general the trends presented by KOTZSCH *et al.* for rCinW2 support the stabilizing influence of salt and destabilizing influence of low pH observed in this study. Here in presence of 1 M NaCl, rCinW2 was stable at pH 8.0 (see **Figure 5.5**) but further decrease in salt concentration led to protein precipitation even at this pH. In presence of 1 M NaCl and at pH 5.5 partial protein precipitation was observed. It resulted in a decrease to about 50% of the initial protein concentration during buffer exchange. The nature of the remaining 50% of protein in solution was not investigated but would be expected to contain at least some smaller, soluble aggregates of rCinW2. The solubility of rCinY2 at low salt concentration is in good agreement with the solubility of rCinY3 under similar conditions but was not further investigated.

Crucial for the discussion of solubility and aggregation behavior of cingulins and their predicted role in template formation within the SDV[14] is of course the comparability of properties of recombinant cingulins to native ones. Cingulins share several structural similarities to silaffins, for example the presence of multiple KXXK motives in the amino acid sequence.[35,38] Analysis of silaffin variants from various diatom species revealed posttranslational modifications especially at the lysine residues as summarized by LECHNER and BECKER.[42] Despite cingulins being part of the insoluble organic matrix, remaining after treatment of diatom biosilica with 10 M NH_4F, and therefore being hard to address in their native form, mass spectrometric analysis on the insoluble organic matrix of *T. pseudonana* by KOTZSCH *et al.* identified various lysine modifications presumably also present in native cingulins.[36] The influence of those modifications on silica precipitation in case of silaffins has been investigated in some detail[265] and might also influence the aggregation of modified peptides and proteins in the first place since a direct relation between supramolecular aggregation and silica precipitation was observed for long-chain polyamines.[43] Recombinant proteins expressed in *E. coli* lack most of these modifications[266] thus comparability might be limited. But the fact that cingulins are part of the *insoluble* organic matrix[36] supports the observations made for the recombinant proteins in regard to aggregation behavior and solubility. Since no isolated native cingulins are available so far, recombinant proteins tend to be the most valuable model components also in regard to possible interactions of cingulins with lipid membranes.

5.3.2 Protein-Membrane Interactions

As cingulins, identified to be incorporated into the biosilica[35] and part of the insoluble organic matrix[36], are most likely also involved in processes inside the SDV, interactions with the silicalemma confining the SDV are possible. Herein the adsorption rCinW2 and rCinY3 on model membranes resembling the overall lipid composition of diatoms[66] (MGDG/DGDG/SQDG/POPG/DOPC, 35:20:15:5:25, see **Chapter 4**) were studied mainly by RIfS. While the good solubility of rCinY3 enabled measuring in acidic buffer at low salt concentrations and without further stabilizing agents (250 mM KCl, 40 mM NaOAc, 0.1 mM EDTA, 0.1 mM NaN_3, pH 5.5 (HOAc)), rCinW2 had to be stabilized by either elevated salt concentrations (2 M NaCl, 50 mM MES, pH 6.0) or addition of ectoine (100 mM KCl, 40 mM NaOAc, 2 M ectoine, pH 5.5 (HOAc)). Both buffers still reflected the acidic conditions also detected in the SDV.[22]

For rCinW2 and concentrations up to 1.8 µM no adsorption on membrane-covered surfaces could be detected. The investigation of rCinY3 adsorption by RIfS at concentrations up to 8 µM showed the reversible deposition of a protein layer with a physical thickness of less than 0.3 nm whereas adsorption of 1 µM rCinW2 on lipid monolayers resulted in the formation of a protein layer with an average physical thickness of approximately 0.1 nm not further quantifiable by SPR.

Both proteins have isoelectric points around 6.2 (pI(rCinW2) = 6.27, pI(rCinY3) = 6.20, see **Appendix**) and are therefore positively charged at pH 5.5–6.0 (at pH 5.5 +11.2 (rCinW2) or +7.7 (rCinY3)).[35,267] The lipid bilayer on the other hand incorporated 20% of negatively charged lipids. Hence at least electrostatic interactions between both partners were expected. In case of measurements on rCinW2, an increase in salt concentration lowered electrostatic interactions between the oppositely charged protein and membrane[236] resulting in no detectable interaction. RIfS measurements on rCinY3 and lower salt concentrations on the other hand showed weak, reversible interactions.

For proteins of roughly the same size that bind to lipid bilayers for example via specific interactions with incorporated receptor lipids greater changes in layer thicknesses would be expected. SHABARADINA *et al.* reported for example on the adsorption of *N*-ERMAD, the globular membrane-binding domain of ezrin with a molecular mass of about 39 kDa, on receptor lipid-containing membranes. At full surface coverage a physical thickness of up to

3 nm was observed (n_2 = 1.46 [262]). On the other hand in the same study the effect of packing of full length ezrin on the surface was discussed and could result in the observation of decreased optical and physical thicknesses. Similar effects could be expected for non-globular proteins. As a lot of other proteins involved in biomineralization processes,[268] cingulins are intrinsically disordered proteins.[35] Intramolecular aggregation affects the degree of hydration and therefore the refractive index n_2 which contributes to the observable optical thickness $OT = n_2 \cdot d$. Depending on the structure of the adsorbed proteins and additional experimental conditions, refractive indices of protein layers can range from 1.36 to 1.55 with smaller refractive indices (closer to the refractive index of water n_1 = 1.33 [269]) measured for higher hydrated proteins as demonstrated by VÖRÖS.[262] In conclusion, physical thicknesses of cingulin layers might be underestimated but only by less than 10%.

For both rCinW2 and rCinY3 protein adsorption was only studied phenomenologically and no thorough isotherms were recorded. As adsorption of proteins is an equilibrium reaction, surface coverage depends on the concentration of protein in solution and is characterized according to LANGMUIR by the equilibrium constant K_D ($K_D = \frac{k_d}{k_{ad}}$; k_d: rate constant of desorption, k_{ad}: rate constant of adsorption).[141] Proteins specifically binding to lipid membranes possess equilibrium constants often in the micro- down to nanomolar range.[132,270,271] Thus in this case with the applied concentrations of 1–8 µM nearly full surface coverage would be expected.

In summary for the first time recombinant cingulins had been investigated in regard to their interaction with lipid bilayers. Using artificial model systems for the silicalemma no significant specific interactions and adsorption of rCinW2 and rCinY3 were observed. Hence no direct interaction between those biomolecules and the SDV confining membrane were assumed to be involved in template formation in the organelle. However, indirect regulation by adaptor proteins binding both the silicalemma and the matrix containing cingulins could not be ruled out. Latest developments in the field of diatom biomolecule research led to the identification of the first putative SDV-transmembrane protein, silicanin-1, published by KOTZSCH *et al.* in 2017.[254] As this protein also ended up in the biosilica and the NH_4F-insoluble organic matrix, it could very well act as a missing link between the silicalemma and the cingulin-containing template for silica formation.

6 LONG-CHAIN POLYAMINES

Besides cingulins (see **Chapter 5**), a second class of biomolecules, identified inside the diatom biosilica[37] and investigated within this study, were the long-chain polyamines (LCPA). In contrast to cingulin proteins, LCPA are small biomolecules with a simple structure. They are linear molecules with repeating amine groups linked by alkyl spacers (see **Figure 1.3**). LCPA had first been isolated from diatom cell walls via dissolution of the biosilica with anhydrous HF by KRÖGER *et al.* in 2000.[37] Most interestingly their study also revealed species-specific mixtures of LCPA with different chain lengths. This observation hinted into the direction of a direct influence of LCPA on controlling the morphogenesis of each species' individual cell wall structure. Later studies revealed a tendency of LCPA to aggregate in solution for example in presence of phosphate ions.[43] Since these aggregates are capable of catalyzing silica precipitation, a phase separation model for control of silica cell wall biogenesis was developed.[59]

Since their discovery and postulation of a role in silica biomineralization, LCPA caught the attention of many scientists. Most of their work focused on the aggregation behavior of LCPA and other model components in solution[43,46–48,98,272,273] as well as their interactions with biomolecules also incorporated into the biosilica.[51,52] While some of these studies employed native LCPA mixtures isolated from diatoms, others had to use model components (*e.g.* polylysine) as most of them suffered on the limited amount of available polyamines. LCPA isolated from diatom biosilica are in the mass range between 600 and 1500 $\mathrm{g{\cdot}mol^{-1}}$ but commercially available are typically only polyamines with up to six amine groups (*e.g.* pentaethylenehexamine, $M = 232\ \mathrm{g{\cdot}mol^{-1}}$) or very heavy polymers of ethylene imine (PEI, $M > 1500\ \mathrm{g{\cdot}mol^{-1}}$). All LCPA used in this study were synthesized by the group of PROF. DR. ARMIN GEYER (Faculty of Chemistry, Philipps-University Marburg). During the past years his group introduced and improved new strategies for polyamine synthesis using solid phase peptide synthesis techniques (see **Chapter 3.1.2**).[43,98,99,273] These synthetic LCPA did not only resemble the physiological relevant chain length but also provided pure samples with well-defined and adjustable structures to address structure specific properties of LCPA.

Even thigh a number of studies on the behavior of LCPA and their model components in solution were published, no research on the interactions of diatom LCPA with lipid membranes had been presented so far. While LCPA of the mass range identified in diatom biosilica are hard to address, some studies on shorter polyamines, which are omnipresent in nature (*e.g.* spermidine or spermine), had been published.[274–278] Influences of these smaller polyamines on lipid membranes involve increased vesicle aggregation and membrane fusion.[279–284] On the other hand PEI can cause defects in solid supported lipid bilayers.[285] Herein for the first time interactions of LCPA of the physiological relevant mass range with solid supported model membranes were investigated. These model membranes also reflected the overall lipid composition in diatoms[66] and therefore remodeled the silicalemma (see **Chapter 4**). To its end, this research should shed light on a possible interaction of the lipid bilayer enclosing the silica deposition vesicle (SDV) and LCPA inside the organelle, which therefore might control biosilica morphogenesis.

Most of the data presented in this chapter was published in the peer-reviewed research article "3D-Membrane stacks on supported membranes composed of diatom lipids induced by long-chain polyamines" (*Langmuir* **2016**, *32*, 10144–10152, co-authors: MARYNA ABACILAR, FABIAN DAUS, PROF. DR. ARMIN GEYER and PROF. DR. CLAUDIA STEINEM; [99]).

6.1 Adsorption on Membrane-Covered Surfaces

The adsorption of LCPA on membrane-covered surfaces was quantified by reflectometric interference spectroscopy (RIfS). Increasing amounts of the synthetic LCPA C3N13 were added to a membrane-covered silicon dioxide surface (MGDG/DGDG/SQDG/POPG/DOPC, 35:20:15:5:25, see **Chapter 4.3.1**). Exemplary kinetic data on polyamine adsorption measured in sample buffer (see **Table 3.9**) is shown in **Figure 6.1 A**. The data was recorded by VANESSA REUSCHE as part of a bachelor project (*Wechselwirkungsstudien über Silika-präzipitierende Biomoleküle und Lipidmembranen mittels reflektometrischer Interferenzspektroskopie*, WS2014/15) supervised by the author.

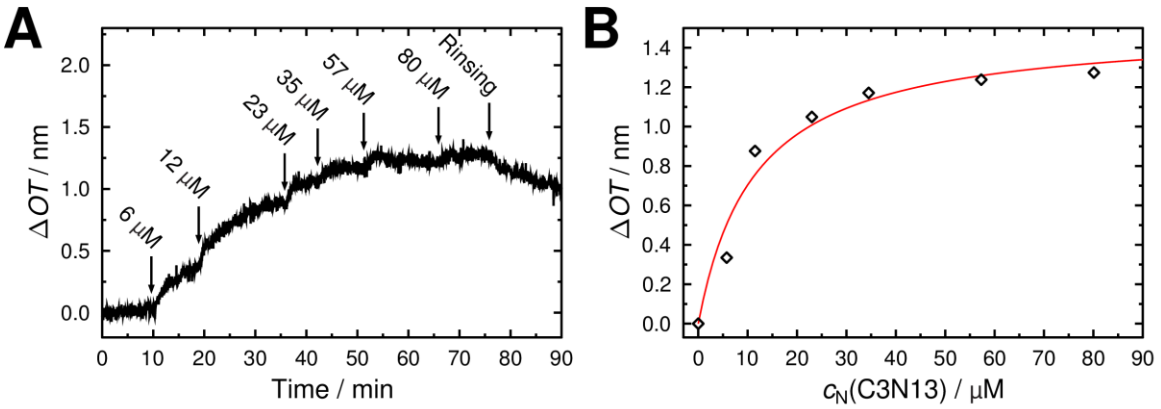

Figure 6.1. Exemplary adsorption kinetics of C3N13 in sample buffer (see Table 3.9) on a membrane-covered surface (MGDG/DGDG/SQDG/POPG/ DOPC, 35:20:15:5:25) recorded by RIfS (A). Optical thicknesses Δ*OT* at the end of each step of LCPA addition were plotted against polyamine concentration (B). The added fit is according to LANGMUIR's model of adsorption[141] and provided an dissociation constant of K_D = (11±8) µM and a maximal change in optical thickness of ΔOT_{max} = (1.5±0.3) nm.

An increase in optical thickness *OT* was observed after each step of LCPA addition going towards saturation at concentrations beyond c_N = 30 µM (see **Figure 6.1 B**; polyamine concentrations in this work are denoted as relative concentrations $c_N = \frac{c}{N}$ adjusted to the number of amine groups per molecule *N*). The observed changes in Δ*OT* indicated the deposition of LCPA on the surface. At the highest applied LCPA concentration (c_N = 80 µM in sample buffer (50 mM KCl, 40 mM NaOAc, pH 5.5 (HOAc)) or sample buffer with additional 0.1 mM EDTA and 0.1 mM NaN_3) a resulting increase in optical thickness of about Δ*OT* = (1.4±0.1) nm (*n* = 2) was detected. In order to determine the physical thickness *d* of the polyamine layer its refractive index had to be estimated. AULIN *et al.* studied the deposition of PEI on silicon oxide and silicon oxynitride surfaces.[286] Depending on the amount of adsorbed PEI and its degree of hydration, refractive indices between n_2 = 1.43 and 1.53 were reported. Since C3N13 is much smaller than PEI and polyamine hydrophobicity increases with chain length[43] causing decreased hydration, the lowest refractive index was approximated for the deposited LCPA layer to calculate its physical thickness $d = \frac{OT}{n_2}$. Under assumption of n_2 = 1.43 a physical thickness of *d* = (0.9±0.1) nm was determined.

Since nearly full saturation of the surface with polyamines was observed above C3N13 concentrations of 30 µM this concentration was chosen for all following experiments to ensure sufficient surface coverage.

In contrast to the shown data recorded in acetate-buffered solution, experiments on C3N13 adsorption performed in phosphate buffer (30–60 mM K_2HPO_4, pH 5.5–6.8) showed no proportional increase in optical thickness as described for example by LANGMUIR's model of adsorption.[141] Since the observation could be explained by the aggregation of LCPA in presence of phosphate ions,[43] phosphate-free, acetate-buffered solutions were used for all following studies.

6.2 Fluorescence Imaging

Besides kinetic and thermodynamic studies on the adsorption of LCPA on lipid membrane surfaces, fluorescence imaging provided additional information on the nature of polyamine-membrane interactions. Incorporation of a lipid-bound dye into solid supported lipid bilayers on mica (MGDG/DGDG/SQDG/POPG/DOPC/TexasRed-DHPE, 34.5:20:15:5:25:0.5, see **Chapter 4.3.2**) revealed changes in bilayer structures, which were clearly resolvable by optical microscopy (see **Chapter 3.4.5**) and resulted in an uneven distributed dye localization. A direct comparison of fluorescence micrographs before and after addition of C3N13 (30 µM in sample buffer (see **Table 3.9**) is shown in **Figure 6.2**.

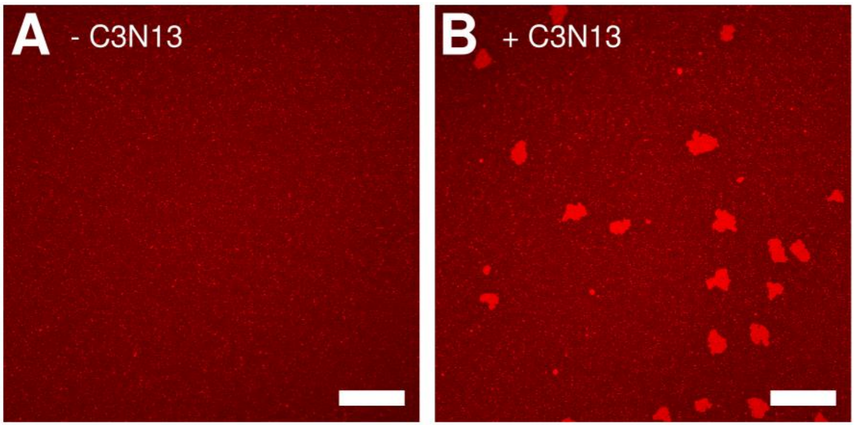

Figure 6.2. Fluorescence micrographs before (A) and after (B) addition of C3N13 (30 µM in sample buffer (see Table 3.9)) to a TexasRed-DHPE-labeled lipid bilayer on mica (MGDG/DGDG/SQDG/POPG/DOPC/TexasRed-DHPE, 34.5:20:15:5:25:0.5). The formation of domains with bright TexasRed fluorescence was observed all over the substrate. Scale bars: 100 µm.

After incubation of the lipid membrane with LCPA-containing solution fluorescence micrographs showed the formation of bright domains all over the formally homogeneous membrane-covered substrate (see **Chapter 4.3.2**). These domains had sizes up to several hundred square micrometers. Outside these domains still full coverage of the surface with fluorescently labeled lipid material was observed indicating no removal of the surface covering lipid bilayer. Alongside the use of the headgroup-labeled dye TexasRed-DHPE, replacement with the fatty acid-labeled dye Bodipy-C_{12}HPC confirmed the observation and ruled out an overlaying influence of interactions between the fluorescent label and the polyamines.

Domain formation was studied in more detail by time laps fluorescence microscopy. Series of fluorescence micrographs were recorded and C3N13 was added at the time $t = 0$. Representative data is shown in **Figure 6.3 A**.

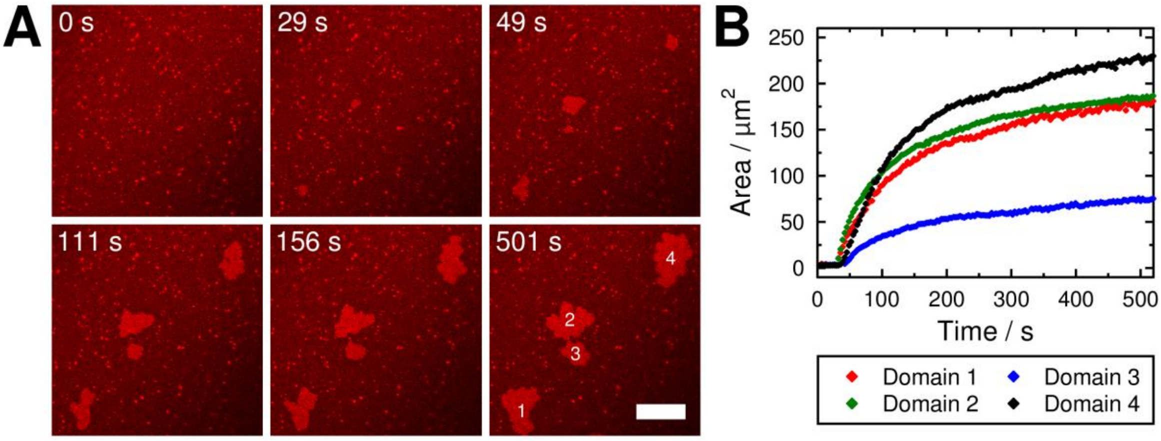

Figure 6.3. Exemplary time series of fluorescence micrographs taken after addition of C3N13 (30 µM in sample buffer (see Table 3.9)) to a TexasRed-DHPE-doped lipid bilayer on mica (MGDG/DGDG/SQDG/POPG/DOPC/TexasRed-DHPE, 34.5:20:15:5:25:0.5; A). The growth of domains with brighter TexasRed-DHPE fluorescence was observed within a few minutes. Areas of these domains were extracted and plotted against time (B). Scale bar: 20 µm.

Growth of bright domains was initiated immediately after addition of C3N13. The growth speed was analyzed from the data by intensity thresholding of the images, particle analysis and size measurement (see **Appendix**). Growing from a central point, domain formation followed an exponential decay function and mostly finished within a few minutes (see **Figure 6.3 B**). Also time scales of only a few seconds were observed. Reasons for very deviating growth rates will be discussed in more detail later as it was related to other preconditions for domain formation (see **Chapter 6.4.1**).

6.3 Characterization of LCPA-Induced Structures

Observation made during addition of the LCPA C3N13 to solid supported lipid bilayers were not comparable, for example, to the formation of defects in lipid bilayers by much larger PEI.[285] Thus, characterization of the formed structures on or within the lipid bilayers was intensified in the following chapter.

6.3.1 Localization of Polyamines

Time lapse fluorescence microscopy revealed the formation of bright domains after addition of C3N13 to a lipid bilayer doped with a lipid-bound dye. Besides the localization of lipid material by means of fluorescence microscopy, it is desirable to also localize LCPA. The synthesis of a fluorescein-labeled derivative of C3N13 (FITC-C3N13) enabled the localization of polyamines in correlation to a TexasRed-DHPE-labeled lipid bilayer (MGDG/DGDG/SQDG/POPG/DOPC/TexasRed-DHPE, 34.5:20:15:5:25:0.5). Typical fluorescence micrographs showing both FITC (green) and TexasRed (red) fluorescence are presented in **Figure 6.4**.

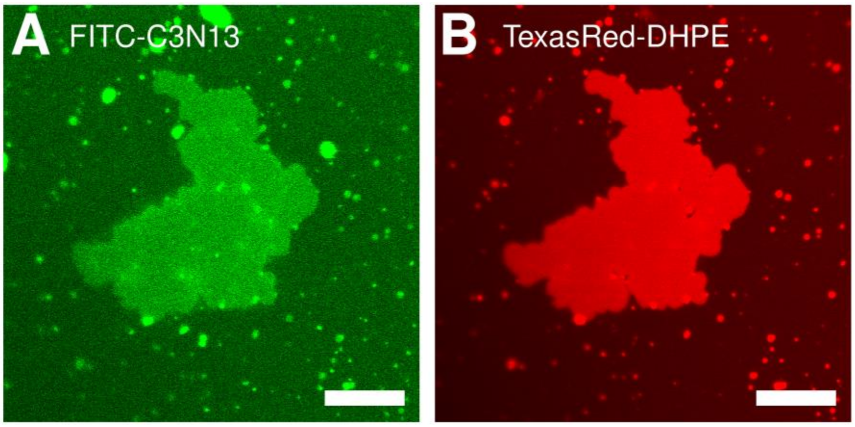

Figure 6.4. Fluorescence micrographs after addition of FITC-C3N13 (30 µM in sample buffer (see Table 3.9)) to a lipid bilayer on mica (MGDG/DGDG/SQDG/POPG/DOPC/TexasRed-DHPE, 34.5:20:15:5:25:0.5). FITC-C3N13 fluorescence visualized an accumulation of LCPA on the surface (A). In contrast, red TexasRed-DHPE fluorescence (B) reveals the localization of lipid material. A clear co-localization between brighter membrane domains and an accumulation of FITC-C3N13 was observed. Scale bars: 10 µm.

A clear co-localization between the formed domains with brighter TexasRed-DHPE fluorescence and increased FITC fluorescence proved an accumulation of FITC-C3N13 in the region of the newly formed domains. Besides confined bright fluorescence inside the domains weaker FITC fluorescence was also observed all over the substrate indicating adsorption of polyamines in these regions, too. A cross-talk between both dyes was ruled out by reference experiments using FITC-C3N13 on unlabeled membranes. While FÖRSTER resonance energy transfer (FRET) between both dyes prevented intensity quantification in presence of TexasRed-DHPE, these reference measurements revealed an intensity ratio between FITC fluorescence in the brighter domains F and the surrounding F_m of $F/F_\mathrm{m} = 2.3\pm0.2$ for about 95% of the structures in a sample of 62 domains (9 images) with the remaining 5% showing increased fluorescence ratios.

In summary and concluding previous observations on the triggering of domain formation by LCPA addition, the formation of membrane domains was proven to be directly connected to an accumulation of LCPA in exact the same regions.

6.3.2 Quantification of Fluorescence Intensities

The increase in local membrane-bound dye fluorescence intensities was analyzed quantitatively as well. Fluorescence intensities F of 1204 domains (49 fluorescence micrographs) on solid supported lipid bilayers (MGDG/DGDG/SQDG/POPG/DOPC/TexasRed-DHPE, 34.5:20:15:5:25:0.5, support: mica) formed after the addition of C3N13 (30 µM in sample buffer (see **Table 3.9**)) were read out. Relative fluorescence intensities F/F_m compared to the intensity F_m of the domain surrounding lipid bilayer were calculated and compiled in a histogram shown in **Figure 6.5**.

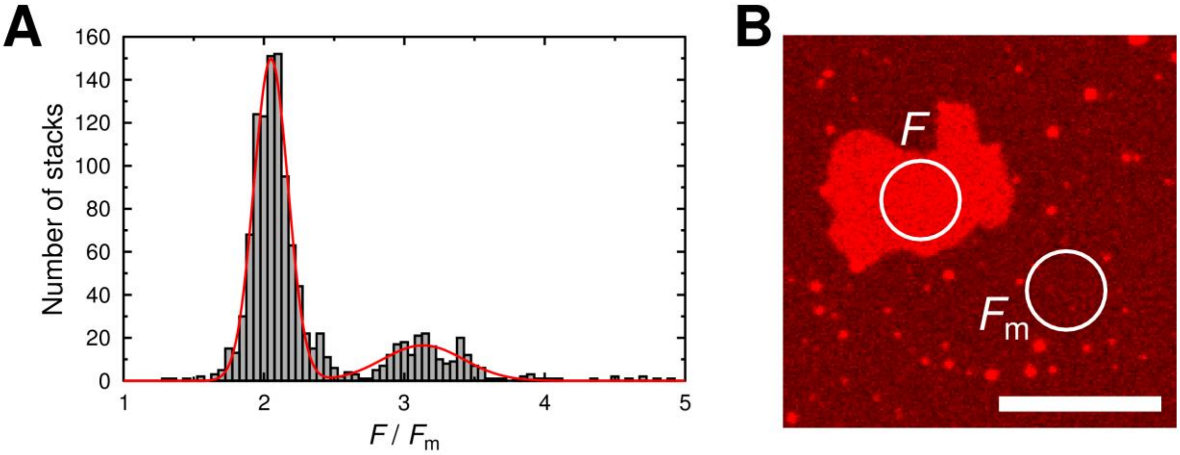

Figure 6.5. Statistical analysis of fluorescence intensities F of lipid-bound dyes in the brighter membrane domains compared to the surrounding membrane F_m (A). The sum of two GAUSSIAN functions is fitted to the data. Domains were formed after addition of C3N13 (30 µM in sample buffer (see Table 3.9)) to solid supported lipid bilayers on mica (MGDG/DGDG/SQDG/POPG/DOPC/TexasRed-DHPE, 34.5:20:15:5:25:0.5). An exemplary fluorescence micrograph illustrates the regions for intensity measurements (B). Scale bar: 10 µm.

Two distinct populations of domains were identified: About 80% showed nearly twice the fluorescence intensity of the surrounding lipid bilayer ($F/F_m = 2.1 \pm 0.2$) while a smaller population of about 20% exhibited an approximately tripled fluorescence intensity ($F/F_m = 3.1 \pm 0.4$).

The observation that membrane domains formed after LCPA addition exclusively showed even multiples of the lipid bilayers fluorescence intensity hinted towards the formation of structures containing multiple lipid bilayers rather than less distinct domains caused for example by local accumulation of labeled lipids within a lipid bilayer.

6.3.3 Topography of LCPA-Induced Domains

Correlative Atomic Force and Fluorescence Microscopy

Local lipid-bound dye accumulation or exclusion within a lipid bilayer can be caused for example by (biomolecule-induced) phase separation inside the lipid bilayer.[287] Depending on packing and the structure of the lipids and the lipid-bound dye, dye molecules become either enriched or depleted inside certain domains. Phase separation normally also involves a change in bilayer thickness for example due to tighter packaging of alkyl chains. Height difference, for example between liquid ordered and liquid disordered domains, are normally in the range of 0.5–1.0 nm.[288] Phase separation could presumably be triggered by specific interactions between LCPA and lipid headgroups (*e.g.* of the glycolipids MGDG, DGDG and SQDG). Additionally also the formation of larger 3D-aggregates was taken into account. The topography of lipid bilayers on mica (MGDG/DGDG/SQDG/POPG/DOPC/TexasRed-DHPE, 34.5:20:15:5:25:0.5) after the addition of C3N13 (30 µM in sample buffer (see **Table 3.9**)) was studied by atomic force microscopy (AFM) in combination with an inverse epifluorescence microscope. In general, imaging of the membrane surface and LCPA-induced domains in particular turned out to be rather challenging. Sequential imaging of the same domain, even in intermittent contact mode, revealed degradation of the domain during imaging. Hence absolute height information gathered by AFM should be treated with caution. Simultaneous observation of the same spot by AFM and epifluorescence microscopy allowed direct correlation between height information and lipid-bound dye distribution. An exemplary topography map and the corresponding fluorescence micrograph are shown in **Figure 6.6**.

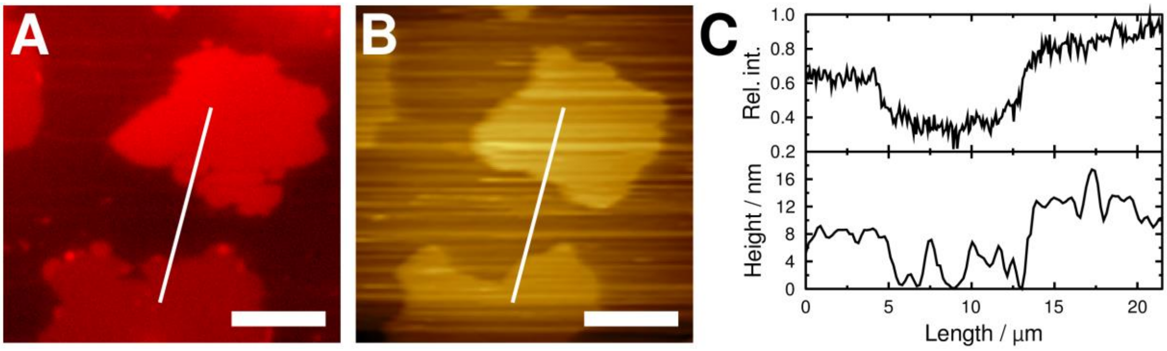

Figure 6.6. Correlative fluorescence micrograph (A) and topography map (B) of membrane stacks formed after addition of C3N13 (30 µM in sample buffer (see Table 3.9)) to a lipid bilayer on mica (MGDG/DGDG/SQDG/POPG/DOPC/TexasRed-DHPE, 34.5:20:15:5:25:0.5). Intensity and height profiles along the white lines were extracted and plotted in C. A co-localization between domains with brighter TexasRed fluorescence and higher structures was observed. Scale bars: 10 µm.

The data revealed a clear co-localization between domains with higher fluorescence intensity and domains with increased height compared to the surrounding lipid bilayers. Deviations in shape of domains between both images are caused by the previously mentioned degradation during AFM imaging. Quantitative comparison of sample heights and relative fluorescence intensities revealed an elevated height of approximately 8 nm for the domain with the doubled fluorescence intensity and of around 15 nm for the domain with three times the fluorescence intensity of the surrounding lipid bilayer.

Height differences measured between LCPA-induced domains and their surrounding, even if assuming an rather large margin of error, significantly exceed the differences caused by lateral phase separation within lipid bilayers.[288] Previous experiments identified a membrane thickness of about 4 nm (see **Chapter 4.3.2**). Combined with the observation of multiplied fluorescence intensities in the domain areas (see **Chapter 6.3.2**) the formation of larger 3D structures with additional lipid bilayers on top of an underlying one and linked by a spacer region containing LCPA was most likely. For this reason LCPA-induced domains are from now on denoted as *membrane stacks*.

Force Spectroscopy on Membrane Stacks

The postulation of such stacked structures was also evaluated by force spectroscopy. Approaching the membrane surface with the cantilever tip and application of force can result in breakthrough events of the tip through one or even more lipid bilayers. Force-distance-curves (FDC) indicate such breakthroughs as abrupt decreases in force during the approach.[194,196,197] Multiple FDC were measured all over a lipid bilayer on mica (MGDG/DGDG/SQDG/POPG/DOPC/TexasRed-DHPE, 34.5:20:15:5:25:0.5) after addition of C3N13 (30 µM in sample buffer (see **Table 3.9**)). The presence of membrane stacks was beforehand confirmed by fluorescence and imaging atomic force microscopy. Four exemplary FDC are shown in **Figure 6.7**.

During the approach of the cantilever to the surface, force was applied to the membrane surface. In result, between zero and up to three breakthrough events were detected until the force setpoint was reached. Each of these breakthroughs was assigned to the cantilever tip breaking through one lipid bilayer. One breakthrough proves the coverage of the mica surface with at least one lipid bilayer. The thickness of this bilayer could be extracted from FDC by the difference in separation between the beginning and end of the tip passing the membrane (see **Figure 3.32**). For single breakthroughs depths of (4±1) nm ($n = 65$) were

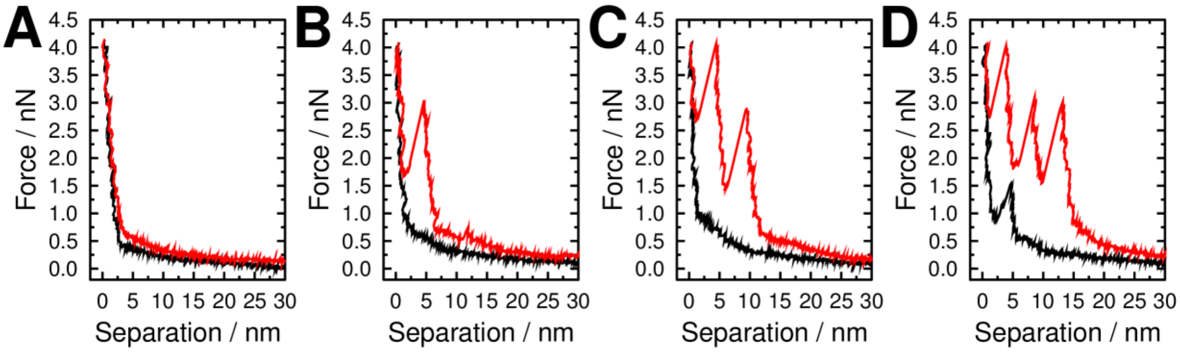

Figure 6.7. Set of exemplary FDC on a mica-supported membrane (MGDG/DGDG/SQDG/POPG/DOPC/TexasRed-DHPE, 34.5:20:15:5:25:0.5) covered with stacks formed after addition of C3N13 (30 µM in sample buffer (see Table 3.9)). Between zero and up to three breakthrough events through lipid bilayers were observed. Separation denotes the relative distance between the cantilever base and the surface and was set to zero at maximal deflection. Traces are plotted in red while the retraces are colored in black.

observed which was in good agreement with the bilayer thickness reported in **Chapter 4.3.2** (see **Figure 4.16**). The additional second or third breakthrough events showed coverage of the membrane surface with one or two additional lipid bilayers. Total depths between all breakthroughs were either (8±2) nm (*n* = 10) or 12 nm (*n* = 1). These heights are smaller than those extracted from the topography maps shown in the previous chapter but this observation could be explained by the very soft character of the surface – especially of the LCPA layers. In general it has to be denoted that very often less breakthrough events were observed. Even when fluorescence imaging proved coverage of the surface with a lipid bilayer, breakthroughs were only observed in a few of the FDC. This observation also concerned the measurements on membrane stacks. Especially for FDC with three breakthroughs the limited amount of data restricted in depth analysis.

Overall force spectroscopy substantiated the observations made by imaging AFM as it provided evidence for the formation of additional lipid bilayers on top of an underlying one.

6.3.4 Fluorescence Recovery after Photobleaching

Fluorescence recovery after photobleaching (FRAP) can be used to study diffusion of (lipid-bound) dye molecules. Previously it was employed to probe formation of continuous lipid bilayers, membrane fluidity and to calculate lipid diffusion coefficients (see **Chapter 4**). Fluorescence recovery is only observed if unbleached dye molecules diffuse into formerly bleached regions. Regarding LCPA-induced membrane stacks FRAP was used to study if a connection between the stacked membrane and the underlying one was present and enabled exchange of lipid material. After bleaching a whole membrane stack unbleached dye

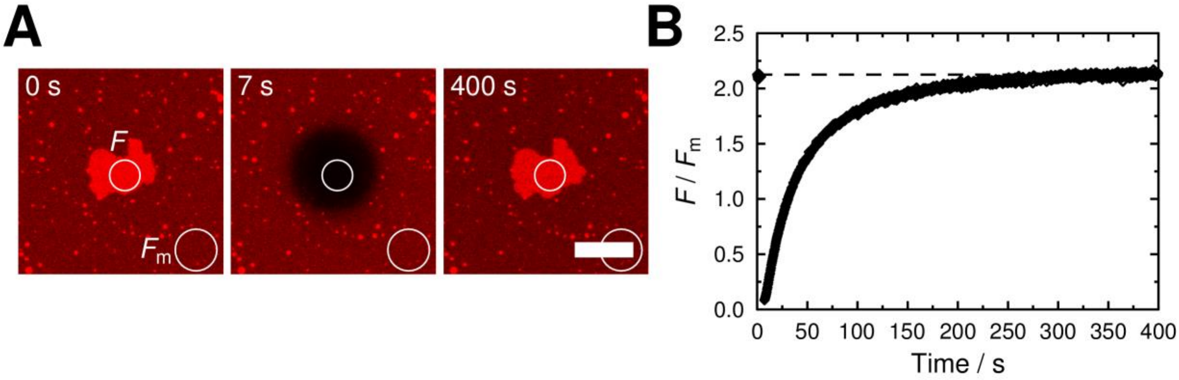

Figure 6.8. Exemplary FRAP experiment on a LCPA-induced (C3N13, 30 µM in sample buffer (see Table 3.9)) membrane stack (MGDG/DGDG/SQDG/POPG/DOPC/TexasRed-DHPE, 34.5:20:15:5:25:0.5) visualized as a series of fluorescence micrographs (A). Fluorescence intensities inside the stack *F* were read out, related to the fluorescence of the surrounding lipid bilayer F_m and plotted against time (B). Full fluorescence recovery was observed within a few minutes. Scale bar: 10 µm.

molecules are only present in the underlying, the stack surrounding lipid bilayer. Recovery could only be observed after mobilization of this pool. A representative FRAP experiment is shown in **Figure 6.8**.

After bleaching of TexasRed-DHPE fluorescence within a whole membrane stack full fluorescence recovery was observed over a few minutes. Multiple FRAP experiments were carried out on both membrane stacks with double ($n = 5$) or tripled ($n = 6$) fluorescence intensity with coinciding results. Variations in stack shape and size did not allow further quantification of fluorescence recovery as both parameters influence the kinetics of fluorescence recovery.

Since full recovery of fluorescence in the stacked membrane region was overserved, the presence of at least one connection between the stacked and underlying membrane was proven. Time lapse fluorescence microscopy documented the growth of membrane stacks after LCPA addition from a central point (see **Chapter 6.2**) hence a closer look at the connectivity between all layers was taken as it influences the exchange of lipid-bound dye molecules between the stacked and the underlying membrane and therefore might be extracted from FRAP data. **Figure 6.9** shows a cross section of fluorescence intensities through a membrane stack and their evolution during a FRAP experiment.

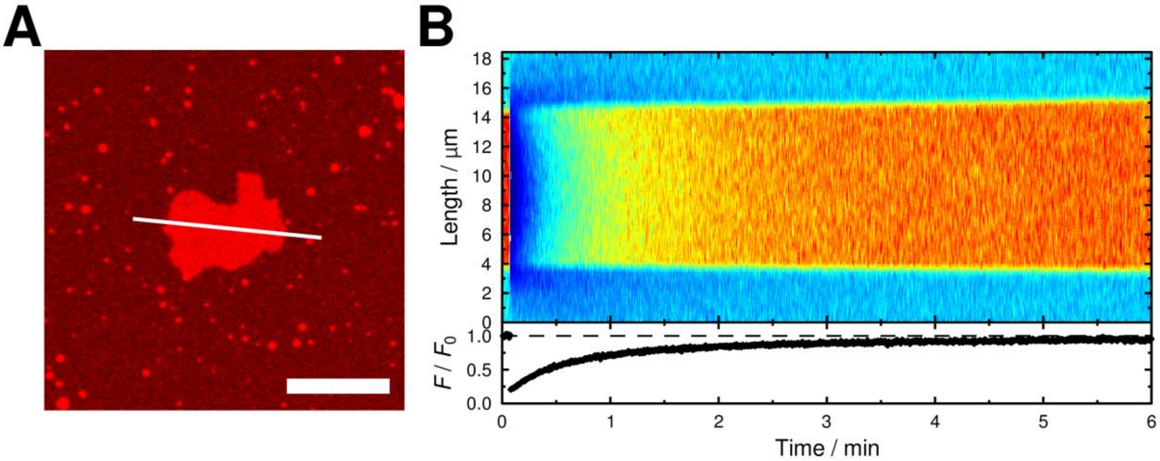

Figure 6.9. Evolution of the bleach profile during a FRAP experiment on a LCPA-induced (C3N13, 30 µM in sample buffer (see Table 3.9)) membrane stack (MGDG/DGDG/SQDG/POPG/DOPC/TexasRed-DHPE, 34.5:20:15:5:25:0.5). Intensity data was read out along a cross section through a membrane stack (A). Both local fluorescence intensities as well as fluorescence intensities *F* averaged over the whole cross section were normalized to the initial fluorescence intensity F_0 and are plotted against time (B). Scale bar: 10 µm.

The radial symmetric bleach profile recovers by diffusion of unbleached lipid-bound dye molecules into the membrane stack. No restricted diffusion into the second membrane layer (*e.g.* through a central "bottle neck") could be observed but no sophisticated simulation of recovery was performed for comparison.

Since full fluorescence recovery in general was very fast and no spatial restrictions were detected, the presence of most likely more than one connection between the stacked lipid bilayers and the underlying one was concluded. In summary FRAP experiments proved a connection between the stack layers allowing the exchange of lipid material.

6.3.5 Experiments on Lipid Monolayers

Since the initial, surface covering lipid bilayer showed a strong connection to the additional layers of the membrane stack (see **Chapter 6.3.4**) its role and incorporation into the LCPA-induced membrane stacks was investigated in more detail by the use of solid supported lipid monolayers. In contrast to lipid bilayers these model membranes contain only one membrane leaflet. The use of lipid monolayers and investigation if LCPA-induced stack formation takes place on theses membranes as well, shed light on the necessity and possible incorporation of the second, surface-facing membrane leaflet within lipid bilayers.

Figure 6.10 shows an exemplary fluorescence micrograph of a lipid monolayer on hydrophobically functionalized glass (MGDG/DGDG/SQDG/POPG/DOPC/TexasRed-DHPE, 34:20:15:5:25:1, see **Chapter 4.2.2**) after the addition of C3N13 (30 µM in sample buffer (see **Table 3.9**)).

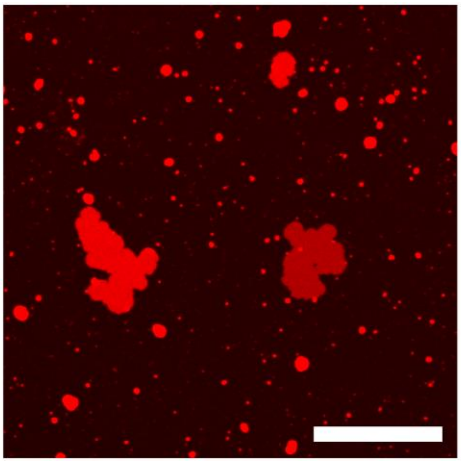

Figure 6.10. Exemplary fluorescence micrograph of LCPA-induced (C3N13, 30 µM in sample buffer (see Table 3.9)) membrane stacks formed on a lipid monolayer on hydrophobically functionalized glass (MGDG/DGDG/SQDG/POPG/DOPC/TexasRed-DHPE, 34:20:15:5:25:1). Scale bar: 20 µm.

After LCPA addition even on lipid monolayers formation of membrane stacks was observed. Within a small sample of seven fluorescence micrographs containing 103 stacks two populations with relative stack intensities of $F/F_m = 2.6 \pm 0.3$ (60%) and $F/F_m = 4.8 \pm 1.2$ (40%) were observed with the second one being much broader. In approximation the fluorescence intensities in the region of the membrane stack were three or five times the intensity of the surrounding membrane. This corresponds to a lipid monolayer with one or two lipid bilayers on top.

FRAP experiments on whole membrane stacks on top of lipid monolayers showed recovery of fluorescence intensities of the stacked membranes as well as of the underlying one.

In conclusion, no lipid bilayers, consisting of two membrane leaflets, were needed for LCPA-induced stack formation. One lipid monolayer was sufficient to provide a surface on which membrane stacks were formed. Additionally even in this case the formation of connections between the stacked underlying membranes were detected as they enabled lipid exchange between the layers.

6.4 Requirements for Membrane Stacking

The previous chapter focused on the characterization of membrane stacks formed on lipid membranes (mainly MGDG/DGDG/SQDG/POPG/DOPC/TexasRed-DHPE, 34.5:20:15:5:25:0.5) after the addition of the LCPA C3N13 (30 µM in sample buffer (see **Table 3.9**)). Besides the clear observations that addition of the polyamine triggered stack formation (see **Figure 6.3**) and labeled polyamines (FITC-C3N13, 30 µM in sample buffer) are accumulated in the region of the membrane stack (see **Figure 6.4**), so far no systematic studies on requirements for stack formation were performed. This chapter focuses on additional factors enabling LCPA-induced stack formation in the first place. Besides investigation on the provision of lipid material, influences of membrane composition and polyamine structure have also been addressed.

6.4.1 Origin of Lipid Material

Membrane stacks formed after addition of LCPA grew up to sizes of several hundred square micrometers (see **Figure 6.2**). Hence rather large amounts of lipid material had to be acquired to form these structures. In general two different origins of the lipid material could be postulated: On the one hand the use of an *internal lipid pool*. Lipids would be withdrawn from the solid supported lipid membrane. The depletion of lipids could therefore lead to the formation of macro- or microscopic defects. Alternatively protrusions, observed all over the membrane surface, could diminish as lipids stored in there are incorporated into membrane stacks. On the other hand an *external lipid pool* could be utilized. Vesicles from solution could fuse after addition of LCPA with the supported lipid membrane forming the stacked lipid bilayers. All of these postulations were addressed by the following experiments.

Internal Pool: Formation of Defects

Depletion of lipids from supported lipid bilayers would sooner or later result in the formation of defects. These defects could either be beyond the resolution limit of optical microscopes (see **Chapter 3.4.5**) or below it. In time lapse fluorescence microscopy studies no formation of macroscopic defects (several square micrometers) was observed (see **Figure 6.2**). Although the formation of smaller defects might not have been resolved sufficiently, their appearance would nevertheless have resulted in a detectable range of decrease in fluorescence intensity in the uncovered membrane parts alongside the local LCPA-induced formation of membrane stacks. **Figure 6.11** visualizes fluorescence intensity changes during stack growth within an exemplary series of fluorescence micrographs.

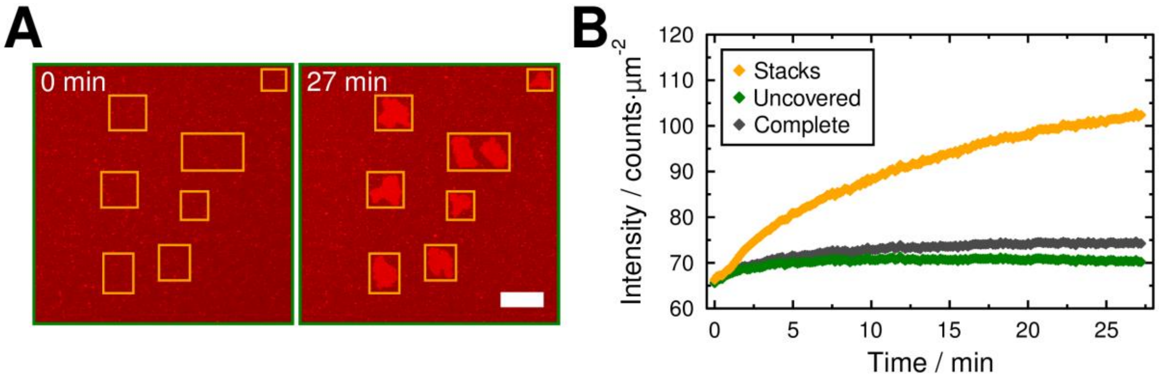

Figure 6.11. Changes in fluorescence intensity during the growth of LCPA-induced (C3N13, 30 µM in sample buffer (see Table 3.9Table 3.9)) membrane stacks on an exemplary lipid bilayer on mica (MGDG/DGDG/SQDG/POPG/DOPC/TexasRed-DHPE, 34.5: 20:15:5:25:0.5). Regions of interest were defined inclosing the formed membrane stacks (A). Fluorescence intensities per area within these regions (Stacks) as well as on the rest of the surface (Uncovered) and the complete images (Complete) are plotted against time (B). Data was not corrected for bleaching or other effects. Increases in fluorescence intensities in both areas, the ones covered with membrane stacks and the uncovered areas, were detected. Scale bar: 50 µm.

In the time-series a significant increase in fluorescence intensity was observed where membrane stacks were formed but on the other hand no significant decrease in fluorescence intensity in the uncovered membrane regions was detected. If lipid material were exclusively recruited from the solid supported membrane, a decrease of fluorescence intensity would be expected. In contrast, the exemplary data even showed an increase in fluorescence intensity in the uncovered membrane regions. This increase could indicate a deposition of lipid material even in these regions, but evaluated data should be reviewed carefully. The experiment did not include an internal reference to correct for bleaching or focus drifts. Bleaching would result in a continuous decrease in fluorescence intensity – opposing the observed trends and therefore strengthening the interpretation made. Focus drifts should also normally result in a decrease in detected fluorescence intensity but can in some cases also cause increases if the sample was slightly out of focus at the start of the experiment. Beside these objections the formation of defects due to translocation of lipids from the underlying, supported membrane into the additional layers of the membrane stacks was ruled out as no significant intensity drop in the uncovered membrane region was observed.

Internal Pool: Depletion of Protrusions

The incorporation of lipids from the supported lipid membrane into the membrane stack might not necessarily result in the formation of defects. As shown before (see **Chapter 4**) the employed model membranes (mainly MGDG/DGDG/SQDG/POPG/DOPC/TexasRed-DHPE, 34.5:20:15:5:25:0.5) contained numerous protrusions all over their surface. These protrusions locally house larger amounts of lipids and could therefore store the material needed for stack formation. Even if the previous analysis of overall fluorescence intensities included the protrusions, their fate was studied in more detail by differential imaging of the membrane surface before and after LCPA addition (C3N13, 30 µM in sample buffer (see **Table 3.9**)) and stack formation (see **Figure 6.12**).

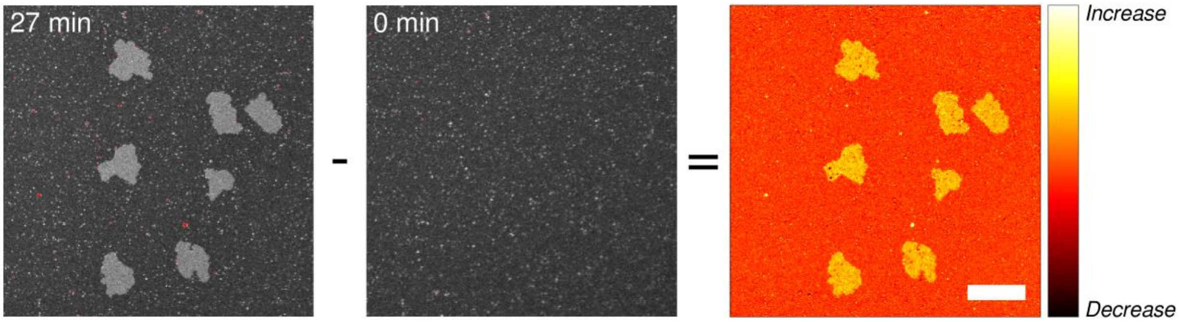

Figure 6.12. Changes in local fluorescence visualized by an exemplary differential fluorescence micrograph before and after the formation of membrane stacks after addition of C3N13 (30 µM in sample buffer (see Table 3.9)) to a solid supported lipid bilayer on mica (MGDG/DGDG/SQDG/POPG/DOPC/TexasRed-DHPE, 34.5:20:15:5:25:0.5). The initial fluorescence intensities (0 min) were subtracted from the fluorescence intensities detected at the end of the time series (27 min). Pixels recorded with overdriven detectors are colored in red. Scale bar: 50 µm.

While a significant increase in fluorescence intensity in the region of the growing membrane stacks was observed, the differential imaging did not reveal significant changes in number and intensity of membrane protrusions. This observation was in good agreement with the previous results on overall changes in fluorescence intensities in the uncovered membrane regions and negates the postulation that lipid material from the supported lipid membrane was used for LCPA-induced stack formation.

External Pool: Vesicles from Solution

An alternative postulation was the utilization of an external lipid pool to gather lipid material for the formation of membrane stacks. Such an external pool could be formed by vesicles that remained in the membrane-covering buffer solution after spreading even after several steps of rinsing. To prove an uptake of vesicular lipid material from solution, surfaces were heavily rinsed with sample buffer (see **Table 3.9**) before addition of C3N13 (30 µM in sample buffer) and small unilamellar vesicles (SUVs) doped with a second lipid-bound dye. A more red-shifted dye was chosen to label SUVs (MGDG/DGDG/SQDG/POPG/DOPC/ TexasRed-DHPE, 34.5:20:15:5:25:0.5). Exclusive excitation enabled localization lipid material originating from externally added SUVs. Solid supported membranes

(MGDG/DGDG/SQDG/POPG/DOPC/dye, 34.5:20:15:5:25:0.5) were labeled with spectrally separated, green dyes, either fatty acid-labeled Bodipy-C_{12}HPC or headgroup-labeled Atto488-DHPE. Fluorescence micrographs after addition of TexasRed-DHPE-labeled SUVs (4 µg·mL^{-1} in sample buffer (see **Table 3.9**)) alongside C3N13 (30 µM) to lipid bilayers doped with Bodipy-C_{12}HPC or Atto488-DHPE are shown in **Figure 6.13**.

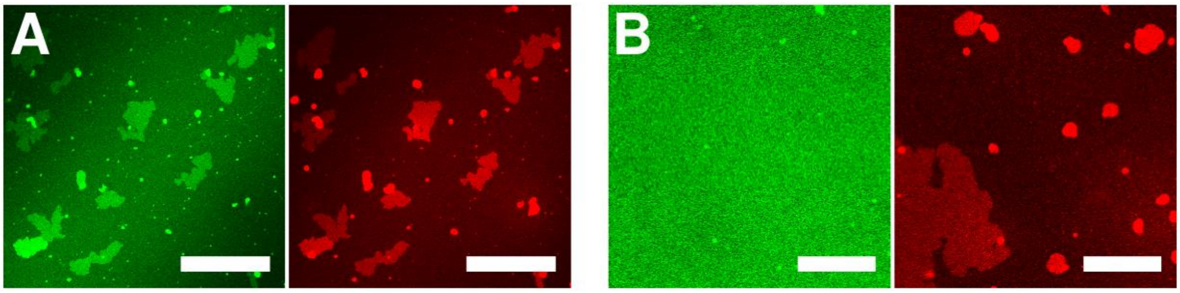

Figure 6.13. Exemplary fluorescence micrographs of lipid bilayers on mica (green channels, MGDG/DGDG/SQDG/POPG/DOPC/dye, 34.5:20:15:5:25:0.5) labeled with Bodipy-C_{12}HPC (A) or Atto488-DHPE (B) after addition of C3N13 (30 µM in sample buffer (see Table 3.9)) alongside TexasRed-DHPE-doped SUVs (red channel, 4 µg·mL^{-1}, lipid ratios identical to solid supported membrane). LCPA-induced stack formation was observed by TexasRed fluorescence in both experiments while only in case of experiments with Bodipy-C_{12}HPC stacks were also detected by the green dye distribution as well. Scale bars: 50 µm.

The formation of membrane stacks was detected by red TexasRed fluorescence additionally proving the incorporation of lipid material from external SUVs. The uptake of lipid material labeled with the red dye was also verified by exclusive excitation of TexasRed by light with longer wavelength (λ_{ex} = 561 nm). Thus a cross-talk adulterating TexasRed fluorescence was ruled out. In the green channel, showing the fluorescence of dye molecules formerly only contained in the solid supported membrane, membrane stacks were only visible on Bodipy-C_{12}HPC containing membranes. Previous FRAP experiment have proven the existence of connections between stacked and underlying layers of the membrane stacks, allowing for an exchange of lipid material (see **Figure 6.8**). The exchange of lipids also included lipid-bound molecules but is restricted by the mobility of the individual molecules within lipid bilayers. Since Atto488-DHPE diffusion turned out to be significantly slower in this model system (see following excursus), full mixing of both dye populations could not yet have been completed.

Excursus: Diffusion of Lipid-Bound Dyes in Solid Supported Lipid Bilayers on Mica

The properties of solid supported lipid bilayers on mica mimicking the lipid composition of diatoms[66] (MGDG/DGDG/SQDG/POPG/DOPC, 35:20:15:5:25) were studied in detail in

Chapter 4.3.2. Due to its high photostability 0.5 mol% of TexasRed-DHPE were added as lipid-bound fluorescent dye in most of the experiments reported in this study. Replacing TexasRed-DHPE with either the green dye Bodipy-C$_{12}$HPC or Atto488-DHPE also allowed deposition of continuous lipid bilayers on mica surfaces. On the other hand diffusion of dye molecules in the lipid bilayer turned out to be heavily affected by the dye's structure. Exemplary FRAP data is summarized in **Figure 6.14**. Diffusion coefficients were calculated according to **Equation 3-34** and **3-35**.

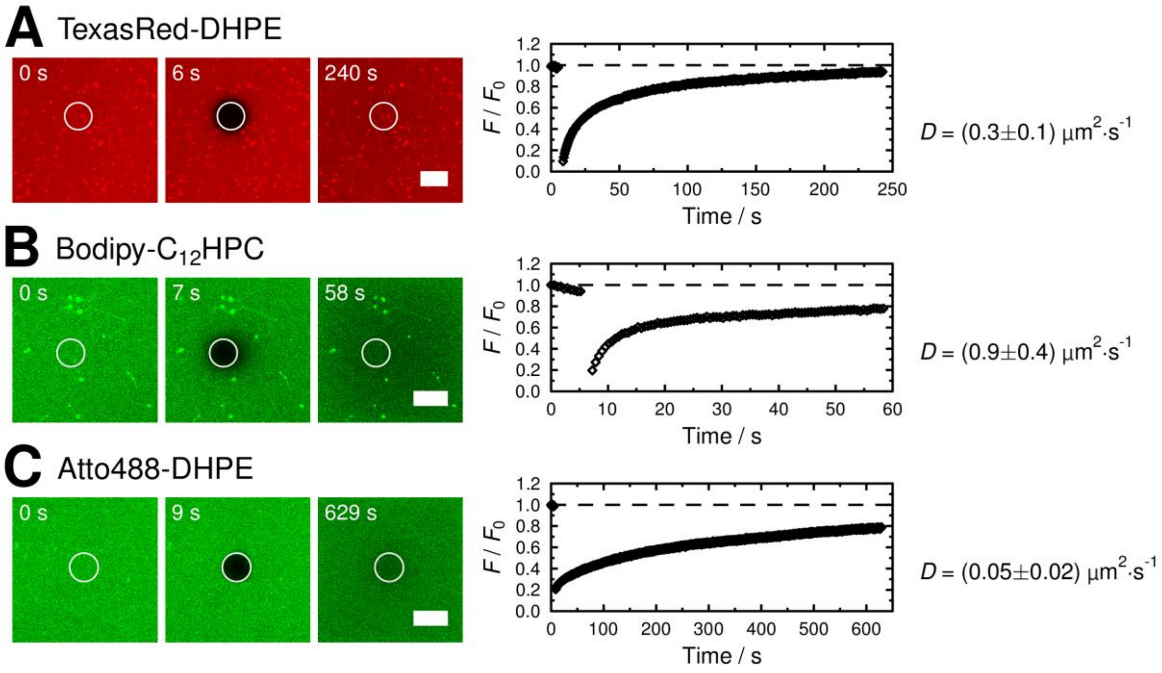

Figure 6.14. Overview on FRAP experiments on solid supported lipid bilayers on mica (MGDG/DGDG/SQDG/POPG/DOPC/dye, 34.5:20:15:5:25:0.5 in sample buffer (see Table 3.9)) incorporating one of the three lipid-bound dyes TexasRed-DHPE (A), Bodipy-C$_{12}$HPC (B) or Atto488-DHPE (C). The data is visualized as series of fluorescence micrographs. Fluorescence intensities in the encircled regions were read out and plotted against time (data for Bodipy-C$_{12}$HPC and Atto488-DHPE included a linear correction for bleaching). Diffusion coefficients were calculated and compiled from several experiments (TexasRed-DHPE: *n* = 9 (see Chapter 4.3.2), Bodipy-C$_{12}$HPC: *n* = 3, Atto488-DHPE: *n* = 8). Scale bars: 10 µm.

For Bodipy-C$_{12}$HPC incorporated into a lipid bilayer on mica a diffusion coefficient of D_{Bodipy} = (0.9±0.4) µm^2·s^{-1} (n = 3) was calculated. This value was slightly higher than the previously determined diffusion coefficient for membrane associated TexasRed-DHPE D_{TexasRed} = (0.3±0.1) µm^2·s^{-1} (n = 9, see **Chapter 4.3.2**) but was still in good agreement with it. In contrast the diffusion of Atto488-DHPE was significantly slower with a diffusion coefficient of D_{Atto488} = (0.05±0.02) µm^2·s^{-1} (n = 8). Notably, similar tendencies had been observed on mica supported pure DOPC membranes with 0.5 mol% of the lipid-bound dyes ($D_{\mathrm{TexasRed,DOPC}}$ = (1.1±0.3) µm^2·s^{-1} (n = 3), $D_{\mathrm{Bodipy,DOPC}}$ = (1.6±0.2) µm^2·s^{-1} (n = 3),

$D_{\text{Atto488,DOPC}} = (0.14 \pm 0.03)\ \mu\text{m}^2 \cdot \text{s}^{-1}$ ($n = 5$)). The composition of the membrane matrix only marginally influences the dye diffusion leading to slightly lower diffusion coefficients for all dyes in case of the glycolipid-containing membranes and was already discussed in **Chapter 4.4**. The hindered diffusion of Atto488-DHPE could most likely be traced back to stronger interactions of the dye's headgroup with the solid support.

6.4.2 Influence of Lipid Composition

Lipid bilayers employed so far all contained high amounts of the three glycolipids MGDG, DGDG and SQDG (MGDG/DGDG/SQDG/POPG/DOPC, 35:20:15:5:25, see **Chapter 4**). Some of these lipids exhibit rather unique properties, for example the non-bilayer forming nature of MGDG (see **Chapter 1.2.4**).[67,73,74] Hence their influence and importance for the formation of LCPA-induced membrane stacks was studied systematically.

Importance of Glycolipids

In order to probe if one of the three glycolipids, incorporated into the commonly used lipid mixture, was essential for stack formation, lipid mixtures omitting one of these lipid types per experiment were deployed, while the ratios of the residual lipids was adjusted accordingly. In addition, a lipid mixture containing no glycolipids at all was used as a reference. An overview on the lipid mixtures is given in **Table 6.1**.

Table 6.1. Overview on lipid mixtures employed to evaluate the need for glycolipids to enable LCPA-induced membrane stacking. A–D refer to the fluorescence micrographs shown in Figure 6.15 while Std. is the lipid mixture used in most of the previous experiments.

	Molar lipid ratios					
	MGDG	**DGDG**	**SQDG**	**POPG**	**DOPC**	**TexasRed-DHPE**
A	-	20	15	5	59.5	0.5
B	34.5	-	15	5	45	0.5
C	34.5	20	-	20	25	0.5
D	-	-	-	20	79.5	0.5
Std.	34.5	20	15	5	25	0.5

Exemplary fluorescence micrographs of solid supported lipid bilayers on mica composed of the alternative lipid mixtures (see **Table 6.1**) after the addition of C3N13 (30 µM in sample buffer (see **Table 3.9**)) are shown in **Figure 6.15**.

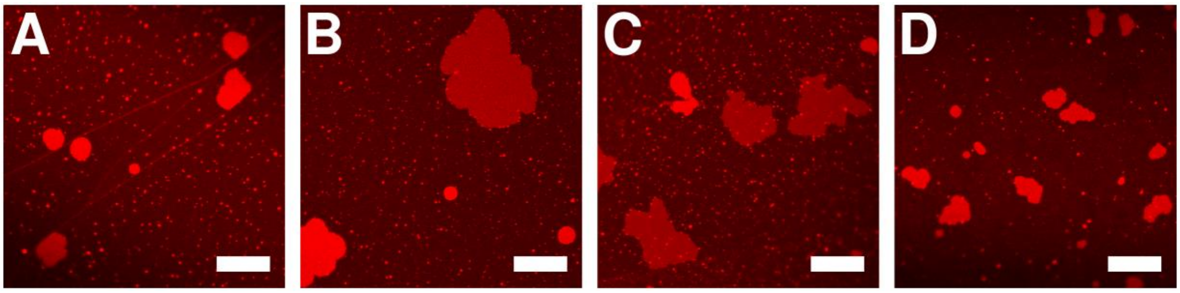

Figure 6.15. Exemplary fluorescence micrographs of membrane stacks formed after addition of C3N13 (30 µM in sample buffer (see Table 3.9)) to solid supported lipid bilayers on mica omitting one or all of the three glycolipids MGDG, DGDG and SQDG. Detailed lipid compositions are denoted in Table 6.1. Scale bars: 20 µm.

On all samples the formation of LCPA-induced membrane stacks was observed. This observation proved that none of the glycolipids MGDG, DGDG or SQDG is essential for stack formation. Additional observation of membrane stacks on POPG/DOPC membranes even provided evidence that no glycolipids are needed at all. Differences in size and number of the membrane stacks were later traced back to varying amounts of SUVs in solution as their necessity was not yet revealed at the time of the experiments.

Effect of Membrane Charge

Even if no need for glycolipids was proven by the previous experiments, a common feature of all employed lipid mixtures was their relatively high content of negatively charged lipids (20 mol%). To evaluate the role of membrane charge reference experiments were performed on neutral solid supported lipid bilayers.

Pure DOPC membranes (doped with 0.5 mol% lipid-bound dye) were chosen as a model to prepare neutral charged solid supported lipid bilayers on mica. Spreading of pure DOPC SUVs required some changes in the preparation protocol (see also **Chapter 3.3.4.2**): Vesicles were added in NaCl-containing buffer (50 mM NaCl, 20 mM Na-citrate, 0.1 mM EDTA, 0.1 mM NaN_3, pH 4.8 (HCl)) because application in the standard spreading buffer (see **Table 3.9**) only lead to adhesion of SUVs without spreading into a continuous lipid bilayer (validation of membrane preparation were performed by fluorescence microscopy and FRAP). Additionally the SUV concentration was reduced to 0.15 $mg \cdot mL^{-1}$ since huge amounts of SUVs stuck to the membrane surface and could hardly be removed by intensive rinsing with sample buffer (see **Table 3.9**). Since both conditions mark only minor changes to the previously employed protocol and measurements were performed after intensive rinsing with sample buffer no interference or incomparability should appear and the final bilayers are expected to be the same.

In contrast to experiments with charged lipid bilayers, the formation of multilayered structures was observed on neural membranes after vesicle spreading even in absence of LCPA. **Figure 6.16 A** shows an exemplary fluorescence micrograph of a DOPC lipid bilayer on mica, where the formation of stack-like multilayered structures was observed.

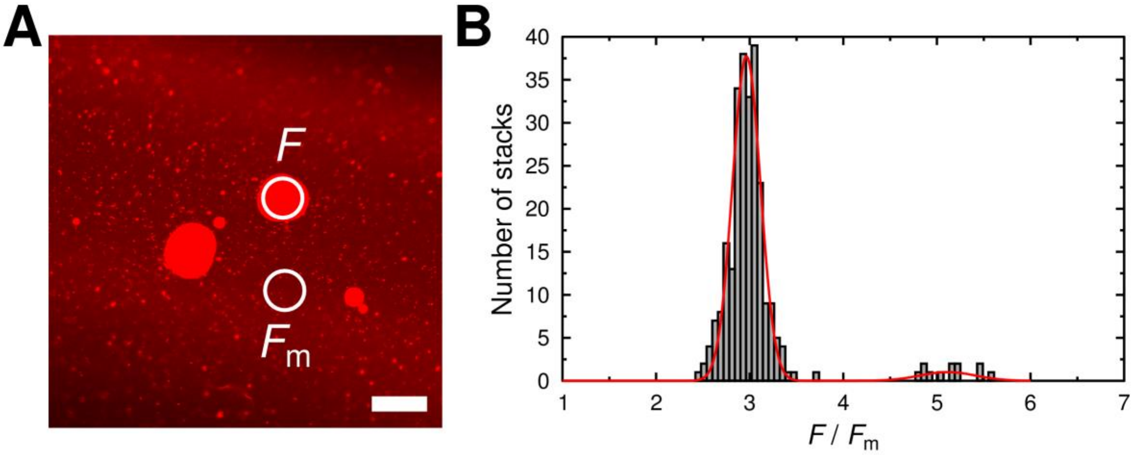

Figure 6.16. Exemplary fluorescent micrograph of stack-like structures formed on a DOPC solid supported lipid bilayer (DOPC/TexasRed-DHPE, 99.5:0.5) in absence of LCPA (A). Fluorescence intensities *F* of 260 structures were read out, compared to the fluorescence intensity of the surrounding lipid bilayer F_m and plotted in a histogram (B). 95% of the stack-like structures had a fluorescence intensity of 3.0±0.2 times the intensity of their surroundings. No structures with twice the fluorescence intensity were observed. Scale bar: 20 µm.

Analysis of fluorescence intensities of these structures (see **Figure 6.16 B**; 260 structures, 28 images) showed remarkable deviations from data on membrane stacks formed on negatively charged lipid membranes after addition of LCPA (see **Figure 6.5**). About 80% of the LCPA-induced stacks had a fluorescence intensity roughly doubled compared to the surrounding lipid bilayer. A smaller fraction of about 20% showed a tripled fluorescence intensity within the stacked region (see **Chapter 6.3.2**). In contrast, the LCPA-independent structures formed on pure DOPC nearly exclusively showed tripled fluorescence intensities F compared to their surrounding F_m (F/F_m = 3.0±0.2 (95%)) with only very few brighter structures but no stack-like aggregates with doubled fluorescence intensity at all. Another difference was the presence of a brighter halo around the structures indicating a higher amount of lipids at the border region. Those observations demonstrated one of the fundamental differences compared to the membrane stacks formed by LCPA. Further differences were revealed by FRAP experiments as shown in **Figure 6.17**.

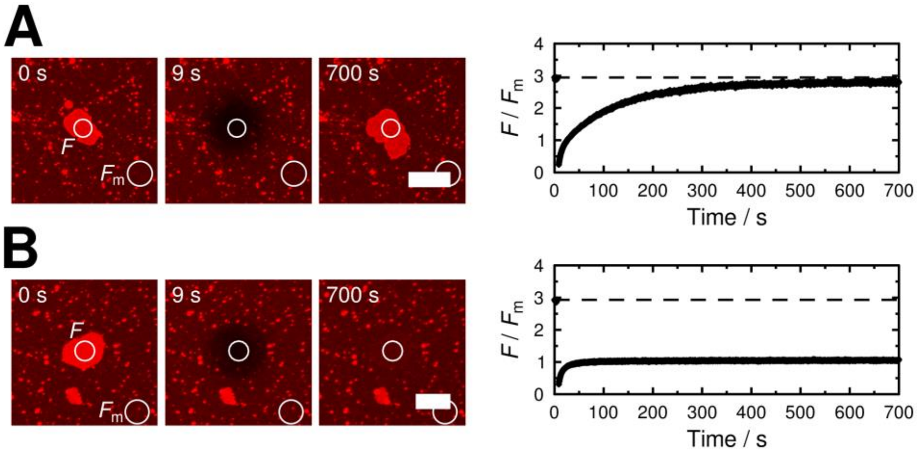

Figure 6.17. Exemplary FRAP data on stack-like structures formed on DOPC lipid bilayers (DOPC/TexasRed-DHPE, 99.5:0.5) on mica in absence of LCPA. Two populations of structures were observed: one showing full fluorescence recovery (A) and one showing no fluorescence recovery beyond the intensity of the surrounding lipid bilayer (B). The shown data was measured in sample buffer (see Table 3.9) after spreading of SUVs in calcium-containing buffer (1 mM $CaCl_2$, 100 mM NaCl, 20 mM TRIS, pH 7.4). Scale bars: 10 µm.

For LCPA-induced membrane stacks a connection of the stacked lipid bilayers to the underlying one was proven by FRAP and the exchange of lipid material allowing for full fluorescence recovery after bleaching of a whole membrane stack (see **Figure 6.8**). The fluorescence recovery behavior of stack-like structures formed in absence of LCPA on pure DOPC membranes showed different and inconsistent behavior. Both full fluorescence recovery of the structures as well as only recovery up to the fluorescence intensity level of the surrounding lipid bilayer were observed. Hence two, otherwise undistinguishable populations of aggregates were formed. One population still connected to the underlying membrane (see **Figure 6.17 A**) and another one secluded from the solid supported membrane (see **Figure 6.17 B**).

To avoid mix-ups of these LCPA-independent aggregates with structures formed by LCPA an experimental set-up inspired by the one for the study of lipid intake from solution (see **Chapter 6.4.1**) was chosen. After extensive rinsing of the membrane surface LCPA (C3N13, 30 µM in sample buffer (see **Table 3.9**)) were added alongside TexasRed-DHPE-labeled SUVs (DOPC/TexasRed-DHPE, 99:1; 4 µg·mL^{-1}) to a Bodipy-C_{12}HPC- or Atto488-DHPE-labeled solid supported bilayer (DOPC/dye, 99.5:0.5). This experiment allowed to probe the intake of lipid material from solution to form membrane stacks on top of the solid supported membrane's surface. Exemplary fluorescence micrographs after LCPA and SUV addition are shown in **Figure 6.18**.

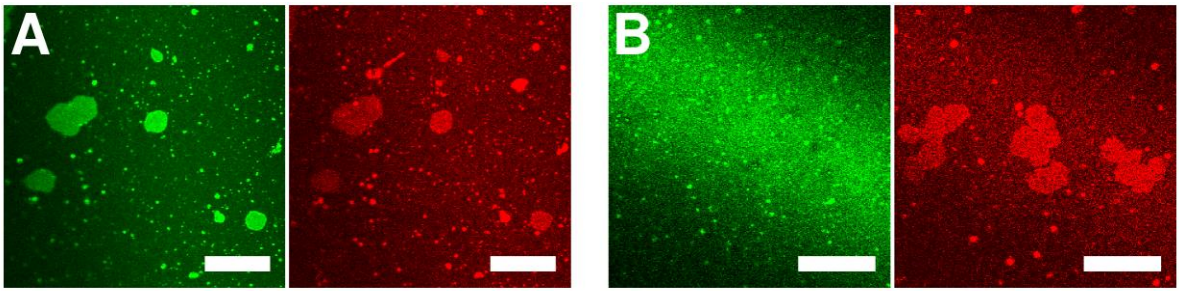

Figure 6.18. Exemplary fluorescence micrographs recorded after the addition of C3N13 (30 µM in sample buffer (see Table 3.9)) and TexasRed-DHPE-labeled SUVs (DOPC/ TexasRed-DHPE, 99:1, 4 µg·mL^{-1}) to solid supported DOPC lipid bilayers on mica doped with 0.5 mol% Bodipy-C$_{12}$HPC (A) or Atto488-DHPE (B). Scale bars: 20 µm.

Similar to previous experiments on negatively charged lipid bilayers (see **Figure 6.13**) the formation of membrane stacks from lipid material added with the TexasRed-DHPE-containing SUVs was observed and proven as the red dye was detected in the membrane stacks. In case of Bodipy-C$_{12}$HPC-labeling, mixing of both dyes was observed while Atto488-DHPE diffusion into the additional lipid layers was not yet observable. In conclusion, stack formation was also observed on neutral lipid membranes.

6.4.3 Influence of Polyamine Chain Length

All previous experiments were carried out with the synthetic LCPA C3N13 which had a molar mass of M = 702 g·mol^{-1} and was therefore suitable as a good model compound for LCPA found in diatom biosilica.[37,97] While no data on the interaction between LCPA with similar molecular mass and lipid membranes was available, influences of shorter polyamines[279–284] or very large PEI[285] on lipid membranes had been discussed in literature, but none of these studies reported the formation of membrane stacks induced by the addition of polyamines. Hence the influence of the polyamine chain length was studied systematically, too.

Synthetic polyamines with molecular masses M ranging from 188 g·mol^{-1} (C3N4) to 988 g·mol^{-1} (C3N18, see **Table 3.1**) were used as well as the two commercially available short polyamines spermidine and spermine (see **Table 3.2**). All polyamines were added in a standardized concentration of c_N = 30 µM (in sample buffer (see **Table 3.9**)), which provided equal amounts of amine functions, to solid supported lipid bilayers on mica (MGDG/DGDG/SQDG/ POPG/DOPC/TexasRed-DHPE, 34.5:20:15:5:25:0.5). Besides polyamines SUVs were added to the samples (4 µg·mL^{-1}, lipid composition identical) to circumvent influences of varying amounts of SUVs remaining after rinsing of the

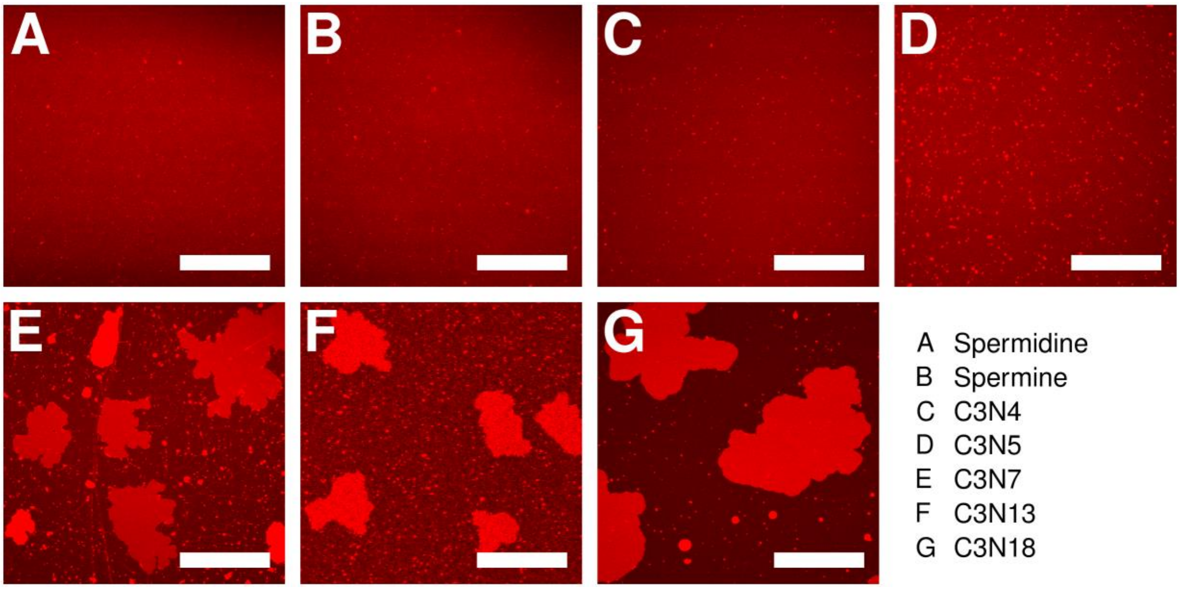

Figure 6.19. Exemplary fluorescence micrographs after the addition of different polyamines (c_N = 30 µM, in sample buffer (see Table 3.9)) and SUVs (4 µg·mL^{-1}; MGDG/DGDG/SQDG/POPG/DOPC/TexasRed-DHPE, 34.5:20:15:5:25:0.5) to solid supported lipid bilayers on mica (lipid composition identical to SUVs). Membrane stack formation was only observed for polyamines with more than five amine groups. Scale bars: 50 µm.

membranes. Exemplary fluorescence micrographs after polyamine application and incubation for 2 h are shown in **Figure 6.19**.

After addition of the shorter polyamines spermidine, spermine, C3N4 and C3N5 no visible changes in membrane structure were observable by fluorescence microscopy (see **Figure 6.19 A–D**). In contrast, the addition of C3N7, C3N13 and C3N18 led to the formation of membrane stacks on the bilayer surface (see **Figure 6.19 E–G**).

In conclusion, a critical polyamine chain length containing more than five amine groups was identified to be required for the formation of membrane stacks.

6.5 Silica Precipitation on Membrane Surfaces

During the *in vivo* formation of the diatom cell wall LCPA become entrapped within the biosilica.[37] *In vitro* studies supported their postulated role in catalysis of silicic acid polymerization, as aggregates of LCPA trigger the precipitation of silica under ambient conditions.[43] Even though silica precipitation of LCPA adsorbed onto membrane surfaces was not yet investigated, BERNECKER *et al.* introduced a model system wherein different amine containing headgroups were added to synthetic lipids with alkyl chains.[100] Preparation of solid supported membranes containing these lipids enabled the study of silica precipitation on the surface by means of ellipsometry or atomic force microscopy.

In this study the effect of the polyamine C3N13 adsorbed on a membrane-covered surface (MGDG/DGDG/SQDG/POPG/DOPC, 35:20:15:5:25; see **Chapter 6.1**) on silica deposition was studied by RIfS. Measurements were performed by VANESSA REUSCHE as part of a Bachelor project (*Wechselwirkungsstudien über Silika-präzipitierende Biomoleküle und Lipidmembranen mittels reflektometrischer Interferenzspektroskopie*, WS2014/15) under the author's supervision. Reference measurements were also performed by KRISTINA BREITHAUPT as part of her Bachelor project (*Fluoreszenzmarkierung von Silika*, SS2015). An exemplary kinetic measurement on the addition of silicic acid to a membrane-covered surface with adsorbed C3N13 (30 µM) is shown in **Figure 6.20 A**.

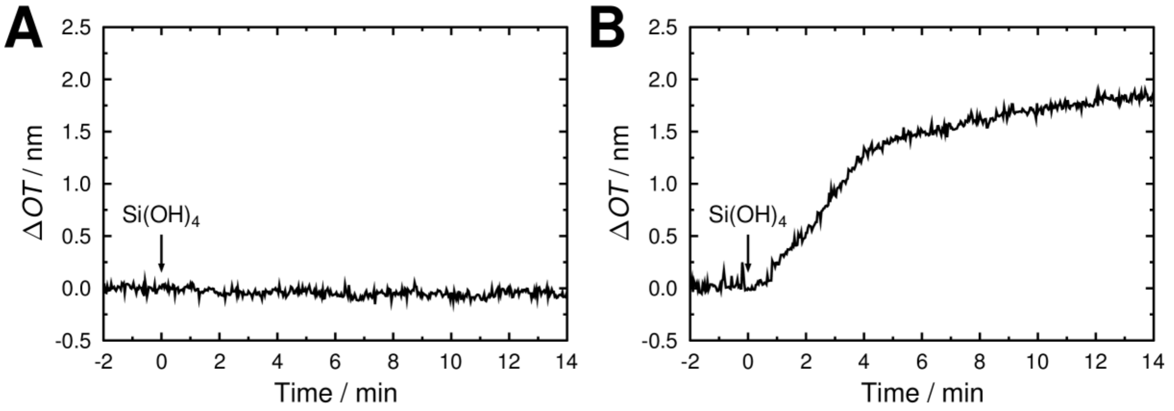

Figure 6.20. Exemplary kinetic data on the addition of silicic acid ($Si(OH)_4$; 100 mM in 50 mM KCl, 40 mM NaOAc, 0.1 mM EDTA, 0.1 mM NaN_3, pH 5.5 (HOAc)) to a membrane-coated surface (MGDG/DGDG/SQDG/POPG/DOPC, 35:20:15:5:25) after adsorption of C3N13 (30 µM, A) and a reference measurement on a pure DOPC membrane (prepared in spreading buffer (see Table 3.9)) in absence of LCPA (B).

After addition of freshly prepared silicic acid (100 mM in 50 mM KCl, 40 mM NaOAc, 0.1 mM EDTA, 0.1 mM NaN_3, pH 5.5 (HOAc)) to the LCPA-coated membranes no significant change in optical thickness *OT* was observed. In order to elucidate the effect of silica formation on the measured optical thickness, a control experiment was performed on a pure DOPC membrane without LCPA (see **Figure 6.20 B**). The choline headgroup showed a catalyzing effect on silicic acid polycondensation as the formation of a silica layer on the surface was observed by an increase in optical thickness of about $\Delta OT = (1.4\pm0.1)$ nm ($n = 2$) within 2–4 min, followed by a slower increase probably due to the growth of the silica layer not directly influenced by the lipid headgroups. For silica layers directly deposited on membrane surfaces a refractive index of $n_2 = 1.409$ was used to calculate the physical thickness.[289] The first silica layer directly catalyzed by the DOPC headgroup had a physical thickness of approximately $d = (1.0\pm0.1)$ nm.

The reference measurement demonstrated that in principle the deposition of a silica layer could be monitored by RIfS but in case of experiments with C3N13 adhered to a membrane-covered surface no significant amount of silica was formed after silicic acid addition. Hence it was demonstrated that LCPA lose their silica precipitating activity once adsorbed onto a membrane surface.

6.6 Discussion

On their journey to unravel the processes in which diatoms form their fine patterned and for each species individual cell wall, scientists reveal a variety of different biomolecules possibly being part of the cell's "tool box" for biomineralization.[8,14] Left in the biosilica, amongst others LCPA were isolated and characterized.[37] Their influence on silica deposition was mainly demonstrated by precipitation experiments in solution which revealed a catalyzing effect of LCPA on silicic acid polycondensation[37] as well as form-giving factor by the length-dependent aggregation of the molecules.[43] LCPA are therefore regarded as a crucial part of the organic matrix in the SDV, which controls cell wall morphogenesis.[14]

Enclosing the organelle, the silicalemma provides a confined compartment in which silicic acid polycondensation takes place *in vivo*.[18,19] But its role might exceed a simple barrier function. Interactions between biomolecules and the silicalemma might also alter the structure of the organic matrix and therefore of the resulting cell wall fragments by influencing the self-aggregation of biomolecules in the organelle. In this study for the first time the interaction between LCPA of a molecular length scale also found in diatoms and solid supported model membranes mimicking the silicalemma (see **Chapter 4**) were investigated *in vitro*.

LCPA used in this study were synthesized and provided by the group of PROF. DR. ARMIN GEYER.[43,98,99] With a molar mass of $M = 702\ \text{g}\cdot\text{mol}^{-1}$ the LCPA C3N13 (see **Figure 3.9**) was used as model component for the great majority of all experiments. Its mass fit in the range for polyamines isolated from diatom biosilica ($M = 600\text{–}1500\ \text{g}\cdot\text{mol}^{-1}$).[37,97] On the other hand solid supported lipid bilayers were employed that mimic the overall lipid composition of diatoms (for the most part MGDG/DGDG/SQDG/POPG/DOPC, 35:20:15:5:25, see **Chapter 4**).[66] To complete the model system and to make it as physiological as possible, regarding the current knowledge about the SDV, all measurements were performed under acidic conditions (50 mM KCl, 40 mM NaOAc, pH 5.5 (HOAc)) as reported for the inside of the organelle.[22]

Investigation of LCPA-membrane-interactions started by monitoring biomolecule adsorption via RIfS. The research was later intensified by imaging LCPA-induced processes at the membrane surface by means of fluorescence and atomic force microscopy. In the end also the deposition of silica on LCPA-coated membranes was investigated.

6.6.1 LCPA Adsorption and Fluorescence Imaging

Isotherms for the adsorption of C3N13 on membrane-coated surfaces were recorded by RIfS (see **Chapter 6.1**). An increase in optical thickness after LCPA addition proved the deposition of a LCPA layer on top of the membrane surface. While saturating at concentrations above $c_N = 30\ \mu\text{M}$ a maximal change in optical thickness of $\Delta OT = (1.4 \pm 0.1)$ nm was detected. Similar to thin PEI layers deposited onto silicon oxide and silicon oxynitride surfaces a refractive index of $n_2 = 1.43$ was approximated.[286] With this information the physical thickness of the LCPA layer was determined to be $d = (0.9 \pm 0.1)$ nm. While all of this data was measured in acetate-buffered solutions, LCPA addition in phosphate-containing buffer did not result in uniformly biomolecule adsorption as described for example in the model by LANGMUIR.[141] Previous studies revealed an aggregation of LCPA in presence of phosphate ions[43] that are apparently adsorbed less efficiently on membrane surfaces.

The nature of interactions between LCPA and solid supported lipid bilayers used in this study might, at first glance, mainly be of electrostatic nature. Incorporating in total 20 mol% of SQDG and POPG, the lipid bilayers carried a negative surface charge even at the chosen acidic pH of 5.5. On the other hand the acidic conditions resulted in partial protonation of amine functions in the C3N13 molecule.[43] For smaller polyamines, such as spermidine, interactions with other negatively charged biomacromolecules, for example nucleic acids, had been reported.[290–292] A detailed review on the interactions of these polyamines with membranes and membrane components is given by SCHUBER.[279] Besides undirected electrostatic interactions, LCPA as well as lipid headgroups are capable of hydrogen bonding. Investigating the protection of phospholipids by polyamines like spermine from peroxidation, TADOLINI reported a direct interaction of polyamines with phosphate groups of the lipid headgroups.[293] Similar interactions of LCPA and inorganic phosphate were also intensively studied in solution by BERNECKER *et al.*[43] The lipid mixture employed for the most part of this study contained 30 mol% of phospholipids that allowed direct binding of LCPA to phosphocholine (PC) or phosphoglycerol headgroups. On the other hand the remaining 70 mol% of glycolipids are also known to interact via hydrogen bond networks.[249] Since most of the previous studies focused on interactions of smaller polyamines with lipid membranes, changes in physical properties while going to longer chain length and their influence on membrane interactions had not been addressed. Skipping the intermediate length region in which LCPA from diatoms are located, information is only available again for very large PEI. HONG *et al.* investigated for example the effect of PEI with a molar mass above 1500 $g \cdot mol^{-1}$ on solid supported lipid bilayers and observed the formation of holes in the supported membrane.[285] Elongation of the polyamine chain length does not only incorporate more amine functions but also increases the hydrophobicity of the molecule.[43]

In order to reveal changes induced by the addition of LCPA on solid supported lipid bilayers, structural changes of the membrane during polyamine addition were monitored by fluorescence microscopy (see **Chapter 6.2**). Within a few minutes after addition of C3N13 formation of domains with brighter fluorescence of the lipid-bound dye incorporated into the solid supported membrane was observed (see **Figure 6.2**). Domains were rather large with final areas of several hundred square micrometers. This observation clearly indicated a change in membrane structure, induced by LCPA, which led to the uneven dye distribution. While growth of the domains was typically finished within a few minutes also time-series were recorded that showed much faster formation of these structures within a few seconds. Later research revealed an additional requirement for domain formation (see **Chapter 6.4.1**) that explained these different observations. Lipid material had to be acquired from solution, thus growth was influenced by the amount of vesicles remaining in solution during LCPA addition.

Regarding the structure of the formed domains and the role or incorporation of LCPA into it, no information was available in literature for polyamines with comparable chain length. The data also showed no similarity to the hole-forming effect of PEI[285] but might be related to the effect of shorter polyamines on lipid bilayers that could lead to clustering or phase separation.[279] Numerous studies showed that structural changes in lipid membranes (*e.g.* phase separation) can lead to uneven distributions of lipid-bound dye molecules in lipid membranes observable by fluorescence microscopy.[287] Interestingly the formed structures were larger than typically expected for domains formed by phase separation within lipid bilayers[294,295] and might include some kind of supramolecular assembly involving the LCPA. To shed light on these processes a number of different experiments were carried out which all contributed step by step to the final identification of the LCPA-induced structures. Those experiments will be discussed in the following chapters in more detail.

6.6.2 Characterization of Membrane Stacks

Characterization of domains formed after addition of LCPA was started with the investigation of the localization of LCPA on the membrane surface. Since polyamine addition triggered the process, a direct correlation between LCPA adsorption and domain formation was postulated. Application of FITC-C3N13, a fluorescein-labeled derivative of C3N13 (see **Figure 3.11**), provided insight into the distribution of polyamines on the membrane surface (see **Chapter 6.3.1**). Additional fluorescent labelling of the membrane revealed domain formation even with this compound, thus disturbance by the label on the polyamine was ruled out. The fluorescence micrographs showed FITC-C3N13 fluorescence all over the substrate, indicating coverage of the surface with polyamines, as well as 2.3±0.2 times higher local fluorescence intensities which perfectly correlated with the location of the domains with brighter membrane fluorescence. Hence an accumulation of polyamines in this regions was concluded which most likely resulted in the formation of the membrane domains in the first place. This observation was still in good agreement with the postulation that LCPA alter the membrane properties leading to lipid clustering or phase separation.[279]

The other fundamental question regarding the LCPA-induced domains was about their actual structure and how lipids were arranged in these regions. First information was gathered by analysis of fluorescence intensities of lipid-bound dyes in different regions on the membrane surface (see **Chapter 6.3.2**). Systematic comparison of fluorescence intensities inside the brighter domains and their surroundings revealed even multiples of signal intensities. Local dye fluorescence was either doubled (F/F_m = 2.1±0.2) or tripled (F/F_m = 3.1±0.4) compared to the surrounding lipid bilayer (see **Figure 6.5**). Observation of these discrete levels pointed towards the formation of well-defined structures after LCPA addition. Since fluorescence intensities were multiples of the intensity of one labeled lipid bilayer, this observation pointed to the formation of structures that incorporated one or two additional lipid bilayers. Such membrane aggregates would on the other hand have a huge influence on the topography of the sample. Phase separation normally also results in changes in membrane thickness but height differences between different phases were normally only about 0.5–1.0 nm.[288] The addition of lipid bilayers on the other hand would at least result in height increases of about the thickness of a lipid bilayer which was prior determined to be about 4 nm (see **Figure 4.16**). Hence the postulation of such a structure should be verifiable by AFM.

The surface of a solid supported lipid bilayer after addition of C3N13 was investigated by correlative fluorescence and atomic force microscopy (see **Chapter 6.3.3**). A clear co-localization between the domains with higher fluorescence of the membrane-bound dye and higher structures, identified in the topography map measured by AFM, was observed (see **Figure 6.6**). The structures turned out to be very fragile and were partially destroyed during AFM measurements. Hence not only imaging was challenging but also determination of absolute heights from the topography maps turned out to be rather complicated and defective due to simultaneous disintegration of the structures. Despite this flaw height differences of about 8 nm or 15 nm compared to the surrounding lipid bilayer were observed. The lower structure corresponded to a membrane domain with doubled fluorescence intensity while the higher one showed tripled intensity in the fluorescence micrograph. A set of different models was developed to describe and discuss the observations and to evaluate the accuracy of each model (see **Figure 6.21**).

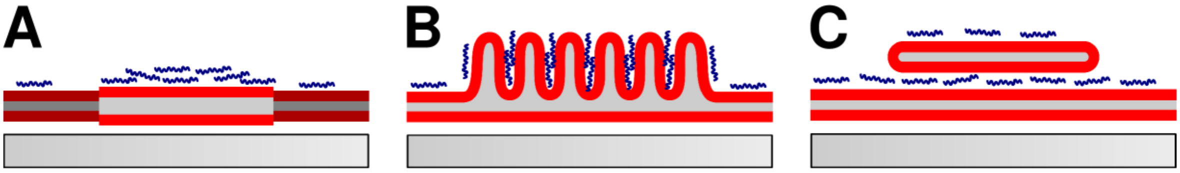

Figure 6.21. Three proposed models describing the structure of the domains formed after addition of LCPA to solid supported membranes. The observation of increased local fluorescence of lipid-bound dyes (red), accumulation of LCPA (blue) as well as elevated domain heights could be explained by LCPA-induced phase separation within the membrane (A), growth and clustering of protrusions (B) or formation of membrane stacks (C).

Figure 6.21 A depicts a lipid bilayer with lateral phase separation. Demixing of lipids would result in an uneven distribution of lipid-bound dye molecules if they fit better or worse in either one of the two phases.[287] Quantization of fluorescence intensities would however rather be unlikely or accidentally. Regarding height differences between different domains, lateral phase separation would most likely result in an elevation of the thickness of the lipid bilayer domains of about 0.5–1.0 nm, as it was also observed for solid supported lipid bilayers with separated liquid ordered and disordered domains.[288] Even an additional layer of accumulated LCPA should not increase the height difference up to the observed level. In conclusion, an exclusive LCPA-induced phase separation within the lipid bilayer was disproved by the experimental data.

A different model to explain the observations made so far is presented in **Figure 6.21 B**. Herein the formation of larger 3D structures was taken into account as protrusions of the underlying lipid bilayer were elongated and stabilized by LCPA. In principle such a structure would allow rather high domains with both increased local fluorescence of the labeled membrane and polyamines but the development of discrete levels would rather be unlikely and even the uniform fluorescence and height within one domain would presumably not have been detected. Overall, this model did not fit the observations.

A third model also describing larger 3D structures is shown in **Figure 6.21 C**. It postulates the formation of additional lipid bilayers on top of an underlying one. This model takes the discrete levels of fluorescence intensities into account, which were either doubled or tripled compared to the surrounding membrane (see **Figure 6.5**) and therefore already indicated the presence of additional lipid bilayers. Height differences between these membrane stacks and their surrounding would at least be of the thickness of a lipid bilayer, which was determined to be around 4 nm (see **Figure 4.16**), plus an additional water and/or LCPA layer in between with a thickness of at least 0.5–1.5 nm.[296,297] Overall, the observed height differences were in good agreement with this model and could be explained by the presence of either one or two additional lipid bilayers and linking layers of about 3–4 nm between each pair of stacked membranes.

The assumption of the formation of membrane stacks was corroborated by data from force spectroscopy (see **Chapter 6.3.3**). FDC on a lipid bilayer covered with domains formed after C3N13-addition showed up to three breakthrough events through presumably lipid bilayers (see **Figure 6.7**). This observation was in very good agreement with the postulation of multilayered membrane structures. Depths of the breakthroughs of (4±1) nm, (8±2) nm and ~12 nm were also extracted from the FDC. These depths correspond very well to the thicknesses of one, two or three lipid bilayers (see **Figure 4.16**). Compared to data extracted from the topography maps these heights are significantly smaller but this might be attributed to a general tendency to underestimate depths determined by FDC and the very softness of the surface-covering and membrane-linking LCPA layers.

In conclusion, the model presented in **Figure 6.21 C** was corroborated and confirmed by several techniques and was therefore regarded as the best description of the LCPA-induced domain's structure. For this reason the domains are denoted *membrane stacks* in the ongoing discussion.

Similar stack structures are found *in vivo* for example in the thylakoid membrane housing the majority of the protein machinery for photosynthesis.[298,299] Even if lipid compositions of both the thylakoid membrane[300] and the employed model membranes (see **Table 3.8**) were very close, the properties of the thylakoid membrane are mainly determined by its high content of transmembrane proteins making both systems hard to compare.[301] *In vitro* similar structures were formed for example after thermal annealing of supported lipid bilayers.[302] Alternatively they could be observed as 3D protein-lipid aggregates after addition of surfactant protein B to lipid monolayers[303] or by linkage of several lipid bilayers by polyethylene glycol-linkers.[304,305] Just recently HEATH *et al.* reported the formation of interconnected membrane multilayers after addition of poly-L-lysine to supported lipid bilayers.[306] With focus on biomolecule-induced morphology changes TRUSOVA *et al.* investigated the influence of lysozyme on lipid bilayers composed of phosphatidylcholine and cardiolipin.[307] They also observed the formation of structures with quantized fluorescence intensity of lipid-bound dyes after protein addition. Another outstanding example for an investigation of membrane stacks formed on solid supported lipid bilayers is the work by ADAMS *et al*.[308] In their publication amongst others the formation of lipid multilayers after the addition of lipopolysaccharide and calcium ions was investigated by fluorescence microscopy. They also concluded the formation of membrane (multi-)stacks from fluorescence micrographs showing domains with discrete intensity levels. Unfortunately ADAMS *et al.* faced similar problems trying to image membrane multilayers by AFM. The instability of these structures did not allow them to successfully measure the topography of the structures.

Regarding the influence of LCPA, the accumulation of polyamines in the region of the membrane stacks was previously described and partially discussed since approximately doubled fluorescence intensity of the labeled LCPA FITC-C3N13 was observed in these regions (see **Figure 6.4**). Only a few structures with brighter FITC-C3N13 fluorescence were observed in the small sample showing 62 stacks in total. The accumulation of LCPA could be caused by an inclusion of LCPA in between stacked lipid bilayers. Positively charged polyamines are able to shield otherwise repulsive electrostatic interactions between negatively charged lipid bilayers and even provide direct linkage between different layers. Smaller polyamines were already known to fulfill similar functions for example by bridging nucleic acids[309] or as they strengthen lipid vesicle aggregation.[281–284] Experience with the bridging of lipid bilayers by polycationic, linear molecules was also reported for example by HEATH *et al*.[306,310] They used poly-L-lysine as spacer molecules for the stepwise deposition of lipid multilayers by vesicle spreading. At this point it was postulated that LCPA fulfill a similar function during the herein described process of membrane stack formation. Adsorption of LCPA on the surface could have provided a surface on which a second lipid bilayer was formed and stabilized.

After identification of the LCPA-induced domains as membrane stacks the next question was if these additional, stacked lipid bilayers were connected to the underlying membrane. A connection would allow lipid diffusion for one layer into the other. A common tool to investigate lipid diffusion is the use of FRAP.[188] After bleaching of lipid-bound dye molecules in a certain area on the surface, the evolution of fluorescence intensity is monitored and eventually processed. If dye molecules are free to diffuse within the membrane, mixing of bleached and unbleached molecules occurs which leads to a regeneration of fluorescence intensity. The basic FRAP experiment was adapted for the investigation of membrane stacks. The bleached area was defined to include a whole membrane stack. After bleaching unbleached dye molecules needed for fluorescence recovery were only present in the surrounding, underlying lipid bilayer. Since the fluidity of the underlying membrane was proven in previous experiments (see **Chapter 4.3.2**), in a gedankenexperiment in general two different scenarios for fluorescence recovery would be expected which are shown in **Figure 6.22**.

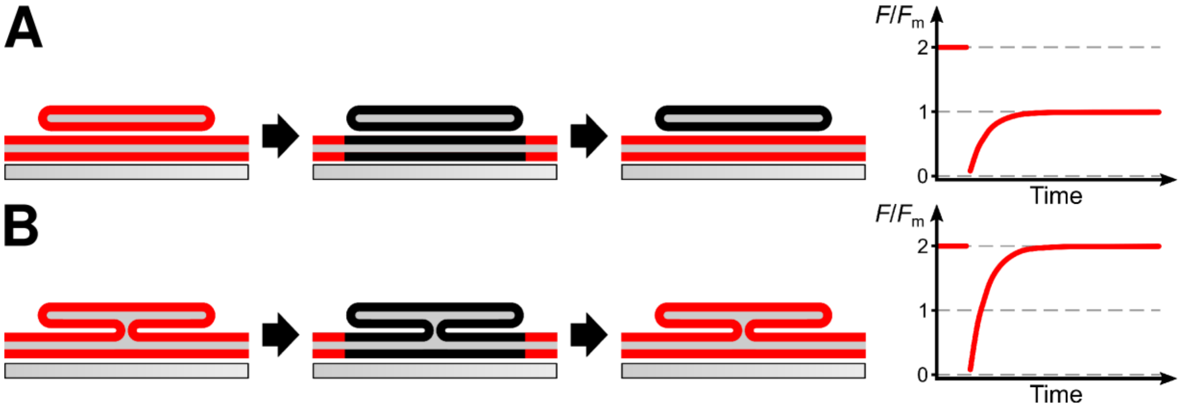

Figure 6.22. Two different scenarios for a FRAP experiment on membrane stacks. If both layers were not connected, fluorescence recovery would only be observed for the underlying membrane (A). In contrast, if a connection between both layers enabled exchange of lipid-bound dye molecules, full fluorescence recovery would be observed (B).

In a first scenario, shown in **Figure 6.22 A**, no connection was formed between the underlying and the stacked lipid bilayer. After bleaching unbleached dye molecules could only diffuse into the bleached part of the underlying membrane. This would lead to fluorescence recovery up to the intensity level observed for the surrounding, single lipid bilayer ($F/F_m(t \rightarrow \infty) = 1$). No further recovery would be observed as the second layer was segregated from the underlying membrane. The second scenario, shown in **Figure 6.22 B**, included a connection between both membrane layers. After bleaching the diffusion of lipid-bound dye molecules leads to fluorescence recovery of all layers of the membrane stack and the initial fluorescence intensity ($F/F_m = 2$ or 3) would be regenerated. The speed of fluorescence recovery would in this case presumably be mainly influenced by the connectivity of the layers as it most likely acts as a bottle neck for lipid diffusion.

FRAP data recorded on membrane stacks with one or two additional lipid bilayers showed in both cases full fluorescence recovery within a few minutes (see **Chapter 6.3.4**). This observation proved the existence of at least one connection between the underlying and the stacked membranes, allowing lipids and lipid-bound dye molecules to diffuse between all layers. The high speed of fluorescence recovery was comparable to recovery rates from FRAP experiments on blank lipid bilayers (see **Chapter 4.3.2**) thus it is most likely that more than one central connection between the different layers existed.

Extraction of intensity profiles through a membrane stack during recovery (see **Figure 6.9**) revealed radii-dependent local fluorescence recovery. Starting from a GAUSSIAN function-like bleach profile followed by diffusion of dye molecules described by FICK's law[190] the intensity profile would constantly increase in a continuous radial symmetric way (see **Equation 3-32**) if FRAP experiments were performed on a homogeneous surface.[189] Translation of this profile into the 3D aggregate of the membrane stack could indicate hindrances of inter layer lipid diffusion. In the recorded data no significant deviations indicating for example transition of lipids only through a central bridge were identified. Remodeling and simulation of fluorescence recovery might have given additional prove but nevertheless the observation and especially the high speed of recovery provided strong evidence for the presence of multiple connections between all layers of the membrane stacks.

ADAMS *et al.* observed the formation of membrane stacks after the addition of lipopolysaccharide and calcium ions to solid supported DOPC bilayers.[308] In their study, FRAP experiments on whole membrane stacks were carried out as well. They also observed rapid recovery of the complete initial fluorescence intensity after bleaching of lipid-bound dyes in the structure. The time scale of recovery was comparable to experiments on blank lipid bilayers. Similar observations were also made just recently by HEATH *et al* who characterized membrane stacks formed after addition of poly-L-lysine to solid supported lipid bilayers.[306] Unfortunately direct comparison and quantification of fluorescence recovery is difficult as recovery time was influenced by the structure of the membrane stack. Stacks observed in this study and in the studies by ADAMS *et al.* and HEATH *et al.* varied in shape and size. Especially differences in non-symmetrical shape influenced the area ratio of stacks within a radial symmetrical bleach spot. Different ratios resulted in different "reservoirs", consisting of the additional lipid bilayers, to be filled with unbleached dye molecules. Hence even the normalized amount of dye molecules needed for full recovery varied and influenced for example measureable half-time values of recovery. For this reason FRAP experiments performed on membrane stacks were not processed quantitatively within this study. However full fluorescence recovery of membrane stacks reported by ADAMS *et al.* – even or especially since the biomolecules causing their formation differ drastically from LCPA – and by HEATH *et al.* marked a common trend for the formation of connections in tightly associated membrane stacks. Unfortunately although lipid multilayers had been used to study lateral lipid diffusion by FRAP since the 1970s[311] nearly no other data regarding inter layer diffusion of lipids in connected membrane stacks is available.

Hand in hand with the discussion of lipid exchange between different layers of the membrane stack occurred the question about the incorporation of the underlying, solid supported lipid bilayer into the membrane stack formed after LCPA addition. The formation of stacks took place on the surface of the solid supported membrane but since lipid diffusion between the stack and the underlying lipid bilayer was observed, a direct connection and incorporation of this underlying membrane into the stack must exist. **Figure 6.23** faces two different models for stacked lipid bilayers each incorporating parts of underlying membrane.

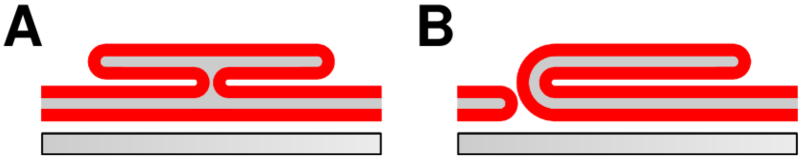

Figure 6.23. Two different models for membrane stacks formed and connected to a solid supported lipid bilayer. The connection between the layers could involve either one (A) or two (B) of the leaflets of the underlying membrane.

Figure 6.23 A shows a membrane stack wherein the connection between different layers is only formed by fusion of neighbored membrane leaflets. On the other hand **Figure 6.23 B** depicts one continuous lipid bilayer that is folded into a membrane stack. This structure is very similar to folded membrane parts formed at the border of spread giant unilamellar vesicles.[312] To distinguish between both scenarios experiments were carried out on solid supported lipid monolayers (see **Chapter 6.3.5**). These model membranes lacked the lower membrane leaflet present in supported lipid bilayers. If only the upper one was involved in stack formation, identical observations should be made on lipid monolayers after addition of LCPA. If a full underlying lipid bilayer was involved in the previous experiments, no formation of LCPA-induced membrane stacks should occur on lipid monolayers. Experimental data (see **Figure 6.10**) clearly showed the formation of membrane stacks even on monolayers thus a model as proposed in **Figure 6.23 B** was ruled out and a structure similar to the one shown in **Figure 6.23 A** was verified.

All information gathered so far about the structure of the LCPA-induced membrane stacks led to the development of the model presented in **Figure 6.24**.

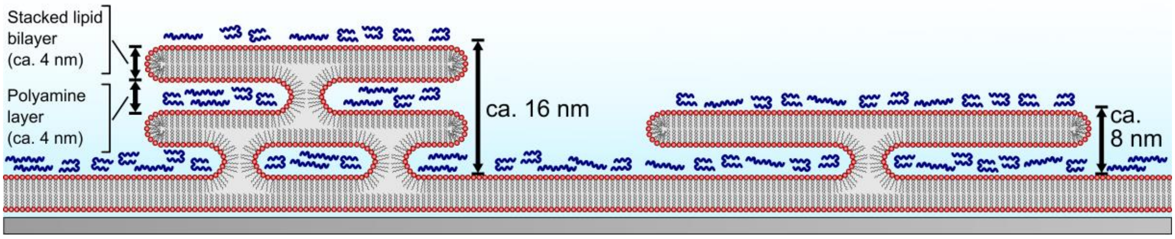

Figure 6.24. Developed model for the structure of membrane stacks formed after LCPA addition to solid supported membranes. Both stacks with one or two additional lipid bilayers were identified. LCPA (blue) covered the whole membrane surface and provided linkage between stacked bilayers. Additional connections between stack layers were detected but their exact number remained speculative. Most likely several connections were formed that enabled fast lipid exchange with the underlying membrane.

Multibilayer structures were formed after the addition of LCPA to solid supported lipid membranes. The LCPA were accumulated in the region of the membrane stacks as they became incorporated in between stacked lipid bilayers and provided linkage of the membranes. Between different layers the formation of connections was proven. Since these connections enabled fast lipid exchange the existence of multiple connections per stack was concluded.

6.6.3 Requirements for LCPA-Induced Membrane Stacking

Previous experiments helped to develop an understanding for the structural properties of membrane stacks formed after LCPA addition (see **Chapter 6.6.2**). In the end the model shown in **Figure 6.24** was introduced summarizing this information. However, requirements for the formation of membrane stacks were not discussed yet and will be the subject of the following chapter.

The triggering of stack formation by addition of the LCPA C3N13 was already demonstrated by time series of fluorescence micrographs recorded during polyamine addition (see **Figure 6.3**). Hence LCPA and their interaction with the supported membranes provided the basis for stack formation. Incorporation of LCPA into the membrane stacks was already discussed earlier (see **Chapter 6.6.2**). Besides LCPA accumulation other parameters might influence membrane stack formation.

Origin of Lipid Material

During growth, stacks reached sizes up to several hundred square micrometers (see **Figure 6.3**). Formation of such huge lipid aggregates required the mobilization of equally huge amounts of lipid material. The first question regarding the preconditions for stack formation was therefore the availability of this lipid material. Lipids had to be stored in some kind of pool from which they were drawn to be incorporated into the membrane stack. In general two different scenarios should be discussed: The use of an *internal lipid pool*, where lipids were moved from within the supported lipid bilayer into the stacks, or alternatively the utilization of an *external lipid pool*, where lipid material was absorbed from the membrane covering solution. These different scenarios, including two different possibilities for an internal lipid pool, are visualized in **Figure 6.25**.

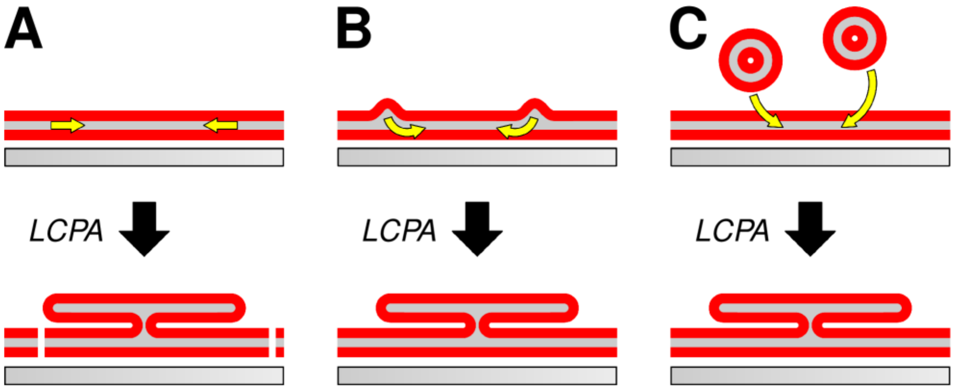

Figure 6.25. Schematic illustration of three different pools of lipids addressable for LCPA-induced membrane stack formation. Withdrawing lipids from the solid supported lipid bilayer would result in the formation of defects (A). On the other hand protrusions harbored high local concentrations of lipid material that might have been moved (B). Both scenarios marked internal lipid pools while lipid material left in buffer solution could act as an external lipid pool (C).

Depletion of lipid material from the supported lipid bilayer, as illustrated in **Figure 6.25 A**, would result in the formation of defects in the underlying membrane. These defects could grow up to a macroscopic size of several square micrometers that would easily have been observed during fluorescence imaging (see **Chapter 6.2**). Analysis of fluorescence micrographs before and after LCPA addition revealed no such macroscopic defects. On the other hand several microscopic defects could have been formed that were not resolved in the fluorescence micrographs. Nevertheless overall fluorescence intensity should be affected by the removal of lipids and lipid-bound dye molecules from the underlying membrane alongside the formation of defects. Changes in fluorescence intensity especially in the uncovered regions of the solid supported membrane were analyzed in **Chapter 6.4.1** (see **Figure 6.11**). No significant decrease in local fluorescence intensity was observed. In contrast even a slight increase was detected in this area. The measurement itself had some drawbacks as for example the lack of an internal reference that would enable precise analysis of intensity changes regardless of bleaching or focus drifts. Nevertheless the formation of defects in the underlying membrane was disproved as no significant decrease in fluorescence intensity was observed. The increase in intensity on the other hand could be caused for example by an actual increase in the amount of labeled lipid material on the membrane surface. Studies on smaller polyamines already demonstrated their ability to amplify the aggregation of vesicles.[281–284] Once adsorbed onto the solid supported membrane's surface LCPA could increase the adhesion and probably fusion of vesicles that remain in solution with the surface. Unfortunately this process was hardly resolved in the recorded time series. Even though no formation of macro- or microscopic defects in the underlying membrane was observed, lipids could nevertheless have been withdrawn from the solid supported lipid membrane to form the membrane stacks. Characterization of the solid supported membranes revealed numerous protrusions all over the surface (see **Chapter 4**). In these areas locally higher amounts of lipids were found. Transfer of those lipids into the membrane stacks would result in depletion of protrusions. Of course this depletion would also contribute to the overall fluorescence intensity in the uncovered parts of the supported membrane and would most likely result in a decrease in fluorescence intensity in this area. **Figure 6.11** already neglected this assumption but nevertheless a closer look on the fate of membrane protrusions during stack growth was taken in **Figure 6.12**. Differential fluorescence micrographs revealed changes in fluorescence intensity and number of protrusions during stack growth but no significant changes in both parameters were observed. Thus also the transition of lipid material from membrane protrusions into the LCPA-induced stacks was disproved.

A third model that might explain the origin of lipid material ending up in the membrane stacks postulated the utilization of an external lipid pool as visualized in **Figure 6.25 B**. Before LCPA addition the solid supported lipid membranes were prepared by spreading of SUVs (see **Chapter 4**). Even after several steps of rinsing some vesicles could have remained in the buffer solution. Polyamine coating could provide a surface on which vesicles adhere, as observed by MAJEWSKI *et al.*,[313] and eventually spread into continuous lipid bilayers, as it was demonstrated by WONG *et al.* for PEI coated quartz substrates.[314,315] Similar results were also reported for example for the function of poly-L-lysine during the stepwise deposition of lipid bilayer.[306,310] LCPA adhered to the membrane surface could therefore provide some kind of cushion on which those vesicles spread into continuous, stacked lipid bilayers. The adhesion force required for spreading could be provided by the strong interactions between polyamines and lipid membranes.[281–284] Answering this question required a more advanced experimental setup which allowed clear identification of lipid material taken up from solution and becoming embedded in the membrane stacks. This task was fulfilled by using two different lipid-bound fluorescent labels for both the solid supported membrane and the later added SUVs. The setup of the experiment is also visualized in **Figure 6.26**.

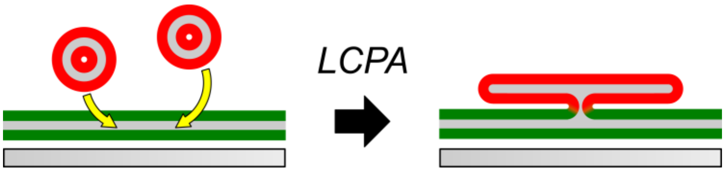

Figure 6.26. Schematic illustration of the experimental setup to detect an intake of lipid material from solution into the membrane stacks formed after LCPA addition. The solid supported lipid membrane was labeled with a green fluorescent dye. After intensive rinsing SUVs labeled with a red lipid-bound dye were added alongside LCPA. The fate of the lipid material from the SUVs was investigated by fluorescence microscopy.

The underlying, solid supported membrane was labeled with a green fluorescent dye. After intensive rinsing, lipid material was intentionally added to the buffer alongside LCPA. SUVs added to the solution carried a red fluorescent label that enabled exclusive excitation of the dye and localization of the lipid-bound dye molecules on the sample. Experiments were performed on both Bodipy-C_{12}HPC- and Atto488-DHPE-containing solid supported membranes (see **Figure 6.13**). After LCPA and SUV addition the formation of membrane stacks was observed in both cases. Using Bodipy-C_{12}HPC as a label for the underlying membrane a mixing of both dyes was observed. Stacks were detected by both Bodipy and TexasRed fluorescence. The previously demonstrated connectivity between all stacked membrane layers (see **Chapter 6.6.2**) allowed exchange of lipids between formed stacks and the underlying membrane and thus a mixing of both lipid-bound dyes as well. The incorporation of TexasRed also proved the use of lipid material from solution to form the membrane stacks. Looking only at the (nearly instantaneously reached) equilibrium state did not allow to conclude about the actual binding of SUVs onto the LCPA-coated membrane surface. Vesicles could either spread on top of the surface but also fuse with the solid supported membrane to provide additional lipid material through the underlying membrane to the growing stacks. Fortunately deviating results on Atto488-labeled solid supported membranes gave additional insight to answer this question. Using this alternative labeling no diffusion of Atto488-DHPE into the additional layers of the membrane stacks was observed. Membrane stacks were still clearly visible by TexasRed-DHPE fluorescence. This observation proved that SUVs from solution directly spread on top of the LCPA-covered underlying membrane rather than budding of the supported lipid bilayer. Differences between both systems could be explained by different diffusion coefficients of the two lipid-bound dye molecules in solid supported lipid bilayers (see **Figure 6.14**). Diffusion of

Atto488-DHPE was found to be significantly slower than diffusion of Bodipy-C_{12}HPC or TexasRed-DHPE within otherwise identically composed lipid bilayers. The diffusion coefficient calculated for lipid bilayers doped with TexasRed-DHPE was already discussed in **Chapter 4.4** and most of the mentioned aspects can also be related to Bodipy-C_{12}HPC-labeled membranes. The influence of the tracer on determined diffusion coefficients measured by fluorescence correlation spectroscopy was investigated by CHIANTIA *et al*.[316] One explanation for varying results was the difference in electrostatic interactions between the negatively charged mica support and the dye molecules. Similar effects were observed for free, charged dye molecules in proximity to glass surfaces, too.[317] In case of the study by CHIANTIA *et al.* either positively charged or neutral dyes were employed. Atto488-DHPE on the other hand carried a total of two negative charges (see **Figure 3.7**). TexasRed-DHPE (see **Figure 3.6**) contained one negative charge and Bodipy-C_{12}HPC (see **Figure 3.8**) is a neutral molecule. Linkage of the equally charged dye molecules and the surface might be possible for example by divalent cations but none of those should be present in the applied buffer solutions at higher concentrations. Influences of the lipid anchor and its incorporation into the lipid bilayer were excluded because both TexasRed and Atto488 were linked to DHPE molecules. Only the length of the linker region between the ethanolamine headgroup and the aromatic system of the fluorescent group was increased in Atto488-DHPE, distancing it further away from the headgroup region of the glycolipids containing sugar moieties. Even though the differences in lipid-bound dye diffusion were not studied in greater detail and could not fully be unraveled within this study, the effect of slowed down Atto488-DHPE diffusion was useful to answer another question regarding the binding of SUVs from solution onto the supported lipid bilayer. After stack formation full mixing of both lipid-bound dyes was not observed as Atto488-DHPE diffusion was too slow to reach a significantly increased level in the area of the membrane stacks to be detectable. In conclusion, the set of experiments proved the spreading of SUVs from solution on top of the LCPA-covered membrane surface which lead to the formation of membrane stacks. In the end this finding also demonstrated the importance of remaining lipid material in buffer solution. While in the first experiments this requirement was fulfilled by accident as rinsing of the surface turned out to be insufficient to remove all residual vesicles, better control of stack formation, surface coverage and reproducibility was achieved by subsequent addition of SUVs alongside the LCPA in the following experiments.

Stepwise fabrication of lipid multibilayers by alternating addition of vesicles and bilayer linking agents was also demonstrated for example by HEATH *et al*.[306,310] They used poly-L-lysine to cover the bilayer surfaces allowing further deposition of additional lipid bilayers. A study by ADAMS *et al.* – while using fundamentally different biomolecules – described the formation of membrane stacks, similar to those observed after LCPA addition, on solid supported lipid bilayers in presence of lipopolysaccharide and calcium ions.[308] They also concluded the deployment of surface associated vesicles to form membrane stacks on the surface.

Influence of Lipid Composition

The initial motivation for this study was the decipherment of interactions between LCPA and the silicalemma using *in vitro* model systems. Hence artificial model membranes were employed that – to the best of the current knowledge – remodel the lipid composition of the SDV membrane (see **Chapter 4**). Quite unique to these membranes was the high content of glycolipids, accurately MGDG, DGDG and SQDG. As the formation of membrane stacks involved interactions between both amines and lipids, some properties of individual lipids might be substantial for membrane stacking. Especially the role of MGDG was of interest as it on the one hand is a non-bilayer forming lipid[67,73,74] and on the other hand plays an important role as the most occurring lipid in stacked thylakoid membranes.[299] Besides the specific role of individual lipid types the general property of the membrane's charge had to be discussed. With membranes carrying a negative surface charge and polyamines being protonated and positively charged under acidic conditions,[43] electrostatic interactions were expected to play an important role in LCPA-membrane interactions (see also the previous discussion on LCPA adsorption on membrane surfaces at the beginning of this chapter).

The necessity for specific lipids within the lipid mixture to enable LCPA-induced stack formation was evaluated by omitting single lipid types during the formation of solid supported lipid bilayers (see **Chapter 6.4.2**). Fluorescence micrographs, taken after the addition of C3N13 (see **Figure 6.15**), revealed that LCPA-induced stack formation did require neither MGDG, DGDG nor SQDG within the supported lipid membrane. Even on lipid bilayers composed only of POPG and DOPC, and not containing any glycolipids at all, the formation of membrane stacks after LCPA addition was observed. These findings proved that stack formation was not caused by specific interaction of LCPA with glycolipid headgroups. Also no lipids with an inverted cone-like structure (*e.g.* MGDG) were needed to stabilize and facilitate the formation of membrane stacks.

Since no specific interactions between LCPA and some of the lipids, initially included in the lipid mixture, were identified, more general aspects of LCPA-membrane interaction were analyzed. All lipid membranes used so far contained about 20 mol% of negatively charged lipids (see **Table 6.1**), hence the influence of membrane charge was evaluated by reference measurements on neutral lipid bilayers.

Pure DOPC membranes prepared on mica surfaces were chosen as reference systems. Unfortunately working with neutral lipid mixtures also affected vesicle spreading and interfered with the protocol established for the preparation of charged membranes (see **Chapter 3.3**). Addition of SUVs in spreading buffer (see **Table 3.9**) onto a mica surface only resulted in adhesion of vesicles and no fusion into a continuous lipid bilayer was observed. Vesicle spreading in general is heavily affected by electrostatic interactions between lipids and the support.[87] These interactions can be modified for example by changes in ionic strength and composition of the buffer solution.[318,319] A common way to trigger spreading of vesicles into continuous lipid bilayers is the addition of calcium ions.[320] These divalent ions do not only bridge both the lipids and the support but are also known to interact with headgroups of multiple lipids thereby altering the bilayers properties.[125,321] Even if calcium should not affect pure PC membranes,[322] the addition of calcium ions was avoided as effects on LCPA binding could not be ruled out and the presence of divalent ions would mark a significant difference compared to all previous studies. In the end vesicle spreading was achieved by replacing potassium chloride by sodium chloride in the spreading buffer. Stronger interactions between DOPC headgroups and sodium ions compared to those with potassium ions were also reported by VÁCHA *et al.* as a result of molecular dynamics simulations.[323] The influence of this change compared to the otherwise used spreading protocol was regarded diminishing, especially as the surface became rinsed multiple times with sample buffer (see **Table 3.9**) and all measurements were performed in exactly this buffer solution for nearly all studies on LCPA-induced membrane stacking so far.

Another different observation compared to all previous studies was the formation of brighter stack-like structures on pure DOPC membranes even in absence of LCPA (see **Figure 6.16 A**). Parallel occurrence of LCPA-dependent and –independent structures could interfere with studies on LCPA-induced membrane stacking as both needed to be clearly distinguishable. Systematic analysis of the properties of the stack-like structures on DOPC revealed fundamental differences compared to membrane stacks induced by LCPA addition on negatively charged membranes. While LCPA-induced stacks mainly had doubled fluorescence intensity compared to their surrounding (see **Figure 6.5**), stack-like structures on pure DOPC nearly exclusively showed tripled fluorescence intensity (see **Figure 6.16 B**). Thus it was concluded that independent phenomena were observed. Structures on DOPC appeared to contain at least two additional lipid bilayers on top of the underlying, solid supported membrane. FRAP experiments performed on the stack-like structures (see **Figure 6.17**) also revealed some differences compared to LCPA-induced membrane stacks. All previously investigated stacks formed after LCPA addition showed full fluorescence recovery after bleaching (see **Figure 6.8**). In contrast the stack-like structures on pure DOPC showed both full recovery and only recovery of the underlying membrane (see **Figure 6.17**). These structures could therefore either be still connected to the underlying membrane or already segregated from it. Combining all information the model shown in **Figure 6.27** was developed.

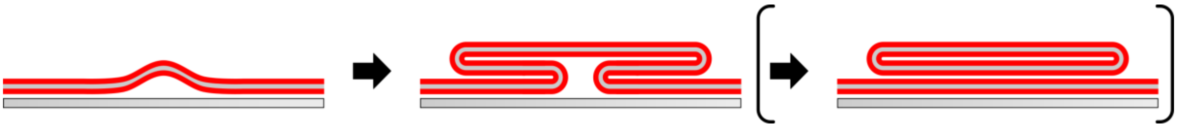

Figure 6.27. Schematic illustration of the formation of stack-like structures observed on pure DOPC membranes in absence of LCPA. Budding of the solid supported membrane led to the generation of multilayered structures. The initial connection to the underlying membrane could eventually become cut explaining the different outcomes of FRAP experiments.

On pure DOPC solid supported lipid bilayers, a LCPA-independent budding of the membrane was observed. This process led to the formation of multilayered structures with three lipid bilayers on top of each other. In the first form, FRAP experiments would show full fluorescence recovery. Additionally, full segregation of the overlying membranes was possible, which disabled exchange of lipid material with the underlying membrane and therefore resulted in limited fluorescence recovery during FRAP experiments.

DOPC multibilayers are heavily used for example for X-ray or neutron diffraction to study membrane properties[324] but the preparation and chemical environment of these systems differ drastically from the conditions present in this study. Hardly any publications were available discussing comparable observations. One of the closest ones was written by CAMBREA and HOVIS who reported on the formation of 3D cap-structures on glass-supported lipid bilayers.[325] Changes in ion strength led to an elevation of parts of the solid supported membrane resulting in the formation of domains with brighter lipid-bound dye fluorescence surrounded by a halo. In contrast to the previously mentioned results, their study reported only FRAP experiments showing full fluorescence recovery and cap formation was limited to lipid mixtures containing phosphatidic acid. Another difference was the choice of the solid support. In their study glass was employed while herein mica was chosen. In direct comparison membrane-substrate interactions are stronger between mica and solid supported lipid bilayers since mica surfaces are atomically flat.[247] Stronger contact should increase the energy barrier for cap formation but might on the other hand also enable the formation of stronger gradients between both sides of the membrane. Such gradients could be caused by differences in osmolarity of spreading and sample buffer (see **Table 3.9**) but also due to evaporation of water from the rather small sample volume. While changes in ionic strength would also affect measurements on charged membranes, the thickness of the water layer between the membrane and the support might indicate the crucial difference as it is increased for negatively charged membranes.[297]

To ensure clear discrimination between stack-like structures formed in absence of LCPA and LCPA-induced membrane stacking, the experimental setup was adjusted compared to the previous measurements with lipid mixtures omitting single lipid types. Previous experiments (see **Chapter 6.4.1**) showed that LCPA trigger the spreading of lipid material from solution onto a LCPA-covered lipid membrane. Evidence for this process was provided by the use of different lipid-bound dye molecules for both the solid supported membrane and vesicles in solution (see **Figure 6.13**). The same setup was chosen for the investigation on pure DOPC membranes (see **Figure 6.18**). Like previously observed on negatively charged membranes, membrane stacks were formed and could be detected by the fluorescence of TexasRed-DHPE which was formerly only incorporated into SUVs added alongside the LCPA C3N13. On Bodipy-C_{12}HPC containing solid supported membranes diffusion of this dye into membrane stacks was observed while Atto488-DHPE has not accumulated in the region of the membrane stacks yet. These observations were consistent with previous experiments on charged membranes and proved LCPA-induced stack formation also on neutral lipid bilayers only composed of PC lipids.

Different ways of LCPA to interact with lipid membranes were already discussed at the beginning of **Chapter 6.6.1**. Besides electrostatic interactions, specific binding of polyamines to phosphate groups was reported. BERNECKER *et al.* investigated the aggregation of LCPA in solution and in presence of inorganic phosphate ions.[43] For the short polyamine spermine, TADOLINI also reported on direct interactions of the polyamine with phosphate groups inside phospholipid headgroups.[293] Such specific interactions not only led to binding of LCPA onto the surface but also provided sufficient attractive forces to trigger spreading of vesicles from solution into membrane stacks. Overall membrane stacking did not require a negatively charged membrane surface as it was also observed on neutral DOPC membranes.

Influence of Polyamine Chain Length

Interactions of short polyamines with lipid membranes are manifold[279] but none of the previously published studies reported the formation of membrane stacks on solid supported membranes. In contrast PEI addition was shown to cause formation of defects in supported lipid bilayers.[285] Regarding both extrema and combining the observations with the insight gained in this study, a clear length dependency of the effect of polyamines on lipid bilayers was concluded.

The capability of polyamines with different chain length to trigger membrane stack formation was studied systematically by the use of synthetic polyamines with different chain length, reaching from C3N4 ($M = 188\ \mathrm{g{\cdot}mol^{-1}}$) to C3N18 ($M = 988\ \mathrm{g{\cdot}mol^{-1}}$, see **Table 3.1**), as well as spermidine and spermine (see **Chapter 6.4.3**). The formation of membrane stacks was only observed after the addition of C3N7, C3N13 or C3N18 to solid supported lipid bilayers (see **Figure 6.19**). In conclusion, polyamines needed more than five amine groups to trigger stack formation. An upper threshold could not be determined as the longest LCPA available (C3N18) still caused the formation of membrane stacks.

Interactions between polyamines and lipids had also been discussed for example in **Chapter 6.6.1**. Direct interactions between both types of molecules were regarded comparable for shorter polyamines (*e.g.* spermidine or spermine) and LCPA as similar trends, for example binding to phospholipids (see previous chapter), were observed. On the other hand the internal properties of polyamines and thus the polyamine layer change with chain length. Aggregation of LCPA was studied for example by BERNECKER *et al*.[43] Polyamine droplets were formed in solution and in presence of phosphate ions. The size of these droplets increased with the chain length of polyamines. The observation was explained by an increase in hydrophobicity of the amine molecules. In **Chapter 6.3.1** fluorescent FITC-C3N13 revealed an accumulation of LCPA co-localizing with the formed membrane stacks. Amongst others this observation led to the development of a model explaining LCPA-induced stack formation as a spreading of vesicles onto a LCPA cushion formed on top of the underlying, solid supported membrane (see **Figure 6.24**). The properties of this cushion, eventually providing enough adhesion force for vesicle spreading,[314] were mainly determined by the polyamines and therefore for example by their hydrophobicity and degree of hydration. The direct influence of these two parameters on membrane formation and the properties of the deposited lipid layers has already been proven for polymer cushions with tunable properties by RENNER *et al*.[326] Besides overall parameters of the polyamine layer, even geometric parameters of individual polyamines could be a crucial factor. With a distance between two lipid bilayers of up to 4 nm (see **Chapter 6.3.3**) even a direct linkage of the two headgroup regions by stretched, longer polyamines might be possible. Direct linkage might also be influenced by the buffer composition as it requires stretched LCPA especially if shorter polyamines were regarded. Multivalent anions promote the curling of polyamines.[43] Thus the addition of such anions might increase the critical chain length for stack formation as less direct linkage could be provided and more amine groups are connected internally. Within this study no systematic buffer screening was performed. Since all measurements were performed in acetate buffer and in absence of multivalent anions, LCPA would most likely be in their stretched conformation.

6.6.4 Silica Precipitation on Membrane Surfaces

LCPA are well known from *in vitro* experiments to catalyze silicic acid polycondensation and the formation of amorphous silica in solution.[37,43,98,273] The postulated mechanism involves acid-base catalysis via the amine groups (see **Figure 1.4**).[44] In the end LCPA become encapsulated in the formed silica particles.

Since an adsorption of LCPA on lipid bilayer surfaces was observed (see **Chapter 6.1**), the deposition of silica on LCPA-covered surfaces was investigated, too. Measurements were performed by RIfS (see **Chapter 6.5**). Reference measurements on pure DOPC lipid bilayers demonstrated the capability of this technique to monitor the formation of an approximately 1 nm thick silica layer on top of the membrane-covered surface. The formation of silica shells on top of pure PC membranes is also frequently used for the preparation of “liposils”, silica-coated liposomes for potential drug delivery.[327] On the other hand, the membranes on which LCPA were bound contained a decreased amount of PC molecules (see **Chapter 4**). In contrast to the reference measurements on pure DOPC membranes, after addition of silicic acid to the LCPA-coated membrane surfaces no deposition of a silica layer was observed (see **Figure 6.20**). The postulated mechanism for polymerization catalysis included the catalytic function of the amine groups in LCPA.[44] Those groups had to be accessible at the interface and must be capable of participating as an acid-base catalyst. The lack of catalytic function of LCPA adhered to the membrane surface indicated a strong interaction of these amine groups with the lipid headgroups that prevents them from interacting with silicic acid in solution.

6.6.5 LCPA-Membrane Interactions in the SDV

In this study the interactions between LCPA and solid supported model membranes mimicking the silicalemma were investigated. In summary the formation of membrane stacks was observed (see **Chapter 6.6.1–6.6.3**) and no LCPA-induced precipitation of silica could be detected after adsorption of the polyamines to the membrane surface (see **Chapter 6.6.4**). *In vivo* LCPA are expected to be located in the SDV and therein promote and control silica cell wall biogenesis.[37,59] This final chapter should now focus on the relevance of the findings made in this study for processes involving LCPA and lipid bilayers in the SDV and during silica biomineralization in diatoms.

SDVs are organelles circumvented by a lipid bilayer, the silicalemma. Up to this date the isolation of SDVs was not successful and only very limited information regarding their biochemical composition is available. Most structural information on SDVs and the silicalemma came from electron micrographs. While first identified by DRUM and PANKRATZ in 1963 and published in 1964[18] later studies by SCHMID and SCHULZ[19] or HILDEBRAND *et al.*[20] gave a more detailed view on the SDV. In the electron micrographs published by these groups no clear indication for a stacked silicalemma was identifiable. Nevertheless, it could be hypothesized that stacked membranes might play a role in certain stages of the SDV's lifespan. During the formation of silica cell wall fragments the SDV grows massively in size before the organelle fuses with the plasma membrane to release the cell wall fragment to the outside (see **Figure 1.2**).[14] This growth comes along with a drastic increase in membrane area. Additional lipids could be provided alongside silicic acid by the silica transport vesicles fusing with the silicalemma.[28] A second pool of lipids could be stored in stacked parts of the silicalemma, formed in the early stages of cell wall formation in the SDV. Regarding the size of membrane stacks, much smaller stacks would be expected *in vivo*. With areas of several hundred square micrometers the size of membrane domains formed *in vitro* exceed the size of the organelle and even the diatom cell since growth was only restricted by the limited amount of vesicles in solution and polyamines but not by spatial barriers. Besides the storage of lipid material in LCPA-supported membrane stacks, adsorbed LCPA could also have a stabilizing effect on the silicalemma during expansion. Stabilization of organelles and cells by polyamines, for example in response to osmotic stress or during growth, has been known for smaller polyamines since the late 1950s.[328–330]

Another observation made in this study was the inhibition of silica deposition on the membrane surface after adsorption of LCPA. This result marked an important contrast to all studies performed so far on LCPA in solution.[37,43,98,273] Apparently LCPA fulfill a more complex role in silica biomineralization as initially expected. Besides a catalytic effect in solution and as part of supramolecular assemblies inside the SDV, LCPA could also inhibit silica deposition at the membrane surface to prevent it from silicification. Amine group-containing lipids (*e.g.* PC) could otherwise promote the formation of a silica shell along the silicalemma[327] which would interfere with the expansion of the organelle as well as the release of cell wall fragments.

An aspect neither discussed nor investigated at all is the interaction of LCPA with membrane associated proteins or transmembrane proteins. Just recently KOTZSCH *et al.* identified the first putative transmembrane protein located in the silicalemma, silicanin-1.[254] Interactions with this or similar proteins could also expand the function of LCPA in diatoms.

7 CONCLUSION

Diatoms employ a sophisticated molecular machinery to transfer 2D genetic information into a fine-patterned 3D silica cell wall. Silica biomineralization takes place in the silica deposition vesicles (SDVs). While different model have been developed to describe controlled silica polymerization in solution, no information on the influence of the organelle-surrounding lipid bilayer is available. This study focused on the characterization of interactions between biomolecules identified in diatom biosilica and artificial lipid bilayers *in vitro*.

The main components of lipid membranes in diatoms are the three glycolipids monogalactosyldiacylglycerol, digalactosyldiacylglycerol and sulfoquinovosyldiacyl-glycerol. Incorporation of all of these lipids into artificial model membranes enables investigation of specific biomolecule-membrane interactions *in vitro*. Herein, for the first time, protocols for the preparation of solid supported lipid monolayers on hydrophobically functionalized gold and glass as well as for the deposition of lipid bilayers on silicon dioxide and mica surfaces were established. Artificial model membranes mimicking the overall lipid composition of diatoms were successfully prepared by vesicle spreading. On both hydrophobic surfaces the formation of continuous lipid monolayers was observed. Vesicle addition to hydrophilic silicon dioxide wafers led to full coverage of the surface with lipid material, while only a part of the vesicles ruptured and fused into continuous lipid bilayers. On mica, by contrast, the formation of substrate spanning continuous and fluid lipid bilayers was observed. The introduction of these model membranes enabled the use of a wide variety of different surface sensing techniques to study biomolecule-membrane interactions under well-defined chemical conditions ensuring lateral mobility.

The first class of diatom biomolecules investigated in this study was the cingulins. For the first time, the interactions between two recombinant cingulins (rCinY3 and rCinW2) and lipid membranes were analyzed. While rCinY3 was provided, rCinW2 was expressed and isolated on site from *Escherichia coli*. A new protocol for the purification of rCinW2, using immobilized metal ion affinity chromatography, was introduced that provided the His_6-tagged target protein in high purity. A systematic study of rCinW2 solubility revealed aggregation and precipitation of the protein under acidic conditions in absence of high salt concentrations. It was possible to stabilize rCinW2 by addition of ectoine and study its interactions with lipid membranes. However, for both, rCinY3 and rCinW2, no significant and specific adsorption on lipid bilayers was observed.

In addition to cingulins, long-chain polyamines (LCPA) and their interactions with lipid membranes were characterized. For the first time, synthetic polyamines with molecular masses matching the ones of LCPA isolated from diatoms were analyzed with regard to their interaction with lipid bilayers. Adsorption of LCPA on membrane surfaces was observed that led to changes in membrane morphology. A combination of fluorescence and atomic force microscopy revealed the formation of membrane stacks after LCPA addition. Bleaching experiments proved a connection between stacked and underlying lipid bilayers that enables exchange of lipids. The lipid material used for stack formation was identified to originate from vesicles in solution. Systematic analysis of additional parameters enabling stack formation revealed an independence from membrane composition. Neither glycolipids nor a negative charge was needed in the model membranes for the formation of LCPA-induced membrane stacks. In contrast, a clear dependence on polyamine chain-length was observed. Polyamines with five or less amine groups did not promote stack formation, while polyamine-induced membrane stacking was observed after addition of polyamines with seven to eighteen amine groups. The study of silicic acid polycondensation revealed no catalyzed precipitation of silica on polyamine-coated membrane surfaces in contrast to solution experiments.

In conclusion, the introduction of artificial model membranes reflecting the overall lipid composition of diatoms was proven to be a viable tool for the study of biomolecule-membrane interactions *in vitro*. Since no specific interactions between cingulins and lipid membranes were observed, a direct influence of such interactions on the biomolecule assembly in the SDV was excluded. On the other hand, LCPA showed strong interactions with lipid bilayers. The role on LCPA *in vivo* might therefore exceed the control of silica precipitation by aggregation in solution as they might directly influence membrane properties during expansion of the SDV and protect the organelle membrane from silification.

APPENDIX

Amino Acid Sequences of Cingulins

Recombinant Cingulin W2

Information on the cDNA encoding native cingulin W2 from *T. pseudonana* is deposited in the National Center for Biotechnology Information GenBank Database (https://www.ncbi.nlm.nih.gov/genbank/) under the access code HQ873962.[35] The genetic information translates into the amino acid sequence of rCinW2 shown in **Figure App.1**.

```
        10         20         30         40         50         60
MQQSSVRGVA TTSSRQLDEW GDDAWGSSDS GSSGKSGKSG GSASSGDGWE TDGWGGDYSS
        70         80         90        100        110        120
SKSGKSGSGK SGKGSSGPHG HWVYIEDDSS DGSGKSGKGS SSKGSKGSSK SSKGSSSDDS
       130        140        150        160        170        180
TDDSWDGGWG GHGGWNGDNS GKSGKGSYGS GKSGKGSSYP SSHWGPSHWG SDDDDSSSSK
       190        200        210        220        230        240
SSKGSSESSS KSSKGSSDSS SKSSKGSSSS EDEGHWEWEG GYGSGKSGKG SYSGSSGKSG
       250        260        270        280        290        300
KSGSGDSWVG DYGSSGKSGK GSYGGDSWGG NYNGWGGHYD VDVDDDDSSS SKSSKGSSKS
       310        320        330        340        350        360
SKGSSEDSSK SSKGSSSKSS KGSSSSEDEG HWVWEGSYGS GKSGKGSYSG SSGKSGKSGS
       370
GDEGWYSGWH HHHHH
```

Figure App.1. Amino acid sequence of rCinW2. Tryptophans are marked in orange, KXXK motives in red and the *C*-terminal hexa histidine tag in blue.

Table App.1. Amino acid composition of rCinW2.

Amino acid	A	R	N	D	C	Q	E	G	H	I	L
Amount	3	2	4	34	0	3	13	87	14	1	1
Ratio	0.8%	0.5%	1.1%	9.1%	0.0%	0.8%	3.5%	23.2%	3.7%	0.3%	0.3%

Amino acid	K	M	F	P	S	T	W	Y	V	U	Total
Amount	40	1	0	3	126	4	19	13	7	0	375
Ratio	10.7%	0.3%	0.0%	0.8%	33.9%	1.1%	5.1%	3.5%	1.9%	0.0%	100%

Table App.2. Physical properties of rCinW2 calculated with the tool ProtParam.[117]

Molar mass *M*	Theoretical pI	Extinction coefficient ε (λ = 280 nm)
37365 Da	6.27	123870 $\mathrm{M}^{-1}\cdot\mathrm{cm}^{-1}$

Recombinant Cingulin Y3

Information on the cDNA encoding native cingulin Y3 from *T. pseudonana* is deposited in the National Center for Biotechnology Information GenBank Database (https://www.ncbi.nlm.nih.gov/genbank/) under the access code HQ873960.[35] The genetic information translates into the amino acid sequence of rCinY3 shown in **Figure App.2**.

```
        10         20         30         40         50         60
MGTNKTLAPT PFPGRPTPPG AGTPFPTENT PAPSPAFGTK PPTPSSYEPP QYSYEPPTTG
        70         80         90        100        110        120
CSKAGKGGKS GSMDYLIDCI DLSSKSGKSG SGYGPSSSKG GKSGSSSAGY GDDYTATTDD
       130        140        150        160        170        180
YSAGADAGKS ENYDEEASRD DGHYGASSKG GKSGSAGYGD EGYGSSAGSS KGGKSEADGY
       190        200        210        220        230        240
GDESYGDSGD SKAGKAEAGY GDDYGASAKS GKGSDGYGSS SKSGKAGSAK SGKGEGYHMF
       250        260        270        280
HDKSGKGGKG SSSGGEGYGY GYDEAHDYGY GRRTRGLRAS QHHHHH
```

Figure App.2. Amino acid sequence of rCinY3. Tyrosines are marked in green, KXXK motives in red and the *C*-terminal hexa histidine tag in blue.

Table App.3. Amino acid composition of rCinY3.

Amino acid	**A**	**R**	**N**	**D**	**C**	**Q**	**E**	**G**	**H**	**I**	**L**
Amount	24	6	3	22	2	2	13	62	10	2	4
Ratio	8.4%	2.1%	1.0%	7.7%	0.7%	0.7%	4.5%	21.6%	3.5%	0.7%	1.4%
Amino acid	**K**	**M**	**F**	**P**	**S**	**T**	**W**	**Y**	**V**	**U**	**Total**
Amount	25	3	4	19	48	15	0	23	0	0	287
Ratio	8.7%	1.0%	1.4%	6.6%	16.7%	5.2%	0.0%	8.0%	0.0%	0.0%	100%

Table App.4. Physical properties of rCinY3 calculated with the tool ProtParam.[117]

Molar mass *M*	**Theoretical pI**	**Extinction coefficient ε (λ = 280 nm)**
28745 Da	6.20	34270 $\mathrm{M}^{-1}\cdot\mathrm{cm}^{-1}$

Self-Written Scripts for Data Analysis

All scripts were written for Matlab R2012b (MathWorks).

Analysis of Stack Growth

The growth of membrane stacks was analyzed by thresholding fluorescence intensities to identify membrane stack with increased local fluorescence. Particle analysis read the area of the stacks in all images and therefore provided time-dependent growth data.

The time-series of fluorescence micrographs had to be saved as 8 bit-TIFF files and image parameters had to be edited in the source code.

```
% ============================================================
%                    Stack growth analysis
% ============================================================
% Loads: 8 bit-TIFF files of time series in selectable folder
%
% Outputs: 1) Size of stacks over time
%          2) Image series with labeled stacks
% ============================================================
clear
% ------------------------------------------------------------
%                    Additional parameters
% ------------------------------------------------------------
% Image parameters:
time_per_frame = 3.247    % time per frame / s
pixel_width = (1/4.831)   % pixel width / µm

%Analysis parameters:
bw_threshold = 0.35       % Threshold for stack intensity
size_threshold = 8*8      % Minimal stack size / µm^2
min_final_size = 20*20    % Minimal final stack size / µm^2
% ------------------------------------------------------------

% ~~~~~~~~~~~~~~~~~~~~~~~~~~~~~~~~~~~~~~~~~~~~~~~~~~~~~~~~~~~~
% Folder selection and initialization
% ~~~~~~~~~~~~~~~~~~~~~~~~~~~~~~~~~~~~~~~~~~~~~~~~~~~~~~~~~~~~
folder_name = uigetdir;                     % folder selection
data_files = dir([folder_name,'\*.tif']);   % list of images
no_images = length(data_files);             % number of images

mkdir([folder_name,'\Results_Growth'])      % creates output path

% ~~~~~~~~~~~~~~~~~~~~~~~~~~~~~~~~~~~~~~~~~~~~~~~~~~~~~~~~~~~~
% Stack identification and analysis
% ~~~~~~~~~~~~~~~~~~~~~~~~~~~~~~~~~~~~~~~~~~~~~~~~~~~~~~~~~~~~
for i = [1:no_images]
    slice{i}.image = imread([folder_name,'\',data_files(i).name]); % loads image

    slice{i}.image_bw = im2bw(slice{i}.image,bw_threshold); % creates binary image
    slice{i}.image_bw_fill = imfill(slice{i}.image_bw,'holes'); % fills holes
    clear slice{i}.image_bw                 % deletes obsolete data
    slice{i}.image_stacks = bwareaopen(slice{i}.image_bw_fill,size_threshold);
                                                             % filters smaller structures
    clear slice{i}.image_bw_fill            % deletes obsolete data

    slice{i}.image_stacks_label = bwlabel(slice{i}.image_stacks); % labels stacks
    slice{i}.props = regionprops(slice{i}.image_stacks_label,'Area','Centroid');
                                                                  % determines stack area

    for j=[1:length(slice{i}.props)]        % compiles stack data
        slice{i}.stack_no = j;
        slice{i}.stack_area(j) = slice{i}.props(j).Area;
```

```
        slice{i}.stack_CoM_x(j) = slice{i}.props(j).Centroid(1);
        slice{i}.stack_CoM_y(j) = slice{i}.props(j).Centroid(2);
    end
end

% ~~~~~~~~~~~~~~~~~~~~~~~~~~~~~~~~~~~~~~~~~~~~~~~~~~~~~~~~~~~~
% Growth analysis
% ~~~~~~~~~~~~~~~~~~~~~~~~~~~~~~~~~~~~~~~~~~~~~~~~~~~~~~~~~~~~
% ~~ Selects stacks by final size ~~~~~~
j = 1;
for i=[1:length(slice{no_images}.stack_area)] % number of stacks in final image
    if slice{no_images}.stack_area(i) >= min_final_size
                                                       % final size must exceed threshold
        stack{j}.stack_area(no_images) = slice{no_images}.stack_area(i);
                                                                    % compiles stack data
        stack{j}.stack_CoM_x(no_images) = slice{no_images}.stack_CoM_x(i);
        stack{j}.stack_CoM_y(no_images) = slice{no_images}.stack_CoM_y(i);
        j = j+1;
    end
end

% ~~ Labels stacks uniformly ~~~~~~~~~~~
for i=linspace((no_images-1),1,(no_images-1))   % goes back within the time series
    for j=[1:length(stack)]                 % iterates for all stacks in the final image
        dist = zeros(1,length(slice{i}.stack_CoM_x));
        for k=[1:length(dist)]         % calculates distances to stacks in current image
            dist(k) = pdist([stack{j}.stack_CoM_x(no_images),...
                stack{j}.stack_CoM_y(no_images);slice{i}.stack_CoM_x(k),...
                slice{i}.stack_CoM_y(k)]);
        end
        [min_dist,ind_min] = min(dist);
                                    % determines the stack with the smallest displacement
        stack{j}.stack_area(i) = slice{i}.stack_area(ind_min); % compiles stack data
        stack{j}.stack_CoM_x(i) = slice{i}.stack_CoM_x(ind_min);
        stack{j}.stack_CoM_y(i) = slice{i}.stack_CoM_y(ind_min);
    end
end

% ~~~~~~~~~~~~~~~~~~~~~~~~~~~~~~~~~~~~~~~~~~~~~~~~~~~~~~~~~~~~
% Data output
% ~~~~~~~~~~~~~~~~~~~~~~~~~~~~~~~~~~~~~~~~~~~~~~~~~~~~~~~~~~~~
% ~~ Images with labeled stacks ~~~~~~~~
for i=[1:length(slice)]                     % outputs all images
    close all
    result1 = figure();
    imshow(slice{i}.image)                  % raw image
    hold on
    for j=[1:length(stack)]                 % inserts labels
        plot(stack{j}.stack_CoM_x(i),stack{j}.stack_CoM_y(i),'.r') % position
        text(stack{j}.stack_CoM_x(i),stack{j}.stack_CoM_y(i),[' ',num2str(j)]) % number
    end
    print(result1,[folder_name,'\Results_Growth\','CoM_',data_files(i).name],'-dpng')
                                                                            % prints data
end

% ~~ Plot of stack size ~~~~~~~~~~~~~~~~
colors = hsv(length(stack));
result2 = figure();
hold on
for i=[1:length(stack)]                     % data for all detected stacks
    no_slices = length(slice);
    x_data = [1:no_slices]*time_per_frame;  % time data
    y_data = rot90(stack{i}.stack_area(:)*pixel_width^2); % Stack size
    plot(x_data,y_data,'-','Color',colors(i,:))
    labels{i} = ['Stack ',num2str(i)];

    output(:,1) = x_data;                   % data for stack as CSV file
    output(:,2) = y_data;
    csvwrite([folder_name,'\Results_Growth\','Stack_growth_',num2str(i),'.csv'],output);
end
xlabel('Time / s')
ylabel('Area / µm^2')
legend(labels,'Location','southeast')
print(result2,[folder_name,'\Results_Growth\','Stack_growth'],'-dpng') % prints data
```

List of Symbols and Abbreviations

A	Area
A_0	Trough area
APS	Ammonium persulfate
Atto488-DHPE	Atto 488 1,2-dihexadecanoyl-*sn*-glycero-3-phosphoethanolamine
B	Magnetic flux density/magnetic field
Bodipy-C$_{12}$HPC	*β*-BODIPY 500/510 1-hexadecanoyl-*sn*-glycero-3-phosphocholine
C	Capacitance; Intensity profile
c	Concentration; Speed of light
C. fusiformis	*Cylindrotheca fusiformis*
C. meneghiniana	*Cyclotella meneghiniana*
C3N13	Dodecapropyltriskaidecamine
C3N18	Pentadecapropyloctadecamine
C3N4	Tripropyltetramine
C3N5	Tetrapropylpentamine
C3N7	Hexapropylheptamine
c_N	Polyamine concentration standardized to the number of nitrogen atoms per molecule
D	Diffusion coefficient
d	Distance
DGDG	Digalactosyldiacylglycerol
DOPC	1,2-Dioleoyl-*sn*-glycero-3-phosphocholine
DPPC	1,2-Dipalmitoyl-*sn*-glycero-3-phosphocholine
DTT	Dithiothreitol
E	Energy
E. coli	*Escherichia coli*
EDTA	Ethylenediaminetetraacetic acid
EIS	Electrochemical impedance spectroscopy
F	Force
FDC	Fore-distance-curve
FITC-C3N13	Fluorescein-labeled dodecapropyltriskaidekamine
FRAP	Fluorescence recovery after photobleaching
FRET	FÖRSTER resonance energy transfer
g	Gaseous phase
h	PLANCK constant
HMDS	Hexamethyldisilazane
I	Signal intensity
IEC	Ion exchange chromatography
IMAC	Immobilized metal ion affinity chromatography

IPTG	Isopropyl β-D-1-thiogalactopyranoside
J	Nuclei spin quantum number
k	Plasmon momentum; Spring constant; Rate constant
K_D	Equilibrium constant
l_c	Liquid condensed phase
LCPA	Long-chain polyamine
l_e	Liquid expanded phase
m	Magnetic quantum number
M	Molar mass
MES	2-(*N*-Morpholino)ethanesulfonic acid
MGDG	Monogalactosyldiacylglycerol
MOPS	3-(*N*-Morpholino)propanesulfonic acid
N	Quantity
n	Refractive index
N_A	AVOGADRO constant
NA	Numerical aperture
Ni-NTA	Nickel nitrilotriacetic acid
NMR	Nuclear magnetic resonance
OD	Optical density
OT	Octanethiol
OT	Optical thickness
P	Nuclei spin
P_0	Laser intensity
PC	Phosphatidylcholine
PEI	Polyethylenimine
PG	Phosphatidylglycerol
PMSF	Phenylmethylsulfonyl fluoride
POPG	1-Palmitoyl-2-oleoyl-*sn*-glycero-3-phosphoglycerol
qHNMR	Quantitative ^{1}H nuclear magnetic resonance
r	Radius; FRESNEL coefficient
R	Resistance; Intensity of reflected light
rCinW2	Recombinant cingulin W2
rCinY3	Recombinant cingulin Y3
RIfS	Reflectometric interference spectroscopy
ROI	Region of interest
s	Solid phase; Path length
SDS	Sodium dodecyl sulfate
SDV	Silica deposition vesicle
SQDG	Sulfoquinovosyldiacylglycerol
SUV	Small unilamellar vesicle

T	Time intervall
T. pseudonana	*Thalassiosira pseudonana*
TEMED	Tetramethylethylenediamine
TexasRed-DHPE	TexasRed 1,2-dihexadecanoyl-*sn*-glycero-3-phosphoethanolamine
TMOS	Tetramethoxysilane
TRIS	Tris(hydroxymethyl)aminomethane
U	Voltage
UHF	Ultra high frequency
UV	Ultra violet light
V	Volume; Potential energy
VIS	Visible light
Z	Impedance
α	Rate constant
γ	Gyromagnetic ratio
ε	Relative permittivity; Lennard-Jones parameter
Θ	Angle of incident or refraction; Phase angle; Contact angle
λ	Wavelength
μ	Dipole moment
ν	Frequency
Π	Surface pressure
ρ	Mass concentration; Density
σ	Surface tension
$\tau_{1/2}$	Half-time value
Φ	Angle of incident
ω	Laser beam half width; Angular frequency

List of Chemicals and Consumables

Acetic acid	ThermoFischer Scientific, Waltham (US)
Acrylamide/bis-acrylamide solution (30%, 37.5:1; Rotiphorese Gel 30)	Carl Roth GmbH, Karlsruhe (DE)
Ampicillin	Carl Roth GmbH, Karlsruhe (DE)
Antibody against mouse antibodies (Goat-anti-mouse HRP)	Santa Cruz Biotechnology, Inc., Dallas (US)
Antibody against penta histidine sequences (Penta His Antibody, BSA-free)	Qiagen, Venlo (NL)

APS	Sigma-Aldrich, St. Louis (US)
Atto488-DHPE	Atto-tec GmbH, Siegen (DE)
Bodipy-C_{12}HPC	Invitrogen, Carlsbad (US)
Bromphenol blue	Carl Roth GmbH, Karlsruhe (DE)
Centrifugal concentrators (molecular weight cut-off: 5 kDa, Vivaspin 500)	Sigma-Aldrich, St. Louis (US)
Chloroform	Sigma-Aldrich, St. Louis (US)
Chromium	Umicore Materials AG, Balzers (DE)
Coomassie G-250	Fluca Chemie GmbH, Buchs (DE)
Cover slides (D263M Schott glass)	Ibidi GmbH, München (DE)
DGDG	Avanti Polar Lipids, Alabaster (US); Larodan, Solna (SE)
DNase I	AppliChem, Darmstadt (DE)
DOPC	Avanti Polar Lipids, Alabaster (US)
DPPC	Avanti Polar Lipids, Alabaster (US)
DTT	Sigma-Aldrich, St. Louis (US)
E. coli DH5α cells	ThermoFischer Scientific, Waltham (US)
Ectoine	AppliChem, Darmstadt (DE)
EDTA	Carl Roth GmbH, Karlsruhe (DE)
Ethanol	Honeywell, Hamburg (DE)
Glass slides	ThermoFischer Scientific, Waltham (US)
Glucose	VWR Prolabo, Radnor (US)
Glycerol	Merck, Darmstadt (DE)
Glycine	Merck, Darmstadt (DE)
Gold (99.99%)	Allgemeine Gold- und Silberschneideanstalt, Pforzheim (DE)
H_2O_2 (30%)	Grüssing GmbH, Filsum (DE)
Hellmanex	Hellma GmbH & Co KG, Müllheim (DE)
HMDS	Merck, Darmstadt (DE)
Imidazole	Sigma-Aldrich, St. Louis (US)
Impedance glass slides ("Menzel-Gläser" 22×22 mm #4, LOT 0685)	ThermoFischer Scientific, Waltham (US)
IPTG	Sigma-Aldrich, St. Louis (US)
Isopropyl alcohol	VWR Prolabo, Radnor (US)
KCl	Merck, Darmstadt (DE)
LMW-SDS Marker Kit	GE Healthcare Life Science, Little Chalfont (UK)
Luminol	Fluca Chemie GmbH, Buchs (DE)
Lysozyme	Carl Roth GmbH, Karlsruhe (DE)
MES	Carl Roth GmbH, Karlsruhe (DE)
Methanol	Sigma-Aldrich, St. Louis (US)
$MgCl_2$	Merck, Darmstadt (DE)
MGDG	Avanti Polar Lipids, Alabaster (US); Larodan, Solna (SE)

$MgSO_4$	Fluca Chemie GmbH, Buchs (DE)
Mica (Glimmer “V5”, Art.-Nr. 52)	Plano GmbH, Wetzlar (DE)
MLCT cantilevers	Bruker Corporation, Billerica (US)
MSNL-10 cantilevers	Bruker Corporation, Billerica (US)
Mucasol universal detergent	Merck, Darmstadt (DE)
Na-citrate	Merck, Darmstadt (DE)
NaCl	Merck, Darmstadt (DE)
NaN_3	Merck, Darmstadt (DE)
NaOAc	Merck, Darmstadt (DE)
NH_4OH (25%)	Fluca Chemie GmbH, Buchs (DE)
Nitrocellulose membrane (Trans-Blot, 0.2 µm)	Bio-Rad Laboratories GmbH, München (DE)
Octanethiol	Merck, Darmstadt (DE)
OMCL-AC160TS-R3 cantilevers	Olympus, Tokyo (JP)
Optical oil (Series B 1.7000)	Cargille Labs, Cedar Grove (US)
PageRuler Plus	ThermoFischer Scientific, Waltham (US)
p-Coumaric acid	Sigma-Aldrich, St. Louis (US)
Photographic developer (GBX)	Carestream, Stuttgart (DE)
Photographic film (Biomax XAR Film)	Carestream, Stuttgart (DE)
Photographic fixer (GBX)	Carestream, Stuttgart (DE)
PMSF	Sigma-Aldrich, St. Louis (US)
PonceauS	Sigma-Aldrich, St. Louis (US)
POPG	Avanti Polar Lipids, Alabaster (US)
Protease inhibitor tablets (Roche complete EDTA-free)	Roche Applied Science, Penzberg (DE)
SDS	AppliChem, Darmstadt (DE)
Si/SiO_2 wafers (WSI04-1011004, <100>, *p*-type (boron))	Active Business Company GmbH, Brunnthal (DE)
Spermidine	Sigma-Aldrich, St. Louis (US)
Spermine	Sigma-Aldrich, St. Louis (US)
SPR glass slides (LaSFN9)	Hellma Optik, Halle (DE)
SQDG	Larodan, Solna (SE)
TEMED	Sigma-Aldrich, St. Louis (US)
TexasRed-DHPE	ThermoFischer Scientific, Waltham (US)
TMOS	Sigma-Aldrich, St. Louis (US)
TRIS	Carl Roth GmbH, Karlsruhe (DE)
Tryptone	Carl Roth GmbH, Karlsruhe (DE)
Tubular cellulose dialysis membranes (molecular weight cut-off: 14 kDa, Visking)	Carl Roth GmbH, Karlsruhe (DE)
Tween 20	Carl Roth GmbH, Karlsruhe (DE)
Urea	Merck, Darmstadt (DE)

UV curing glue (Norland optical adhesive)	Norland Products, Cranbury (US)
Whatman paper	Sigma-Aldrich, St. Louis (US)
Yeast extract	Carl Roth GmbH, Karlsruhe (DE)

List of Devices and Software

Confocal laser scanning microscope

FV-1200	Olympus, Tokyo (JP)
UMPLFLN 20XW	Olympus, Tokyo (JP)
LUMPLFLN 60XW	Olympus, Tokyo (JP)
ImageJ (version 1.48)	http://imagej.nih.gov/ [192]

Atomic force microscope and inverse epifluorescence microscope

MFP-3D	Asylum Research, Santa Barbara (US)
IX51	Olympus, Tokyo (JP)
LUCPLFLN 60X	Olympus, Tokyo (JP)
Infinity 2	Lumenera, Ottawa (US)
Igor Pro (version 6.37)	WaveMetrics, Inc., Portland (US)
Gwyddion (version 2.45)	http://gwyddion.net/ [206]

Surface plasmon resonance spectrometer

RT2005	Res-Tec, Framersheim (DE)
Ismatec 795C	IDEX Health & Science, Wertheim (DE)
WinSpall (version 3.02)	Res-Tec, Framersheim (DE)

Reflectometric interference spectrometer

HL-2000-FHSA	Ocean Optics, Dunedin (US)
NanoCalc-2000	Ocean Optics, Dunedin (US)
SD2000	Ocean Optics, Dunedin (US)
Ismatec 795C	IDEX Health & Science, Wertheim (DE)
Spectra Suite	Ocean Optics, Dunedin (US)

Other spectrometer

Inova 600	Varian, Palo Alto (US)
MestReNova (version 8.0.0)	Mestrelab Research S.L., Santiago de Compostela (ES)
Cary Scan 50	Varian, Palo Alto (US)
Nanodrop 2000c	ThermoFischer Scientific, Waltham (US)

Additional software

Matlab R2012b	MathWorks, Natick (US)
Office 2013	Microsoft Corporation, Redmond (US)

Water purification system

MilliQ Gradient A 10	Millipore, Eschborn (DE)
MilliQ Elix 5	Millipore, Eschborn (DE)

Surface coating

Zepto	Diener electronics, Ebbhausen (DE)
MED020	Bal-Tec, Wetzlar (DE)

Scales

Pioneer	Ohaus, Kirchheim (DE)
Adventurer	Ohaus, Kirchheim (DE)
CP2202S	Satorius, Göttingen (DE)
CP225D	Satorius, Göttingen (DE)

Centrifuges

3K30	Sigma, Taufkirchen (DE)
Allegra X-22R	Beckman Coulter, Brea (US)
Heraeus Fresco 17	ThermoFischer Scientific, Waltham (US)
Galaxy Mini	VWR International, Darmstadt (DE)

Biochemical devices

Incubator SM3	Eduard Bühler GmbH, Tübingen (DE)
Autoclave 2540EL	Tuttnauer, Breda (DE)
Laminar flow box HVR2448	Labotect, Göttingen (DE)
Thermomixer Compact	Eppendorf, Hamburg (DE)
Gel aperture 45-1010-i	Peqlab Biotechnologie GmbH, Erlangen (DE)
Trans-Blot SD	Bio-Rad Laboratories GmbH, München (DE)
Power supply Power Pac 200	Bio-Rad Laboratories GmbH, München (DE)

Miscellaneous devices

Waterbath WNE 29	Memmert GmbH & Co. KG, Schwabach (DE)
Vacuum drying chamber VD23	Binder, Tuttlingen (DE)
Sonoplus UW2070	Bandelin electronic, Berlin (DE)
pH meter 766 Calimatic	Knick, Berlin (DE)
Ultrasonic bath Sonorex RK255H	Bandelin electronic, Berlin (DE)
UV lamp UV-4 SL	Herolab, Wiesloch (DE)

List of Figures

1.1. Electron micrograph of the diatom species *Thalassiosira oceanica.* 2
1.2. Schematic illustration of the diatom cell cycle. 3
1.3. Chemical structures of LCPA from diatoms. 4
1.4. Postulated mechanism for acid-base catalysis of silicic acid polycondensation by polyamines. 5
1.5. Structure of native Silaffin-1A$_1$ from *C. fusiformis.* 6
1.6. Schematic illustration of cingulin primary structures. 7

1.7. Phase separation model for the control of silica morphogenesis by aggregates of biomolecules inside the SDV. 8
1.8. Six exemplary artificial model membrane systems. 10
3.1. Structure of the predominant component of isolated MGDG. 15
3.2. Structure of the predominant component of isolated DGDG. 16
3.3. Structure of the predominant component of isolated SQDG. 16
3.4. Structure of POPG. 17
3.5. Structure of DOPC. 17
3.6. Structure of the headgroup-labeled lipid dye TexasRed-DHPE. 18
3.7. Structure of the headgroup-labeled lipid dye Atto488-DHPE. 18
3.8. Structure of the fatty acid-labeled lipid dye Bodipy-C_{12}HPC. 18
3.9. Molecular structure of the long-chain polyamine C3N13. 19
3.10. Synthesis of LCPA with odd numbers of amine functions. 19
3.11. Structure of the fluorescent LCPA FITC-C3N13. 20
3.12. Synthesis of LCPA with even or odd numbers of amine groups. 21
3.13. Reaction scheme of the acidic hydrolysis of TMOS. 21
3.14. Schematic illustration of the isolation of rCinW2. 22
3.15. Schematic illustration of a Western blot. 26
3.16. Schematic illustration of the formation of a lipid monolayer on a gold surface. 32
3.17. Schematic illustration of the formation of a lipid monolayer on a hydrophobically functionalized glass substrate. 33
3.18. Schematic energy diagram of splitting energy levels in an external *B*-field. 36
3.19. Schematic illustration of a LANGMUIR-BLODGETT trough. 38
3.20. Exemplary illustration of a Π/A-isotherm of a lipid monolayer. 39
3.21. Illustrated procedure to calculate areas per molecules A_{20} by a combination of qHNMR and Π/A-isotherm measurements. 41
3.22. Schematic plot of dispersion relation of free and prism-coupled photons as well as surface plasmons and an illustration of the KRETSCHMANN configuration. 43
3.23. Schematic angle-reflectivity spectra and time-resolved recording of reflectivity at a specific angle. 43
3.24. Schematic illustration of interference at a thin film and an reflectivity spectrum. 46
3.25. Equivalent circuit for a solid supported membrane 48
3.26. Schematic energy diagram with two electronic states S_0 and S_1 as well as four of their vibrational states and absorption and emission spectra of a fluorescent dye. 50

3.27. Schematic illustration of the optical path of an epifluorescence microscope. 51
3.28. Schematic illustration of the optical path of a CLSM. 52
3.29. Exemplary intensity data from a FRAP experiment. 54
3.30. Illustration of a LENNARD-JONES potential. 56
3.31. Schematic illustration of an AFM. 57
3.32. Schematic illustration of a FDC on a solid supported lipid bilayer. 58
3.33. Schematic illustration of a droplet of liquid on a solid support. 59
4.1. Exemplary Π-A_0-isotherm of DPPC on ultrapure water at 20 °C. 63
4.2. Exemplary ^{1}H-NMR spectrum of POPG in $CDCl_3/CD_3OD$. 64
4.3. Exemplary Π-A-isotherms of MGDG, DGDG, SQDG and POPG at 20 °C. 65
4.4. Typical impedance spectrum of an OT layer on gold, visualized as BODE plot. .. 67
4.5. SPR data for the preparation of a lipid monolayer on OT-functionalized gold. ... 68
4.6. Exemplary impedance spectrum of a hybrid membrane on OT-functionalized gold visualized as BODE plot. 69
4.7. Water droplets on glass cover slides before and after treatment with HMDS. 70
4.8. Topography of a glass cover slide before and after functionalization with HMDS. 71
4.9. Fluorescence micrograph of a lipid monolayer on hydrophobically functionalized glass. 72
4.10. FRAP experiment on a lipid monolayer on hydrophobically functionalized glass. 73
4.11. Kinetics of the adsorption of SUVs on hydrophilized silicon/ silicon dioxide wafers. 74
4.12. Fluorescence micrograph of a silicon dioxide surface after addition of TexasRed-DHPE-doped SUVs. 75
4.13. FRAP experiment on a silicon/silicon dioxide wafer after SUV addition. 76
4.14. Fluorescence micrograph of an exemplary lipid bilayer on mica. 77
4.15. Exemplary FRAP experiment on mica after spreading of SUVs. 77
4.16. Topographical map of a solid supported lipid bilayer on mica. 79
4.17. Overview on the different model membrane systems introduced in this study. ... 84
5.1. Growth of *E. coli* cells before and during expression of rCinW2. 88
5.2. LAEMMLI SDS-PAGE gels from cell lysis and immobilized metal ion affinity chromatography. 89

5.3. Comparison of SDS-PAGE gels after protein isolation and purification with or without 4 M urea in all deployed buffers. 90

5.4. Schematic illustration of the steps involved in buffer exchange. 91

5.5. Summary of different approaches to exchange the buffer containing rCinW2. 92

5.6. Two exemplary kinetic studies by RIfS on the adsorption of rCinW2 on membrane-covered surfaces. 94

5.7. Exemplary kinetic data on the binding of rCinY3 to a membrane-covered surface. 95

5.8. Exemplary SPR data for the addition of rCinY3 to a lipid monolayer. 96

6.1. Exemplary adsorption kinetics of C3N13 in sample buffer on a membrane-covered surface. 105

6.2. Fluorescence micrographs before and after addition of C3N13 to a TexasRed-DHPE-labeled lipid bilayer on mica. 106

6.3. Exemplary time series of fluorescence micrographs taken after addition of C3N13 to a TexasRed-DHPE-doped lipid bilayer on mica. 107

6.4. Fluorescence micrographs after addition of FITC-C3N13 to a lipid bilayer on mica. 108

6.5. Statistical analysis of fluorescence intensities of lipid-bound dyes in the brighter membrane domains compared to the surrounding membrane. 109

6.6. Correlative fluorescence micrograph and topography map of membrane stacks formed after addition of C3N13 to a lipid bilayer on mica. 110

6.7. Set of exemplary FDC on a mica-supported membrane covered with stacks formed after addition of C3N13. 112

6.8. Exemplary FRAP experiment on a LCPA-induced membrane stack. 113

6.9. Evolution of the bleach profile during a FRAP experiment on a LCPA-induced membrane stack. 114

6.10. Exemplary fluorescence micrograph of LCPA-induced membrane stacks formed on a lipid monolayer on hydrophobically functionalized glass. 115

6.11. Changes in fluorescence intensity during the growth of LCPA-induced membrane stacks on an exemplary lipid bilayer on mica. 117

6.12. Changes in local fluorescence visualized by an exemplary differential fluorescence micrograph before and after the formation of membrane stacks after addition of C3N13 to a solid supported lipid bilayer on mica. 118

6.13. Exemplary fluorescence micrographs of lipid bilayers on mica labeled with Bodipy-C_{12}HPC or Atto488-DHPE after addition of C3N13 alongside TexasRed-DHPE-doped SUVs. 119

6.14. Overview on FRAP experiments on solid supported lipid bilayers on mica. 120

6.15. Exemplary fluorescence micrographs of membrane stacks formed after addition of C3N13 to solid supported lipid bilayers on mica omitting one or all of the three glycolipids MGDG, DGDG and SQDG. 122

6.16. Exemplary fluorescent micrograph of stack-like structures formed on a DOPC solid supported lipid bilayer in absence of LCPA. 123

6.17. Exemplary FRAP data on stack-like structures formed on DOPC lipid bilayers on mica in absence of LCPA. 124

6.18. Exemplary fluorescence micrographs recorded after the addition of C3N13 and TexasRed-DHPE-labeled SUVs to solid supported DOPC lipid bilayers. 125

6.19. Exemplary fluorescence micrographs after the addition of different polyamines and SUVs to solid supported lipid bilayers on mica. 126

6.20. Exemplary kinetic data on the addition of silicic acid to a membrane-coated surface after adsorption of C3N13. 127

6.21. Three proposed models describing the structure of the domains formed after addition of LCPA to solid supported membranes. 132

6.22. Two different scenarios for a FRAP experiment on membrane stacks. 135

6.23. Two different models for membrane stacks formed and connected to a solid supported lipid bilayer. 137

6.24. Developed model for the structure of membrane stacks formed after LCPA addition to solid supported membranes. 138

6.25. Schematic illustration of three different pools of lipids addressable for LCPA-induced membrane stack formation. 139

6.26. Schematic illustration of the experimental setup to detect an intake of lipid material from solution into the membrane stacks formed after LCPA addition. 141

6.27. Schematic illustration of the formation of stack-like structures observed on pure DOPC membranes in absence of LCPA. 145

App.1. Amino acid sequence of rCinW2. vii

App.2. Amino acid sequence of rCinY3. viii

List of Tables

1.1. Overview on posttranslational modifications in silaffins of different diatom species as well as their influence on silica precipitation. 6
1.2. Overall lipid composition of the diatom *C. meneghiniana*. 9
3.1. Overview on synthetic polyamines with different chain lengths. 20
3.2. Overview on two commercially available short polyamines used in this study. 21
3.3. Composition of media used for cell transformation. 23
3.4. Composition of buffers used during protein isolation and purification. 24
3.5. Buffer solutions used for SDS polyacrylamide gel electrophoresis. 27
3.6. Buffer solutions used for Western blot analysis. 28
3.7. Extinction coefficients of rCinW2 and rCinY3. 29
3.8. Comparison of the overall lipid composition of *Cyclotella meneghiniana* and the lipid composition used in this study for the formation of model membranes. 31
3.9. Composition of sample and spreading buffers. 31
3.10. Liquid subphases used for Π/A-isotherm measurements. 40
3.11. Refractive indices of all layers used as starting points for spectra fitting by the software WinSpall. 44
3.12. Lasers and filters used for confocal laser scanning microscopy. 54
4.1. Exemplary concentration dataset from one preparation. 64
4.2. Molecular surface areas A_{20} at a surface pressure of $\Pi = 20\ \mathrm{mN \cdot m^{-1}}$ and the temperature $T = 20\ °\mathrm{C}$ for the five major lipids used in this study. 65
4.3. Parameters chosen for the fitting of the SPR data. 68
6.1. Overview on lipid mixtures employed to evaluate the need for glycolipids to enable LCPA-induced membrane stacking. 121
App.1. Amino acid composition of rCinW2. vii
App.2. Physical properties of rCinW2. vii
App.3. Amino acid composition of rCinY3. viii
App.4. Physical properties of rCinY3. viii

BIBLIOGRAPHY

[1] S. Mann, *Biomineralization. Principles and concepts in bioinorganic materials chemistry*, Oxford University Press, New York, **2005**.

[2] V. Prasad Shastri, Biomineralization: A confluence of materials science, biophysics, proteomics, and evolutionary biology, *MRS Bull.* **2015**, *40*, 473–477.

[3] A. L. Boskey, Biomineralization: Conflicts, challenges, and opportunities, *J. Cell. Biochem.* **1998**, *72*, 83–91.

[4] H. A. Lowenstam, Minerals formed by organisms, *Science* **1981**, *211*, 1126–1131.

[5] F. Nudelman, N. Sommerdijk, Biomineralization as an inspiration for materials chemistry, *Angew. Chem. Int. Ed.* **2012**, *51*, 6582–6596.

[6] R. Tacke, Milestones in the biochemistry of silicon: From basic research to biotechnological applications, *Angew. Chem. Int. Ed.* **1999**, *38*, 3015–3018.

[7] M. Groß, Das geheimnisvolle Glashaus der Diatomeen, *Nachr. Chem.* **2011**, *59*, 734–736.

[8] M. Sumper, E. Brunner, Learning from diatoms: Nature's tools for the production of nanostructured silica, *Adv. Funct. Mater.* **2006**, *16*, 17–26.

[9] J. Kristiansen, *Biogeography of freshwater algae*, Springer, Dordrecht, London, **2011**.

[10] F. E. Round, R. M. Crawford, D. G. Mann, *The Diatoms. Biology & morphology of the genera*, Cambridge University Press, Cambridge, New York, **1990**.

[11] C. E. Hamm, R. Merkel, O. Springer, P. Jurkojc, C. Maier, K. Prechtel, V. Smetacek, Architecture and material properties of diatom shells provide effective mechanical protection, *Nature* **2003**, *421*, 841–843.

[12] A. J. Milligan, A proton buffering role for silica in diatoms, *Science* **2002**, *297*, 1848–1850.

[13] T. Fuhrmann, S. Landwehr, M. El Rharbi-Kucki, M. Sumper, Diatoms as living photonic crystals, *Appl. Phys. B* **2004**, *78*, 257–260.

[14] N. Kröger, N. Poulsen, Diatoms — From cell wall biogenesis to nanotechnology, *Annu. Rev. Genet.* **2008**, *42*, 83–107.

[15] D. Losic, J. G. Mitchell, N. H. Voelcker, Diatomaceous lessons in nanotechnology and advanced materials, *Adv. Mater.* **2009**, *21*, 2947–2958.

[16] S. A. Crawford, M. J. Higgins, P. Mulvaney, R. Wetherbee, Nanostructure of the diatom frustule as revealed by atomic force and scanning electron microscopy, *J. Phycol.* **2001**, *37*, 543–554.

[17] M. Hildebrand, E. York, J. I. Kelz, A. K. Davis, L. G. Frigeri, D. P. Allison, M. J. Doktycz, Nanoscale control of silica morphology and three-dimensional structure during diatom cell wall formation, *J. Mater. Res.* **2006**, *21*, 2689–2698.

[18] R. W. Drum, H. S. Pankratz, Post mitotic fine structure of *Gomphonema parvulum*, *J. Ultrastruct. Res.* **1964**, *10*, 217–223.

[19] A.-M. M. Schmid, D. Schulz, Wall morphogenesis in diatoms: Deposition of silica by cytoplasmic vesicles, *Protoplasma* **1979**, *100*, 267–288.

[20] M. Hildebrand, S. Kim, D. Shi, K. Scott, S. Subramaniam, 3D imaging of diatoms with ion-abrasion scanning electron microscopy, *J. Struct. Biol.* **2009**, *166*, 316–328.

[21] T. L. Simpson, B. E. Volcani, *Silicon and siliceous structures in biological systems*, Springer-Verlag, New York, **2011**.

[22] E. G. Vrieling, W. W. C. Gieskes, T. P. M. Beelen, Silicon deposition in diatoms: Control by the pH inside the silicon deposition vesicle, *J. Phycol.* **1999**, *35*, 548–559.

[23] Y. D. Amo, M. A. Brzezinski, The chemical form of dissolved Si taken up by marine diatoms, *J. Phycol.* **1999**, *35*, 1162–1170.

[24] M. Hildebrand, B. E. Volcani, W. Gassmann, J. I. Schroeder, A gene family of silicon transporters, *Nature* **1997**, *385*, 688–689.

[25] N. Javaheri, R. Dries, J. Kaandorp, P. Curnow, Understanding the sub-cellular dynamics of silicon transportation and synthesis in diatoms using population-level data and computational optimization, *PLoS Comput. Biol.* **2014**, *10*, e1003687.

[26] K. Thamatrakoln, M. Hildebrand, Silicon uptake in diatoms revisited: A model for saturable and nonsaturable uptake kinetics and the role of silicon transporters, *Plant Physiol.* **2008**, *146*, 1397–1407.

[27] M. J. Knight, L. Senior, B. Nancolas, S. Ratcliffe, P. Curnow, Direct evidence of the molecular basis for biological silicon transport, *Nat. Commun.* **2016**, *7*, 11926-1-11926-11.

[28] N. Poulsen, A. Scheffel, V. C. Sheppard, P. M. Chesley, N. Kröger, Pentalysine clusters mediate silica targeting of silaffins in *Thalassiosira pseudonana*, *J. Biol. Chem.* **2013**, *288*, 20100–20109.

[29] K. Shimizu, Y. Del Amo, M. A. Brzezinski, G. D. Stucky, D. E. Morse, A novel fluorescent silica tracer for biological silicification studies, *Chem. Biol.* **2001**, *8*, 1051–1060.

[30] V. Martin-Jezequel, M. Hildebrand, M. A. Brzezinski, Silicon metabolism in diatoms: Implications for growth, *J. Phycol.* **2000**, *36*, 821–840.

[31] D. J. Belton, O. Deschaume, C. C. Perry, An overview of the fundamentals of the chemistry of silica with relevance to biosilicification and technological advances, *FEBS J.* **2012**, *279*, 1710–1720.

[32] X. Wang, H. C. Schröder, K. Wang, J. A. Kaandorp, Müller, Werner E. G., Genetic, biological and structural hierarchies during sponge spicule formation: From soft sol–gels to solid 3D silica composite structures, *Soft Matter* **2012**, *8*, 9501–9518.

[33] E. Jackson, M. Ferrari, C. Cuestas-Ayllon, R. Fernández-Pacheco, J. Perez-Carvajal, J. de la Fuente, V. Grazú, L. Betancor, Protein-templated biomimetic silica nanoparticles, *Langmuir* **2015**, *31*, 3687–3695.

[34] E. Bäuerlein, Biomineralization of unicellular organisms: An unusual membrane biochemistry for the production of inorganic nano- and microstructures, *Angew. Chem. Int. Ed.* **2003**, *42*, 614–641.

[35] A. Scheffel, N. Poulsen, S. Shian, N. Kröger, Nanopatterned protein microrings from a diatom that direct silica morphogenesis, *PNAS* **2011**, *108*, 3175–3180.

[36] A. Kotzsch, D. Pawolski, A. Milentyev, A. Shevchenko, A. Scheffel, N. Poulsen, A. Shevchenko, N. Kröger, Biochemical composition and assembly of biosilica-associated insoluble organic matrices from the diatom *Thalassiosira pseudonana*, *J. Biol. Chem.* **2016**, *291*, 4982–4997.

[37] N. Kröger, R. Deutzmann, C. Bergsdorf, M. Sumper, Species-specific polyamines from diatoms control silica morphology, *PNAS* **2000**, *97*, 14133–14138.

[38] N. Kröger, R. Deutzmann, M. Sumper, Polycationic peptides from diatom biosilica that direct silica nanosphere formation, *Science* **1999**, *286*, 1129–1132.

[39] S. Wenzl, R. Hett, P. Richthammer, M. Sumper, Silacidins: Highly acidic phosphopeptides from diatom shells assist in silica precipitation *in vitro*, *Angew. Chem. Int. Ed.* **2008**, *120*, 1753–1756.

[40] N. Kröger, R. Wetherbee, Pleuralins are involved in theca differentiation in the diatom *Cylindrotheca fusiformis*, *Protist* **2000**, *151*, 263–273.

[41] E. Brunner, P. Richthammer, H. Ehrlich, S. Paasch, P. Simon, S. Ueberlein, K.-H. van Pée, Chitin-based organic networks: An integral part of cell wall biosilica in the diatom *Thalassiosira pseudonana*, *Angew. Chem. Int. Ed.* **2009**, *48*, 9724–9727.

[42] C. C. Lechner, C. F. W. Becker, Silaffins in silica biomineralization and biomimetic silica precipitation, *Mar. Drugs* **2015**, *13*, 5297–5333.

[43] A. Bernecker, R. Wieneke, R. Riedel, M. Seibt, A. Geyer, C. Steinem, Tailored synthetic polyamines for controlled biomimetic silica formation, *J. Am. Chem. Soc.* **2010**, *132*, 1023–1031.

[44] E. Bäuerlein (Ed.), Biomineralization. *From biology to biotechnology and medical application*, Wiley-VCH, Weinheim, **2000**.

[45] F. Neville, A. Seyfaee, Real-time monitoring of *in situ* polyethyleneimine-silica particle formation, *Langmuir* **2013**, *29*, 14681–14690.

[46] E. Brunner, K. Lutz, M. Sumper, Biomimetic synthesis of silica nanospheres depends on the aggregation and phase separation of polyamines in aqueous solution, *Phys. Chem. Chem. Phys.* **2004**, *6*, 854–857.

[47] C. A. Bauer, D. B. Robinson, B. A. Simmons, Silica particle formation in confined environments via bioinspired polyamine catalysis at near-neutral pH, *Small* **2007**, *3*, 58–62.

[48] M. Sumper, Biomimetic patterning of silica by long-chain polyamines, *Angew. Chem. Int. Ed.* **2004**, *43*, 2251–2254.

[49] N. Kröger, R. Deutzmann, M. Sumper, Silica-precipitating peptides from diatoms: The chemical structure of silaffin-1A from *Cylindrotheca fusiformis*, *J. Biol. Chem.* **2001**, *276*, 26066–26070.

[50] N. Kröger, S. Lorenz, E. Brunner, M. Sumper, Self-assembly of highly phosphorylated silaffins and their function in biosilica morphogenesis, *Science* **2002**, *298*, 584–586.

[51] N. Poulsen, M. Sumper, N. Kröger, Biosilica formation in diatoms: Characterization of native silaffin-2 and its role in silica morphogenesis, *PNAS* **2011**, *100*, 12075–12080.

[52] N. Poulsen, N. Kröger, Silica morphogenesis by alternative processing of silaffins in the diatom *Thalassiosira pseudonana*, *J. Biol. Chem.* **2004**, *279*, 42993–42999.

[53] M. Sumper, R. Hett, G. Lehmann, S. Wenzl, A code for lysine modifications of a silica biomineralizing silaffin protein, *Angew. Chem.* **2007**, *119*, 8557–8560.

[54] S. Wenzl, R. Deutzmann, R. Hett, E. Hochmuth, M. Sumper, Quaternary ammonium groups in silica-associated proteins, *Angew. Chem. Int. Ed.* **2004**, *43*, 5933–5936.

[55] A. I. Manurung, A. R. Pratiwi, D. Syah, M. T. Suhartono, Isolation and characterization of silaffin that catalyze biosilica formation from marine diatom *Chaetoceros gracilis, HAYATI J. Biosci.* **2007**, *14*, 119–122.

[56] E. V. Armbrust, J. A. Berges, C. Bowler, B. Green, D. Martinez, C. Putnam, S. Zhou, A. E. Allen, K. E. Apt, M. Bechner, Brezinski, M.A., Chaal, B.K., A. Chiovitti, A. K. Davis, M. S. Demarest, J. C. Detter, T. Glavina, D. Goodstein, M. Z. Hadi, U. Hellsten, M. Hildebrand, B. D. Jenkins, J. Jurka, V. V. Kapitonov, N. Kröger, W. Lau, T. W. Lane, F. W. Larimer, J. C. Lippmeier, S. Lucas, M. Medina, A. Montsant, M. Obornik, M. Schnitzler Parker, B. Palenik, G. J. Pazour, P. M. Richardson, T. A. Rynearson, M. A. Saito, D. C. Schwartz, K. Thamatrakoln, K. Valentin, A. Vardi, F. P. Wilkerson, D. S. Rokhsar, The genome of the diatom *Thalassiosira pseudonana*: Ecology, evolution, and metabolism, *Science* **2004**, *306*, 79–86.

[57] J. Parkinson, Y. Brechet, R. Gordon, Centric diatom morphogenesis: A model based on a DLA algorithm investigating the potential role of microtubules, *Biochim. Biophys. Acta, Mol. Cell. Res.* **1999**, *1452*, 89–102.

[58] E. G. Vrieling, T. P. M. Beelen, R. A. van Santen, W. W. C. Gieskes, Mesophases of (bio)polymer - Silica particles inspire a model for silica biomineralization in diatoms, *Angew. Chem. Int. Ed.* **2002**, *41*, 1543–1546.

[59] M. Sumper, A phase separation model for the nanopatterning of diatom biosilica, *Science* **2002**, *295*, 2430–2433.

[60] D. H. Robinson, C. W. Sullivan, How do diatoms make silicon biominerals?, *Trends Biochem. Sci.* **1987**, *12*, 151–154.

[61] E. Schnepf, G. Deichgräber, G. Drebes, Morphogenetic processes in *Attheya decora* (*Bacillariophyceae, Biddulphiineae*), *Pl. Syst. Evol.* **1980**, *135*, 265–277.

[62] M. Kates, B. Volcani, Lipid components of diatoms, *Biochim. Biophys. Acta, Lipids Lipid Metab.* **1966**, *116*, 264–278.

[63] V. M. Dembitsky, O. A. Rozentsvet, E. E. Pechenkina, Glycolipids, phospholipids and fatty acids of brown algae species, *Phytochem.* **1990**, *29*, 3417–3421.

[64] S. Khotimchenko, Lipids from the marine alga *Gracilaria verrucosa*, *Chem. Nat. Compd.* **2005**, *41*, 285–288.

[65] M. A. Borowitzka, *Algae for biofuels and energy*. *Developments in Applied Phycology 5*, Springer, Dordrecht, **2013**.

[66] A. Vieler, C. Wilhelm, R. Goss, R. Süß, J. Schiller, The lipid composition of the unicellular green alga *Chlamydomonas reinhardtii* and the diatom *Cyclotella meneghiniana* investigated by MALDI-TOF MS and TLC, *Chem. Phys. Lipids* **2007**, *150*, 143–155.

[67] J. Hoyo, E. Guaus, J. Torrent-Burgués, Monogalactosyldiacylglycerol and digalactosyldiacylglycerol role, physical states, applications and biomimetic monolayer films, *Eur. Phys. J. E* **2016**, *39:39*.

[68] S. Duchêne, P.-A. Siegenthaler, Do glycerolipids display lateral heterogeneity in the thylakoid membrane?, *Lipids* **2000**, *35*, 739–744.

[69] S. Schaller-Laudel, D. Latowski, M. Jemioła-Rzemińska, K. Strzałka, S. Daum, K. Bacia, C. Wilhelm, R. Goss, Influence of thylakoid membrane lipids on the structure of aggregated light-harvesting complexes of the diatom *Thalassiosira pseudonana* and the green alga *Mantoniella squamata*, *Physiol Plantarum* **2017**, *accepted*.

[70] B. Lepetit, R. Goss, T. Jakob, C. Wilhelm, Molecular dynamics of the diatom thylakoid membrane under different light conditions, *Photosynth. Res.* **2012**, *111*, 245–257.

[71] K. Gounaris, J. Barber, Monogalactosyldiacylglycerol: The most abundant polar lipid in nature, *Trends in Biochemical Sciences* **1983**, *8*, 378–381.

[72] I. Brentel, E. Selstam, G. Lindblom, Phase equilibria of mixtures of plant galactolipids. The formation of a bicontinuous cubic phase, *Biochim. Biophys. Acta, Biomembr.* **1985**, *812*, 816–826.

[73] V. Castro, S. V. Dvinskikh, G. Widmalm, D. Sandström, A. Maliniak, NMR studies of membranes composed of glycolipids and phospholipids, *Biochim. Biophys. Acta, Biomembr.* **2007**, *1768*, 2432–2437.

[74] A. A. Foley, A. P. Brain, P. J. Quinn, J. L. Harwood, Permeability of liposomes composed of binary mixtures of monogalactosyldiacylglycerol and digalactosyldiacylglycerol, *Biochim. Biophys. Acta, Biomembr.* **1988**, *939*, 430–440.

[75] K. Gounaris, A. Sen, A. P. Brain, P. J. Quinn, W. Patrick Williams, The formation of non-bilayer structures in total polar lipid extracts of chloroplast membranes, *Biochim. Biophys. Acta, Biomembr.* **1983**, *728*, 129–139.

[76] M. Shimojima, Biosynthesis and functions of the plant sulfolipid, *Prog. Lipid Res.* **2011**, *50*, 234–239.

[77] M. S. Webb, B. R. Green, Permeability properties of large unilamellar vesicles of thylakoid lipids, *Biochim. Biophys. Acta, Biomembr.* **1989**, *984*, 41–49.

[78] M. S. Webb, B. R. Green, Effects of neutral and anionic lipids on digalactosyldiacylglycerol vesicle aggregation, *Biochim. Biophys. Acta, Biomembr.* **1990**, *1030*, 231–237.

[79] R. Kraayenhof, G. J. Sterk, H. W. Wong Fong Sang, K. Krab, R. M. Epand, Monovalent cations differentially affect membrane surface properties and membrane curvature, as revealed by fluorescent probes and dynamic light scattering, *Biochim. Biophys. Acta, Biomembr.* **1996**, *1282*, 293–302.

[80] C. Yang, S. Boggasch, W. Haase, H. Paulsen, Thermal stability of trimeric light-harvesting chlorophyll a/b complex (LHCIIb) in liposomes of thylakoid lipids, *Biochim. Biophys. Acta, Bioenerg.* **2006**, *1757*, 1642–1648.

[81] D. K. Hincha, Effects of α-tocopherol (vitamin E) on the stability and lipid dynamics of model membranes mimicking the lipid composition of plant chloroplast membranes, *FEBS Lett.* **2008**, *582*, 3687–3692.

[82] F. Zhou, S. Liu, Z. Hu, T. Kuang, H. Paulsen, C. Yang, Effect of monogalactosyldiacylglycerol on the interaction between photosystem II core complex and its antenna complexes in liposomes of thylakoid lipids, *Photosynth. Res.* **2009**, *99*, 185–193.

[83] B. Fuks, F. Homblé, Permeability and electrical properties of planar lipid membranes from thylakoid lipids, *Biophys. J.* **1994**, *66*, 1404–1414.

[84] A. Kerth, T. Brehmer, A. Meister, P. Hanner, M. Jakob, R. B. Klösgen, A. Blume, Interaction of a Tat substrate and a Tat signal peptide with thylakoid lipids at the air-water interface, *ChemBioChem* **2012**, *13*, 231–239.

[85] J. Schneider, Y. F. Dufrêne, W. R. Barger, G. U. Lee, Atomic force microscope image contrast mechanisms on supported lipid bilayers, *Biophys. J.* **2000**, *79*, 1107–1118.

[86] R. P. Richter, Him, J. L. K., A. Brisson, Supported lipid membranes, *Mater. Today* **2003**, *6*, 32–37.

[87] R. P. Richter, R. Bérat, A. R. Brisson, Formation of solid-supported lipid bilayers: An integrated view, *Langmuir* **2006**, *22*, 3497–3505.

[88] C. Steinem, A. Janshoff, Modellmembranen auf Oberflächen. Verankert und doch mobil, *Chem. unserer Zeit* **2008**, *42*, 116–127.

[89] Y.-H. M. Chan, S. G. Boxer, Model membrane systems and their applications, *Curr. Opin. Chem. Biol.* **2007**, *11*, 581–587.

[90] H. Brockman, Lipid monolayers: Why use half a membrane to characterize protein-membrane interactions?, *Curr. Opin. Struct. Biol.* **1999**, *9*, 438–443.

[91] Y. Tamba, M. Yamazaki, Single giant unilamellar vesicle method reveals effect of antimicrobial peptide Magainin 2 on membrane permeability, *Biochem.* **2005**, *44*, 15823–15833.

[92] P. van Gelder, F. Dumas, M. Winterhalter, Understanding the function of bacterial outer membrane channels by reconstitution into black lipid membranes, *Biophys. Chem.* **2000**, *85*, 153–167.

[93] C. A. Keller, B. Kasemo, Surface specific kinetics of lipid vesicle adsorption measured with a quartz crystal microbalance, *Biophys. J.* **1998**, *75*, 1397–1402.

[94] M. L. Wagner, L. K. Tamm, Tethered polymer-supported planar lipid bilayers for reconstitution of integral membrane proteins: Silane-polyethyleneglycol-lipid as a cushion and covalent linker, *Biophys. J.* **2000**, *79*, 1400–1414.

[95] T. Stora, J. H. Lakey, H. Vogel, Ion-channel gating in transmembrane receptor proteins: Functional activity in tethered lipid membranes, *Angew. Chem. Int. Ed.* **1999**, *38*, 389–392.

[96] J. R. Silvius, *Thermotropic phase transitions of pure lipids in model membranes and their modifications by membrane proteins*, John Wiley & Sons, Inc., New York, **1982**.

[97] M. Sumper, N. Kröger, Silica formation in diatoms: The function of long-chain polyamines and silaffins, *J. Mater. Chem.* **2004**, *14*, 2059–2065.

[98] M. Abacilar, F. Daus, A. Geyer, Chemoselective silicification of synthetic peptides and polyamines, *Beilstein J. Nanotechnol.* **2015**, *6*, 103–110.

[99] O. Gräb, M. Abacilar, F. Daus, A. Geyer, C. Steinem, 3D-Membrane stacks on supported membranes composed of diatom lipids induced by long-chain polyamines, *Langmuir* **2016**, *32*, 10144–10152.

[100] A. Bernecker, J. Ziomkowska, S. Heitmüller, R. Wieneke, A. Geyer, C. Steinem, Formation of silica precipitates on membrane surfaces in two and three dimensions, *Langmuir* **2010**, *26*, 13422–13428.

[101] H. P. Sørensen, K. K. Mortensen, Advanced genetic strategies for recombinant protein expression in *Escherichia coli*, *J. Biotechnol.* **2005**, *115*, 113–128.

[102] M. Ludolphs, *Spezifität der Wechselwirkung von Collybistin 2 mit Phosphatidylinositolphosphaten: Einfluss der verschiedenen Proteindomänen*. *Dissertation*, Göttingen, **2015**.

[103] J. Porath, Immobilized metal ion affinity chromatography, *Protein Expression Purif.* **1992**, *3*, 263–281.

[104] T.-T. Yip, T. W. Hutchens, Immobilized metal ion affinity chromatography, *Mol. Biotechnol.* **1994**, *1*, 151–164.

[105] V. Gaberc-Porekar, V. Menart, Perspectives of immobilized-metal affinity chromatography, *J. Biochem. Bioph. Methods* **2001**, *49*, 335–360.

[106] M. H. Klapper, The independent distribution of amino acid near neighbor pairs into polypeptides, *Biochem. Biophys. Res. Commun.* **1977**, *78*, 1018–1024.

[107] F. H. Arnold, Metal-affinity separations: A new dimension in protein processing, *Nat. Biotechnol.* **1991**, *9*, 151–156.

[108] U. K. Laemmli, Cleavage of structural proteins during the assembly of the head of bacteriophage T4, *Nature* **1970**, *227*, 680–685.

[109] R. Pitt-Rivers, F. S. A. Impiombato, The binding of sodium dodecyl sulphate to various proteins, *Biochem. J.* **1968**, *109*, 825–830.

[110] S. Magdeldin, *Gel electrophoresis*. *Principles and basics*, InTech, Rijeka, Crotia, **2012**.

[111] H. Schägger, G. von Jagow, Tricine-sodium dodecyl sulfate-polyacrylamide gel electrophoresis for the separation of proteins in the range from 1 to 100 kDa, *Anal. Biochem.* **1987**, *166*, 368–379.

[112] W. Burnette, "Western Blotting": Electrophoretic transfer of proteins from sodium dodecyl sulfate-polyacrylamide gels to unmodified nitrocellulose and radiographic detection with antibody and radioiodinated protein A, *Anal. Biochem.* **1981**, *112*, 195–203.

[113] H. Towbin, T. Staehelin, J. Gordon, Electrophoretic transfer of proteins from polyacrylamide gels to nitrocellulose sheets: Procedure and some applications, *PNAS* **1979**, *76*, 4350–4354.

[114] Y. Feng, Z.-W. Yu, P. J. Quinn, Effect of urea, dimethylurea, and tetramethylurea on the phase behavior of dioleoylphosphatidylethanolamine, *Chem. Phys. Lipids* **2002**, *114*, 149–157.

[115] K. N. Barton, M. M. Buhr, J. S. Ballantyne, Effects of urea and trimethylamine *N*-oxide on fluidity of liposomes and membranes of an elasmobranch, *Am. J. Physiol.* **1999**, *276*, R397-406.

[116] N. Poklar, N. Petrovčič, M. Oblak, G. Vesnaver, Thermodynamic stability of ribonuclease A in alkylurea solutions and preferential solvation changes

accompanying its thermal denaturation: A calorimetric and spectroscopic study, *Protein Sci.* **1999**, *8*, 832–840.

[117] E. Gasteiger, C. Hoogland, A. Gattiker, S. Duvaud, M. R. Wilkins, R. D. Appel, A. Bairoch (Eds.) *The Proteomics Protocols Handbook*, Humana Press, **2005**.

[118] A. Janshoff, C. Steinem, Transport across artificial membranes – An analytical perspective, *Anal. Bioanal. Chem.* **2006**, *385*, 433–451.

[119] L. J. Johnston, Nanoscale imaging of domains in supported lipid membranes, *Langmuir* **2007**, *23*, 5886–5895.

[120] I. Czolkos, A. Jesorka, O. Orwar, Molecular phospholipid films on solid supports, *Soft Matter* **2011**, *7*, 4562–4576.

[121] T. Tadros, J. Lyklema, Adsorption of potential-determining ions at the silica-aqueous electrolyte interface and the role of some cations, *J. Electroanal. Chem. Interfacial Electrochem.* **1968**, *17*, 267–275.

[122] J. Wang, A. G. Kalinichev, R. J. Kirkpatrick, Asymmetric hydrogen bonding and orientational ordering of water at hydrophobic and hydrophilic surfaces: A comparison of water/vapor, water/talc, and water/mica interfaces, *J. Phys. Chem. C* **2009**, *113*, 11077–11085.

[123] D. A. McKeown, M. I. Bell, E. S. Etz, Vibrational analysis of the dioctahedral mica; 2M 1 muscovite, *Am. Mineral.* **1999**, *84*, 1041–1048.

[124] R. Koynova, M. Caffrey, Phases and phase transitions of the phosphatidylcholines, *Biochim. Biophys. Acta, Rev. Biomembr.* **1998**, *1376*, 91–145.

[125] J. A. Braunger, C. Kramer, D. Morick, C. Steinem, Solid supported membranes doped with PIP_2, *Langmuir* **2013**, *29*, 14204–14213.

[126] J. C. Love, L. A. Estroff, J. K. Kriebel, R. G. Nuzzo, G. M. Whitesides, Self-assembled monolayers of thiolates on metals as a form of nanotechnology, *Chem. Rev.* **2005**, *105*, 1103–1170.

[127] J. W. Kuhlmann, I. P. Mey, C. Steinem, Modulating the lateral tension of solvent-free pore-spanning membranes, *Langmuir* **2014**, *30*, 8186–8192.

[128] S. Terrettaz, T. Stora, C. Duschl, H. Vogel, Protein binding to supported lipid membranes: Investigation of the cholera toxin-ganglioside interaction by simultaneous impedance spectroscopy and surface plasmon resonance, *Langmuir* **1993**, *9*, 1361–1369.

[129] C. D. Geddes, J. R. Lakowicz (Eds.), Topics in fluorescence spectroscopy, Springer, New York, **2005**.

[130] S. Bosk, *Dynamische Strukturen am Zellcortex: Aktivierbarkeit und Akkumulation von Ezrin in Abhängigkeit von PIP_2. Dissertation*, Göttingen, **2011**.

[131] V. Shabardina, C. Kramer, B. Gerdes, J. Braunger, A. Cordes, J. Schäfer, I. Mey, D. Grill, V. Gerke, C. Steinem, Mode of ezrin-membrane interaction as a function of PIP_2 binding and pseudophosphorylation, *Biophys. J.* **2016**, *110*, 2710–2719.

[132] M. Ludolphs, D. Schneeberger, T. Soykan, J. Schäfer, T. Papadopoulos, N. Brose, H. Schindelin, C. Steinem, Specificity of collybistin-phosphoinositide interactions, *J. Biol. Chem.* **2016**, *291*, 244–254.

[133] E. W. Radoslovich, The structure of muscovite, $KAl_2(Si_3Al)O_{10}(OH)_2$, *Acta Cryst.* **1960**, *13*, 919–932.

[134] L. Pauling, The structure of the micas and related minerals, *PNAS* **1930**, *16*, 123–129.

[135] E. Bonaccurso, M. Kappl, H.-J. Butt, Hydrodynamic force measurements: Boundary slip of water on hydrophilic surfaces and electrokinetic effects, *Phys. Rev. Lett.* **2002**, *88*, 076103-1-076103-4.

[136] R. P. Richter, A. R. Brisson, Following the formation of supported lipid bilayers on mica: A study combining AFM, QCM-D, and ellipsometry, *Biophys. J.* **2005**, *88*, 3422–3433.

[137] E. B. Cogan, G. B. Birrell, O. H. Griffith, A robotics-based automated assay for inorganic and organic phosphates, *Anal. Biochem.* **1999**, *271*, 29–35.

[138] D. K. Martin, *Nanobiotechnology of biomimetic membranes*, Springer Science+Business Media, LLC, Boston, MA, **2007**.

[139] G. F. Pauli, B. U. Jaki, D. C. Lankin, Quantitative ^1H NMR: Development and potential of a method for natural products analysis, *J. Nat. Prod.* **2005**, *68*, 133–149.

[140] G. F. Pauli, T. Gödecke, B. U. Jaki, D. C. Lankin, Quantitative ^1H NMR. Development and potential of an analytical method: An update, *J. Nat. Prod.* **2012**, *75*, 834–851.

[141] R. Winter, F. Noll, C. Czeslik, *Methoden der biophysikalischen Chemie*, Vieweg + Teubner, Wiesbaden, **2011**.

[142] P. W. Atkins, J. de Paula, *Physikalische Chemie*, Wiley-VCH, Weinheim, **2006**.

[143] H. Mohwald, Phospholipid and phospholipid-protein monolayers at the air/water interface, *Annu. Rev. Phys. Chem.* **1990**, *41*, 441–476.

[144] M. Deleu, M. Paquot, P. Jacques, P. Thonart, Y. Adriaensen, Y. F. Dufrêne, Nanometer scale organization of mixed surfactin/phosphatidylcholine monolayers, *Biophys. J.* **1999**, *77*, 2304–2310.

[145] R. Backov, C. M. Lee, S. R. Khan, C. Mingotaud, G. E. Fanucci, D. R. Talham, Calcium oxalate monohydrate precipitation at phosphatidylglycerol Langmuir monolayers, *Langmuir* **2000**, *16*, 6013–6019.

[146] H. E. Gottlieb, V. Kotlyar, A. Nudelman, NMR chemical shifts of common laboratory solvents as trace impurities, *J. Org. Chem.* **1997**, *62*, 7512–7515.

[147] J. Homola, S. S. Yee, G. Gauglitz, Surface plasmon resonance sensors: Review, *Sens. Actuators, B* **1999**, *54*, 3–15.

[148] J. Homola, Present and future of surface plasmon resonance biosensors, *Anal. Bioanal. Chem.* **2003**, *377*, 528–539.

[149] W. Knoll, Interfaces and thin films as seen by bound electromagnetic waves, *Annu. Rev. Phys. Chem.* **1998**, *49*, 569–638.

[150] N. Horn, M. Kreiter, Plasmon spectroscopy: Methods, pitfalls and how to avoid them, *Plasmonics* **2010**, *5*, 331–345.

[151] J. Homola, M. Piliarik in *Springer Series on Chemical Sensors and Biosensors* (Ed.: J. Homola), Springer Berlin Heidelberg, Berlin, Heidelberg, **2006**.

[152] A. V. Zayats, I. I. Smolyaninov, A. A. Maradudin, Nano-optics of surface plasmon polaritons, *Phys. Rep.* **2005**, *408*, 131–314.

[153] F. Baldini, *Optical chemical sensors,* Springer, Dordrecht, **2006**.

[154] V. Nanduri, A. K. Bhunia, S.-I. Tu, G. C. Paoli, J. D. Brewster, SPR biosensor for the detection of *L. monocytogenes* using phage-displayed antibody, *Biosens. Bioelectron.* **2007**, *23*, 248–252.

[155] C. Ayela, F. Roquet, L. Valera, C. Granier, L. Nicu, M. Pugnière, Antibody–antigenic peptide interactions monitored by SPR and QCM-D, *Biosens. Bioelectron.* **2007**, *22*, 3113–3119.

[156] M. A. Cooper, A. C. Try, J. Carroll, D. J. Ellar, D. H. Williams, Surface plasmon resonance analysis at a supported lipid monolayer, *Biochim. Biophys. Acta, Biomembr.* **1998**, *1373*, 101–111.

[157] Z. Salamon, M. F. Brown, G. Tollin, Plasmon resonance spectroscopy: Probing molecular interactions within membranes, *Trends Biochem. Sci.* **1999**, *24*, 213–219.

[158] M. Signo, *Surface Plasmons on Smooth and Rough Surfaces and on Gratings*, Springer Berlin Heidelberg, **1988**.

[159] M. N. Polyanskiy, *Refractive index database,* http://refractiveindex.info.

[160] *SCHOTT Zemax catalog 2015-07-22*.

[161] A. D. Rakić, A. B. Djurišić, J. M. Elazar, M. L. Majewski, Optical properties of metallic films for vertical-cavity optoelectronic devices, *Appl. Opt.* **1998**, *37*, 5271–5283.

[162] G. Gauglitz, A. Brecht, G. Kraus, W. Mahm, Chemical and biochemical sensors based on interferometry at thin (multi-) layers, *Sens. Actuators, B* **1993**, *11*, 21–27.

[163] G. Gauglitz, Direct optical sensors: Principles and selected applications, *Anal. Bioanal. Chem.* **2005**, *381*, 141–155.

[164] G. Gauglitz, Multiple reflectance interference spectroscopy measurements made in parallel for binding studies, *Rev. Sci. Instrum.* **2005**, *76*, 062224-1-062224-10.

[165] G. Gauglitz, Direct optical detection in bioanalysis: An update*, Anal. Bioanal. Chem.* **2010**, *398*, 2363–2372.

[166] C. Hänel, G. Gauglitz, Comparison of reflectometric interference spectroscopy with other instruments for label-free optical detection, *Anal. Bioanal. Chem.* **2002**, *372*, 91–100.

[167] R. Renneberg, F. Lisdat, *Biosensing for the 21st Century*, Springer-Verlag Berlin Heidelberg, Berlin, Heidelberg, **2008**.

[168] M. Stephan, C. Kramer, C. Steinem, A. Janshoff, Binding assay for low molecular weight analytes based on reflectometry of absorbing molecules in porous substrates, *Analyst* **2014**, *139*, 1987–1992.

[169] R. Krick, R. A. Busse, A. Scacioc, M. Stephan, A. Janshoff, M. Thumm, K. Kühnel, Structural and functional characterization of the two phosphoinositide binding sites of PROPPINs, a β-propeller protein family, *PNAS* **2012**, *109,* E2042.

[170] O. S. Heavens, Optical properties of thin films, *Rep. Prog. Phys.* **1960**, *23*, 1–65.

[171] E. Sackmann, Supported membranes: Scientific and practical applications, *Science* **1996**, *271*, 43–48.

[172] C. Steinem, A. Janshoff, W.-P. Ulrich, M. Sieber, H.-J. Galla, Impedance analysis of supported lipid bilayer membranes: A scrutiny of different preparation techniques, *Biochim. Biophys. Acta, Biomembr.* **1996**, *1279*, 169–180.

[173] E. Barsoukov, J. R. Macdonald, *Impedance spectroscopy. Theory, experiment, and applications*, Wiley-Interscience, Hoboken, N.J, **2005**.

[174] D. Ende, K.-M. Mangold, Impedanzspektroskopie, *Chem. unserer Zeit* **1993**, *27*, 134–140.

[175] J. R. Macdonald, Impedance spectroscopy, *Ann. Biomed. Eng.* **1992**, *20*, 289–305.

[176] H. Coster, J. R. Smith, The molecular organization of bimolecular lipid membranes. A study of the low frequency Maxwell-Wagner impedance dispersion, *Biochim. Biophys. Acta, Biomembr.* **1974**, *373*, 151–164.

[177] R. Fettiplace, D. M. Andrews, D. A. Haydon, The thickness, composition and structure of some lipid bilayers and natural membranes, *J. Membr. Biol.* **1971**, *5*, 277–296.

[178] T. Hanai, D. A. Haydon, J. Taylor, Polar group orientation and the electrical properties of lecithin bimolecular leaflets, *J. Theor. Biol.* **1965**, *9*, 278–296.

[179] J. W. Lichtman, J.-A. Conchello, Fluorescence microscopy, *Nat. Meth.* **2005**, *2*, 910–919.

[180] B. Amos, G. McConnell, T. Wilson. Comprehensive Biophysics in *Comprehensive Biophysics*, 3–23.

[181] P. Davidovits, M. D. Egger, Scanning Laser Microscope, *Nature* **1969**, *223*, 831.

[182] P. Davidovits, M. D. Egger, Scanning Laser Microscope for Biological Investigations, *Appl. Opt.* **1971**, *10*, 1615–1619.

[183] J. G. White, An evaluation of confocal versus conventional imaging of biological structures by fluorescence light microscopy, *J. Cell Biol.* **1987**, *105*, 41–48.

[184] J.-A. Conchello, J. W. Lichtman, Optical sectioning microscopy, *Nat. Meth.* **2005**, *2*, 920–931.

[185] S. Wilhelm, B. Gröbler, M. Gluch, H. Heinz, Confocal laser scanning microscopy principles, *ZEISS Jena*.

[186] R. W. Cole, T. Jinadasa, C. M. Brown, Measuring and interpreting point spread functions to determine confocal microscope resolution and ensure quality control, *Nat. Protoc.* **2011**, *6*, 1929–1941.

[187] Y. Chen, B. C. Lagerholm, B. Yang, K. Jacobson, Methods to measure the lateral diffusion of membrane lipids and proteins, *Methods* **2006**, *39*, 147–153.

[188] D. Axelrod, D. E. Koppel, J. Schlessinger, E. Elson, W. W. Webb, Mobility measurement by analysis of fluorescence photobleaching recovery kinetics, *Biophys. J.* **1976**, *16*, 1055–1069.

[189] F. Savić, *Theorie und Design von FRAP-Experimenten auf komplexen Geometrien*, Springer Fachmedien Wiesbaden, Wiesbaden, **2015**.

[190] A. Fick, Über Diffusion, *Ann. Phys. Chem.* **1855**, *170*, 59–86.

[191] P. Jönsson, M. P. Jonsson, J. O. Tegenfeldt, F. Höök, A method improving the accuracy of fluorescence recovery after photobleaching analysis, *Biophys. J.* **2008**, *95*, 5334–5348.

[192] M. D. Abramoff, P. J. Magalhães, S. J. Ram, Image processing with ImageJ, *Biophotonics intern.* **2004**, 36–42.

[193] A. Janshoff, C. Steinem, Scanning force microscopy of artificial membranes, *ChemBioChem* **2001**, *2*, 798–808.

[194] S. Morandat, S. Azouzi, E. Beauvais, A. Mastouri, K. El Kirat, Atomic force microscopy of model lipid membranes, *Anal. Bioanal. Chem.* **2013**, *405*, 1445–1461.

[195] R. Richter, A. Mukhopadhyay, A. Brisson, Pathways of lipid vesicle deposition on solid surfaces: A combined QCM-D and AFM study, *Biophys. J.* **2003**, *85*, 3035–3047.

[196] C. Canale, M. Jacono, A. Diaspro, S. Dante, Force spectroscopy as a tool to investigate the properties of supported lipid membranes, *Microsc. Res. Tech.* **2010**, *73*, 965–972.

[197] S. Attwood, Y. Choi, Z. Leonenko, Preparation of DOPC and DPPC supported planar lipid bilayers for atomic force microscopy and atomic force spectroscopy, *IJMS* **2013**, *14*, 3514–3539.

[198] H. A. Rinia, B. de Kruijff, Imaging domains in model membranes with atomic force microscopy, *FEBS Lett.* **2001**, *504*, 194–199.

[199] K. El Kirat, S. Morandat, Y. F. Dufrêne, Nanoscale analysis of supported lipid bilayers using atomic force microscopy, *Biochim. Biophys. Acta, Biomembr.* **2010**, *1798*, 750–765.

[200] S. Dieluweit, A. Csiszár, W. Rubner, J. Fleischhauer, S. Houben, R. Merkel, Mechanical properties of bare and protein-coated giant unilamellar phospholipid vesicles. A comparative study of micropipet aspiration and atomic force microscopy, *Langmuir* **2010**, *26*, 11041–11049.

[201] A. Janshoff, C. Steinem, Mechanics of lipid bilayers: What do we learn from pore-spanning membranes?, *Biochim. Biophys. Acta, Mol. Cell. Res.* **2015**, *1853*, 2977–2983.

[202] N. A. Dencher, H. Seelert, A. Poetsch, A. Engel, H. Stahlberg, D. J. Müller, Structural biology: Proton-powered turbine of a plant motor, *Nature* **2000**, *405*, 418–419.

[203] R. Howland, L. Benatar, *A practical guide to scanning probe microscopy*, ThermoMicroscopes, **2000**.

[204] A. Engel, Atomic force microscopy: A powerful tool to observe biomolecules at work, *Trends Cell Biol.* **1999**, *9*, 77–80.

[205] R. Lévy, M. Maaloum, Measuring the spring constant of atomic force microscope cantilevers: Thermal fluctuations and other methods, *Nanotechnology* **2001**, *13*, 33–37.

[206] D. Nečas, P. Klapetek, Gwyddion: An open-source software for SPM data analysis, *Open Physics* **2012**, *10*, 181–188.

[207] D. Y. Kwok, A. W. Neumann, Contact angle measurement and contact angle interpretation, *Adv. Colloid Interface Sci.* **1999**, *81*, 167–249.

[208] F. M. Fowkes, W. A. Zisman, *Contact angle, wettability and adhesion*. *The Kendall award symposium honoring William A. Zisman, Los Angeles, Calif., April 2-3, 1963*, American Chemical Society, Washington, D.C, **1964**.

[209] R. J. Good, Contact angle, wetting, and adhesion: A critical review, *J. Adhes. Sci. Technol.* **1992**, *6*, 1269–1302.

[210] J. Bauer, G. Drescher, M. Illig, Surface tension, adhesion and wetting of materials for photolithographic process, *J. Vac. Sci. Technol., B* **1996**, *14*, 2485–2492.

[211] A. F. Stalder, T. Melchior, M. Müller, D. Sage, T. Blu, M. Unser, Low-bond axisymmetric drop shape analysis for surface tension and contact angle measurements of sessile drops, *Colloids Surf., A* **2010**, *364*, 72–81.

[212] A. F. Stalder, G. Kulik, D. Sage, L. Barbieri, P. Hoffmann, A snake-based approach to accurate determination of both contact points and contact angles, *Colloids Surf., A* **2006**, *286*, 92–103.

[213] M. S. Kent, J. K. Murton, F. J. Zendejas, H. Tran, B. A. Simmons, S. Satija, I. Kuzmenko, Nanosilica formation at lipid membranes induced by the parent sequence of a silaffin peptide, *Langmuir* **2009**, *25*, 305–310.

[214] R. van't Hof, R. A. Demel, K. Keegstra, B. de Kruijff, Lipid-peptide interactions between fragments of the transit peptide of ribulose-1,5-bisphosphate carboxylase/oxygenase and chloroplast membrane lipids, *FEBS Lett.* **1991**, *291*, 350–354.

[215] A. Orth, *Einfluss des Zellkortex auf die Plasmamembran: Modulation von Mikrodomänen in Modellmembranen*. *Dissertation*, Göttingen, **2012**.

[216] C. Bottier, J. Géan, F. Artzner, B. Desbat, M. Pézolet, A. Renault, D. Marion, V. Vié, Galactosyl headgroup interactions control the molecular packing of wheat lipids in Langmuir films and in hydrated liquid-crystalline mesophases, *Biochim. Biophys. Acta, Biomembr.* **2007**, *1768*, 1526–1540.

[217] K. Matsumoto, H. Sakai, K. Ohta, H. Kameda, F. Sugawara, M. Abe, K. Sakaguchi, Monolayer membranes and bilayer vesicles characterized by α- and β-anomer of sulfoquinovosyldiacyglycerol (SQDG), *Chem. Phys. Lipids* **2005**, *133*, 203–214.

[218] A. Sen, W. Williams, P. J. Quinn, The structure and thermotropic properties of pure 1,2-diacylgalactosylglycerols in aqueous systems, *Biochim. Biophys. Acta, Lipids Lipid Metab.* **1981**, *663*, 380–389.

[219] M. Tomoala-Cotişel, J. Zsakó, E. Chifu, P. J. Quinn, Influence of electrolytes on the monolayer properties of saturated galactolipids at the air-water interface, *Chem. Phys. Lipids* **1983**, *34*, 55–64.

[220] D. G. Bishop, J. R. Kenrick, J. H. Bayston, A. S. Macpherson, S. R. Johns, Monolayer properties of chloroplast lipids, *Biochim. Biophys. Acta, Biomembr.* **1980**, *602*, 248–259.

[221] P. Lenz, C. M. Ajo-Franklin, S. G. Boxer, Patterned supported lipid bilayers and monolayers on poly(dimethylsiloxane), *Langmuir* **2004**, *20*, 11092–11099.

[222] B. Sanii, A. N. Parikh, Surface-energy dependent spreading of lipid monolayers and bilayers, *Soft Matter* **2007**, *3*, 974–977.

[223] M. C. Howland, A. R. Sapuri-Butti, S. S. Dixit, A. M. Dattelbaum, A. P. Shreve, A. N. Parikh, Phospholipid morphologies on photochemically patterned silane monolayers, *J. Am. Chem. Soc.* **2005**, *127*, 6752–6765.

[224] T. Ishida, S. Tsuneda, N. Nishida, M. Hara, H. Sasabe, W. Knoll, Surface-conditioning effect of gold substrates on octadecanethiol self-assembled monolayer growth, *Langmuir* **1997**, *13*, 4638–4643.

[225] A. Ulman, Formation and structure of self-assembled monolayers, *Chem. Rev.* **1996**, *96*, 1533–1554.

[226] L. H. Dubois, R. G. Nuzzo, Synthesis, structure, and properties of model organic surfaces, *Annu. Rev. Phys. Chem.* **1992**, *43*, 437–463.

[227] C. D. Bain, G. M. Whitesides, Modeling organic surfaces with self-assembled monolayers, *Angew. Chem. Int. Ed.* **1989**, *28*, 506–512.

[228] C. D. Bain, E. B. Troughton, Y. T. Tao, J. Evall, G. M. Whitesides, R. G. Nuzzo, Formation of monolayer films by the spontaneous assembly of organic thiols from solution onto gold, *J. Am. Chem. Soc.* **1989**, *111*, 321–335.

[229] E. Boubour, R. B. Lennox, Insulating properties of self-assembled monolayers monitored by impedance spectroscopy, *Langmuir* **2000**, *16*, 4222–4228.

[230] M. French, S. E. Creager, Enhanced barrier properties of alkanethiol-coated gold electrodes by 1-octanol in solution, *Langmuir* **1998**, *14*, 2129–2133.

[231] A. L. Plant, Self-assembled phospholipid/alkanethiol biomimetic bilayers on gold, *Langmuir* **1993**, *9*, 2764–2767.

[232] C. R. Vistas, A. C. Águas, G. N. Ferreira, Silanization of glass chips – A factorial approach for optimization, *Appl. Surf. Sci.* **2013**, *286*, 314–318.

[233] R. Förch, H. Schönherr, Jenkins, A. Tobias A, *Surface design*. *Applications in bioscience and nanotechnology*, Wiley-VCH, Weinheim, **2009**.

[234] Z. Salamon, H.A. Macleod, G. Tollin, Coupled plasmon-waveguide resonators: A new spectroscopic tool for probing proteolipid film structure and properties, *Appl. Surf. Sci.* **2013**, *286*, 314–318.

[235] V. M. Kaganer, H. Möhwald, P. Dutta, Structure and phase transitions in Langmuir monolayers, *Rev. Mod. Phys.* **1999**, *71*, 779–819.

[236] J. N. Israelachvili, *Intermolecular and surface forces*. *Revised Third Edition*, Elsevier Science & Technology Books, San Diego, CA, USA, **2011**.

[237] D. M. Small, Lateral chain packing in lipids and membranes, *J. Lipid Res.* **1984**, *25*, 1490–1500.

[238] R. Demel, L. van Deenen, B. A. Pethica, Monolayer interactions of phospholipids and cholesterol, *Biochim. Biophys. Acta*, *Biomembr.* **1967**, *135*, 11–19.

[239] A. J. Hoff, R. Lipowsky (Eds.), Handbook of biological physics, Elsevier, Amsterdam, **2005**.

[240] N. Kučerka, M.-P. Nieh, J. Katsaras, Fluid phase lipid areas and bilayer thicknesses of commonly used phosphatidylcholines as a function of temperature, *Biochim. Biophys. Acta, Biomembr.* **2011**, *1808*, 2761–2771.

[241] J. W. Grate, M. G. Warner, J. W. Pittman, K. J. Dehoff, T. W. Wietsma, C. Zhang, M. Oostrom, Silane modification of glass and silica surfaces to obtain equally oil-wet surfaces in glass-covered silicon micromodel applications, *Water Resour. Res.* **2013**, *49*, 4724–4729.

[242] R. K. Gupta, K. A. Suresh, AFM studies on Langmuir-Blodgett films of cholesterol, *Eur. Phys. J. E* **2004**, *14*, 35–42.

[243] R. Tero, T. Urisu, H. Okawara, K. Nagayama, Deposition of lipid bilayers on OH-density-controlled silicon dioxide surfaces, *J. Vac. Sci. Technol., A* **2005**, *23*, 751–754.

[244] D. Hoekstra, *Cell lipids*, Academic Press, San Diego, **1994**.

[245] A. Benda, M. Beneš, V. Mareček, A. Lhotský, W. T. Hermens, M. Hof, How to determine diffusion coefficients in planar phospholipid systems by confocal fluorescence correlation spectroscopy, *Langmuir* **2003**, *19*, 4120–4126.

[246] C. Scomparin, S. Lecuyer, M. Ferreira, T. Charitat, B. Tinland, Diffusion in supported lipid bilayers: Influence of substrate and preparation technique on the internal dynamics, *Eur. Phys. J. E* **2009**, *28*, 211–220.

[247] R. Macháň, M. Hof, Lipid diffusion in planar membranes investigated by fluorescence correlation spectroscopy, *Biochim. Biophys. Acta, Biomembr.* **2010**, *1798*, 1377–1391.

[248] M. Hetzer, S. Heinz, S. Grage, T. M. Bayerl, Asymmetric molecular friction in supported phospholipid bilayers revealed by NMR measurements of lipid diffusion, *Langmuir* **1998**, *14*, 982–984.

[249] J. M. Boggs, Lipid intermolecular hydrogen bonding: Influence on structural organization and membrane function, *Biochim. Biophys. Acta, Rev. Biomembr.* **1987**, *906*, 353–404.

[250] A. K. Sum, R. Faller, de Pablo, J. J., Molecular simulation study of phospholipid bilayers and insights of the interactions with disaccharides, *Biophys. J.* **2003**, *85*, 2830–2844.

[251] G. van den Bogaart, N. Hermans, V. Krasnikov, A. de Vries, B. Poolman, On the decrease in lateral mobility of phospholipids by sugars, *Biophys. J.* **2007**, *92*, 1598–1605.

[252] G. A. Thompson, Lipids and membrane function in green algae, *Biochim. Biophys. Acta, Lipids Lipid Metab.* **1996**, *1302*, 17–45.

[253] S. Yoshida, M. Uemura, Lipid composition of plasma membranes and tonoplasts isolated from etiolated seedlings of mung bean (*Vigna radiata L.*), *Plant Physiol.* **1986**, *82*, 807–812.

[254] A. Kotzsch, P. Gröger, D. Pawolski, P. Bomans, N. Sommerdijk, M. Schlierf, N. Kröger, A highly conserved diatom membrane protein involved in silica biomineralization **2017**, *submitted*.

[255] T. Weihua, Z. Jingliu, W. Zongyang, H. Mengmin, The cause of deviation made in determining the molecular weight of His-tag fusion proteins by SDS-PAGE, *Acta Phytophysiol. Sinica* **2000**, *26*, 64–68.

[256] G. I. Makhatadze, P. L. Privalov, Protein interactions with urea and guanidinium chloride, *J. Mol. Biol.* **1992**, *226*, 491–505.

[257] Q. Zou, S. M. Habermann-Rottinghaus, K. P. Murphy, Urea effects on protein stability: Hydrogen bonding and the hydrophobic effect, *Proteins Struct. Funct. Bioinf.* **1998**, *31*, 107–115.

[258] B. J. Bennion, V. Daggett, The molecular basis for the chemical denaturation of proteins by urea, *PNAS* **2003**, *100*, 5142–5147.

[259] Y. Oberdörfer, S. Schrot, H. Fuchs, E. Galinski, A. Janshoff, Impact of compatible solutes on the mechanical properties of fibronectin: A single molecule analysis, *Phys. Chem. Chem. Phys.* **2003**, *5*, 1876–1881.

[260] A. Roychoudhury, D. Haussinger, F. Oesterhelt, Effect of the compatible solute ectoine on the stability of the membrane proteins, *PPL* **2012**, *19*, 791–794.

[261] R. K. Harishchandra, S. Wulff, G. Lentzen, T. Neuhaus, H.-J. Galla, The effect of compatible solute ectoines on the structural organization of lipid monolayer and bilayer membranes, *Biophys. Chem.* **2010**, *150*, 37–46.

[262] J. Vörös, The density and refractive index of adsorbing protein layers, *Biophys. J.* **2004**, *87*, 553–561.

[263] *Discover a star-studded cast of competent cells: For all your transformation needs*, Invitrogen life technologies, **2003**.

[264] A. K. Patra, R. Mukhopadhyay, R. Mukhija, A. Krishnan, L. Garg, A. K. Panda, Optimization of inclusion body solubilization and renaturation of recombinant human growth hormone from *Escherichia coli*, *Protein Expression Purif.* **2000**, *18*, 182–192.

[265] C. C. Lechner, C. F. W. Becker, Exploring the effect of native and artificial peptide modifications on silaffin induced silica precipitation, *Chem. Sci.* **2012**, *3*, 3500–3504.

[266] F. R. Schmidt, Recombinant expression systems in the pharmaceutical industry, *Appl. Microbiol. Biotechnol.* **2004**, *65*, 363–372.

[267] C. Putnam, *Protein calculator v3.4,* http://protcalc.sourceforge.net/.

[268] L. Kalmar, D. Homola, G. Varga, P. Tompa, Structural disorder in proteins brings order to crystal growth in biomineralization, *Bone* **2012**, *51*, 528–534.

[269] G. M. Hale, M. R. Querry, Optical constants of water in the 200 nm to 200 μm wavelength region, *Appl. Opt.* **1973**, *12*, 555–563.

[270] S. Bosk, J. A. Braunger, V. Gerke, C. Steinem, Activation of F-actin binding capacity of ezrin: Synergism of PIP_2 interaction and phosphorylation, *Biophys. J.* **2011**, *100*, 1708–1717.

[271] W. Cho, L. Bittova, R. V. Stahelin, Membrane binding assays for peripheral proteins, *Anal. Biochem.* **2001**, *296*, 153–161.

[272] M. Sumper, S. Lorenz, E. Brunner, Biomimetic control of size in the polyamine-directed formation of silica nanospheres, *Angew. Chem. Int. Ed.* **2003**, *42*, 5192–5195.

[273] M. Abacilar, F. Daus, C. Haas, S. I. Brückner, E. Brunner, A. Geyer, Synthesis and NMR analysis of ^{13}C and ^{15}N-labeled long-chain polyamines (LCPAs), *RSC Adv.* **2016**, *6*, 93343–93348.

[274] A. Edreva, Polyamines in plants, *Bulg. J. Plant Physiol.* **1996**, *22*, 73–101.

[275] T. Smith. Biochemistry and physiology of polyamines in plants in *Biochemistry and physiology of polyamines in plants*, 1–22.

[276] S. S. Cohen, *A guide to the polyamines*, Oxford University Press, New York, **1998**.

[277] C. W. Tabor, H. Tabor, Polyamines, *Ann. Rev. Biochem.* **1984**, *53*, 749–790.

[278] H. M. Wallace, The physiological role of the polyamines, *Eur. J. Clin. Invest.* **2000**, *30*, 1–3.

[279] F. Schuber, Influence of polyamines on membrane functions, *Biochem J.* **1989**, *260*, 1–10.

[280] L. Chung, G. Kaloyanides, R. McDaniel, A. McLaughlin, S. McLaughlin, Interaction of gentamicin and spermine with bilayer membranes containing negatively charged phospholipids, *Biochem.* **1985**, *24*, 442–452.

[281] P. Meers, K. Hong, J. Bentz, D. Papahadjopoulos, Spermine as a modulator of membrane fusion: Interactions with acidic phospholipids, *Biochem.* **1986**, *25*, 3109–3118.

[282] F. Schuber, K. Hong, N. Duzgunes, D. Papahadjopoulos, Polyamines as modulators of membrane fusion: Aggregation and fusion of liposomes, *Biochem.* **1983**, *22*, 6134–6140.

[283] K. Hong, F. Schuber, D. Papahadjopoulos, Polyamines: Biological modulators of membrane fusion, *Biochim. Biophys. Acta, Biomembr.* **1983**, *732*, 469–472.

[284] S. Ohki, J. Duax, Effects of cations and polyamines on the aggregation and fusion of phosphatidylserine membranes, *Biochim. Biophys. Acta, Biomembr.* **1986**, *861*, 177–186.

[285] S. Hong, P. R. Leroueil, E. K. Janus, J. L. Peters, M.-M. Kober, M. T. Islam, B. G. Orr, J. R. Baker, M. M. Banaszak Holl, Interaction of polycationic polymers with supported lipid bilayers and cells: Nanoscale hole formation and enhanced membrane permeability, *Bioconjugate Chem.* **2006**, *17*, 728–734.

[286] C. Aulin, I. Varga, P. M. Claesson, L. Wågberg, T. Lindström, Buildup of polyelectrolyte multilayers of polyethyleneimine and microfibrillated cellulose studied by *in situ* dual-polarization interferometry and quartz crystal microbalance with dissipation, *Langmuir* **2008**, *24*, 2509–2518.

[287] T. Baumgart, G. Hunt, E. R. Farkas, W. W. Webb, G. W. Feigenson, Fluorescence probe partitioning between L_o/L_d phases in lipid membranes, *Biochim. Biophys. Acta, Biomembr.* **2007**, *1768*, 2182–2194.

[288] H. A. Rinia, M. M. Snel, J. van der Eerden, B. de Kruijff, Visualizing detergent resistant domains in model membranes with atomic force microscopy, *FEBS Lett.* **2001**, *501*, 92–96.

[289] J. M. Ziomkowska, *Untersuchungen zu Silica präzipitierenden Eigenschaften von Silaffin-Analoga in planaren Membransystemen*. *Diplomarbeit*, Göttingen, **2009**.

[290] J. Chroboczek, Interaction of spermidine with viral RNA and its influence on protein synthesis, *Plant Mol. Biol.* **1985**, *4*, 23–30.

[291] R. W. Wilson, V. A. Bloomfield, Counterion-induced condensation of deoxyribonucleic acid. A light-scattering study, *Biochem.* **1979**, *18*, 2192–2196.

[292] E. Raspaud, M. de la Cruz, J.-L. Sikorav, F. Livolant, Precipitation of DNA by polyamines: A polyelectrolyte behavior, *Biophys. J.* **1998**, *74*, 381–393.

[293] B. Tadolini, Polyamine inhibition of lipoperoxidation. The influence of polyamines on iron oxidation in the presence of compounds mimicking phospholipid polar heads, *Biochem. J.* **1988**, *249*, 33–36.

[294] G. W. Feigenson, Phase diagrams and lipid domains in multicomponent lipid bilayer mixtures, *Biochim. Biophys. Acta, Biomembr.* **2009**, *1788*, 47–52.

[295] P. Cicuta, S. L. Keller, S. L. Veatch, Diffusion of liquid domains in lipid bilayer membranes, *J. Phys. Chem. B* **2007**, *111*, 3328–3331.

[296] V. Parsegianm, N. Fuller, R. P. Rand, Measured work of deformation and repulsion of lecithin bilayers, *PNAS* **1979**, *76*, 2750–2754.

[297] J. Kim, G. Kim, P. S. Cremer, Investigations of water structure at the solid/liquid interface in the presence of supported lipid bilayers by vibrational sum frequency spectroscopy, *Langmuir* **2001**, *17*, 7255–7260.

[298] I. J. Ryrif, J. M. Anderson, D. J. Goodchild, The role of the light-harvesting chlorophyll a/b -protein complex in chloroplast membrane stacking, *Eur. J. Biochem.* **1980**, *107*, 345–354.

[299] E. Janik, J. Bednarska, M. Zubik, M. Puzio, R. Luchowski, W. Grudzinski, R. Mazur, M. Garstka, W. Maksymiec, A. Kulik, G. Dietler, W. I. Gruszecki, Molecular architecture of plant thylakoids under physiological and light stress conditions: A study of lipid-light-harvesting complex II model membranes, *Plant Cell* **2013**, *25*, 2155–2170.

[300] J. Wintermans, Concentrations of phosphatides and glycolipids in leaves and chloroplasts, *Biochim. Biophys. Acta* **1960**, *44*, 49–54.

[301] A. G. Lee, Membrane lipids: It's only a phase, *Curr. Biol.* **2000**, *10*, R377–R380.

[302] S. F. Gilmore, D. Y. Sasaki, A. N. Parikh, Thermal annealing triggers collapse of biphasic supported lipid bilayers into multilayer islands, *Langmuir* **2014**, *30*, 4962–4969.

[303] S. Krol, M. Ross, M. Sieber, S. Künneke, H.-J. Galla, A. Janshoff, Formation of three-dimensional protein-lipid aggregates in monolayer films induced by surfactant protein B, *Biophys. J.* **2000**, *79*, 904–918.

[304] L. A. Lautscham, C. Y. Lin, V. Auernheimer, C. A. Naumann, W. H. Goldmann, B. Fabry, Biomembrane-mimicking lipid bilayer system as a mechanically tunable cell substrate, *Biomat.* **2014**, *35*, 3198–3207.

[305] D. E. Minner, P. Rauch, J. Käs, C. A. Naumann, Polymer-tethered lipid multi-bilayers: A biomembrane-mimicking cell substrate to probe cellular mechano-sensing, *Soft Matter* **2014**, *10*, 1189–1198.

[306] G. R. Heath, M. Li, H. Rong, V. Radu, S. Frielingsdorf, O. Lenz, J. N. Butt, Jeuken, Lars J. C., Multilayered lipid membrane stacks for biocatalysis using membrane enzymes, *Adv. Funct. Mater.* **2017**, *11*, 1606265-1-1606265-9.

[307] V. M. Trusova, G. P. Gorbenko, I. Akopova, J. G. Molotkovsky, I. Gryczynski, J. Borejdo, Z. Gryczynski, Morphological changes of supported lipid bilayers induced

by lysozyme: Planar domain formation vs. multilayer stacking, *Colloids Surf., B* **2010**, *80*, 219–226.

[308] P. G. Adams, L. Lamoureux, K. L. Swingle, H. Mukundan, G. A. Montaño, Lipopolysaccharide-induced dynamic lipid membrane reorganization: Tubules, perforations, and stacks, *Biophys. J.* **2014**, *106*, 2395–2407.

[309] A. M. Liquori, L. Costantino, V. Crescenzi, V. Elia, E. Giglio, R. Puliti, M. De Santis Savino, V. Vitagliano, Complexes between DNA and polyamines: A molecular model, *J. Mol. Biol.* **1967**, *24*, 113–122.

[310] G. R. Heath, M. Li, I. L. Polignano, J. L. Richens, G. Catucci, P. O’Shea, S. J. Sadeghi, G. Gilardi, J. N. Butt, Jeuken, Lars J. C., Layer-by-layer assembly of supported lipid bilayer poly-L-lysine multilayers, *Biomacromol.* **2016**, *17*, 324–335.

[311] E. Wu, K. Jacobson, D. Papahadjopoulos, Lateral diffusion in phospholipid multibilayers measured by fluorescence recovery after photobleaching, *Biochem.* **1977**, *16*, 3936–3941.

[312] M. Kocun, T. D. Lazzara, C. Steinem, A. Janshoff, Preparation of solvent-free, pore-spanning lipid bilayers: Modeling the low tension of plasma membranes, *Langmuir* **2011**, *27*, 7672–7680.

[313] J. Majewski, J. Y. Wong, C. K. Park, M. Seitz, J. N. Israelachvili, G. S. Smith, Structural studies of polymer-cushioned lipid bilayers, *Biophys. J.* **1998**, *75*, 2363–2367.

[314] J. Y. Wong, J. Majewski, M. Seitz, C. K. Park, J. N. Israelachvili, G. S. Smith, Polymer-cushioned bilayers. I. A structural study of various preparation methods using neutron reflectometry, *Biophys. J.* **1999**, *77*, 1445–1457.

[315] J. Y. Wong, C. K. Park, M. Seitz, J. Israelachvili, Polymer-cushioned bilayers. II. An investigation of interaction forces and fusion using the surface forces apparatus, *Biophys. J.* **1999**, *77*, 1458–1468.

[316] S. Chiantia, J. Ries, N. Kahya, P. Schwille, Combined AFM and two-focus SFCS study of raft-exhibiting model membranes, *ChemPhysChem* **2006**, *7*, 2409–2418.

[317] C. R. Daniels, C. Reznik, C. F. Landes, Dye diffusion at surfaces: Charge matters, *Langmuir* **2010**, *26*, 4807–4812.

[318] P. Nollert, H. Kiefer, F. Jähnig, Lipid vesicle adsorption versus formation of planar bilayers on solid surfaces, *Biophys. J.* **1995**, *69*, 1447–1455.

[319] P. S. Cremer, S. G. Boxer, Formation and spreading of lipid bilayers on planar glass supports, *J. Phys. Chem. B* **1999**, *103*, 2554–2559.

[320] I. Reviakine, A. Brisson, Formation of supported phospholipid bilayers from unilamellar vesicles investigated by atomic force microscopy, *Langmuir* **2000**, *16*, 1806–1815.

[321] J. Wilschut, D. Hoekstra, Membrane fusion: From liposomes to biological membranes, *Trends Biochem. Sci.* **1984**, *9*, 479–483.

[322] I. Reviakine, A. Simon, A. Brisson, Effect of Ca^{2+} on the morphology of mixed DPPC−DOPS supported phospholipid bilayers, *Langmuir* **2000**, *16*, 1473–1477.

[323] R. Vácha, Siu, Shirley W. I., M. Petrov, R. A. Böckmann, J. Barucha-Kraszewska, P. Jurkiewicz, M. Hof, M. L. Berkowitz, P. Jungwirth, Effects of alkali cations and halide anions on the DOPC lipid membrane, *J. Phys. Chem. A* **2009**, *113*, 7235–7243.

[324] J. P. Bradshaw, C. E. Dempsey, A. Watts, A combined X-ray and neutron diffraction study of selectively deuterated melittin in phospholipid bilayers: Effect of pH, *Mol. Membr. Biol.* **2009**, *11*, 79–86.

[325] L. R. Cambrea, J. S. Hovis, Formation of three-dimensional structures in supported lipid bilayers, *Biophys. J.* **2007**, *92*, 3587–3594.

[326] L. Renner, T. Osaki, S. Chiantia, P. Schwille, T. Pompe, C. Werner, Supported lipid bilayers on spacious and pH-responsive polymer cushions with varied hydrophilicity, *J. Phys. Chem. B* **2008**, *112*, 6373–6378.

[327] B. Attaf (Ed.), Advances in composite materials for medicine and nanotechnology, InTech, Rijeka, Croatia, **2011**.

[328] J. Mager, The stabilizing effect of spermine and related polyamines and bacterial protoplasts, *Biochim. Biophys. Acta* **1959**, *36*, 529–531.

[329] C. W. Tabor, The stabilizing effect of spermine and related amines on mitochondria and protoplasts, *Biochem. Biophys. Res. Commun.* **1960**, *2*, 117–120.

[330] C. W. Tabor, Stabilization of protoplasts and spheroplasts by spermine and other polyamines, *J. Bacteriol.* **1962**, *83*, 1101–1111.

CURRICULUM VITAE

OLIVER GRÄB

born September, 9th 1987 in Kassel, Germany

Citizenship: German

EDUCATION

2013–2017	**Ph.D. thesis** at the Georg-August University of Göttingen (Prof. Dr. Claudia Steinem). Title of thesis: *Solid Supported Model Membranes Containing Plant Glycolipids: A Tool to Study Interactions between Diatom Biomolecules and the Silicalemma in vitro*
2011–2013	**Graduate studies** in chemistry at the Georg-August University of Göttingen (Prof. Dr. Claudia Steinem). Master thesis: *Sekundärstrukturanalyse Ezrins in Abhängigkeit der PIP_2-Bindung und Phosphorylierung mittels ATR-FTIR-Spektroskopie*, overall grade: 1.4
2008–2011	**Undergraduate studies** in chemistry at the Georg-August University of Göttingen (Prof. Dr. Claudia Steinem). Bachelor thesis: *Rekonstitution von ATP-Synthase in Lipidvesikel*, overall grade: 1.8
2007–2008	**Civil service** at the Evangelisches Forum in Kassel
1998–2007	**Secondary school** at the Albert-Schweitzer-Schule in Kassel, degree: Abitur, overall grade: 1.2
1994–1998	**Elementary school** at the Grundschule Harleshausen in Kassel

PEER-REVIEWED PUBLICATIONS

O. Gräb, M. Abacilar, F. Daus, A. Geyer, C. Steinem, 3D-Membrane stacks on supported membranes composed of diatom lipids induced by long-chain polyamines, *Langmuir* **2016**, *32*, 10144–10152.

ORAL PRESENTATIONS

O. Gräb, *Diatom biomolecules and their interactions with solid supported model membranes*, **DFG FOR 2038 Retreat**, Goslar, Germany, **2016**.

O. Gräb, *Model systems for the SDV: In vitro studies on biomolecule-membrane interactions*, **DFG FOR 2038 Retreat**, Eisenach, Germany, **2015**.

POSTER PRESENTATIONS

O. Gräb, M. Abacilar, F. Daus, A. Geyer, C. Steinem, *Solid supported model membranes from plant lipids and their interactions with long-chain polyamines*, **Annual Meeting of the German Biophysical Society**, Erlangen, Germany, **2016**.

O. Gräb, M. Abacilar, A. Geyer, C. Steinem, *Introduction and application of in vitro model systems for plant plasma membranes*, **22nd International Symposium on Plant Lipids**, Göttingen, Germany, **2016**.

O. Gräb, M. Abacilar, A. Geyer, A. Kotzsch, N. Kröger, C. Steinem, *Model systems for the silica deposition vesicle*, **Engineering Life 2015**, Dresden, Germany, **2015**.

O. Gräb, M. Abacilar, A. Geyer, A. Kotzsch, N. Kröger, C. Steinem, *Silica biomineralization at the SDV membrane surface*, **10th European Biophysics Congress**, Dresden, Germany, **2015**.

TEACHING

SS2016, SS2015, SS2014	Practical course **Biomolekulare Chemie** for master students of chemistry (planning and assistance)
SS2016, SS2015, SS2014	Seminar **Biomolekulare Chemie** for master students of chemistry (planning and assistance)
WS2015/16, WS2014/15, WS2013/14	Seminar and practical course **Chemie für Mediziner** for students of medicine (assistance)
WS2015/16	**Lab student** SARMINI NAGESWARAN
WS2015/16, SS2016	**Master thesis** PHILIPP SCHWARZ: *Isolierung des rekombinanten Proteins SiMat7 aus E. coli und seine Rekonstitution in artifizielle Lipidmembranen*
WS2015/16	**Lab student** PHILIPP SCHWARZ
SS2015	**Bachelor thesis** KRISTINA BREITHAUPT: *Fluoreszenzmarkierung von Silika*
WS2014/15	**Bachelor thesis** VANESSA REUSCHE: *Wechselwirkungsstudien über Silika-präzipitierende Biomoleküle und Lipidmembranen mittels reflektometrischer Interferenzspektroskopie*

DANKSAGUNG

An erster Stelle möchte ich mich bei **PROF. DR. CLAUDIA STEINEM** für die Möglichkeit, meine Promotion in ihrem Arbeitskreis anfertigen zu können, bedanken. Das von ihr vorgeschlagene Thema dieser Arbeit hat von Anfang an mein Interesse gefunden und mir neue Einblicke in ein interessantes Wissenschaftsfeld eröffnet. Während all meiner Arbeiten – sei es bei der Lösung von konkreten fachlichen Problemstellungen oder bis hin zur Vorbereitung diverser Vorträgen – hatte sie immer ein offenes Ohr und konnte mich mit ihrem Rat unterstützen.

PROF. DR. DANIEL JACKSON möchte ich für die freundliche Übernahme des Korreferats danken sowie für die fachliche Unterstützung während des kompletten Verlaufs meiner Promotion.

Zusätzliche möchte ich mich auch bei allen anderen **Mitgliedern der Prüfungskommission** für die Übernahme dieser Aufgabe bedanken.

Für die finanzielle Unterstützung dieses Projektes danke ich der **Deutschen Forschungsgemeinschaft**.

Als Teil der Forschergruppe FOR 2038 möchte ich mich auch bei allen anderen **Nanomee-Mitgliedern** bedanken. Nur durch die enge Zusammenarbeit innerhalb dieser Gruppe wurde diese Arbeit erst möglich gemacht. Zusätzlich möchte ich einigen Mitgliedern noch im besonderen Danken:

Zum einen **PROF. DR. NILS KRÖGER** und seinem Arbeitskreis, insbesondere **DR. ALEXANDER KOTZSCH**, **DAMIAN PAWOLSKI** und **JULIA PALM**. Über den gesamten Verlauf dieser Promotion hatten wir einen sehr engen Austausch gepflegt und ich hatte sogar die Möglichkeit, vor Ort in Dresden die Isolierung von Cingulinen zu erproben. Ich bin froh, dass ich von ausgesprochenen Experten auf diesem Fachgebiet lernen konnte!

Zum anderen **PROF. DR. ARMIN GEYER** und seinen Arbeitskreis, insbesondere **MARYNA ABACILAR** und **FABIAN DAUS**. Sie haben die Synthese der langkettigen Polyamine übernommen und somit einen Großteil dieser Arbeit überhaupt erst ermöglicht.

Der **NMR-Abteilung** gilt mein Dank für die gemeinsame Planung und die Messung sämtlicher NMR-Spektren im Rahmen dieser Arbeit.

DR. INGO MEY möchte ich für seine Diskussionsbereitschaft und viele interessante Ideen danken, die mir während meiner Promotion an so mancher Stelle weitergeholfen haben.

Ein ganz besonderer Dank geht auch an meinen Masterstudenten **PHILIPP SCHWARZ**, meine beiden Bachelorstudentinnen **VANESSA REUSCHE** und **KRISTINA BREITHAUPT** sowie meine Abteilungspraktikantin **SARMINI NAGESWARAN**, die mich durch ihre Arbeit unterstützt haben. Ich hoffe, dass auch ich euch einiges für euren weiteren Weg mitgeben konnte und ihr auch weiterhin so erfolgreich und mit so großer Motivation an der Umsetzung eurer Ziele arbeitet.

JUTTA GERBER-NOLTE und **MICHAELA KLINGEBIEL** möchte ich für die tatkräftige Unterstützung sowohl bei meinen eigenen Experimenten als auch bei der Betreuung der Studenten im Praktikum „Biomolekulare Chemie“ danken.

Dem **Sekretariat** danke ich für die Übernahme und die Hilfe bei zahlreichen organisatorischen Aufgaben.

Des Weiteren möchte ich auch allen anderen Mitgliedern des **Arbeitskreises STEINEM** für die gemeinsame Zeit danken. Durch unsere enge Zusammenarbeit und dem ständigen Wissensaustausch haben wir alle gemeinsam voneinander profitiert und uns gegenseitig weitergeholfen. Aber nicht nur auf fachlicher Ebene war ich froh als Teil dieses Arbeitskreises meine Promotion anfertigen zu können. Ich habe mich in eurer Mitte sehr wohl gefühlt. Durch viele gemeinsame Aktionen wurde der Zusammenhalt in der Gruppe gestärkt und ein sehr angenehmes Arbeitsklima geschaffen. Ich hoffe, dass auch in Zukunft die Tradition von gemeinsamen Grill- und Kegelabenden fortgeführt wird und sich auch zukünftige Mitglieder bei euch so wohl fühlen können, wie ich das getan habe.

Allen **Korrekturlesern** dieser Arbeit möchte ich zusätzlich für Ihre Rückmeldungen und Verbesserungsvorschläge danken.

Bedanken möchte ich mich außerdem bei meinen **Freunden in Kassel und Göttingen**, die mich während der ganzen letzten Jahre immer wieder unterstützt haben und mir geholfen haben, auch immer mal wieder etwas Abstand von der Arbeit zu gewinnen und so neue Kraft zu sammeln.

Zum Schluss möchte ich mich nun noch bei den Menschen bedanken, die mich über all die Jahre hinweg wohl am meisten unterstützt haben: **meinen Eltern und meinen Bruder**. Die Rolle, die euch zukommt, ist nur schwer in Worte zu fassen. Ihr habt mich immer auf meinem Weg unterstützt und mich so motiviert durchzuhalten und weiterzumachen. Ohne euch würde ich sicher nicht an diesem Punkt stehen. Deshalb Danke für alles, was ihr für mich getan habt!